

**Burning Rates and Instabilities in the Combustion of
Droplet and Vapour Mixtures**

by

Shaharin Anwar Sulaiman

Submitted in accordance with the requirements for the degree of
Doctor of Philosophy

School of Mechanical Engineering
The University of Leeds

December 2006

The candidate confirms that the work submitted is his/her own and that appropriate credit has been given where reference has been made to the work of others.

This copy has been supplied on the understanding that it is copyright material and that no quotation from the thesis may be published without proper acknowledgement.

Acknowledgements

I wish to express my gratitude to Dr. Malcolm Lawes, for his invaluable support, guidance and motivation throughout this study. I also wish to thank him for his constructive criticisms during the preparation of this thesis.

I am grateful to, Prof. Derek Bradley for all his help and for his invaluable suggestions in my work. I also wish to thank to Prof. Chris Sheppard and Dr. Alex Burluka for their interest and valuable advice in my work.

I would like to thank Dr. Robert Woolley for his technical help and guidance during the experimental set up and data processing. I would also like to thank Dr. Kexin Liu for his friendship and his assistance in numerical calculations.

My thanks are due to John Groves, Brian Leach and Mark Batchelor from the Thermodynamics Laboratory for their support in the experimental work, Ted Allwood and Graham Blyth for their assistance with computing, and Pat Richardson, Simer Kaur and Fiona Slade for their help and support.

Many thanks are also due to Mohamed Abd-Ellatif, Ali Al-Shahrany, Waleed Alrefae, Novid Behesti, Alla Daud, Matthew Harker, Tim Hattrell, Gunnar Larsson, Harry Mandilas, Numa Marquez, Pascal Nicholas, Matthew Ormsby, Ahmad Murad, Clara Serrano, Mandeep Singh, Andrew Smallbone, Jason Wu and all the others from the Combustion Group for their friendship and assistance throughout the period of research. I would also like to express my thankfulness to Asri Ali, Tabassumul Haque, Nigel Humphreys, Ahmad Kamil, Ugur Malayoglu, Faisal Reza, and Marian Sedley for their support and motivation.

The financial and moral support from Universiti Teknologi Petronas, Malaysia throughout the period of this research is gratefully acknowledged.

Finally, I would like to express my thanks to my parents for their love and encouragement, and to my lovely wife and children for their understanding and support during the last three enduring years.

Abstract

It is well established that the laminar burning rate plays an important role in turbulent combustion and previous work at Leeds has suggested that the laminar burning velocity of an aerosol mixture is little different from that of a gaseous mixture at similar conditions. However, it has been shown that flames within well defined droplet suspensions (aerosols) more readily become unstable than for gaseous ones. Flame instabilities, characterised by wrinkling and cellular surface structure, increase the burning rate due to the associated increase in surface area. For gaseous mixtures, the effect has been shown theoretically and experimentally to be a function of Markstein number and critical Peclet number, which marks the flame radius at which cellularity is first observed. In aerosol combustion, the presence of liquid droplets has been shown to influence instabilities by causing earlier onset of cellularity than for gaseous flames. Therefore it is imperative to conduct a fundamental study to understand the complex interactions between droplets and combustion.

In the present work, spherically expanding flames were employed to quantify the burning rates in gaseous and aerosol flames and to determine their differences. Iso-octane-air aerosols were generated by expansion of the gaseous pre-mixture, based on the Wilson cloud chamber principle of expansion cooling, to produce a homogeneously distributed suspension of fuel droplets. Flames were centrally ignited for quiescent aerosols at near atmospheric pressures, drop sizes of up to 30 μm and overall equivalence ratios between 0.8 to 2.0. The flame progress was monitored using high-speed schlieren photography, from which burning rates were determined. In turbulent studies, measurements were made for stoichiometric aerosols at root mean square turbulence velocities of between 1.0 and 4.0 m/s. For comparison, gaseous combustion at conditions similar to those of aerosols were studied.

From the laminar study, it was shown that the burning rate of lean mixtures is independent of droplet diameter. However, at higher equivalence ratios, the burning rate became a strong function of droplet diameter and equivalence ratio. This was associated with the onset of instabilities, which were, in turn, related to measured values of Markstein number and critical Peclet number for aerosol flames in a similar manner to those for gaseous flames. Heat loss from the flame due to droplet evaporation is probably the main reason for instabilities in aerosol flames. Interestingly, droplets which were assumed by previous workers to be fully evaporated at the flame front, were shown, at certain conditions in the present work,

to survive behind the flame front. Thus other possible mechanisms for instabilities in aerosol flames could be important.

For very rich mixtures, gaseous flames were shown to be partially smooth, slow, and were strongly affected by natural convection. Conversely, with the presence of droplets at similar mixture conditions, flames were found to be fully cellular and faster, with little sign of the effect of natural convection. This was suggested to be due to early instabilities caused by the presence of droplets, which, in turn, increased the burning rates.

Oscillating flames, in which the flame speed and flame structure alternated between low and high values and smooth and cellular respectively, during flame development, were observed for some experimental conditions. These oscillations were most probably caused by aerodynamic interaction between droplets and gas motion ahead of the flame. This was examined using simultaneous laser sheet imaging and PIV analysis, with a simple model proposed by Atzler *et al.* (2001) which simulated aerodynamic interaction between droplets and gas phase motion ahead of the flame front.

A dimensionless comparison between turbulent flames of aerosol and gaseous mixtures showed similar burning rates. The measurements were compared with existing turbulent burning velocity expressions and correlations. In general, these expressions are in quite good agreement with the present results, particularly at low stretch rate.

Publications

The following papers, based on sections of this thesis, have been published or are in preparation:

1. Lawes, M., Marquez, N, and *Sulaiman, S. A.*, On Instabilities and Flame Structures of Laminar Aerosol Flames, Proc. of the European Combustion Meeting 2005, Paper No. 81, Louvain-la-Neuve, Belgium, 2005.
2. Atzler, F., Lawes, M., *Sulaiman, S. A.*, and Woolley, R., Effects of Droplets on the Flame Speed of Laminar Iso-Octane and Air Aerosols, ICLASS06, Paper No. E4- 04-258, Kyoto, Japan, 2006.
3. Atzler, F., Lawes, M., Lee, Y., and *Sulaiman, S. A.*, Burning Velocities and Instabilities in Centrally Ignited Laminar Aerosol Flames of Iso-octane-Air Mixtures, Combustion and Flame, in preparation.

Contents

Acknowledgements	ii
Abstract.....	iii
Publications	v
Contents	vii
List of Figures.....	ix
List of Tables	xv
Nomenclature	xvii
Chapter 1 Introduction.....	1
1.1. Overview of Trends in Practical Spray Combustion	2
1.2. Burning Rate and Markstein Lengths	4
1.3. Effect of Instabilities in Laminar Flames.....	7
1.4. Turbulent Premixed Flames	10
1.5. Characterisation of Droplet Clouds	13
1.6. Fundamentals of Spray Combustion.....	16
1.6.1. Categories of Aerosol Combustion Analyses	16
1.6.2. Laminar Flames within Droplet Clouds.....	19
1.6.3. Turbulent Flames within Droplet Clouds	21
1.7. Objectives	22
1.8. Thesis Outline.....	23
Chapter 2 Apparatus and Techniques	32
2.1. Combustion Vessel	32
2.1.1. Explosion Vessel	33
2.1.2. Expansion System.....	35
2.1.3. Ignition Systems.....	36
2.1.3.1. Electric Discharge Spark Ignition	36
2.1.3.2. Laser Induced Ignition	36
2.2. Synchronization And Data Acquisition System.....	37
2.3. Mixture Preparation.....	38
2.3.1. Pre-Heating of the Explosion Vessel	39

2.3.2. Preparation of Gaseous Pre-Mixtures	40
2.3.3. Generation of Aerosols	41
2.4. Instrumentation for Aerosol and Flame Analysis	41
2.4.1. Phase Doppler Anemometer System	42
2.4.2. Laser Attenuation System	43
2.4.3. High Speed Schlieren Photography	45
2.4.4. Laser Sheet Imaging.....	46
2.4.4.1. Technique of Laser Sheet Imaging	46
2.4.4.2. Analysis of Planar Laser Sheet Images	47
2.4.4.3. Particle Image Velocimetry.....	48
Chapter 3 Characterisation of Aerosols.....	57
3.1 Aerosol Property Calculations	57
3.1.1. Gas Phase in Equilibrium	58
3.1.2. Mass Fraction and Equivalence Ratio.....	59
3.2. Temperature and Pressure Measurements	63
3.2.1. Initially Quiescent Conditions	63
3.2.2. Turbulent Conditions	64
3.3. Droplet Size Measurements	65
3.3.1. Initially Quiescent Conditions	65
3.3.2. Turbulent Conditions	67
3.4. Droplet Number Density.....	67
3.4.1. Initially Quiescent Conditions	68
3.4.2. Turbulent Conditions	70
3.5. Summary.....	71
Chapter 4 Results	82
4.1 Laminar Flame Observations.....	82
4.1.1. Ignition.....	83
4.1.2. Laminar Flame Propagation.....	84
4.1.3. Comparison of Flame Images Obtained with Different Cameras	86
4.1.4. Laser Sheet Images	87
4.1.5. Effects of Flying Molten Metals from Spark Electrodes	89

4.2. Burning Rates of Laminar Gaseous and Aerosol Flames	92
4.2.1. Initially Stable Flames	93
4.2.2. Flames with Early Onset of Instabilities	96
4.3. Instabilities due to Buoyancy Effects	99
4.4. Oscillating Flames	101
4.5. Turbulent Flame Observation	104
4.6. Burning Rates of Turbulent Gaseous and Aerosol Flames	106
4.6.1. Gaseous Studies	106
4.6.2. Aerosol Studies	108
Chapter 5 Discussion	138
5.1 Ignitibility of Quiescent Aerosol	138
5.1.1. Effect of Droplet Size	139
5.1.2. Effect of Ignition Energy	140
5.2 Laminar Burning Rates	141
5.2.1. Enhancement in Burning Rates	141
5.2.2. Instabilities in Laminar Flames of Aerosols	146
5.2.3. Mechanisms for Oscillating Flames	149
5.2.3.1. Effect of Acoustic Waves	149
5.2.3.2. Effect of Radiation from Burning Particles	149
5.2.3.3. Effect of Droplet Inertia	150
5.3 Turbulent Studies	156
5.3.1. Flame and Droplet Induced Turbulence	156
5.3.2. Effects of Stretch Rate and Turbulence	157
Chapter 6 Conclusions and Suggestions for Further Research	169
6.1 Conclusions	169
6.2 Suggestions for Further Research	178
References	182
Appendix	195

List of Figures

Figure 1.1	Variation of flame speed with flame stretch for a methane-air mixture at 512 kPa and 350 K. Reproduced from Haq (1998).....	27
Figure 1.2	Typical sequences of photographs of cellular flames for premixed iso-octane-air showing spectrum of different cell sizes. The mixture was ignited at $\phi = 1.5$, $T = 303$ K and $P = 100$ kPa.....	27
Figure 1.3	Theoretical wave numbers, n , at limits of flame stability for different Ma_{sr} , as a function of Peclet number, with $\sigma = 6$. Shaded area is peninsular of instability for $Ma_{sr} = 8$. Reproduced from Bradley <i>et al.</i> (2000).....	28
Figure 1.4	Sketch of the modified peninsular of instabilities, as in Fig. 1.3, with the allowance for a lag in the full development of the instability	29
Figure 1.5	Correlation of turbulent burning velocities. Broken curves show $R_L/(Le)^2$, with R_L evaluated for the fully developed r.m.s. turbulent burning velocity, u' , equal to u'_k . Reproduced from Bradley (1992)	29
Figure 1.6	Schematic of liquid-spray group combustion (Chiu and Croke, 1981, Chiu, 1995)	30
Figure 1.7	Variation of flame speed with droplet size and mass fraction for stoichiometric iso-octane droplet-vapour-air mixture at atmospheric pressure. Reproduced from Polymeropoulos (1984).....	30
Figure 1.8	Influence of mainstream velocity and mean drop size on flame speed. Reproduced from (Myers and Lefebvre, 1986).....	31
Figure 2.1	Photograph of the cylindrical explosion vessel, with one end plate removed. Reproduced from Marquez (2003).....	51
Figure 2.2	Schematic of aerosol combustion apparatus with schlieren system. Reproduced from Atzler (1999).....	52
Figure 2.3	Schematic of laser ignition optical setup	53
Figure 2.4	Arrangement of PDA apparatus for droplet size measurement	53
Figure 2.5	Experimental set-ups for laser attenuation and schlieren measurements.....	54
Figure 2.6	Schematic of the control circuit for ignition, camera and laser systems	54
Figure 2.7	Schematic of laser sheet imaging system. Reproduced from Marquez (2003)	55

Figure 2.8	Variation of number of white pixels with radial distance from electrode for determination of flame radius from a typical laser sheet image	55
Figure 2.9	Computed composition and temperature profiles for a one-dimensional adiabatic premixed flame in a stoichiometric methane-air mixture at 100 kPa and 300 K. Reproduced from Haq (1998).	56
Figure 2.10	(a) Ideal digitised image divided into equal interrogation areas, (b) Ideal interrogation area showing particle displacement. Reproduced from Atashkari (1997)	56
Figure 3.1	Expansion paths for iso-octane in the present work on (a) P_f-v diagram, and (b) $T-s$ diagram	74
Figure 3.2	Variation in pressure and temperature in the explosion vessel with time during the expansion of initially quiescent stoichiometric iso-octane-aerosol from 200 kPa and 303 K	75
Figure 3.3	Typical average variation in pressure and temperature with time for stoichiometric turbulent iso-octane aerosols expanded from 200 kPa and 303 K at u' of 1.0 m/s	75
Figure 3.4	Variation of individual droplet diameter, D_{10} , and standard deviation $\sigma_{D_{10}}$ with time for initially quiescent iso-octane-air aerosol ($\phi_{ov} = 0.8$) expanded from 250 kPa and 303 K	76
Figure 3.5	Variation of D_{10} with time for initially quiescent iso-octane-air aerosol expanded from 250 kPa and 303K at various equivalence ratios	76
Figure 3.6	Spatial variation of individual droplet diameter and σ_D with time for iso-octane aerosols ($\phi_{ov} = 1.0$) expanded from 200 kPa and 303 K at six different positions in the explosion vessel. Reproduced from Marquez (2003).	77
Figure 3.7	Variation of droplet diameter with time for turbulent iso-octane-air aerosol expanded from 200 kPa and 303 K; at $u' = 1.0$ m/s, at various ϕ_{ov}	77
Figure 3.8	Variation of D_{10} with time for turbulent stoichiometric iso-octane-air aerosol expanded from 200 kPa, 303K at various u'	78
Figure 3.9	Variations of droplet number density and laser power attenuation with time from start of expansion for initially quiescent stoichiometric iso-octane aerosols expanded from various initial pressures	78
Figure 3.10	Variations of droplet number density and laser power attenuation with time from start of expansion for initially quiescent iso-octane aerosols expanded from 200 kPa and 303K, at various ϕ_{ov}	79
Figure 3.11	Comparison of laser power attenuation results with those of Marquez (2003), for iso-octane aerosols ($\phi_{ov} = 1.0$) expanded from 150 and 250 kPa	79

Figure 3.12	Typical multiple laser power attenuation produced by clouds of initially quiescent iso-octane aerosols at $\phi_{ov} = 1.0$ expanded from 200 kPa, 303 K	80
Figure 3.13	Laser power attenuation produced by clouds of turbulent stoichiometric iso-octane aerosols expanded from 200 kPa, 303 K, at various u'	80
Figure 3.14	Typical variation of droplet size and number density of droplets, temperature and fuel mass against time for initially quiescent iso-octane aerosols expanded from 250 kPa, 303 K, at $\phi_{ov} = 1.0$	81
Figure 4.1	Effect of droplets on ignition and initial kernel growth. A gaseous flame and several aerosol flames with different droplet diameters are shown for iso-octane-air at $\phi_{ov} = 2.0$, (a) schlieren images for up to 3 ms after ignition, (b) variation of flame speed with radius. The circles indicate the flame radius at 2 ms after ignition	114
Figure 4.2	Sequences of schlieren images of flames within aerosols at $\phi_{ov} = 1.0$, and (a) $P = 185$ kPa, $T = 281$ K, and $\phi_g = 0.92$, (b) $P = 172$ kPa, $T = 278$ K, and $\phi_g = 0.78$, and (c) $P = 155$ kPa, $T = 272$ K, and $\phi_g = 0.63$	115
Figure 4.3	Comparison, at various ϕ_{ov} , between schlieren images of flames for iso-octane-air aerosols at $D_{10} = 8$ μm and pressures and temperatures between 122 and 170 kPa, and 271 and 292 K respectively, and for the equivalent gaseous flames at $P = 100$ kPa, $T = 303$ K; $r \approx 50$ mm.....	116
Figure 4.4	Map of flame regimes for iso-octane-air mixtures at various ϕ_{ov} , D_{10} , pressures between 90 and 150 kPa, and temperatures between 260 and 303 K.....	117
Figure 4.5	Comparison of observed flame structures of iso-octane-air aerosol at $\phi_{ov} = 1.2$ obtained by different imaging recording systems; (a) with digital camera, at $P = 139$ kPa, $T = 279$ K, $D_{10} = 10$ μm , and (b) with drum camera (Atzler, 1999) $P = 137$ kPa, $T = 278$ K, $D_{32} = 10$ μm	118
Figure 4.6	Typical laser sheet image of iso-octane aerosol droplet flame at $\phi_{ov} = 0.8$, $D_{10} = 12$ μm , $P = 110$ kPa, $T = 265$ K, $r \approx 69$ mm	119
Figure 4.7	Sequences of simultaneous laser sheet and schlieren images for iso-octane-air aerosol at $\phi_{ov} = 1.0$, $P = 162$ kPa, $T = 277$ K, $D_{10} = 17$ μm	119
Figure 4.8	Natural light imaging of spark in air at $P = 100$ kPa and $T = 303$ K....	120
Figure 4.9	Natural imaging of laminar flames for aerosol at $\phi_{ov} = 1.2$, $P = 112$ kPa, $T = 271$ K and $D_{10} = 24$ μm	120
Figure 4.10	Schlieren images of laminar flames for aerosol at $\phi_{ov} = 1.0$, $P = 89$ kPa and $T = 268$ K; (a) with laser ignition, and (b) with electric discharge spark ignition.	121

Figure 4.11	Variation of flame speeds with (a) radius and (b) stretch rate, for gaseous iso-octane-air at $\phi_{ov} = 0.8$, $P = 100$ kPa, and $T = 303$ K	122
Figure 4.12	Variation of flame speed with time after ignition for aerosols at $D_{10} = 8$ μm , and $\phi_{ov} = 0.8$ (triangles), $\phi_{ov} = 1.0$ (circles), and $\phi_{ov} = 1.2$ (diamonds). Also shown for each case are flame contour tracings throughout propagation at intervals of 2 ms.....	122
Figure 4.13	Variation of flame speed with radius for the aerosol flames in Fig. 4.12. Also shown for each case are the last flame images within the field of view of the access windows	123
Figure 4.14	Variation of flame speed with stretch for the aerosol flames in Fig. 4.12	123
Figure 4.15	Variation of u_l with D_{10} for iso-octane-air aerosol flames at various ϕ_{ov} ...	124
Figure 4.16	Variation of Ma_{sr} with D_{10} for iso-octane-air aerosol flames at pressures of between 82 and 241 kPa, temperatures of between 265 and 287 K, and various equivalence ratios	125
Figure 4.17	Typical variation of flame speed with stretch rate for rich iso-octane-air aerosols; crosses are for $\phi_{ov} = 1.2$ and $D_{10} = 4$ μm , and circles are for $\phi_{ov} = 1.6$ and $D_{10} = 14$ μm	125
Figure 4.18	Variation of $S_{n,48}$ with ϕ_{ov} and D_{10} for iso-octane-air mixtures.....	126
Figure 4.19	Flame propagation distance from spark electrode as a function of time from start of ignition for iso-octane-air mixtures at $\phi_{ov} = 2.0$; (a) gaseous and (b to d) aerosol	127
Figure 4.20	Comparison of vertical flame propagation distance from spark electrode as a function of time for iso-octane-air gaseous and aerosol at $\phi_{ov} = 2.0$. Negative distances indicate downward flame propagation	128
Figure 4.21	Typical variation of flame speed with radius for an oscillating flame of iso-octane-air aerosol at $\phi_{ov} = 0.8$, $D_{10} = 12$ μm , $P = 110$ kPa, $T = 265$ K. Also shown are the corresponding schlieren images and superimposition of flame edges throughout propagation.....	129
Figure 4.22	Variation of flame speed with radius for iso-octane-air aerosol at $\phi_{ov} = 0.8$ and D_{10} of 12 and 15 μm	130
Figure 4.23	Variation of flame speed with radius for iso-octane-air aerosol at $\phi_{ov} = 0.8$ at D_{10} between 0 and 15 μm , pressures between 94 and 138 kPa, and temperatures between 261 and 277 K.....	130
Figure 4.24	Typical velocity vectors obtained from PIV analysis of laser sheet images of droplets between 44 ms and 45 ms after ignition, for an oscillating flame of iso-octane-air aerosol at $D_{10} = 12$ μm , $P = 110$ kPa and $T = 264$ K.....	131

Figure 4.25	Schlieren images of turbulent flames in stoichiometric iso-octane-air using the same spark electrode and energy for, (a) to (e) aerosols at $P = 128$ kPa, $T = 283$ K, $D_{10} = 4$ μm , and u' as shown, and (f) gas at $u' = 4.0$ m/s, $P = 100$ kPa, $T = 303$ K.....	132
Figure 4.26	Laser sheet images of flames of turbulent stoichiometric iso-octane-air mixtures at $P = 128$ kPa, $T = 283$ K, and (a) $u' = 1.0$ m/s and (b) $u' = 4.0$ m/s.....	133
Figure 4.27	Schlieren image of turbulent flames with laser ignition for stoichiometric iso-octane-air aerosol at same conditions with that in Fig. 4.25(e).....	133
Figure 4.28	Flame radius against time for turbulent gaseous mixtures of stoichiometric iso-octane-air ignited using different ignition energies at $P = 100$ kPa, $T = 303$ K and u' of 1.0 and 4.0 m/s	134
Figure 4.29	Magnification of the initial stage of the graph in Fig. 4.28. For clarity, the symbols have been removed	134
Figure 4.30	Variation of S_t with time for the turbulent gaseous flames in Fig. 4.28.....	135
Figure 4.31	Variation of S_t with radius for the turbulent gaseous flames in Fig. 4.28... ..	135
Figure 4.32	Variation of average S_t with time for the turbulent gaseous flames in Fig. 4.30	136
Figure 4.33	Variation of average S_t with radius for the turbulent gaseous flames in Fig. 4.31	136
Figure 4.34	Variation of S_t with time for turbulent flames of stoichiometric iso-octane aerosol ignited at $P = 128$ kPa, $T = 283$ K, $D_{10} = 4$ μm , and u' of 1.0 and 2.5 m/s	137
Figure 4.35	Variation of S_t with radius for turbulent flames of stoichiometric iso-octane aerosol ignited at $P = 128$ kPa, $T = 283$ K, $D_{10} = 4$ μm , and u' of 1.0 and 2.5 m/s	137
Figure 5.1	Effect of droplet size on the predicted minimum ignition energy calculated using the correlations of Ballal and Lefebvre (1978). Data are for stoichiometric iso-octane-air aerosol at $P = 100$ kPa, $T = 270$ K.....	160
Figure 5.2	Variation of ignition energy with spark duration for kerosene sprays ($\phi_{ov} = 0.75$) in flowing air at various air velocities and mean droplet sizes. Reproduced from Rao and Lefebvre (1976)	160
Figure 5.3	Variation of flame speed with radius for stoichiometric methane-air mixtures at different ignition energies. Reproduced from Bradley <i>et al.</i> (1996)	161
Figure 5.4	Variation of flame speed with radius for different ignition types and energies. Laminar flames within aerosols at $\phi_{ov} = 1.0$, $T = 270$ K, $P = 120$ kPa and $D_{10} = 14$ μm	161

Figure 5.5	Pe_{cl} and Pe_{cr} for stoichiometric iso-octane-air aerosol flames as a function of D_{10} , at pressures of between 134 and 185 kPa, and temperatures of between 267 and 281 K.....	162
Figure 5.6	Variations of Pe_{cl} with Ma_{sr} for various gaseous flames. Reproduced from Gu <i>et al.</i> (2000).....	162
Figure 5.7	Variations of Pe_{cl} with Ma_{sr} for aerosol flames at $\phi_{ov} = 1.0$ (diamonds and crosses) and at $\phi_{ov} = 1.1$ (circles). Also shown is the linear curve fit for the gaseous flames (Gu <i>et al.</i> , 2000) in Fig. 5.6.....	163
Figure 5.8	Dimensionless burning velocity, u_n / u_{n-Pecl} , as a function of Pe for gaseous and aerosol iso-octane-air flames.....	164
Figure 5.9	Dimensionless burning velocity, u_n / u_{n-Pecl} , as a function of Pe for aerosol and gaseous flames, obtained from data of previous works..	164
Figure 5.10	Estimation of droplet lifetime using the d^2 -law for stoichiometric iso-octane-air aerosol at $P = 100$ kPa, $T = 273$ K, assuming $T_\infty = 2275$ K.....	165
Figure 5.11	Graphical representation of Eq. (5.4). Variation of ϕ , S_n , u_g and u_l with u_D for an iso-octane aerosol at $\phi_{ov} = 1.0$ and $\phi_g = 0.75$. Reproduced from Atzler <i>et al.</i> (2001).....	165
Figure 5.12	Variation of S_n with time for an oscillating aerosol flame of iso-octane; comparison of experimental ($\phi_{ov} = 1.0$, $\phi_g = 0.75$) and numerical results ($\phi_{ov} = 0.95$). Reproduced from Atzler <i>et al.</i> (2001).....	166
Figure 5.13	Variation of S_n , u_g , and u_D with time after ignition for an aerosol flame at $\phi_{ov} = 0.8$, $P = 110$ kPa, $T = 265$ K, $D_{10} = 12$ μm . Also shown are values of S_n , estimated by Marquez (2003), for gaseous flames at $\phi = 0.59$, $\phi = 0.8$ and $\phi = 1.1$	166
Figure 5.14	Variation of S_t with time for the turbulent flames in Figs. 4.31 and 4.34 at $u' = 1.0$ m/s.....	167
Figure 5.15	Variation of S_t with radius for the turbulent flames in Fig. 4.30 and 4.35 at $u' = 1.0$ m/s.....	167
Figure 5.16	Comparison of the variation of turbulent burning velocity in terms of dimensionless groups for iso-octane-air flames at $\phi_{ov} = 1.0$	168
Figure 5.17	Variations of $U (u_l/u_k')$ with $K Ma_{sr}$ for iso-octane-air in the present work and Ormsby (2005), and for the theoretical expression by Bradley <i>et al.</i> (2005).....	168

List of Tables

Table 1.1	Relationship between drop size and drop spacing as a function of fuel and equivalence ratio, calculated by Atzler (1998) for 293 K, 100 kPa, vapour-liquid equilibrium.....	24
Table 1.2	Characteristics of group combustion modes (Chiu and Liu, 1977, and Nakamura et al., 2005).....	25
Table 1.3	Main characteristics of droplet generator types; reproduced from (Gokalp et al., 1999).....	26
Table 3.1	Initial (pre-expansion) conditions for aerosol characterisation in the present work.....	73
Table 4.1	Laminar aerosol flames investigated in the present work.....	109

Nomenclature

A	m^2, mm^2	flame area
B		Spalding number or transfer number
c	$\text{J kg}^{-1}\text{K}^{-1}$	heat capacity of a solid
c_p	$\text{J kg}^{-1}\text{K}^{-1}$	specific heat (at constant pressure)
c_v	$\text{J kg}^{-1}\text{K}^{-1}$	specific heat (at constant volume)
D	μm	drop diameter
D_{10}	μm	length mean droplet diameter
D_{20}	μm	area mean droplet diameter
D_{30}	μm	volume mean droplet diameter
D_{32}	μm	Sauter mean droplet diameter
D_{ij}	m^2s^{-1}	mass diffusivity
E	mJ, J	ignition energy
f	Hz, mm	frequency, focal length
F		burning velocity enhancement factor
F_o		Frössling coefficient
\bar{F}		dimensionless frequency (turbulence)
\bar{F}_k		lower-limit dimensionless frequency (turbulence)
h	$\text{W m}^{-2}\text{K}^{-1}$	convective heat transfer coefficient
I		intensity of the laser beam (laser attenuation)
k	$\text{W m}^{-1}\text{K}^{-1}$	thermal conductivity,
K		Karlovitz stretch factor
K_{cl}		critical Karlovitz stretch factor, $K_{cl} = [(\rho_b Pe_{cl} / 2\rho_u) + Ma_{sr}]^{-1}$
K_o		fuel evaporation constant of quiescent mixture
K_t		fuel evaporation constant of turbulent mixture
l	$\mu\text{m}, \text{m}$	drop spacing, length

L	mm	integral length scale of turbulence
L_b, L_c, L_{cr}	mm	Markstein lengths, as defined
L_s, L_{sr}		
Le		Lewis number
m	kg	mass
M		magnification factor (optical system)
\bar{M}	kg/kmol	molar mass
Ma, Ma_{sr}		Markstein numbers, as defined
n	moles	ratio of refractive indexes, number of moles, polytropic index, cell wavenumber
N_d	m^{-3}	number density of droplets
N_T		total number of drops in a cluster
P, P_1, P_2	kPa	pressures, as defined
P_v, P_w, P_f		
Pe_{cl}		critical Peclet number for onset of acceleration
Pe_{cr}		critical Peclet number for onset of instability
\bar{Q}_e		mean extinction efficiency (laser attenuation)
r	mm	flame radius
r_v	mm	flame radius at which the volume of unburned gas inside a sphere of this radius is equal to the volume of burned gas outside it
R	kJ/kg.K	gas constant
R_L		turbulent Reynolds number based on the integral scale of turbulence
Re		Reynolds number
s	kJ/kmol.K	entropy
S		generalised function for the effect of the flame thickness, see Eq. (1.4)
\bar{S}		power spectral density
S_n	m/s	stretched flame speed
$S_{n,48}$	m/s	stretched flame speed at $r \approx 48$ mm

S_s	m/s	unstretched flame speed
S_t	m/s	turbulent flame speed
Sc		Schmidt number, ($Sc = \nu / D_{ij}$)
$\overline{S}(\overline{F})$		dimensionless one-dimensional power spectral density function
t	s, ms	time
t_k	s, ms	elapsed time from flame initiation (turbulent)
T	K	temperature
T_∞	K	far field temperature relative droplet location
T_{boil}	K	boiling point temperature
U	m/s	local (time averaged) flow velocity
u	m/s, J/kg	velocity, internal energy per unit mass
u'	m/s	root mean square turbulent velocity
u'_k	m/s	effective root mean square turbulence velocity
u_D	m/s	droplet velocity
u_g	m/s	gas velocity
u_l	m/s	unstretched laminar burning velocity
u_t	m/s	turbulent burning velocity
u_n	m/s	stretched laminar burning velocity, based on the rate of disappearance of cold unburned gas
u_{nr}	m/s	stretched mass burning velocity, based on rate of appearance of burned gas
v	m ³ /kg	specific volume
V	m/s, m ³ , volts	flow velocity, volume, voltage

Greek Symbols

α	$s^{-1}, m^2 s^{-1}$	stretch rate, thermal diffusivity
δ_l	m	flame thickness
ϕ		equivalence ratio
ϕ_{ov}		overall equivalence ratio (two-phase mixture)
ϕ_g		Gaseous phase equivalence ratio (two-phase mixture)
ϕ_l		liquid phase equivalence ratio (two-phase mixture)
γ		index of isentropic expansion
λ	nm	wave length, Taylor microscale of turbulence
ν	m^2/s	kinematic viscosity
ρ	$kg\ m^{-3}$	density
σ		density ratio, $\sigma = \rho_u/\rho_b$
σ_D	μm	standard deviation of individual droplet diameter
σ_e	m^2	extinction cross section (laser attenuation)
τ_D	s	droplet lifetime
Λ		cell wavelength
ω	rpm	fan speed

Subscripts

<i>1</i>	pre-expansion
<i>2</i>	during expansion
<i>a</i>	air
<i>b</i>	burned
<i>c, cr</i>	curvature (rate)
<i>d</i>	droplets
<i>f</i>	fuel, entering the flame
<i>g</i>	gas
<i>l</i>	liquid
<i>m</i>	mass
<i>min</i>	minimum
<i>max</i>	maximum
<i>ov</i>	overall
<i>r</i>	reduced, remote from flame front
<i>s, sr</i>	strain (rate)
<i>t</i>	turbulent
<i>u</i>	unburned
<i>v</i>	vapour or gas close to saturation, volume

Chapter 1

Introduction

Driven by the continuing needs to improve fuel economy and to reduce exhaust emissions, a fundamental understanding of the combustion processes in aerosols is required to optimise the performance of spray combustion systems and to minimise explosion hazards. However, studies in practical systems are unsuitable for this purpose, due to the multiplicity of dependent parameters. The flame propagation rate in the two-phase-environment must be analysed in isolation from the complex processes of fuel injection and mixing, often within a turbulent flow field. At present, the interaction of these processes does not allow for adequate mathematical modelling. Therefore, a fundamental study of droplet cloud combustion is required to investigate the parameters of importance.

This chapter presents a review of the fundamentals of the combustion of homogeneous droplet-vapour-air mixtures. Section 1.1 deals with the trends in practical spray combustion in industrial applications that draw attention to the need for fundamental study of spray combustion. Section 1.2 presents a brief review of the burning rate of homogeneous gaseous mixtures, which forms the foundation for the present study. In Section 1.3 the phenomenon of combustion instability in gaseous flames is reviewed because instabilities in droplet-vapour-air mixtures are probably triggered, in part, by the same mechanisms. A review of a number of fundamental studies with regard to droplet-vapour-air mixture parameters and their effect on burning rate is presented in Section 1.4. Finally, the main objective of the thesis and the thesis outline are presented in Sections 1.5 and 1.6.

1.1 Overview of Trends in Practical Spray Combustion

Applications of spray combustion are widely used and much research has been undertaken to improve thermodynamic performance while simultaneously complying with the increasingly stringent emission requirements. Nevertheless, there are several phenomena relating to the burning of sprays that are still not fully understood. This is due to the complexity of practical spray combustion systems, in which various critical parameters such as evaporation rate, burning rate and turbulence interact. The succeeding sections present an overview of some of the practical applications of sprays in combustion, their challenges and the recent trends in their development. These include, but are not limited to, applications in automotive spark ignition engines, diesel engines and aero-engines.

The concept of lean combustion in piston engines is one method to achieve a reduction in CO and NO emissions as well as in fuel consumption (Fujimoto *et al.*, 1995). However, for spark ignition engines, in which the charge is fully premixed, an inherent disadvantage of this concept is the slow and sometimes unstable combustion of the highly diluted charge (Heywood, 1988). This can be avoided by using stratification of the in-cylinder charge, although this does not offer the same reductions in CO and NO in S.I. engines. Diesel and Direct Injection Spark Ignition (DISI) engines are inherently suitable for charge stratification, particularly since the advent of electronic control of high pressure injection equipment. The combination of good atomisation from high pressure injection systems and complete flexibility of injection timing offers a wide variety of controls over the combustion event (Su *et al.*, 1995). However, some fundamental phenomena in such DISI engines are still unclear, for example, on how to organize the fuel-air mixture to give the best combustion (Ishima *et al.*, 2002).

Combustion in aero-engines involves the burning of a fuel spray in air. Different from automotive engines, the typical operating droplet sizes in aero-engines ranges to a few hundred microns. In addition, combustion occurs in a continuous mode rather than intermittent. A vital criterion of an aero-engine is its ignition performance, often characterised by the wide-range and adverse operating conditions due to changes in altitude. In the event of flame extinction at altitudes above which the low pressure and temperature prevents successful ignition, it would be necessary to reduce altitude for relighting. In a recent work, Mokhtar (2001) showed that laser ignition could be a potential solution to this problem. However, it would probably take another decade before a suitable lightweight laser system could be made available for application in aircraft. Nevertheless, the capability for relighting in aero-engines is a complex process and is still not fully understood.

In aero-engines, reduction of the objectionable constituents of exhaust emissions, which are mainly NO_x , CO and CO_2 , has motivated the development of new concepts of fuel atomization, pre-vaporization, and staged injection (Brundish *et al.*, 1997) to achieve lean burn low NO_x gas turbine combustors. However, thermo-acoustic combustion instabilities, known for their destructive potential in stationary gas turbines, have also become more prominent in aero-engines (Eckstein *et al.*, 2005). This phenomenon, also known as rumble, may cause large fluctuations in pressure and heat release, which increases vibration and heat transfer that shorten the life of the combustor. Combustors with fuel spray atomizers are particularly susceptible to low frequency oscillations, typically in the range 50-120 Hz. Fluctuations in pressure at the injector probably cause fluctuations in droplet size, air-to-fuel ratio, fuel flow rate and air flow rate (Greenhalgh *et al.*, 2004), which in turn can affect the heat release rate. Theoretical work also has been performed using a computational fluid dynamics (CFD) model to

simulate the response to inlet air and fuel supply (Zhu *et al.*, 1999) and the onset of self-excited oscillations (Zhu *et al.*, 2000). In a more recent work, an approach that involved integrating one-dimensional linear stability analysis and CFD has been developed to predict the modes of oscillation in a combustor, their frequencies and growth rates (Zhu *et al.*, 2001). However, the mechanism of thermo-acoustic combustion instability related to aero-engines is still not fully understood.

1.2 Laminar Burning Rates and Markstein Lengths

Investigation of the combustion of a homogeneous spray necessitates the understanding of gaseous combustion because many theoretical descriptions and experimental methods are used for both. Although there are several techniques available to measure burning rates, large scatter resulted from early measurements by different groups as was reported by Andrews and Bradley (1972). The reason for the discrepancies was found to be due to failure to account for the effects of stretch (Bradley *et al.*, 1996). Conversely, the use of spherically expanding flames has been found to be suitable for measurement purposes because the flame stretch is uniform and clearly defined (Dixon-Lewis, 1990, Dowdy *et al.*, 1991, Bradley *et al.*, 1996).

The velocity of the flame front, also known as the flame speed, S_n , is obtained directly from the measured flame front radius, r , by

$$S_n = \frac{dr}{dt} \quad (1.1)$$

Flame speed is not a unique property of a combustible mixture but is the sum of the gas expansion velocity, u_g , and stretched laminar burning velocity, u_n , based on the propagating flame front

$$S_n = u_g + u_n \quad (1.2)$$

Mass conservation yields the relationship between S_n and u_n ,

$$u_n = S S_n \frac{\rho_b}{\rho_u} \quad (1.3)$$

where ρ_b and ρ_u are the burned and unburned gas densities. S is a generalised function that accounts for the effect of the flame thickness on the mean density of the burned gases (Bradley *et al.*, 1996), and is given by

$$S = 1 + 1.2 \left[\frac{\delta_l}{r} \left(\frac{\rho_u}{\rho_b} \right)^{2.2} \right] - 0.15 \left[\frac{\delta_l}{r} \left(\frac{\rho_u}{\rho_b} \right)^{2.2} \right]^2 \quad (1.4)$$

where δ_l is the laminar flame thickness given by $\delta_l = \nu/u_l$, in which ν is the kinematic viscosity of the unburned mixture and u_l is the unstretched laminar burning velocity. Although Eq. (1.4) was generated from modelled methane-air flames at 0.1 MPa, Bradley *et al.*, (1998) suggested that it would be unlikely to be significantly different for iso-octane-air flames.

For a spherically propagating flame, the rate at which unburned gas is entrained into the front is not the same as the rate of formation of the burned product because of the finite flame thickness. Hence, two definitions of laminar burning velocity exist (Bradley *et al.*, 1996). The first, u_n , is based on the rate of disappearance of cold unburned gas, and is determined from photographic observation of the cold flame front. The second, u_{nr} , is based on the rate of appearance of burned gas, and is determined from measurements of pressure rise in closed vessels (e.g. Metghalchi and Keck, 1982). At small radii, the effect of δ_l is important, but it is less so at larger radii. As the radius tends to infinity, both u_n and u_{nr} tend towards the unstretched laminar burning velocity, u_l . Bradley *et al.* (1996) expressed the relationship between u_n and u_{nr} by

$$u_{nr} = \frac{\rho_b}{\rho_b - \rho_u} (u_n - S_n) \quad (1.5)$$

Flame sheets are subject to transverse velocity components (rate of strain) and curvature which stretch the flame. This stretch can increase or decrease the burning velocity (Bradley *et al.*, 1998; Aung *et al.*, 1995). The rate of flame stretch, α , is defined as the time derivative of the area, A , of an infinitesimal element divided by the area, and for a spherical flame, this becomes

$$\alpha = \frac{1}{A} \frac{dA}{dt} = \frac{1}{4\pi r^2} \frac{d(4\pi r^2)}{dt} = \frac{2}{r} \frac{dr}{dt} = \frac{2}{r} S_n \quad (1.6)$$

A burned gas Markstein length, L_b , expresses the sensitivity of flame speed to stretch (Clavin, 1985), such that

$$S_s - S_n = L_b \alpha \quad (1.7)$$

where S_s is the unstretched flame speed, and is obtained as the intercept value of S_n at $\alpha = 0$ in the plot of S_n against α , for example, as depicted in Fig. 1.1. Similar to Eq. (1.3), the unstretched laminar burning velocity, u_l , can be calculated from S_s , by

$$u_l = S_s \frac{\rho_b}{\rho_u} \quad (1.8)$$

However, Eq. (1.8) is valid only for large flames in which δ_l is very much smaller than the flame radius, r , and the flame stretch tends towards zero (Gillespie *et al.*, 2000). Bradley *et al.* (1998) quantified the contribution of rate of strain, $\alpha_s = 2 u_g/r$, and curvature, $\alpha_c = 2 u_n/r$, to the stretch rate; the total stretch being the sum of the two

$$\alpha = \alpha_s + \alpha_c \quad (1.9)$$

The variation in burning velocity due to stretch is given by

$$u_l - u_n = L_s \alpha_s + L_c \alpha_c \quad (1.10)$$

where L_s and L_c are the Markstein lengths associated, respectively, with strain and curvature (Bradley *et al.*, 1996). The Markstein lengths for u_{nr} , in Eq. (1.5), and u_l are, in general, different, hence

$$u_l - u_{nr} = L_{sr}\alpha_s + L_{cr}\alpha_c \quad (1.11)$$

where L_{sr} and L_{cr} are the Markstein lengths associated with strain and curvature, respectively for u_{nr} (Bradley *et al.*, 1996). Normalization of the Markstein lengths by the flame thickness, δ_l , results in (dimensionless) Markstein numbers Ma_s , Ma_c , Ma_{sr} and Ma_{cr} . However, Bradley *et al.* (1996) emphasized that Ma_{sr} (strain rate Markstein number) is the most relevant for many aspects of combustion. This is because in spherical explosions the flame stretch rate due to aerodynamic strain (α_s) is typically 4 - 5 times higher than that due to curvature (α_c), since u_g is usually much larger than u_n .

1.3 Effect of Instabilities in Laminar Flames

Flame front instability plays an important role in the investigation of gaseous combustion. A smooth flame front that is subjected to non-planar disturbances experiences wrinkles and cells and these contribute to increase in the flame surface area followed by a relative increase in flame speed. All spherically propagating laminar flames are initially stable because of the high stretch rate at small radii (Gillespie *et al.*, 2000), as denoted in Eq. (1.6). Eventually, a critical radius is reached at which the rate of stretch no longer provides a sufficient stabilising influence and cellularity develops. The critical radius, r_{cr} , defines a critical Peclet number, Pe_{cr} , which is given by r_{cr}/δ_l (Harper, 1989). These instabilities, which were observed in several experiments with spherical explosion of gaseous flames

(Groff, 1982, Kwon *et al.*, 1992, Bradley *et al.*, 1998, Gu *et al.*, 2000), become manifest as flame wrinkling over a range of wavelengths (cell sizes). Figure 1.2 shows a typical sequence of photographs for cellular flames of premixed iso-octane-air at $\phi = 1.5$, $T = 303$ K and $P = 100$ kPa, which shows the spectrum of different cell sizes as the radius increases. Initially after the onset of cellularity (at Pe_{cr}) there is little or no change in burning velocity since it takes time for its effect to manifest itself. However, after a short delay, the cellular flames give rise to an increase in burning velocity at a higher critical radius, r_{cl} , which defines another critical Peclet number, Pe_{cl} (Bradley *et al.*, 1998; Gu *et al.*, 2000). This point is also depicted by the break point 'X' in Fig. 1.1, after which the flame rapidly accelerates.

Darrieus (1938) and Landau (1944), in their theoretical works, showed that a gaseous flame advancing into unburnt gas is inherently unstable. Two major sources of flame instabilities in premixed flames are caused by the hydrodynamic and diffusive-thermal effects (Law, 1988). Similar to experiments, the mathematical analyses of flame instability for gaseous laminar mixtures (Sivashinsky, 1977, Groff, 1982, Bradley and Harper, 1994, Ashurst, 1997) reported the development of instability in the form of wrinkles as a precursor to a cellular structure. The mechanisms of instabilities and their interaction with flame stretch are likely to be important also in flames of two-phase mixtures.

Bechtold and Matalon (1987) described both the hydrodynamic and diffusive-thermal influence upon the stability of an outwardly propagating spherical flame using linear stability analysis. They showed that, depending upon the Markstein number, there can exist a range of perturbing wavelengths, which are also expressed by the wave number, n ,

$$n = \frac{2\pi Pe}{\Lambda} \quad (1.12)$$

where Pe is the Peclet number and Λ is the associated wavelength, normalized by the flame thickness (Bradley, 1999). Figure 1.3 shows the results of the analysis by Bechtold and Matalon (1987) in terms of theoretical values of n and Pe for various values of Ma_{sr} , with a density ratio, $\sigma = \rho_u/\rho_b$, of 6 (Bradley *et al.*, 2000). The smallest value of Pe for instability at the tip of the peninsular is Pe_{cr} . The lower limit wave number, n_l , is associated with the longest unstable wavelength. The upper limit wave number, n_s , is associated with the shortest unstable wavelength. The range of unstable wavelengths that contribute to flame acceleration only exists in the area within the instability peninsula shown in Fig. 1.3, where Pe is greater than Pe_{cr} . Clearly, Fig. 1.3 shows that the range of unstable wave numbers increases with an increase in Pe and also with a decrease in Ma_{sr} . Since full cellularity and associated flame acceleration occur only at Pe_{cb} , the analysis by Bechtold and Matalon (1987) over-predicts the spectrum of wave number. Bradley (1999) modified the analysis to allow for a lag in the full development of the instability by introducing $f(n_s/n_l)$, where f is a numerical constant less than unity. This is illustrated in Figure 1.4, which shows a sketch of the peninsular of instabilities (similar to Fig. 1.3) after the modification by Bradley (1999).

An increase in the wave number results in an increase in the surface area of the flame and thus the burning velocity, u_n . Al-Shahrany *et al.* (2005) employed the theory of Bechtold and Matalon (1987) and Bradley (1999) to predict the increases in u_n above u_l , in terms of the increasing range of unstable wavelengths. They expressed this as the ratio of burning velocities with and without instabilities

$$\left(\frac{u_n}{u_l} \right)_{Pe} = \left(f \frac{n_s}{n_l} \right)_{Pe}^{1/3} \quad (1.13)$$

provided that the effects of flame stretch on the local burning velocity can be neglected. However, in their work on laminar spherical explosions within iso-

octane-air aerosols, Lawes *et al.* (2005) were interested in the enhancement due to cellularity with respect to the burning rate prior to cellular flame acceleration.

Therefore, for convenience, they modified Eq. (1.13)

$$\left(\frac{u_n}{u_{n,Pecl}} \right)_{Pe} = \left(f \frac{n_s}{n_l} \right)_{Pe}^{1/3} \quad (1.14)$$

where $u_{n,Pecl}$ is the burning velocity immediately before the onset of the cellular flame acceleration.

1.4 Turbulent Premixed Flames

Measurements of turbulent burning velocities are complicated due to the influence of turbulence parameters, such as the root mean square (r.m.s.) turbulence velocity, u' , and the resulting flame brush (Gillespie *et al.*, 2000). Thus the use of the schlieren radius for the measurement of turbulent flame propagation (Abdel Gayed *et al.*, 1986) may be confusing. Haq (1998) introduced a flame radius, r_v , at which the volume of unburned gas inside a sphere of this radius is equal to the volume of burned gas outside it. Bradley *et al.* (2003) demonstrated that at the spherical surface defined by r_v , the rate of disappearance of cold unburned gas is equal to the rate of appearance of burned gas, and showed that r_v can be identified by planar sheet imaging. They presented a turbulent burning velocity for gaseous mixtures,

$$u_t = \left(0.9 \frac{\rho_b}{\rho_u} \right) S_t \quad (1.15)$$

where the value of S_t is measured from two-dimensional schlieren imaging, and the constant value of 0.9 is obtained from the best linear relationship between measurements from schlieren and laser sheet images.

A review by Abdel-Gayed *et al.* (1987) of experimental values of turbulent burning velocity from a variety of resources revealed the significance of turbulence on the burning rate of gaseous mixtures. When a turbulent flame develops from its ignition source, as in an explosion, the initial flame front is not exposed to the full spectrum of turbulence. It is only affected by the higher frequencies of turbulence (eddies smaller than the flame kernel), while the lower frequencies (eddies larger than the flame kernel) convect the whole flame kernel without affecting the flame front significantly. As the flame propagates, the reaction front becomes affected by ever-lower frequencies of the turbulent spectrum and the turbulent burning velocity increases toward a fully developed value. This leads to the definition of the effective r.m.s. turbulence velocity, u'_k , which is smaller than u' during the initial stages of flame development but tends to this value as the flame develops. Abdel-Gayed *et al.* (1987) derived a non-dimensional power spectrum from laser Doppler velocimetry measurements of isotropic turbulence in an explosion vessel. For an elapsed time from flame initiation, t_k , the value of u'_k is given by

$$u'_k = u' \left[\int_{\bar{F}_k}^{\infty} \bar{S}(\bar{F}) d\bar{F} \right]^{1/2} \quad (1.16)$$

where \bar{F} is a dimensionless frequency, $\bar{S}(\bar{F})$ is a dimensionless one-dimensional power spectral density function, and \bar{F}_k is a lower-limit dimensionless frequency. Abdel-Gayed *et al.* (1987) and Scott (1992) studied measured spectra for a wide range of Reynolds numbers and produced a curve fit to that data and showed that $\bar{S}(\bar{F})$ can be expressed as:

$$\bar{S}(\bar{F}) = \frac{3.3}{1 + (2\pi\bar{F})^{5/3} + (0.25\bar{F})^4 + (0.08\bar{F})^7} \quad (1.17)$$

In a seminal work, Bradley *et al.* (1992) presented a correlation of turbulent burning velocity from about 1650 experimental values, obtained in burners and stirred bombs. The correlation suggests that

$$\frac{u_t}{u_l} = f\left(\frac{u'_k}{u_l}, K, Le \text{ (or } Ma)\right) \quad (1.18)$$

The ratio of u_t/u_l represents the increase in burning velocity due to the presence of turbulence. The ratio u'_k/u_l , is a wrinkling factor, which is the normalized effective r.m.s. turbulence velocity in the cold pre-mixture. Turbulent flame stretch is represented in Eq. (1.18) by the Karlovitz stretch factor, K , given by

$$K = \left(\frac{u'}{\lambda}\right) / \left(\frac{u_l}{\delta_l}\right) \quad (1.19)$$

where the numerator is the turbulent strain rate (Abdel-Gayed *et al.*, 1984), in which λ is the Taylor micro scale of turbulence, and the denominator represents a chemical strain rate. The Lewis number, Le , in Eq. (1.18) is the ratio of thermal diffusivity, α , to the diffusion coefficient of the deficient reactant, D_{ij}

$$Le = \frac{\alpha}{D_{ij}} \quad (1.20)$$

Bradley (1992) suggested that for laminar flamelet modelling of turbulent combustion, the group (KMa) expresses the reduction in burning velocity due to stretch. However, at that time (1992), reliable values of Ma were only recently available for a limited range of conditions, through the experiments of Searby and Quinard (1990). Therefore, pending the availability of more data on Ma , Bradley (1992) decided to correlate experimental values of u_t/u_l in terms of the wrinkling factor, u'_k/u_l , and the flame stretch factor KLe , as shown in Fig. 1.5. They also emphasized that the experimental points, which are not shown in Fig. 1.5, correlate

better with KLe than solely with K . The correlation in Eq. (1.18) and in Fig. 1.5 is described approximately by

$$\frac{u_t}{u_l} = 0.88 \frac{u'_k}{u_l} (KLe)^{-0.3} \quad (1.21)$$

and has been widely used in the validation of mathematical models of turbulent combustion in general, and in determining combustion rates in engine cycle and explosion models (Bradley *et al.*, 1992).

Equation (1.19) can also be considered as a ratio of chemical to eddy lifetimes, $(\delta/u) / (\lambda/u')$. For isotropic turbulence, with λ related to the integral length-scale, L , by Abdel Gayed *et al.* (1984)

$$\frac{\lambda^2}{L} = 40.4 \frac{\nu}{u'} \quad (1.22)$$

it can be shown that

$$K = 0.157 \left(\frac{u'}{u_l} \right)^2 R_L^{-0.5} \quad (1.23)$$

where R_L is the turbulent Reynolds number based on the integral scale of turbulence. In a more recent work, Bradley *et al.* (2005) used a different constant in Eq. (1.22) so that Eq. (1.23) now becomes

$$K = 0.25 \left(\frac{u'}{u_l} \right)^2 R_L^{-0.5} \quad (1.24)$$

1.5 Characterisation of Droplet Clouds

Annamalai and Ryan (1992) defined a droplet cloud as having a large number of droplets, usually much higher than 10. Depending on the nature of formation, droplet clouds can exist in the form of droplets-air mixture such as sprays in diesel

engines, or droplets-vapour-air mixture as in an aerosol generated by expansion of gaseous fuel. The present work deals with droplets-vapour-air mixtures. In order to study the combustion of these mixtures, the parameters involved in characterising them must be clarified.

The simplest parameter, used by most researchers (e.g. Burgoyne *et al.*, 1954, Mizutani *et al.*, 1973b) to define an aerosol mixture is the overall equivalence ratio, ϕ_{ov} . This includes all fuel present, irrespective of phase. Since the behaviour of an aerosol flame is primarily dependent on the gaseous equivalence ratio (Myers and Lefebvre, 1986), this is a key parameter. Two different equivalence ratios are therefore defined to accommodate the gaseous and liquid phases, ϕ_g and ϕ_l . These are discussed in detail in Section 3.1.

Atzler (1999) suggested that the evaporation of droplets ahead of the flame front changes both the gaseous and liquid equivalence ratios. Thus, the amount of gaseous fuel available in the reaction zone is difficult to determine experimentally and there were no measurements attempted in the works included in this review. However, ϕ_g was used in a computational model by Polymeropoulos (1983) to predict the burning velocity in an aerosol. Other workers, e.g. Burgoyne *et al.* (1954), calculated the change in drop size, and the subsequent change in ϕ_g , in the preheat zone of the flame from the scaled temperature profile of a homogeneous flame. However, this is not without problems since aerosol flames can be much thicker than gaseous flames. Therefore, experimental results usually have been correlated in terms of cold gas parameters.

The drop size is the parameter most frequently used for the correlation of the combustion behaviour of an aerosol. If all drops in an aerosol are of the same size, then the obvious statement is that of droplet diameter. Such an aerosol is termed monosized or monodisperse. However, any fuel injection process such as

atomization gives rise to a spectrum of different droplet sizes, in which the resultant droplet size distribution rarely fits the usual statistical functions (Lawes, 2004). Thus a form of averaging to determine a suitable mean size that properly represents the physical properties of droplets is necessary (Lefebvre, 1989). One of the commonly used mean sizes is the Sauter Mean Diameter (SMD), or D_{32} , which is given by

$$D_{32} = \frac{\sum_{i=1}^k n_i D_i^3}{\sum_{i=1}^k n_i D_i^2} \quad (1.25)$$

where, n_i is the number of droplets within a range centred on diameter D_i , and k is the number of ranges. The Sauter Mean Diameter is an average diameter with a volume to surface area ratio equal to that of the droplets. It is an indicator of the degree of atomization produced by an injector.

Another representative of droplet diameters is the surface mean diameter, D_{20} , which represents an average diameter with a surface area equal to the mean surface area of all the droplets. This is given by:

$$D_{20} = \sqrt{\frac{\sum_{i=1}^k n_i D_i^2}{\sum_{i=1}^k n_i}} \quad (1.26)$$

The surface mean diameter is used for surface controlled applications such as absorption. The mean arithmetic diameter is given by:

$$D_{10} = \frac{\sum_{i=1}^k n_i D_i}{\sum_{i=1}^k n_i} \quad (1.27)$$

Other mean droplet size terminologies have been defined in, for example, Schick (1997). For monodisperse or near monodisperse aerosols, all the mean droplet diameters tend to be the same. It is worth noting that, in the context of spray

combustion, the use of mean diameters such as SMD to characterize flame instability may lead to mistaken conclusions since it is important to distinguish the homogeneity of the droplet spatial distribution (Greenberg, 2002).

Conditions in the droplet cloud can also be expressed in terms of the liquid volume of fuel present per unit volume of mixture. This is a function of the average size of the droplets and the average inter-drop distance. Burgoyne & Cohen (1954) combined the drop diameter D and the inter-drop distance l to the non-dimensional drop spacing l/D , to express the limiting conditions for flame propagation, in terms of flammability of the aerosol. Shown in Table 1.1 are inter-drop distances for various fuels at 20°C, overall equivalence ratios of 0.5, 1.0 and 1.5 and drop sizes of between 10 and 40 μm , as calculated by Atzler (1998) with the assumption that all of the fuel was present in liquid form. These data show that the drop spacing does not vary greatly for the range of experimental conditions compiled in this review.

1.6 Fundamentals of Spray Combustion

1.6.1 Categories of Aerosol Combustion Analyses

Real sprays are complex because of the many important parameters (Faeth, 1983) such as evaporation rate, burning rate, and drop-turbulence interactions that are coupled together. Hence it is difficult to isolate fundamental parameters that enable improved understanding of the basic processes. For example, in Fig. 1.6, which shows a schematic of a liquid-fuel spray flame, Chiu and Croke (1981) demonstrated that a spray flame is subdivided into several zones that co-exist within the flame. Therefore, in order to give correct interpretation of observed phenomena, the mechanisms of droplet combustion have been categorized into three modes: single droplet, droplet clouds and sprays. An idealised, simplified, system

such as the single droplet or droplet clouds provides well-defined and well-controlled conditions to further improve understanding.

To accommodate for complex processes in sprays, Chiu and Liu (1977) introduced the group combustion number, G , which characterizes different group combustion regimes. The group combustion number corresponds to the ratio of the gross droplet evaporation to the inward oxygen diffusion, and this is given by

$$G = 1.5 Le \left(1 + 0.276 Re^{0.5} Sc^{0.33} \right) N_T^{0.66} (D_{10} / l) \quad (1.28)$$

where Le is the Lewis number, Re is the droplet Reynolds number, Sc the Schmidt number, N_T is the total number of droplets in a cluster, D_{10} is the arithmetic mean drop diameter and l is the drop spacing. Four principal group combustion modes within stationary droplet clouds have been identified as external group combustion, internal group combustion, sheath combustion, and single droplet combustion. The characteristics of each mode are presented in Table 1.2. As the group combustion number increases, it is generally suggested that the mode changes from that of single droplet combustion to that of the external sheath. The applicability of the group combustion number was verified qualitatively in experiments by Akamatsu *et al.* (1996) and Tsushima *et al.* (1998) by applying advanced laser-based diagnostics with high temporal and spatial resolutions to spray flames in a turbulent jet and in laminar counter flows to measure mean separation distance between droplet centres and the total number of droplets within each droplet cluster. The group combustion number (Chiu and Liu, 1977) is valid for application in a diesel and gas turbine engines, in which fuel is sprayed into the flame. However, this may not be suitable in a DISI engine where fuel spray is injected earlier, and thus a mixture of liquid-vapour-air can exist within the reaction zone.

An idealised, simplified, system such as the single droplet or droplet cloud provides well-defined and well-controlled conditions to further improve understanding. Godsave (1952) found that the time taken for a single droplet suspended in still air to burn out is a square function of its diameter. He established the so-called d^2 -law for the situation in which the difference in temperature between the drop and the surrounding atmosphere is considerable

$$D^2 = D_o^2 - K_o t \quad (1.29)$$

Here D_o and D are the drop sizes initially and at time, t , respectively, and K_o is the fuel evaporation constant, determined directly from the slope of plots of D^2 against t .

For a quiescent mixture, K_o is given by

$$K_o = \frac{8k_g}{\rho_l c_{pg}} \ln(1+B) \quad (1.30)$$

where k_g and c_{pg} are the gas-phase specific thermal conductivity and specific heat, respectively, and ρ_l is the liquid phase density of the fuel (Turns, 2000). The parameter, B , which is referred to as the Spalding number or transfer number (Spalding, 1952), is given by

$$B = \frac{c_{pg}(T_\infty - T_{boil})}{h_{fg}} \quad (1.31)$$

where T_{boil} and h_{fg} are the boiling point temperature and the heat of vaporization of the fuel, respectively, and T_∞ is the far field temperature. In practice, droplets are not usually stationary, as was assumed by Godsave (1952). However, it has been experimentally confirmed by Gökalg *et al.* (1992) that the d^2 -law given in Eqn. (1.29) is still applicable, and in such a situation of non-stationary droplet, an empirically derived relation for the fuel evaporation constant, K_t , is given by

$$K_t = K_o \left(1.0 + F_o Re^{0.5} Sc^{0.33} \right) \quad (1.32)$$

where Re is the droplet Reynolds number, Sc the Schmidt number, K_o is the fuel evaporation constant at $Re = 0$, and F_o is the Frössling coefficient (Frössling, 1938).

The droplet lifetime, τ_D , is obtained from Eq. (1.29), by equating D to 0

$$\tau_D = \frac{D_o^2}{K_o} \quad (1.33)$$

The classical d^2 -law established for single droplet combustion has been useful in providing a fundamental foundation on which to develop empirical descriptions of spray combustion. Nevertheless, in a review by Annamalai and Ryan (1992), it was shown that droplets in clouds behave very differently from a single isolated droplet, in which a common flame may be formed around an array, or cluster, of droplets, as a result of inter-droplet interaction and mixture composition.

1.6.2 Laminar Flames within Droplet Clouds

Experimental and theoretical fundamental studies of flame propagation through droplet clouds are scarce, due to the complex nature of droplet combustion and the difficulties of the experimental methods. Table 1.3 summarises typical spray generation methods together with some criteria used for their selection. It is clear that there is no single method of droplet generation that can perfectly meet all the criteria required for an ideal study (Gökalp *et al.*, 1999). However, a significant number of fundamental works have been conducted.

The visual appearance of aerosol flames was frequently used to try to explain possible mechanisms of aerosol combustion. Burgoyne and Cohen (1954) used a dilute cloud of mono-sized tetralin droplets, condensed out of a gaseous mixture flowing through a glass tube. For drop sizes smaller than 10 μm they observed that

the resulting flame front was smooth. They concluded that the droplets were fine enough for complete evaporation in the pre-heating zone of the flames. Burgoyne and Cohen also found that between drop diameters of 10 and 40 μm the flames took the form of a brush-like spray of discrete burning drops and the corresponding burning velocity was significantly higher than that for aerosol of smaller droplet size. A similar, so called, burning velocity enhancement was observed in later experimental works using various methods, for example: ultrasonic atomiser (Mizutani and Nakajima, 1973), expansion cloud chamber (Hayashi and Kumagai, 1974), and burner (Nakabe *et al.*, 1988). Such works were extensively reviewed by Atzler (1999).

The expansion apparatus, which was operated based on the principle of the Wilson cloud chamber (Wilson, 1897), was used by Hayashi and Kumagai (1974). It was a novel technique for the generation of monodisperse aerosol that enabled good control of droplet sizes of up to 30 μm . They concluded that the flame speed was a function of liquid fuel concentration and droplet size. In a more recent work, Atzler (1999), who employed the Wilson cloud chamber technique using the same apparatus as the present Author, not only showed burning velocity enhancement, but also observed cellularity associated with instabilities (Section 1.3), which further increased the burning rate.

Even though most of the previous authors observed that the burning rate generally increased with droplet size, the opposite effect on burning rate was shown by Ballal and Lefebvre (1981), in which aerosol fuel mixtures of iso-octane, diesel oil and heavy fuel oil at drop diameters of between 30 and 100 μm were studied. They also correlated the results with a theoretical model which assumed the quench time of the reaction zone to be the sum of the evaporation and chemical reaction times. The model was modified by Polymeropoulos (1984) to allow for a wider

range of droplet size by considering an energy balance for the reaction zone. Figure 1.7 shows the effect of droplet size and fuel-vapour fraction on the flame speed predicted by the model (Polymeropoulos, 1984) and from the experiments (Ballal and Lefebvre, 1981). It is clearly shown in Fig. 1.7 that the burning velocity enhancement due to the presence of droplets is effective only for droplet sizes of up to approximately 20 μm .

1.6.3 Turbulent Flames within Droplet Clouds

Myers and Lefebvre (1986) investigated the influence of mean droplet size and mainstream velocity on flame speed using mixtures of JP 7 (aviation) fuel drops and air in a circular duct with air velocity between 10 and 33 m/s. As in Fig. 1.8, they showed that the measured flame speed was inversely proportional to mean drop size. It is also clear from the Fig. 1.8 that an increase in the mainstream velocity enhances the flame speed, which Myers and Lefebvre suggested was a result of increase in the associated turbulence intensity. A similar trend of the influence of mean droplet diameter on turbulent flame speed to that shown in Myers and Lefebvre, was also reported by Mizutani and Nishimoto (1972), El-Banhawy and Whitelaw (1981), Richards and Lefebvre (1989) and Stårner *et al.* (2005). Both El-Banhawy and Whitelaw (1981) and Myers and Lefebvre (1986) suggested that droplet evaporation rates were controlling the turbulent flame speed. However, El-Banhawy and Whitelaw also suggested that droplet evaporation would only have an influence on the combustion process if a time characteristic of the turbulent mixing between fuel and air were comparable to that which characterizes droplets evaporation.

In a recent work with turbulent flames of aerosol, Marquez (2003) showed that the burning velocity of iso-octane-air aerosol mixtures can be potentially lower than that of gaseous flames. However, the aerosols and gaseous mixtures in Marquez's

comparison were at different conditions. For example, the difference in the initial temperatures between the aerosol and gaseous mixtures was 96 K, which was significantly large. It was shown by Bradley *et al.* (1998) through experiments with laminar gaseous flames that such a large increase in initial temperature would result in an increase in the laminar burning velocity by approximately 30 %. Hence, the comparison between the burning velocities of aerosol and gaseous flames by Marquez could be misleading due to the significant differences in the conditions of the mixtures.

1.7 Objectives

Previous fundamental research on combustion of droplet clouds have generally been useful in discovering the various potential effects of the presence of fuel droplets in flames, as reviewed in Sections 1.6.2 and 1.6.3. However, these were undertaken within a narrow range of conditions. Thus, fundamental data on the burning rate of droplet clouds is still scarce and requires further investigation. Therefore, in the present work, experimental investigation of spherically propagating flames of droplet clouds (droplets-vapour-air mixture) in a combustion apparatus, based on the principle of the Wilson cloud chamber (Wilson, 1897), was undertaken. The droplet clouds had near a monodisperse distribution of drop size, which is an important criterion in the fundamental study of droplet cloud combustion.

The main objectives of the present research are:

- to compare the effect of the presence of fuel droplet clouds in flames, in terms of burning rate and flame surface structure, at a wide range of equivalence ratio;

- to investigate, experimentally, the mechanisms that cause burning rate enhancement in droplet clouds flames. This is addressed in Section 1.6.2;
- to quantify flame instabilities and burning rate enhancement in cellular flames within droplet clouds;
- to explore the effects of turbulence on aerosol flames and to investigate and quantify any burning rate enhancement.

1.8 Thesis Outline

The experimental apparatus and methods employed during the present study are described in Chapter 2. Flame photography, mainly with the schlieren technique, was used to analyse the surface structure of the flame and to quantify the burning properties.

Droplet clouds generated in the vessel under laminar and turbulent conditions were characterised using a Laser Doppler Anemometer system by measuring droplet size and concentration of liquid fuel during the process of expansion cooling. Simultaneously, temperature and pressure were recorded and used as a basis to calculate aerosol properties. The results of the characterisation of droplet clouds are presented in Chapter 3.

Results from combustion studies are presented and discussed in Chapter 4. The results and discussions in Chapter 4 are extended in Chapter 5 to include analysis of the present and other works. Chapter 6 summarises the findings of the present study and gives recommendations for future work.

Table 1.1 Relationship between drop size and drop spacing as a function of fuel and equivalence ratio, calculated by Atzler (1998) for 293 K, 100 kPa, vapour-liquid equilibrium.

Substance	Formula	Drop spacing l in [μm]				Ratio (l/D)
		D_{32}				
		10 μm	20 μm	30 μm	40 μm	
$\phi = 1.0$						
Ethanol	$\text{C}_2\text{H}_5\text{OH}$	295	590	885	1180	29.5
n-Octane	C_8H_{18}	234	469	704	939	23.5
Decane	$\text{C}_{10}\text{H}_{22}$	174	348	522	697	17.4
Tetralin	$\text{C}_{10}\text{H}_{12}$	180	360	540	721	18.0
Dodecane	$\text{C}_{12}\text{H}_{26}$	170	340	510	681	17.0
$\phi = 1.5$						
Ethanol	$\text{C}_2\text{H}_5\text{OH}$	173	346	520	694	17.6
Tetralin	$\text{C}_{10}\text{H}_{12}$	157	314	470	628	15.7
$\phi = 0.5$						
Tetralin	$\text{C}_{10}\text{H}_{12}$	228	457	686	914	22.9

Table 1.2 Characteristics of group combustion modes (Chiu and Liu, 1977, and Nakamura *et al.*, 2005).

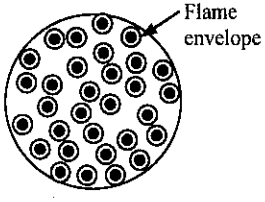
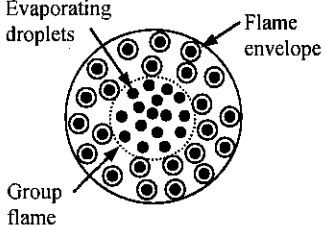
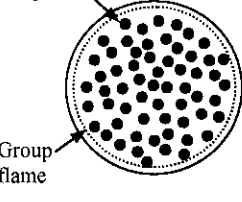
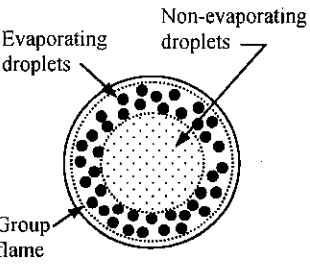
Combustion Mode	Group Number	Characteristics	
Single droplet	$G < 0.01$	All droplets in a group burn with envelope flames, unaffected by other droplets	
Internal group	$0.01 < G < 0.1$	Droplets inside the group flame just evaporate, and droplets outside the group flame burn with envelope flames	
External group	$0.1 < G < 100$	The group flame encloses the whole droplet group	
External sheath	$G > 100$	Non-evaporating region is found inside the evaporating region in the droplet group	

Table 1.3 Main characteristics of droplet generator types; reproduced from (Gökalp *et al.*, 1999).

Method Criteria	Liquid jet Atomizer	Air Assisted Atomizer	Jet Instabilities	Surface instabilities	Electrostatic Spray	Condensation Aerosol
Droplet size dispersion	Broad	Broad	Very narrow	Narrow	Very narrow	Narrow
Possible liquid flow rate	Small to large	Small to large	Very small	Small	Small	Very small
Initial droplet kinetic energy	Very high	High	High	Small	Small	Very small
Design and fabrication	Intermediate	Easy	Difficult	Intermediate	Intermediate	Difficult
Use at high pressure	Easy	Intermediate	Easy	Easy	Easy	Difficult

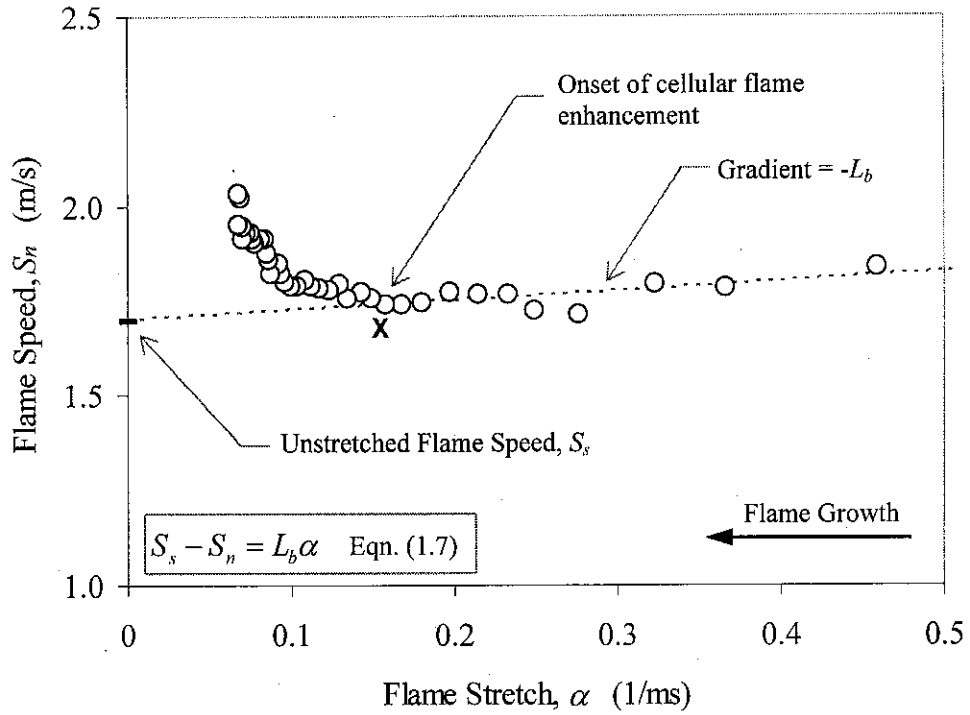


Figure 1.1 Variation of flame speed with flame stretch for a stoichiometric methane-air mixture at 512 kPa and 350 K. Reproduced from Haq (1998).

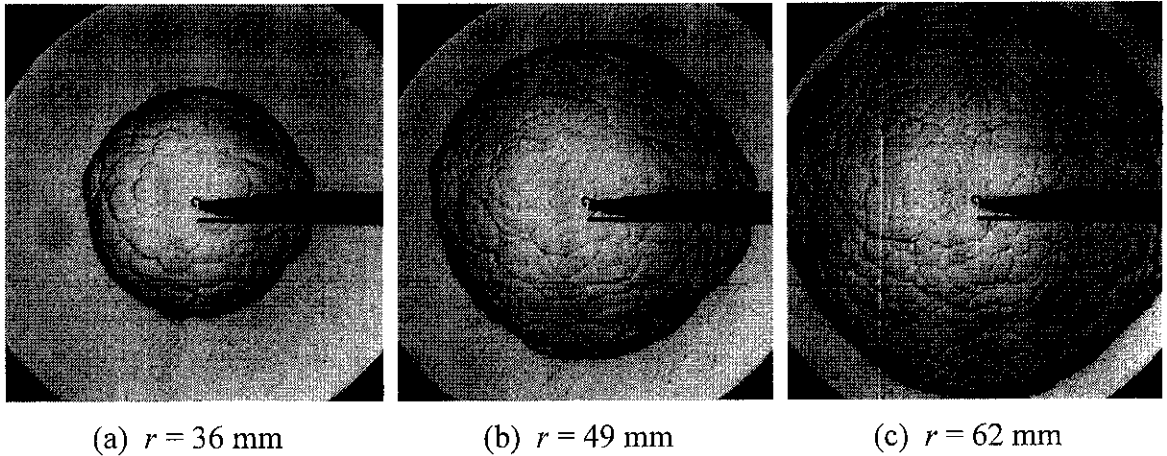


Figure 1.2 Typical sequences of photographs of cellular flames for premixed iso-octane-air showing spectrum of different cell sizes. The mixture was ignited at $\phi = 1.5$, $T = 303$ K and $P = 100$ kPa.

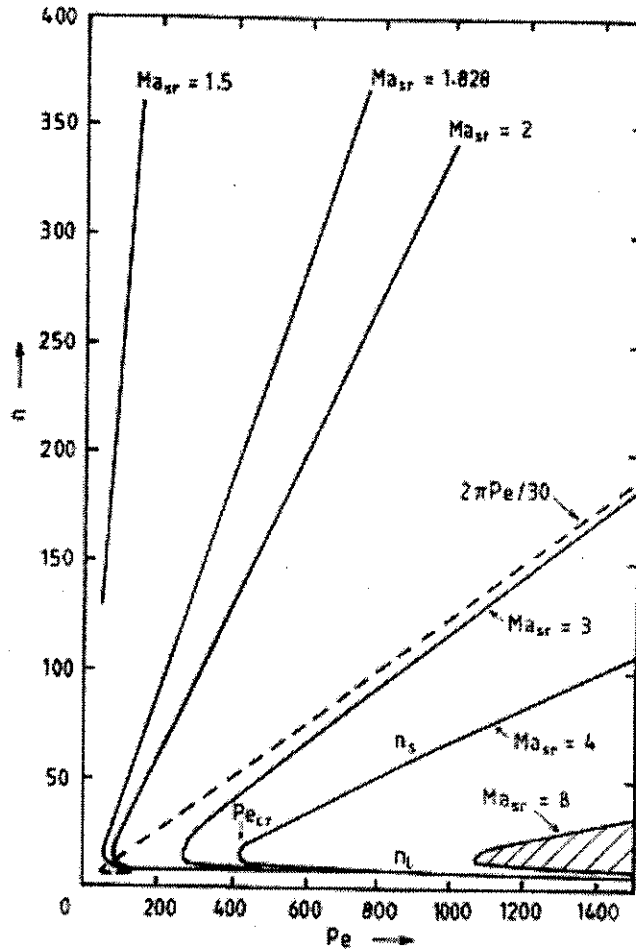


Figure 1.3 Theoretical wave numbers, n , at limits of flame stability for different Ma_{sr} , as a function of Peclet number, with $\sigma = 6$. Shaded area is a peninsular of instability for $Ma_{sr} = 8$. Reproduced from Bradley *et al.* (2000).

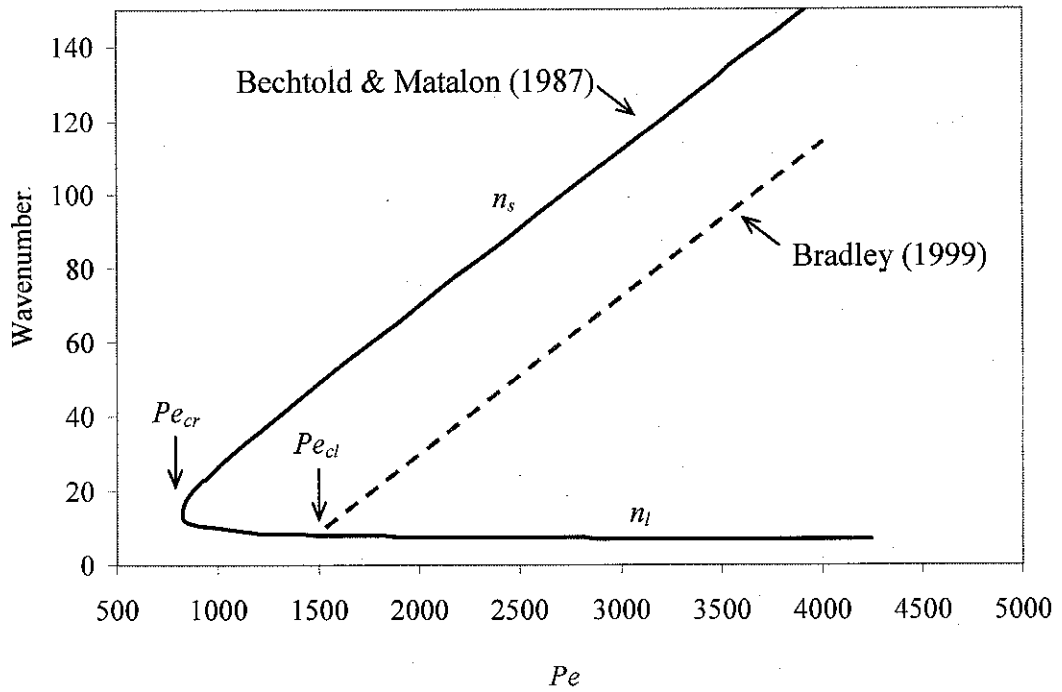


Figure 1.4 Sketch of the modified peninsular of instabilities, as in Fig. 1.3, with the allowance for a lag in the full development of the instability.

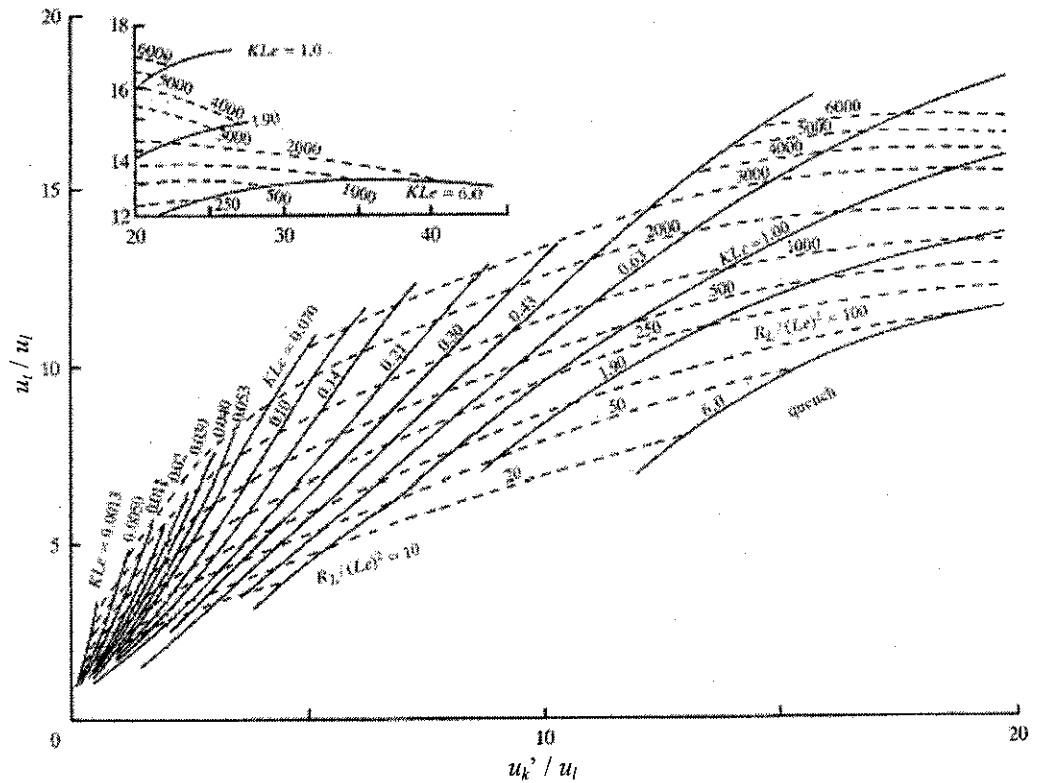


Figure 1.5 Correlation of turbulent burning velocities. Broken curves show $R_L/(Le)^2$, with R_L evaluated for the fully developed r.m.s. turbulent burning velocity, u' , equal to u'_k . Reproduced from Bradley (1992).

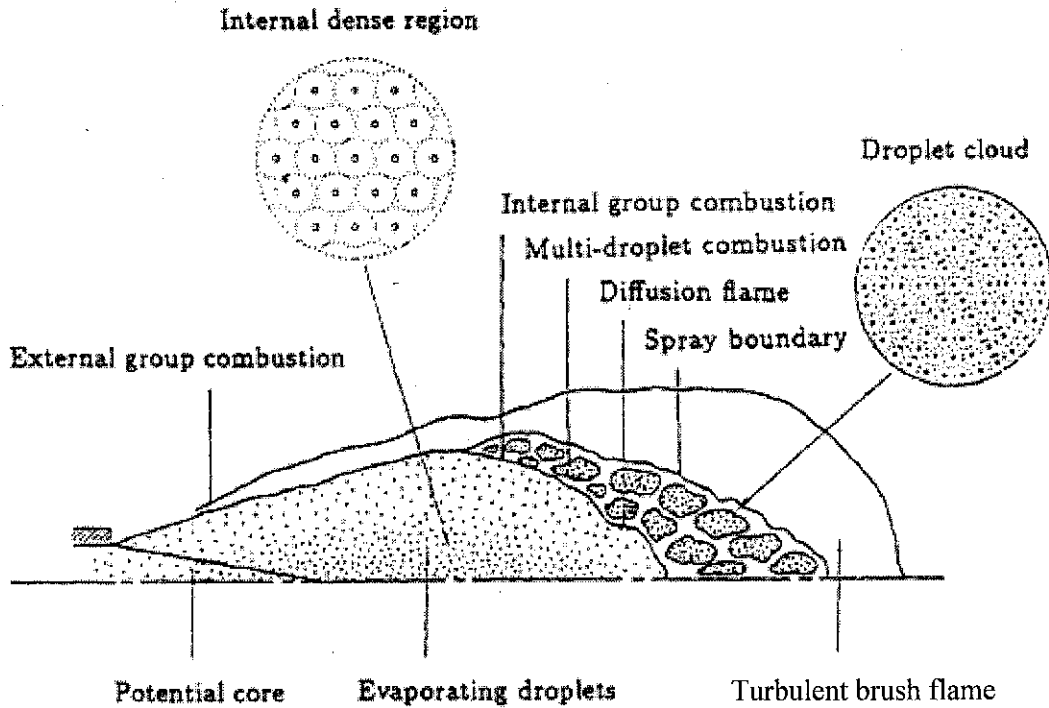


Figure 1.6 Schematic of liquid-spray group combustion (Chiu and Croke, 1981, Chiu, 1995).

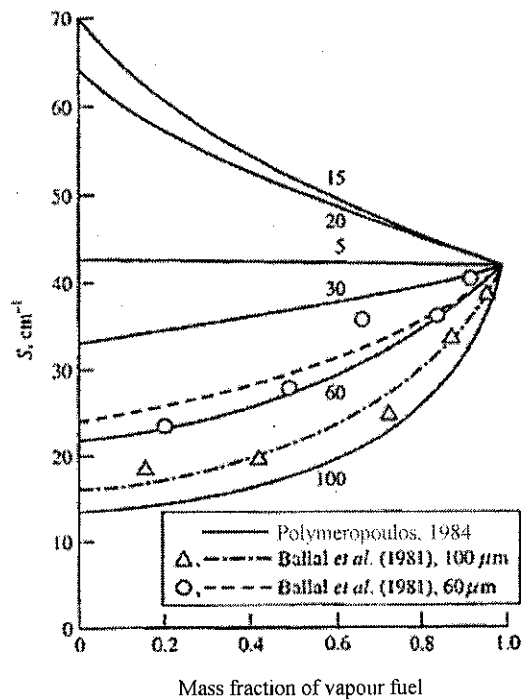


Figure 1.7 Variation of flame speed with droplet size and mass fraction for stoichiometric iso-octane droplet-vapour-air mixture at atmospheric pressure. Reproduced from Polymeropoulos (1984).

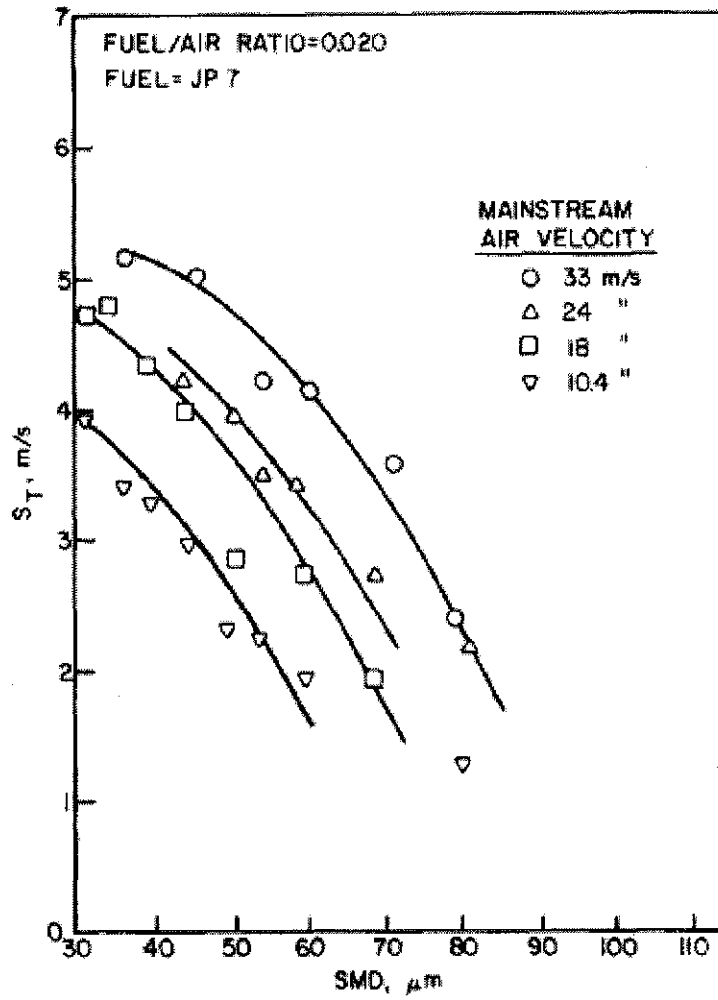


Figure 1.8 Influence of mainstream velocity and mean drop size on flame speed. Reproduced from (Myers and Lefebvre, 1986).

Chapter 2

Apparatus and Techniques

Described in this chapter are the apparatus and techniques used for the study of flame propagation in iso-octane and air aerosols at a variety of initial conditions. Aerosols were generated in a fan stirred explosion vessel using the Wilson cloud chamber principle (Wilson, 1897). The apparatus is described in Sections 2.1 and 2.2 and the mixture preparation technique is presented in Section 2.3.

Extensive measurements of pressure, temperature and aerosol properties during expansion were undertaken to characterise aerosol properties at the time of ignition. The instrumentation used for this is presented in Section 2.4. Combustion events were recorded using high speed schlieren photography and laser sheet imaging. These systems also are presented in Section 2.4 and the associated image processing techniques are set out in Section 2.5. Only brief descriptions are given when detailed information exists elsewhere.

2.1 Combustion Vessel

The present combustion vessel was developed by Atzler (1999) and also used by Marquez (2003). Fuel aerosols were generated in situ, using the Wilson cloud chamber principle as described by Wilson (1897 & 1911). In this, a homogeneous fuel air mixture is cooled by expansion until the fuel condenses into a fog of liquid droplets as described in Section 2.3. Prior to the work of Atzler (1999), the method was used for combustion studies by Hayashi & Kumagai (1974, 1976).

The system is shown photographically in Fig. 2.1 and schematically in Fig. 2.2. The apparatus comprised the combustion vessel, an expansion tank and interconnecting pipework, various valves and control systems, and measurement instrumentation. Each is discussed below.

2.1.1 Explosion Vessel

A comprehensive description of the present rig can be found in Atzler (1999). As shown in Fig. 2.1, it comprised a cast steel cylinder of 305 mm diameter and 305 mm length and its working volume was 23.2 litres. Optical quality BK7 windows, of 150 mm diameter and 39 mm thick, were fitted in each end. Four identical eight-bladed fans were fitted, equi-spaced around the central circumferential plane at 45° to the horizontal. These were connected to 3-phase 1.5 kW motors and electronic motor controllers. For studies of turbulent combustion, the fans provided the required flow field. They were also used in laminar studies for the mixing of fuel and air, prior to experiments. The fans generated isotropic turbulence within the field of view of the windows. The vessel turbulence was characterised by Lawes (1987) and the turbulence velocity was found to be a linear function of fan speed given by

$$u' = 0.0016 \omega \quad (2.1)$$

where ω is the fan speed in rpm.

As shown in Figs. 2.1 and 2.2, the explosion vessel was connected by a ½" BSP fitting at the top of it to a central fill and discharge valve, which linked the vessel with the air supply and to the exhaust. A pressure transducer, used to monitor the mixture initial pressure, also was connected to this port, as discussed in Section 2.2.1. The pressure transducer was protected from combustion pressure,

using an additional isolating valve that was fitted immediately adjacent to the port. Four 1" BSP ports were equi-spaced around the explosion vessel, as shown in Fig. 2.2. The top port was permanently connected to the expansion pipe (Section 2.1.2). All other ports were used as appropriate for ignition, thermometry and an additional 25.4 mm (1") diameter window.

Two electrical heaters with a total installed power of 4.5 kW were used to raise the vessel temperature to that required for an experiment. Each heater was mounted close to the surface of the end plates and, in conjunction with the running fans during heating, provided a homogeneous temperature distribution throughout the explosion vessel. Both heaters were controlled by a CAL 3200 electronic controller.

Measurements of total static absolute pressure, as well as measurements of the pressure change during expansion were performed using a precision pressure transducer-amplifier/readout system, DRUCK PDCR 911 and DPI 260. It was fitted 400 mm from the inner surface of the explosion vessel, behind the isolating valve. The transducer had a range of 0 to 700 kPa (absolute), with a resolution of 0.1 kPa, and was calibrated by the manufacturer.

Temperature measurements during expansion were required to determine the initial conditions for combustion experiments. Two sizes of K-type thermocouples were used. For the required high frequency response during calibration studies of the expanding mixture, a 25 μm fine wire thermocouple was used. However, fine wires were too fragile to be used during combustion studies. Hence, in all work not requiring a fast response, a 200 μm thermocouple was employed. The thermocouples were connected, as required, via a home-built 12-way input selector to a Digitron 2751-K digital readout, with analogue output. The analogue output was used for the computer recording of temperature histories.

2.1.2 Expansion System

Aerosols were prepared, as discussed in Section 2.3, by expanding, at a controlled rate, a gaseous pre-mixture from the explosion vessel, into an expansion tank with a volume of 28 litres which was connected to the explosion vessel through the top port, as shown in Fig. 2.1. Prior to its use in the present system, the expansion tank was itself a combustion vessel, although documentation no longer exists. The tank was linked to the exhaust system via a ball valve which was connected to a $\frac{1}{2}$ " BSP port.

The explosion vessel and expansion tank were connected via a pipeline of 38 mm internal diameter, into which was fitted an expansion valve comprising a ball valve of 26 mm internal diameter. This was operated pneumatically, and was used to separate the explosion vessel and expansion tank. It was placed immediately outside the explosion vessel. Mixture expansion was controlled by a throttle, which comprised of interchangeable orifice plates. An orifice of 6 mm produced an expansion time to pressure equilibrium between the two vessels of approximately 4 seconds. This long time duration, relative to that for combustion, allowed for easy synchronisation of the spark and diagnostics with respect to the desired state of mixture expansion. The slow expansion also minimised any resulting flow disturbances within the combustion chamber. For turbulent experiments, more rapid expansion was required because the rate of droplet evaporation, following formation by the expansion process, was much higher than for laminar work, due to turbulent heat transfer from the wall region. The expansion time was reduced to 0.15 seconds, by using a 25 mm diameter orifice.

2.1.3 Ignition Systems

Throughout most of the present research, fuel-air mixtures were ignited using an electric spark discharge. In addition, a small number of experiments used laser induced ignition (Sections 4.1.5 and 4.5). Each is discussed below.

2.1.3.1 Electric Discharge Spark Ignition

The electric discharge spark ignition unit was previously used and described by Atzler (1999). The unit comprised a capacitor discharge unit and a discharge trigger switch. The voltage across the capacitor was monitored by a voltmeter. The trigger produced a small coil generated spark at the spark electrodes, thus providing an ionised electrical path for the release of the capacitor charge, which supplied the main spark. The capacitor was charged to typically between 35 and 40V using an adjustable DC power supply. The voltage across the capacitor was monitored by a voltmeter.

The aerosol mixture was ignited centrally in the explosion vessel with a standard Miniglo model aircraft engine spark plug. The plug was held on an extension screwed into one of the horizontal 1" BSP ports of the vessel. It produced a spark with energy of approximately 300 - 400 mJ (Atzler, 1999).

In addition, a low energy ignition unit was used in a small number of turbulent experiments with gaseous flames, addressed in Section 5.6.1. The unit comprised a Lucas 12 V transistorised automotive ignition coil system, which was connected to the spark electrode assembly.

2.1.3.2 Laser Induced Ignition

During the electric spark discharge ignition in some experiments, flying molten metal from the electrodes was observed, as addressed in Section 5.1.5, and these might influence the properties of the resulting flame propagation. Since a laser

induced ignition does not introduce any similar particle. It was used in the present research for comparison.

A detailed description of the laser ignition system is given in Mokhtar (2001) and is shown schematically in Fig. 2.3. An intense narrow laser pulse from a Spectron SL800 pulsed Nd:YAG ($\lambda = 1064$ nm) laser system was directed by 45° high energy mirrors to beam steering optics. A beam stopper prevented the laser from passing through the optics until it was required. A polarizer ensured that the output beam was linearly polarized to avoid occurrence of multiple simultaneous breakdowns close to the focal point. The combination of a half wave plate (HWP) and a second polarizer allowed adjustment of the laser energy that was transmitted to the explosion vessel. The beam was expanded from 6 mm to 24 mm diameter, by a plano concave lens, $f = 50$ mm (Lens 1), and a plano convex lens, $f = 300$ mm (Lens 2). This allowed a tighter focus than otherwise. A further focusing lens, $f = 200$ mm (Lens 3), focused the beam at the centre of the vessel through a 25 mm lateral window as shown in Fig. 2.3. With the optical setup used in the present experiment, the laser ignition focal point diameter was $41 \mu\text{m}$.

2.2 Synchronization and Data Acquisition System

Accurate control of experimental conditions and data acquisition required the precise synchronisation of measurement equipment and data acquisition systems with the expansion and combustion events. The datum parameter for all experiments was the start of expansion. All equipment were triggered by a principal trigger switch, PTS, fitted to the expansion valve. This consisted of a micro switch which was actuated by the expansion valve lever, within 2° of lever movement and before

the actual start of valve opening. Consistency of valve opening was assessed and discussed by Atzler (1999).

Pressure and temperature records were digitised on a 16-bit National Instruments PCI-6034E analogue-to-digital conversion (ADC) board. The signal inputs to the ADC were analogue voltages from the thermometer and pressure transducer amplifier. The output sensitivity of the thermometer was 1 mV/K and that of the transducer amplifier 1 mV/kPa. A typical temperature measurement had a dynamic range of approximately 50 K, or 50 mV and a typical pressure measurement had one of approximately 100-200 kPa or 100-200 mV. In addition to errors associated with the thermometer and ADC systems, the raw data displayed fluctuations of approximately ± 1.2 K at a frequency of approximately 50 Hz, which indicated electro-magnetic noise from the mains electricity supply. This was minimised using a 5-point moving average smoothing routine, which reduced the fluctuations to about ± 0.2 K. The control and monitoring of the measurements were done using LabView version 7.1 software, which was installed into a desktop computer.

2.3 Mixture Preparation

The principal fuel used for this research was iso-octane, which is the closest single component fuel to gasoline. It was chosen because data for its gaseous combustion have been obtained for a wide range of experimental conditions at Leeds and elsewhere, and are available for comparison with results from the present research. Atzler (1999) demonstrated that the evaporation and condensation properties of iso-octane were suitable for use in the current research apparatus, with regard to the temperature and pressure limitations of the rig. Iso-octane, 2-2-4-

trimethylpentane, was supplied by Ultrafine Ltd. and was specified to be at least 99.99% pure with 50 ppm maximal water content. Its molar mass was 114.23 kg/kmol.

Bottled industrial grade dry air, with molar mass of 28.97 kg/kmol, was used in the fuel-air mixtures to minimise the possibility of water droplet generation during the expansion process, which might occur if inadequately dried air from the laboratory's compressed air supply were used. The air was supplied by BOC Gases, with a specified composition of: 78 % N₂, 21 % O₂, 0.9 % Ar, H₂O < 250 ppm, CO < 10 ppm, CO₂ < 500 ppm and oil < 1 ppm. Boilson *et al.* (2003) demonstrated in their experimental work that the addition of argon to a hydrogen plasma would increase the negative ion density, and thus this could probably increase the ignition energy. However, the amount of argon in the bottled dry air is equivalent to that in the atmosphere (Groves, 2006). Furthermore, in ignition studies with mixtures of C₂H₄-O₂ and 98 % Ar (Kalitan *et al.*, 2005), it was shown that argon displayed negligible effect on ignition energy. The effects of foreign species in the bottled dry air on combustion were assumed to be negligible.

The preparation of aerosol comprised: pre-heating the expansion vessel to the initial temperature; the preparation of a gaseous pre-mixture; and the expansion process that generated the aerosol. These procedures are presented in Sections 2.3.1 to 2.3.3.

2.3.1 Pre-Heating of the Explosion Vessel

Prior to experiments the explosion vessel was heated, with its internal heaters, to a temperature of 303 K. This temperature ensured complete evaporation of the liquid fuel. It also provided the required temperature datum to enable comparison with the data of other workers, for both gaseous and aerosol experiments.

To ensure spatially homogeneous condensation, a uniform temperature throughout the mixture was required. For this, the explosion vessel was heated to a preliminary value above the desired initial temperature and then left to cool and homogenise for approximately one hour. Temperature uniformity was ascertained by monitoring the temperature at several locations around the outside of the vessel. Good temperature homogeneity across the vessel was assumed when the difference between the measurements was less than 2 K.

2.3.2 Preparation of Gaseous Pre-Mixtures

Before the introduction of fresh combustible mixture, the explosion and expansion vessels were evacuated and flushed with air to remove residuals from previous experiments. After flushing, the explosion and expansion vessels were, again, evacuated before the valve connecting them was closed. Liquid iso-octane was then injected into the explosion vessel, through a needle valve. The low pressure ensured complete and fast evaporation. Further, the fans were run at 1500 rpm to improve vaporisation of the liquid fuel. The appropriate volume of liquid fuel for given initial conditions in terms of temperature, pressure and overall equivalence ratio, was calculated, as described in Chapter 3, using the stoichiometric equation and the ideal gas law. The fuel was injected using either a 5 ml or 10 ml Hamilton Microliter glass syringe, depending on the volume required. Atzler (1999) found that the accuracy of the injected volumes was better than ± 0.015 ml and ± 0.03 ml, respectively, yielding an equivalence ratio accuracy of within $\pm 0.5\%$. After fuel injection, air was added to the initial pressure for the experiment, typically at 200 kPa.

2.3.3 Generation of Aerosols

The Wilson cloud chamber method (Wilson, 1911) was used to generate a homogeneously distributed aerosol in the explosion vessel with a near monosize distribution of droplet diameters. Following mixture preparation as described in Section 2.3.2, the expansion valve was opened and the mixture was allowed to expand into the expansion tank. When the temperature became significantly lower than the saturation temperature of the fuel, condensation occurred.

For combustion studies, the aerosol was ignited at selected times after the start of expansion, allowing variation of the initial conditions at ignition, in terms of liquid and gaseous phase equivalence ratio, droplet size, pressure and temperature. Combustion occurred while the mixture was expanding. However, since the combustion duration was short, typically of the order of 20 to 60 ms, relative to the expansion duration of about four seconds for laminar conditions, quasi steady state was assumed in the unburnt mixture.

For turbulent experiments, the expansion duration to pressure equilibrium was approximately 0.15 seconds. This was required because the rapid heat transfer from the chamber walls, when the fans were switched on, allowed the maintenance of an aerosol for only a very short period. The combustion duration was typically less than 10 ms and, hence, the assumption of quasi steady conditions also was applied for turbulent conditions.

2.4 Instrumentation for Aerosol and Flame Analysis

Aerosol properties were determined with a Phase Doppler Anemometer, PDA, laser attenuation measurements and by equilibrium calculations based on pressure, temperature and overall equivalence ratio. The flame growth in an aerosol mixture

was recorded with high speed schlieren cine photography, to obtain flame speeds and burning velocities, and with laser sheet imaging.

2.4.1 Phase Doppler Anemometer System

A Phase Doppler Anemometry (PDA) system was available to the author from the EPSRC (Engineering and Physical Science Research Council) loan pool for a period of 3 months during the present research. PDA is an optical technique used to simultaneously measure size and velocity of spherical particles. The main advantages of PDA are that it is a non-intrusive measurement, can be used on-line and in-situ, it is an absolute measurement technique (no calibration is required), it has very high accuracy and very high spatial resolution (small measurement volume).

A good description of the principle of operation is given in Eder and Jordan (2001). The PDA technique, which is based upon phase Doppler principles, measures droplet size at a local point in a flow field. It is operated with the assumption that the droplet is spherical and transparent. When a droplet passes through the intersection of a pair of coherent laser beams, the light is scattered by reflection and refraction. Two photo detectors, arranged at slightly different locations, receive the scattered light waves with different phases. The phase shift between these two signals is proportional to the diameter of the particle.

The arrangement of apparatus is shown in Fig. 2.4. It used instrumentation manufactured by Dantec Measurement Technology A/S and comprised the following components:

- (a) a 300mW argon-ion laser source, LaserPhysics Reliant 500m;
- (b) a laser splitter and manipulator, Dantec 60 × 26;
- (c) a signal processor, Dantec 58N80-MultiPDA;

- (d) optical-fiber cables, to convey the beams to the transmitter;
- (e) a transmitter with a convergent lens, $f = 600$ mm;
- (f) a receiver with a convergent lens, $f = 300$ mm;
- (g) a traverse system Dantec 57G15; and
- (h) operating software, Sizeware 2.3, installed into a desktop computer.

For the present research a pair of green beams ($\lambda = 514$ nm) was used. The receiver and transmitter were positioned at an angle of 31° as shown in Fig. 2.4; this being the optimal angle for PDA measurements. A Transistor-Transistor Logic (TTL) signal from the expansion valve (Section 2.1.2) generated a 5 V square signal from a TTI TGP 110 pulse generator. This was used to synchronize the expansion event with PDA data acquisition. The square wave signal was taken to an encoder in the signal processor, which marked the point at which expansion started.

2.4.2 Laser Attenuation System

This standard technique, extensively described in the literature (e.g. Mathieu, 1975), measures intensity attenuation of a laser beam due to its passage through a specific fluid medium. An arrangement of the present system is shown in Fig. 2.5. The experiments were undertaken for two reasons. First, laser attenuation enabled assessment of the starting point of condensation, by measuring the reduction in laser power when the first droplets appeared. Second, laser attenuation during the expansion event was used to calculate the number density (N_D) using the *Beer-Lambert* law:

$$\frac{I}{I_o} = \exp(-N_D \sigma_e L) \quad (2.2)$$

where I_o and I are the intensities of the original and attenuated laser beam respectively, N_D is the number density, L is the optical path length taken to be

305 mm, which is the length of the vessel, and σ_e is the extinction cross section which is constant for visible light frequencies. It is defined by (Bachalo, 1991):

$$\sigma_e = \frac{\pi}{4} \bar{Q}_e D_{20}^2 \quad (2.3)$$

where \bar{Q}_e is the mean extinction efficiency and D_{20} is the diameter of droplet that would have the same surface area as the average for the whole spray. During the present work, values of D_{20} were calculated only for a limited number of cases. When such values were unavailable, values of the length mean diameter, D_{10} , were substituted using values determined from PDA measurements (Section 2.4.1). This was considered by Marquez (2003) to be a reasonable approximation, because the narrow distribution of drop size resulted in little difference between D_{10} , D_{20} , D_{30} and D_{32} .

Figure 2.5 shows the setup for laser attenuation experiments. Most experiments recorded the average for the whole field of view of the windows. However, some measurements recorded the radial variations and used the setup illustrated in the inset of Fig. 2.5. For the main experiments, a 20 mW He-Ne laser ($\lambda = 632$ nm) was expanded up to a diameter of 150 mm by an Olympus A40 microscope lens, where it was collimated by a 150 mm diameter plano-convex lens ($f = 1000$ mm). After passing through the two windows of the explosion vessel, a second, identical lens was used to refocus the parallel beam onto a pinhole. The laser was detected by a power meter and was converted into an analogue voltage output, which was received by the ADC system, described in Section 2.2. When measurements of spatial variations were required, the two 150 mm diameter lenses were replaced by four 25 mm diameter plano-convex lenses ($f = 100$ and 500 mm), and the single pinhole / power meter arrangement was replaced by four as shown in the inset in Fig. 2.5. This allowed the measurement of spatial variations within a

radius of 60 mm. Marquez (2003) measured spatial variations of D_{10} using PDA. However, due to geometrical constraints of PDA, this was possible only within the much smaller radius of 30 mm.

An input-output calibration undertaken by Marquez (2003), using absorptive neutral density filters of known attenuation, showed that the power meter has a linear response in voltage for intensity attenuation throughout the whole range of operating conditions. This is given by:

$$\frac{I}{I_o} = \frac{\left(\frac{V}{V_o} + 0.0279\right)}{1.0483} \quad (2.4)$$

where the voltage ratio V/V_o was obtained from experiment.

2.4.3 High Speed Schlieren Photography

The rate of flame growth was recorded using high speed schlieren cine photography. The arrangement of equipment in this case was very similar to the one for laser attenuation experiments shown in Fig. 2.5 (same optics). However, the laser was replaced by a 50 W halogen light and the power meter was replaced by a Phantom V4 high-speed digital camera. The camera was operated with Phantom Camera Control 7.0 software. The system generated monochrome 512 by 512 pixel images with a sensitivity equivalent to 1600 ASA. At full resolution it was capable of recording movies at 1000 frames per second.

The circuit shown in Fig. 2.6 was used to synchronize with the expansion process, both the start of the high speed camera and the time of ignition. When the expansion valve opened, it activated the principal trigger switch, PTS, which sent a signal to start an Omron H8GN countdown timer. The signal from the timer was converted by the signal converter into break (OFF) and make (ON) signals for the

camera and ignition systems respectively. The signal for the camera trigger was converted into a light pulse by the opto-isolator depicted in Fig. 2.6. This isolated the camera trigger system from signal interference generated by the ignition unit.

The processing technique for the schlieren images was described by Ormsby (2005), and only brief details are given here. The flame images were originally in a greyscale format. Using Adobe Photoshop software the images were thresholded to yield a white flame image on a black background using the 'colorburn' layer blending mode. The resulting black and white image was then converted into an encapsulated postscript (eps) file. A FORTRAN computer program, Edge, developed by Dr. Robert Woolley, formerly a Research Fellow in the School of Mechanical Engineering, read the eps file as a data input and calculated the number of white pixels in each image, which represented the cross-sectional area of the flame. A transparent grid of 10mm \times 10mm, attached to the window of the vessel, was used to scale the measurements to true distances. The flame radius was calculated as the radius of a circle with the same area as the flame. From time and distance measurements, flame radius against time data were calculated. These were analysed to derive flame speed and burning velocity.

2.4.4 Laser Sheet Imaging

2.4.4.1 Technique of Laser Sheet Imaging

Planar Mie Scattering uses a thin sheet of laser light to produce a cross-sectional two dimensional image of a three dimensional flame. The light is scattered from seed particles, which, in the present work, were the fuel droplets. The droplets evaporate or burn as they cross the flame front and consequently do not scatter light from the products, while the droplets in the unburnt mixture do so. A planar cross-section of the flame is imaged, perpendicular to the incident light sheet and the

flame is identified as the frontier between the bright unburned, and the dark burned regions in the illuminated zone (Duraó and Heitor, 1990).

The arrangement of apparatus for planar Mie scattering is shown in Fig. 2.7. The system used in the present work was fully described by Gillespie (1998), and only brief details are given here. A high speed digital camera (Section 2.4.4), was used in conjunction with a copper vapour laser, Model LS20-50, supplied by Oxford Lasers. The laser wavelength was 510.6 nm (green), and the light energy was 2 mJ/pulse, which provided sufficient light for flame photography.

As shown in Fig. 2.7, the laser beam, 25 mm in diameter, was manipulated, using a combination of a spherical bi-convex lens, $f = 1000$ mm, to focus the laser beam, and a plano-convex cylindrical lens, $f = 1000$ mm, to expand the beam in one plane to form a sheet. The sheet passed through a vertical plane in the centre of the explosion vessel, orthogonal to the direction of flame observation. The sheet thickness was approximately 0.7 mm, which is thin enough, relative to the overall dimensions of the flame, to provide a true 2-dimensional image. Laser sheet imaging required synchronisation of the digital camera, copper vapour laser and the spark with the expansion event. The circuit is also incorporated in Fig. 2.6. The device for synchronising the digital camera and the laser operation was developed and built by Mr Brian Leach, Thermodynamics Laboratory technician in the School of Mechanical Engineering. When the digital camera received a trigger signal from the timer, it also sent a synchronization signal to a pulse generator to ensure that the camera operated in time with the laser source.

2.4.4.2 Analysis of Planar Laser Sheet Images

Images obtained with the laser sheet imaging technique, were processed to yield flame speed from consecutive images and to obtain the velocity of the droplets

ahead of the flame front by particle image velocimetry, PIV. This is explained in Section 2.4.4.3.

Shown by the insertion in Fig. 2.8 is a typical laser sheet image of laminar aerosol flame, which indicates the burned and unburned region. Detailed description of this image is given in Section 4.1.4. From this, the FORTRAN program, Edge, described in Section 2.4.3, counted the number of white pixels (region occupied by droplets) within a band between r and $r + \delta r$, where r is the flame radius measured from the centre of ignition and δr is the increment of radius corresponding to 1 pixel. The graph in Fig. 2.8 shows the variation of the number of white pixels with radial distance from the electrode. The steep gradient in the graph at a flame radius of about 86 mm represents the boundary between burned product and unburnt aerosol mixture. The flame radius was obtained by taking the mid-point of the gradient, as shown in Fig. 2.8. The profile of the plot does not agree with the typical profiles of temperature and heat release at the flame front as illustrated in Fig. 2.9 (reproduced from Haq, 1994). In Fig. 2.8 the change of radius between the two extremes of fully burned and fully unburned is approximately 2 mm, whereas in (Haq, 1994) it is less than 0.5 mm. The disagreement between the profiles of the plots in Figs. 2.8 and 2.9, is probably due to the non-concentricity of the flame edge in Fig. 2.8 with that of a true circle.

2.4.4.3 Particle Image Velocimetry

Particle Image Velocimetry comprises a class of flow measuring techniques that is characterised by the recording of the displacement of small particles suspended in a fluid. Atashkari (1997) produced a detailed description of the principles of PIV. Atzler (1999), Mokhtar (2001) and Marquez (2003) used the technique for ignition studies in a droplet cloud. With this technique, the flow field is illuminated with a strong light source to record the scattered light from the droplet

particles, as described in Section 2.4.4.1. In the present work, the field of view was approximately 60×120 mm, which provided a sufficiently large, yet detailed image, for analysis.

The original greyscale laser sheet images were processed with the help of Mr. Gunnar Larsson, another research student in the School of Mechanical Engineering, using the DaVis 7.0.3 software package from LaVision GmbH. The images were processed to yield flame radius from consecutive images and to obtain the velocity of the droplets ahead of the flame front. The measurement of velocity involved the measurement of a travelled distance in a known time interval. Two spatially coincident laser sheets at a known time separation provide two images of particles on the recording medium. Shown in Fig. 2.10(a) is a sketch of a typical interrogation plane of the digitised image that was divided into equal interrogation areas, reproduced from Atashkari (1997). In the present work, the size of each interrogation area was 16×16 pixels. Provided that the dimensions of the interrogation area were larger than the maximum particle displacement between two successive images, there were particle image pairs which were related to the motion of the recorded flow. In most practical cases an interrogation area included many particle image pairs along with some single images due to particles crossing the plane or leaving/arriving in the interrogation area between laser pulses. Consecutively, each individual interrogation area was examined to evaluate its corresponding velocity vector. As shown in Fig.2.10(b) the horizontal and vertical displacements in the object plane, the plane at which the sheet intersected the flow, were found by determining the displacements in the image plane, Δx_i and Δy_i , on the recording medium. Knowing the magnification, M , of the optical system, and the time separation between the two sheets, Δt , the velocity projections on the measurement plane, u_x and u_y , can be evaluated by

$$u_x = M \frac{\Delta x_i}{\Delta t} \quad (2.5)$$

and

$$u_y = M \frac{\Delta y_i}{\Delta t} \quad (2.6)$$

Further descriptions of the PIV processing techniques are available in Larsson (in preparation).

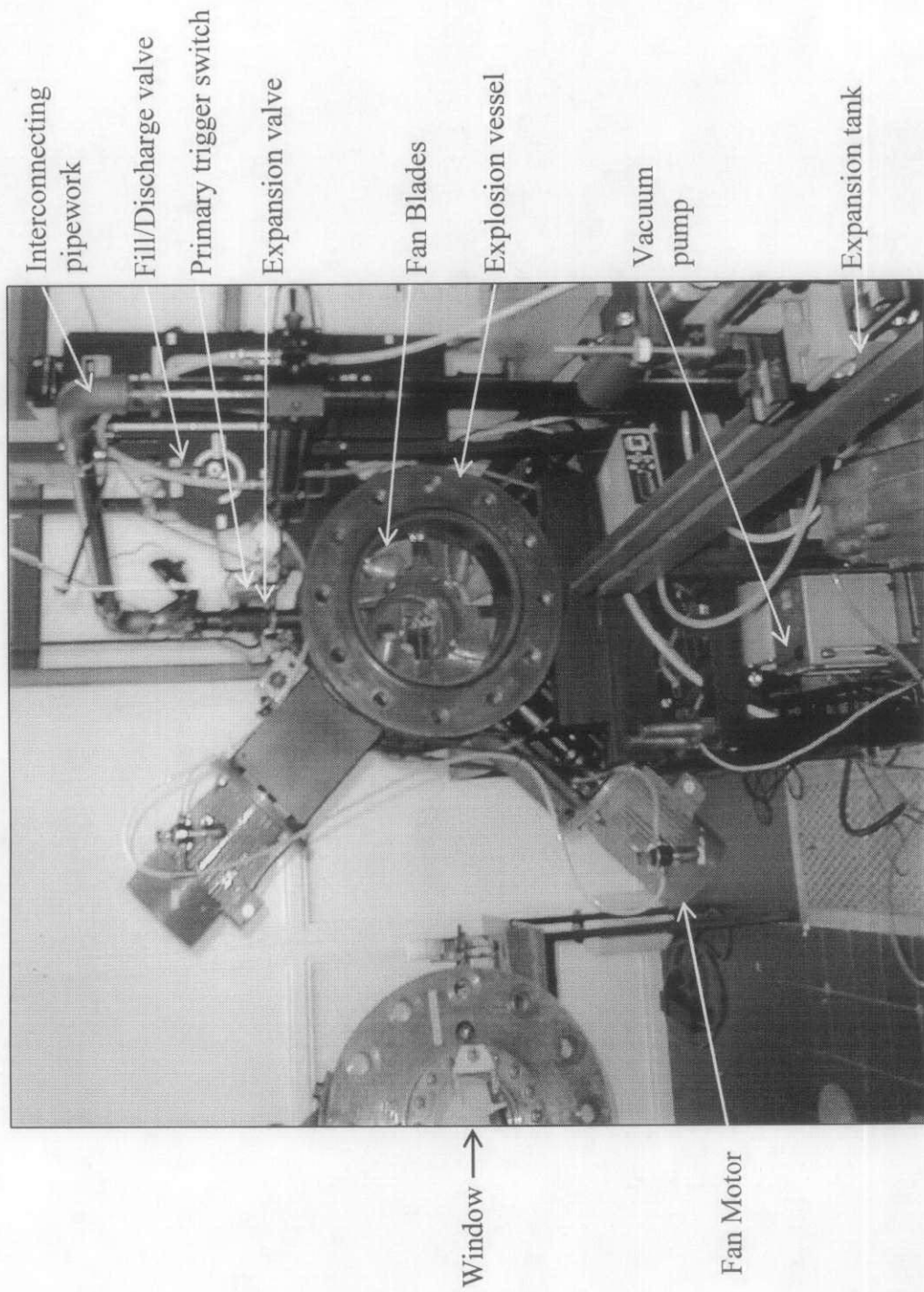


Figure 2.1 Photograph of the cylindrical explosion vessel, with one end plate removed. Reproduced from Marquez (2003).

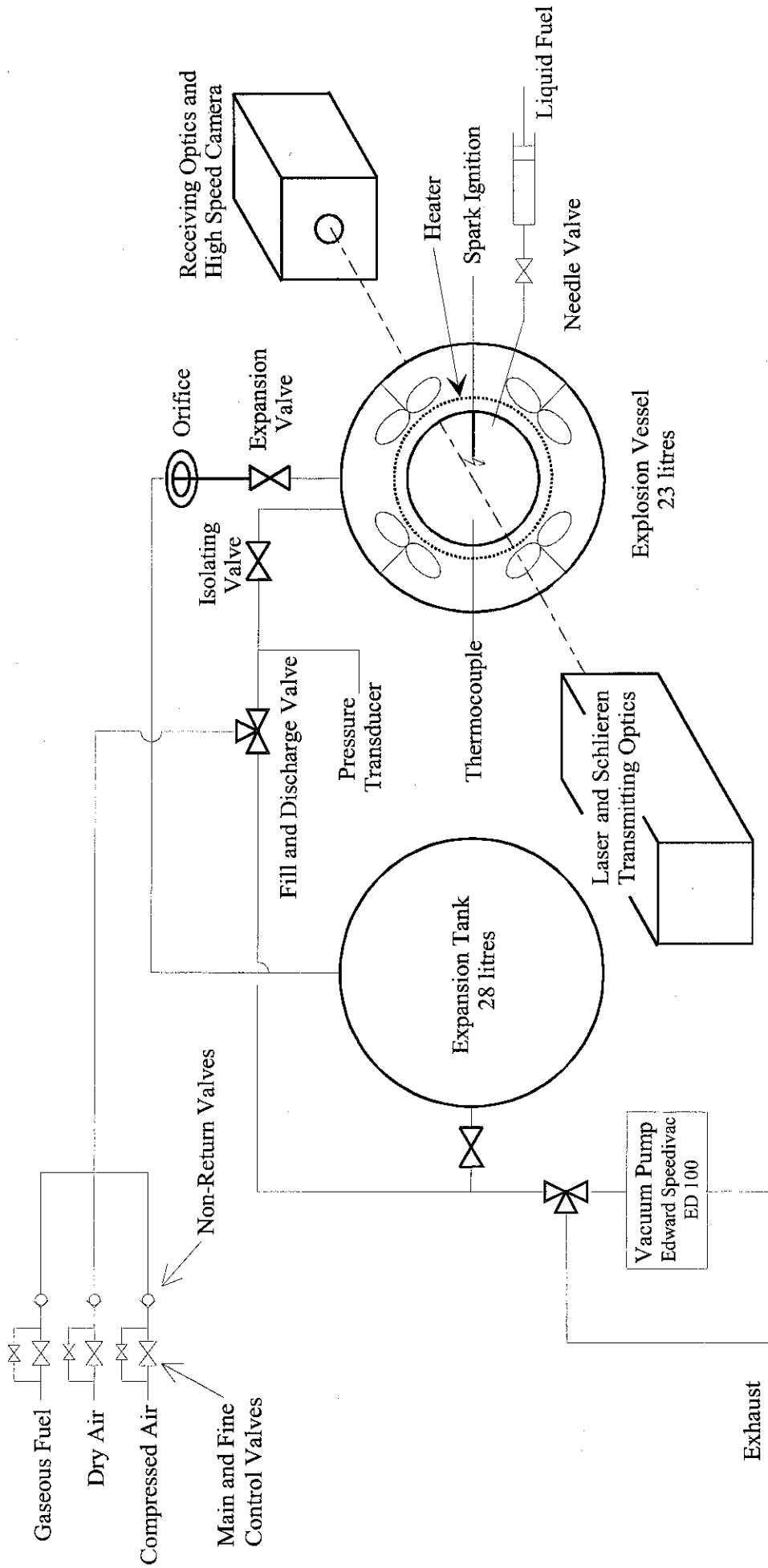


Figure 2.2 Schematic of aerosol combustion apparatus with schlieren system. Reproduced from Atzler (1999).

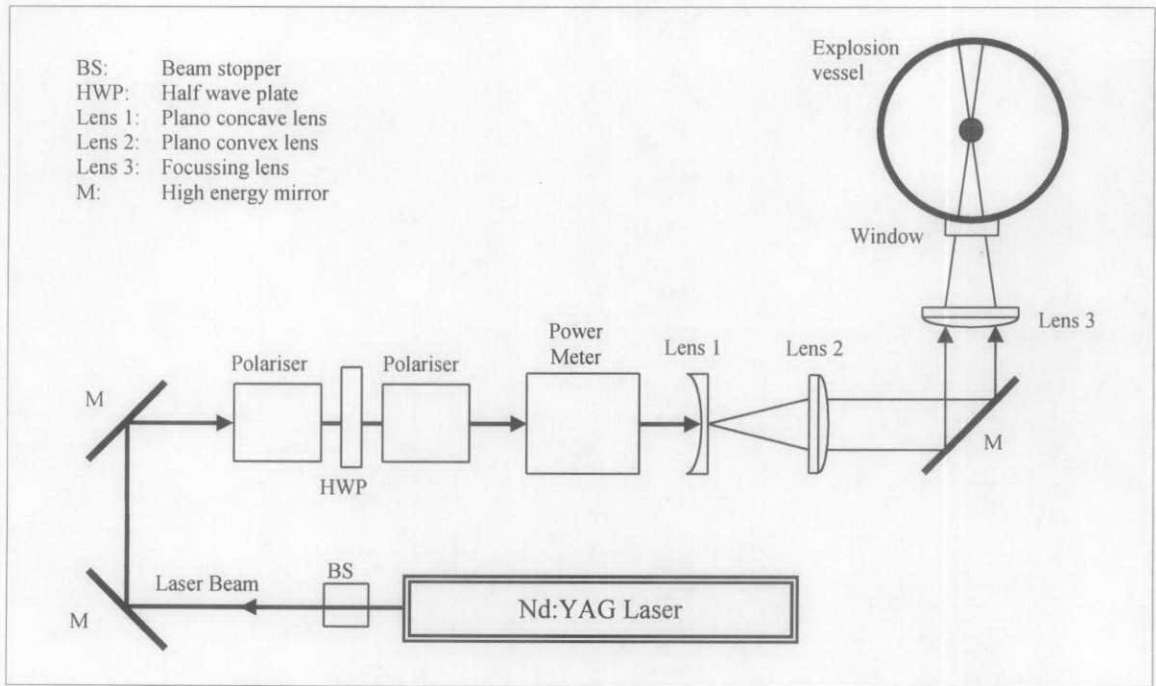


Figure 2.3 Schematic of laser ignition optical setup.

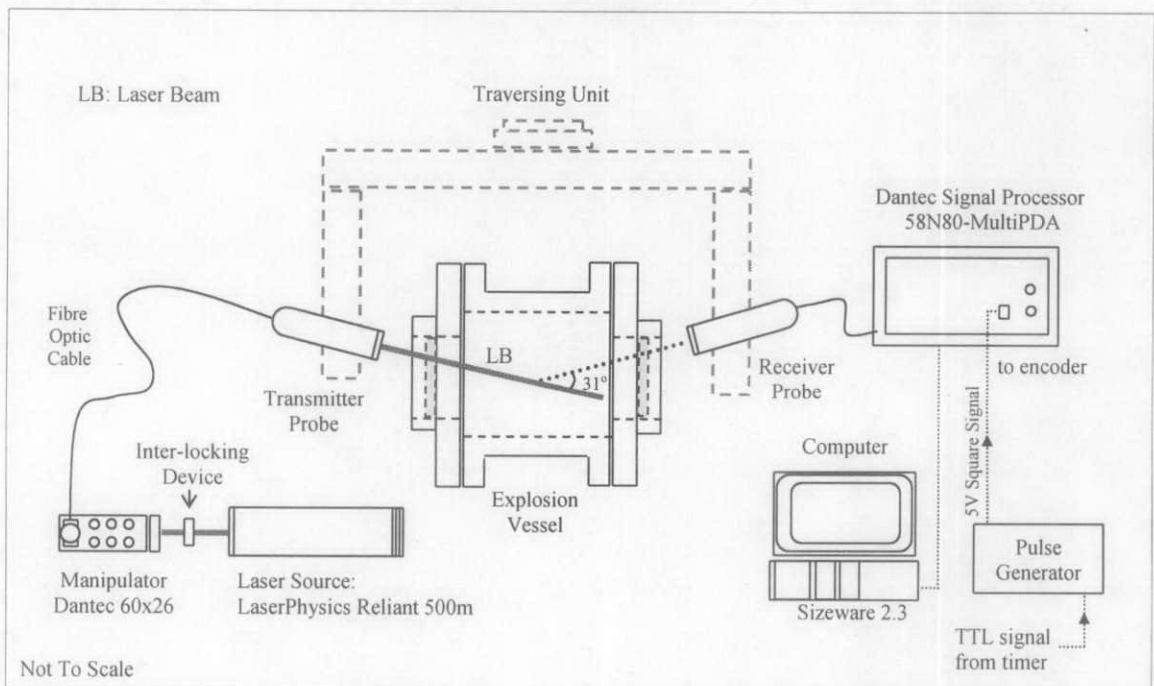


Figure 2.4 Arrangement of PDA apparatus for droplet size measurement.

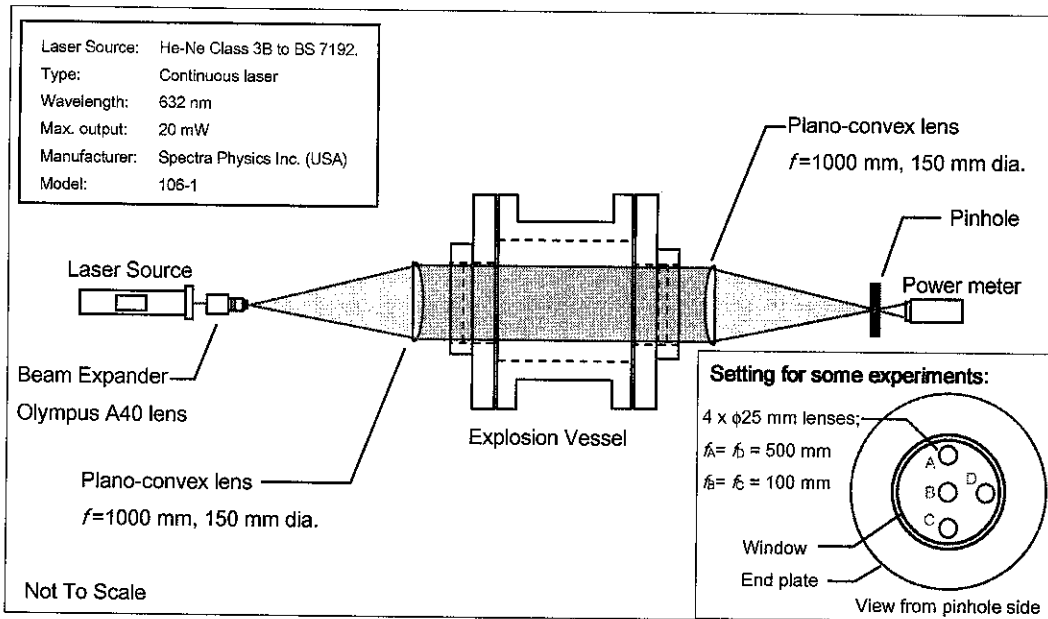


Figure 2.5 Experimental set-ups for laser attenuation and schlieren measurements.

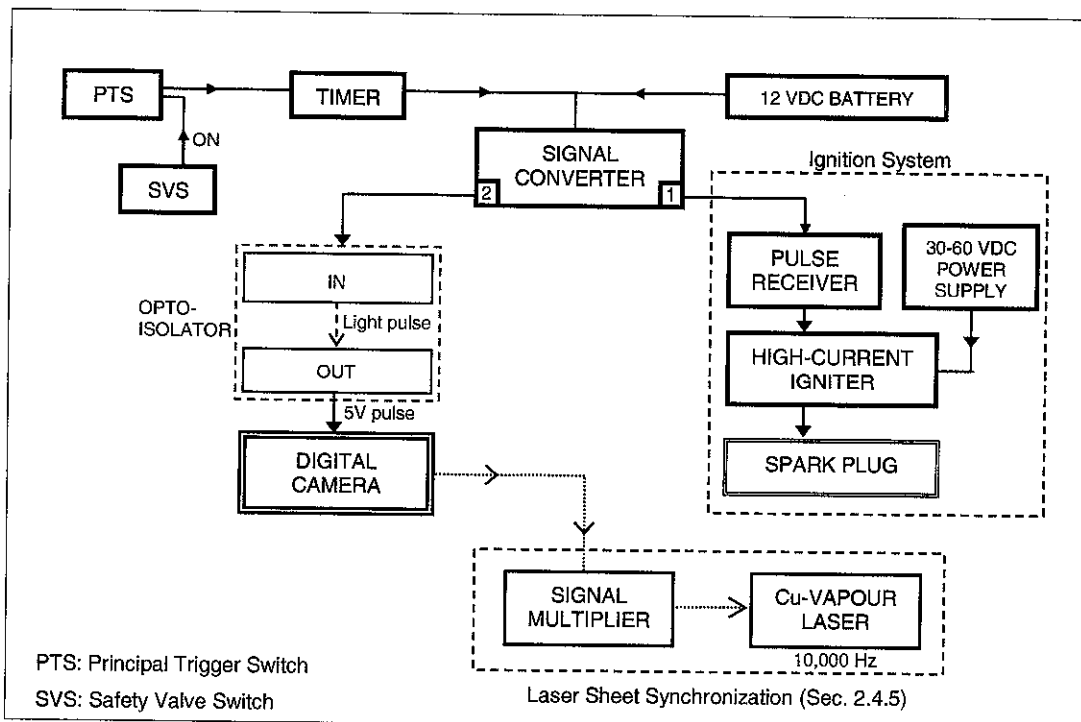


Figure 2.6 Schematic of the control circuit for ignition, camera and laser systems.

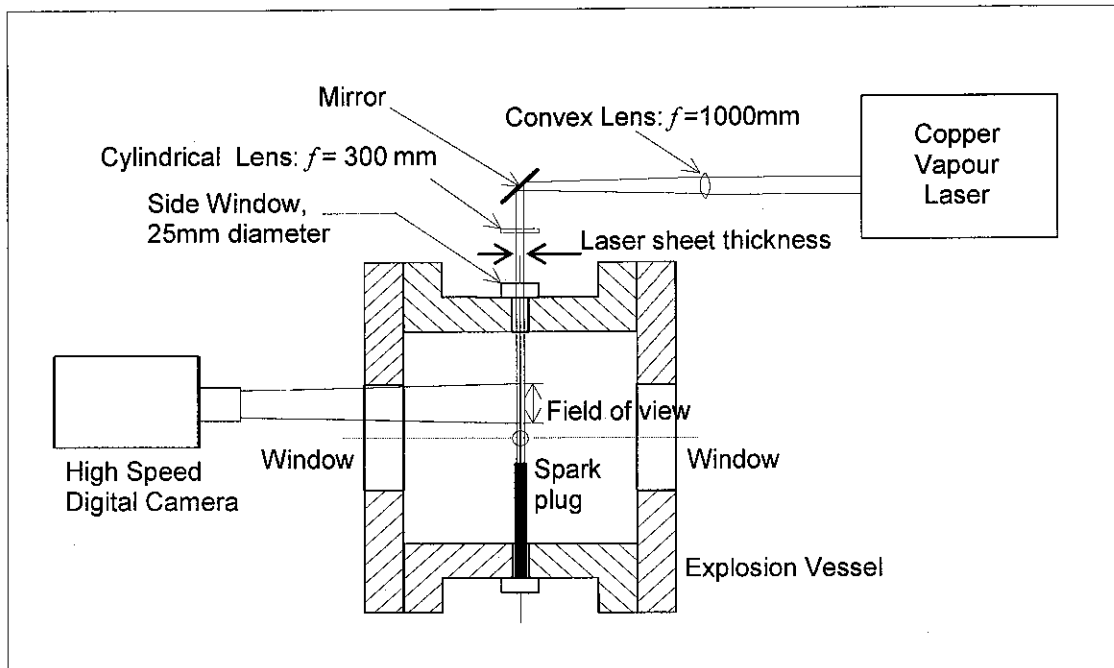


Figure 2.7 Schematic of laser sheet imaging system. Reproduced from Marquez (2003).

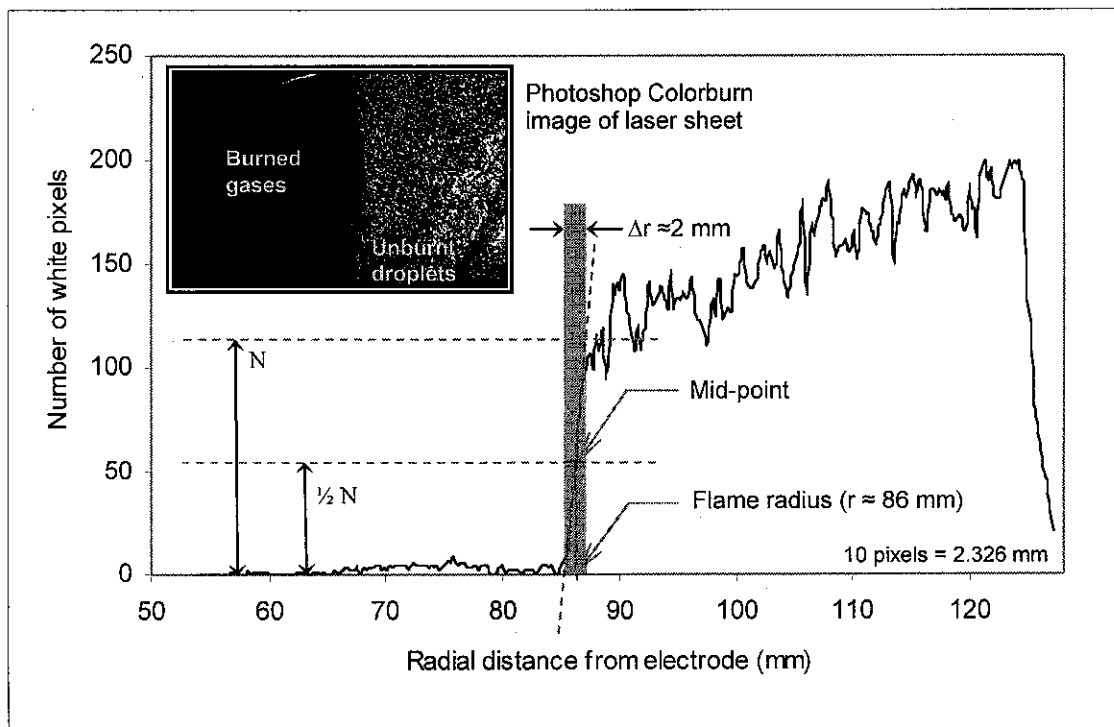


Figure 2.8 Variation of number of white pixels with radial distance from electrode for determination of flame radius from a typical laser sheet image.

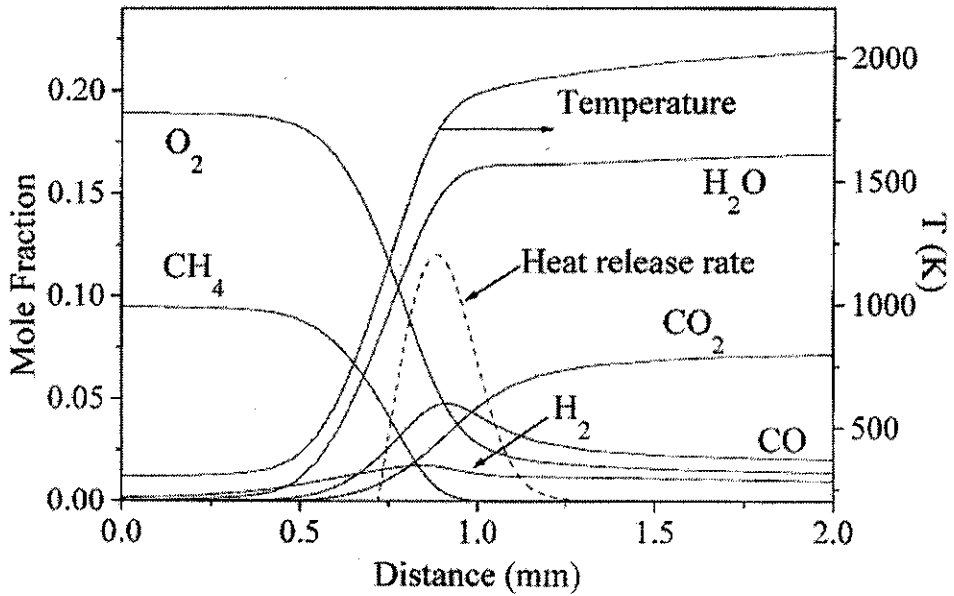


Figure 2.9 Computed composition and temperature profiles for a one-dimensional adiabatic premixed flame in a stoichiometric methane-air mixture at 100 kPa and 300 K. Reproduced from Haq (1998).

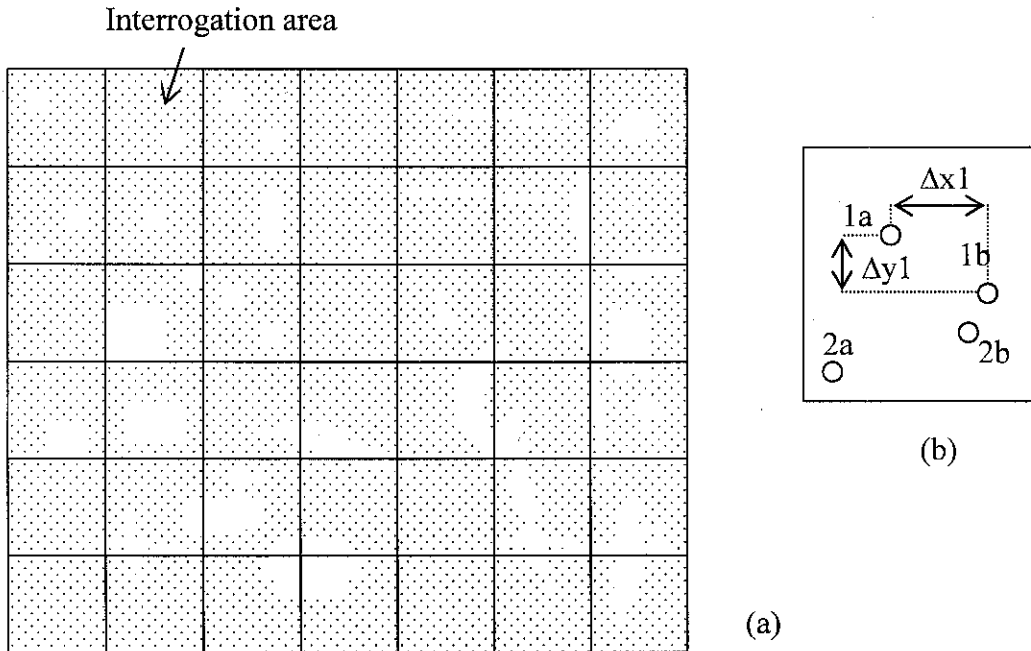


Figure 2.10 (a) Ideal digitised image divided into equal interrogation areas, (b) Ideal interrogation area showing particle displacement. Reproduced from Atashkari (1997).

Chapter 3

Characterisation of Aerosols

This Chapter presents an analysis of the two-phase mixture composition, in terms of gaseous and liquid fractions of the fuel and drop size, as a function of time during the expansion process. In Section 3.1, a theoretical analysis is presented. It is based on the thermodynamic principle that, given any two properties of a system, in this case pressure and temperature, any other property, here the liquid fraction, can be calculated. In Section 3.2, experimental data on temperature and pressure during expansion of iso-octane air mixtures are presented. The results of droplet size measurements, using the PDA technique, are shown in Section 3.3. Experimental data on laser attenuation measurements under quiescent conditions are presented in Section 3.4. Calculations of number density and of gas and liquid mass fractions and equivalence ratios are also included in Section 3.4. The combustion studies, presented in Chapter 4, make use of the data presented in this chapter.

3.1 Aerosol Property Calculations

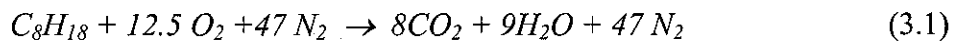
During the fuel-air mixture expansion process (Section 3.3.3), the iso-octane within the mixture undergoes a phase change. Figure 3.1 shows a schematic of the expansion process on P - v and T - s diagrams, with two extreme assumptions of constant specific entropy (dashed line) and constant temperature (dotted line). During expansion the wall temperature is, essentially, constant. The mixture temperature reduces due to expansion but receives heat from the walls. If expansion

is fast, the heat transfer from the walls will be negligible, hence isentropic. Conversely if the expansion is slow, the process will be at constant temperature. Considering first the isentropic case, at the start of expansion (state 1), the fuel is completely vaporised and superheated. Thus the system is in gas phase equilibrium until saturation of the fuel vapour is reached (state 2) when its partial pressure is equal to its vapour pressure, as shown in Figs 3.1 (a) and (b). In the two-phase regime, for instance at state 3, a fraction of the fuel is in the vapour phase, and the rest in the liquid phase. Next, considering the constant temperature case, from state 1 to state 4, the fuel vapour will never reach the saturation point due to the heat supplied from the walls, and hence the mixture remains in the gas phase throughout expansion. In reality, as shown in Section 3.2, the process is very close to isentropic.

The fractions of liquid and vapour phase of the fuel, as depicted in Fig. 3.1, are important parameters for the determination of aerosol properties; this section presents the method of calculating them.

3.1.1 Gas Phase in Equilibrium

The molar composition of a stoichiometric mixture of iso-octane and air can be calculated from the stoichiometric equation



For a non-stoichiometric mixture, the reactants on the left hand side of Eq. (3.1) can be expressed as



where ϕ is the equivalence ratio. Normalised to one mole of mixture, this is

$$1 \text{ mole reactants} = \frac{\phi}{59.5 + \phi} C_8H_{18} + \frac{59.5}{59.5 + \phi} Air \quad (3.3)$$

From Eq. (3.3), the mole fractions of air and fuel are

$$\frac{n_a}{n} = \frac{59.5}{59.5 + \phi} \quad (3.4)$$

and

$$\frac{n_f}{n} = \frac{\phi}{59.5 + \phi} \quad (3.5)$$

where n_a , n_f and n are the numbers of moles of air, fuel and the total mixture. The ratio of the partial pressures of two gaseous species is equal to their mole fractions, such that

$$\frac{n_a}{n_f} = \frac{P_a}{P_f} \quad (3.6)$$

where P_f and P_a are the fuel and air partial pressures. Eq. (3.6) is only valid for an ideal gas and cannot be used for liquid. Following from Eqs. (3.5) and (3.6), the partial pressure of the fuel can be expressed as

$$P_f = P \frac{\phi}{59.5 + \phi} \quad (3.7)$$

3.1.2 Mass Fraction and Equivalence Ratio

The state, at which the fuel is completely vaporised and superheated, such that it is well away from saturation conditions, is defined by the ideal gas law

$$P_f V = n_f R T \quad (3.8)$$

where V is the volume occupied by the mixture and R is the universal gas constant. Equation (3.8) can also be represented by

$$P_f v = R T \quad (3.9)$$

where v is the specific volume of the vapour. In an ideal system, saturation of the fuel vapour is reached when its partial pressure is equal to its vapour pressure. In the wet region, the partial pressure cannot be used to characterise the total fuel content

because some of it is liquid. However, the gaseous portion of the fuel, if in equilibrium, can be approximated by making the assumption

$$P_f = P_v \quad (3.10)$$

where the subscript v denotes the vapour pressure of the fuel. This is calculated from the mixture temperature (in Kelvin), using a function of the form:

$$P_v = 133.3224 \times 10^{(A+B/T+C\log T+DT+ET^2)} \quad (3.11)$$

with the coefficients $A = 50.3422$, $B = -3278.9$, $C = -16.111$, $D = 0.007426$ and $E = -9.1804\text{E-}14$, (Yaws, 1993). The constant, 133.3224, accounts for the conversion of pressure from *mm Hg* to *Pa*.

At saturation conditions, the ideal gas law is, strictly, not valid. However, it does give a good approximation, which is demonstrated by comparing the ideal gas law with tabulated data. Equation (3.9) gives

$$R = \frac{P_f v}{T} \quad (3.12)$$

in which $R = \bar{R}/\bar{M} = 0.0728$ kJ/kg.K for gaseous octane, where \bar{R} is the universal gas constant and \bar{M} is the mol mass of the gas. Substitution of tabulated values of P_f , v and T (for example at $T = 303$ K, $P = 145$ kPa, $\phi = 1.0$ and $P_f = 2.4$ kPa) gives $R = 0.0716$ kJ/kg.K. This is only 1.6 % lower than the value calculated from $R = \bar{R}/\bar{M}$. Hence, it can be assumed that the decrease in the specific volume of vapour, due to the condensation of fuel during mixture expansion, is negligible. Thus, with Eq. (3.8), and using the vapour pressure of the fuel to represent its partial pressure in the wet or saturation region, Eq. (3.10), the number of moles of gaseous fuel in the wet mixture is

$$n_{fg2} = \frac{P_v V}{RT_2} \quad (3.13)$$

Here, suffix 2 denotes the state of the mixture at any time in the saturation region (Fig. 3.1) and g the vapour state. The liquid molar fraction of fuel can be expressed in terms of the gaseous fraction

$$\frac{n_{fl}}{n_f} = \frac{(n_f - n_{fg})}{n_f} = 1 - \frac{n_{fg}}{n_f} \quad (3.14)$$

The expansion of the mixture from a fixed-volume chamber into an expansion tank introduces an additional problem. The total amount of mixture in the explosion vessel decreases during the process. However, it is assumed that the overall air-fuel ratio (ϕ_{ov}) in the explosion vessel, irrespective of the state of matter of the fuel, remains constant during expansion. This assumption is reasonable on the grounds that condensed drops and the remaining fuel vapour-air mixture are essentially at the same temperature and the droplets are small enough to follow the flow. As droplets condense from the gas phase at the local flow velocity, they are transported out of the bomb at the same rate as that of the gaseous mixture (Atzler, 1999).

The total number of moles of fuel in the explosion vessel at the start of expansion, when all the fuel is fully vaporised can be expressed using Eqs. (3.7) and (3.8)

$$n_{f1} = \frac{P_{f1} V}{RT_1} = \frac{\phi_{ov}}{59.5 + \phi_{ov}} \frac{P_1 V}{RT_1} \quad (3.15)$$

where suffix 1 denotes the state of the mixture immediately prior to the start of expansion.

However, values of n_f within the condensation regime must be calculated by assuming a constant mixture composition, since the method presented in Eq. (3.15) does not account for the liquefied fuel. Constant mixture composition implies

$$\frac{n_{a1}}{n_{f1}} = \frac{n_{a2}}{n_{f2}} \quad (3.16)$$

Hence

$$n_{f2} = n_{f1} \frac{n_{a2}}{n_{a1}} \quad (3.17)$$

The number of moles of air in the wet region is

$$n_{a2} = \frac{P_{a2}V}{RT_2} = \frac{(P_2 - P_v)V}{RT_2} \quad (3.18)$$

The initial number of moles of air, using Eq. (3.4), is

$$n_{a1} = \frac{59.5}{59.5 + \phi_{ov}} \frac{P_1V}{RT_1} \quad (3.19)$$

Substituting Eqs. (3.15), (3.18) and (3.19) into Eq. (3.17) yields

$$n_{f2} = \frac{\phi_{ov}}{59.5} \frac{(P_2 - P_v)V}{RT_2} \quad (3.20)$$

Substitution of Eqs. (3.13) and (3.20) into Eq. (3.14), returns

$$\frac{n_{f2}}{n_{f2}} = 1 - \frac{59.5}{\phi_{ov}} \frac{P_v}{(P_2 - P_v)} \quad (3.21)$$

The mass of gaseous fuel present in the explosion vessel at condition 2 can be calculated, from its molar mass M_f

$$m_{f2} = n_{f2}M_f \quad (3.22)$$

where n_{f2} is obtained from Eq. (3.20). The instantaneous mass of liquid fuel can be obtained from

$$m_{f2} = \frac{n_{f2}}{n_{f2}} m_{f2} \quad (3.23)$$

The fraction of fuel in the liquid (lmf) and gas phases (gmf) are

$$lmf = \frac{m_{f2}}{m_{f2}}, \quad gmf = \frac{m_{f2}}{m_{f2}} \quad (3.24)$$

The gaseous phase and liquid phase equivalence ratios are given by

$$\phi_l = \phi_{ov} - \phi_g \quad (3.25)$$

and

$$\phi_g = \frac{(F/A)}{(F/A)_{stoic}} = \frac{(m_{fg2}/m_a)}{(m_f/m_a)_{stoic}} \quad (3.26)$$

where F/A are the fuel-air ratio, and M_f and M_a are the molar mass of fuel and air respectively. The stoichiometric fuel-air ratio can be found from Eqs. (3.1) and (3.2) as

$$(F/A)_{stoic} = \frac{M_f}{59.5M_a} \quad (3.27)$$

3.2 Temperature and Pressure Measurements

Temperature and pressure are key parameters for the control and determination of liquid and gaseous fractions of fuel, at any instant during expansion. In addition to mixture composition, data on these are essential prerequisites for the analysis of the combustion process, discussed in Chapter 4. This Section presents experimental values of the variation in temperature and pressure with time for a range of initial pressures, temperatures, expansion ratios, and overall equivalence ratios as summarised in Table 3.1. These data were used for the calculation of vapour and liquid fractions and equivalence ratios following the analysis presented in Section 3.1. Pressure and temperature data also were used for the prediction of ignition conditions in terms of temperature, liquid fraction and drop size.

3.2.1 Initially Quiescent Conditions

Pressure measurements were obtained simultaneously with temperature and droplet size measurements. Figure 3.2 shows typical measurements in a combined graph of pressure and temperature during the expansion of a stoichiometric iso-

octane aerosol from an initial temperature and pressure of 303 K and 200 kPa. During the first 1.38 s of expansion, the measured temporal variations of temperature and pressure exhibited a polytropic relationship

$$T_2 = T_1 \frac{P_2^{\left(\frac{\gamma-1}{\gamma}\right)}}{P_1} \quad (3.28)$$

as shown by the thick curve in Fig. 3.2. Using the ratio of specific heats of the iso-octane-air mixture, the index of isentropic expansion, γ , for the aerosol was calculated to be 1.35. It is shown in Fig. 3.2 that, prior to condensation, the mixture temperature, $T_{\gamma=1.35}$, calculated using Eq. (3.28) was found to agree with that of the measured temperature. Also shown in Fig. 3.2, for comparison, is the predicted temperature for the isentropic expansion of dry air for which $\gamma_{air} = 1.4$. At the start of nucleation, the measured temperature departed from that of polytropic expansion, in part, due to the latent heat of condensation, but also, possibly, due to the increase in thermocouple temperature caused by condensation on it, which might be higher than in the free stream due to it acting as a nucleation site. Additional pressure and temperature measurements for all conditions used for combustion studies in Chapter 4 are shown in Appendix.

3.2.2 Turbulent Conditions

Figure 3.3 shows typical mean pressures and temperatures, obtained from four experiments, in a combined graph as a function of time during expansion of stoichiometric iso-octane aerosols at an initial pressure of 200 kPa, initial temperature of 303 K, and rms turbulent velocity, u' , of 1.0 m/s. The orifice size was 25 mm, as discussed in Section 3.1.2, to compensate for the higher rate of droplet evaporation as a result of turbulent heat transfer from the wall region. The cycle-to-cycle variations in pressure and temperature are small as indicated by the error bars.

Also shown in Fig. 3.3 are curves of the variation of temperature with time for the isentropic expansion ($\gamma = 1.35$) and for expansion with polytropic index of 1.17. It is clear that under turbulent condition, expansion is far from adiabatic and this is due to the high turbulent convective heat transfer from the walls. Additional graphs of pressure and temperature variations with time under turbulent conditions are shown in Appendix for various r.m.s. turbulent velocities.

3.3 Droplet Size Measurements

Drop size and mixture composition, in terms of gaseous and liquid fractions of the fuel, are important parameters in the combustion of aerosols. This section presents measurements of the variation of individual and length mean diameter, D_{10} , with time through the expansion process. These measurements were obtained with the Phase Doppler Anemometer system presented in Chapter 2, and were taken in situ.

3.3.1 Initially Quiescent Conditions

Figure 3.4 shows a typical variation of droplet diameter with time, for an expansion of iso-octane aerosol at $\phi_{ov} = 0.8$, from an initial pressure and temperature of 250 kPa and of 303 K. Each symbol represents measurement of an individual droplet. Also shown in Fig. 3.4 by the solid line are values of D_{10} averaged over 0.1 s. Shown by the crosses and dashed line are values of standard deviation averaged over the same time interval, σ_D . In most cases, the present system could not adequately detect droplets of less than about 2 μm , and hence, could not resolve the onset of nucleation. However, this was obtained by extrapolation of the curve fit of the average droplet size to zero diameter. During the initial droplet growth period,

up to about 2.7 s, a narrow distribution of sizes was obtained, as indicated by the standard deviation of about 2.5 μm . After this period, considerable and increasing scatter was obtained. After 3.0 s, there was further increased scatter and a droplet size reduction, probably due to evaporation by heat transfer from the walls of the explosion vessel.

Figure 3.5 shows the temporal variation of D_{10} with time for iso-octane aerosols expanded from an initial pressure of 250 kPa and initial temperature of 303 K, at values of ϕ_{ov} between 0.8 and 1.4. Each curve was obtained from a single expansion, and the cycle-to-cycle repeatability is indicated by the error bars. The onset of droplet formation is a strong function of ϕ_{ov} , being at 0.7 s after the start of expansion for ϕ_{ov} of 1.4, and at later times for leaner mixtures. The richer mixtures experience earlier start of condensation due to the higher values of P_f (being equal to P_v , as described in Section 3.1.2). The maximum attainable D_{10} during the measured period is also a function of ϕ_{ov} . Similar data for a range of initial expansion pressure and equivalence ratio are shown in the Appendix.

Figure 3.6 shows the spatial variation of individual droplet diameters for stoichiometric iso-octane-air aerosol measured at six locations within the central region of the explosion vessel (Marquez, 2003). The solid line in Fig. 3.6 is a curve fit through the experimental values and the dashed line represents that for the standard deviation, σ_D , within a 0.1 s time interval. It is shown that although σ_D increases slightly with time, the spatial variation is low (within $\pm 3 \mu\text{m}$), and this indicates that the droplet size is spatially homogeneous.

3.3.2 Turbulent Conditions

Figure 3.7 shows, for turbulent conditions, a typical variation of droplet diameter with time for iso-octane aerosols expanded from an initial pressure and temperature of 200 kPa and of 303 K, at a range of ϕ_{ov} , from 0.8 to 2.0, and at $u' = 1.0$ m/s. The solid lines in Fig. 3.7 are curve fits through the experimental values. The trend in droplet diameter variation is similar to that in Fig. 3.5 except that droplet development is much faster under turbulence, than for initially quiescent conditions. This was due to the quicker expansion rate, as a result of the use of a larger orifice, addressed in Section 2.1.2, for the expansion of turbulent mixture.

Shown in Fig. 3.8 is a graph of temporal distribution of individual diameter, similar to Fig. 3.7 except that the mixture was stoichiometric and the values of u' were varied between 1.0 and 4.0 m/s. The influence of u' on the variation of droplet size with time was small for u' of between 1.0 and 3.0 m/s; the maximum deviation was about 2 μm . However, at u' of 4.0 m/s, the graph is shifted slightly downward. The reason for this is unclear but it may be due to the higher heat transfer rate from the walls, leading to increased evaporation.

3.4 Droplet Number Density

Laser attenuation measurements were used for the estimation of droplet number density, using Eq. (2.2) and measurements of D_{10} (Sections 2.4.1 and 3.3). This section presents measurements of the variations of laser attenuation and droplet number density with time through the expansion process under initially quiescent (Section 3.4.1) and turbulent (Section 3.4.2) conditions. In addition, the results from the multiple laser attenuation experiments, described in Section 3.4.2, are discussed

in Section 3.4.3. The calculated values of liquid and gas mass fraction and equivalence ratio are presented in Section 3.4.4.

3.4.1 Initially Quiescent Conditions

Shown in Fig. 3.9 are the typical variations of laser power attenuation and number density of droplets, N_D , addressed in Section 2.4.2, with time during the expansion of initially quiescent stoichiometric iso-octane aerosols expanded from an initial temperature of 303K, and initial pressures between 150 to 300 kPa. The attenuation in the intensity of the laser beam is given as a ratio of the voltage output (V/V_o) of the laser power meter, where V_o is the initial non attenuated voltage before the onset of condensation. The voltage signal representing laser attenuation in Fig. 3.9 remained constant until the onset of condensation. This corresponds very well with the determination of onset of nucleation by extrapolating to zero a curve fit through the experimental values of D_{10} as described in Section 3.3.1. It is also shown in Fig. 3.9 that condensation starts earlier for mixtures with higher initial pressure; this is due to quicker expansion rate, and thus earlier arrival at the saturation region (Section 3.1), than those of lower initial pressure. Following the onset of condensation, the ratio V/V_o decreased with time due to the combined effect of an increase in size and number density of droplets, until a minimum value was attained. Following this, the signal increased due to droplet evaporation. The droplet number density, N_D , is shown in Fig. 3.9 to rise very rapidly to an approximately constant value, in the order of 10^{10} , immediately after the start of condensation. In addition, it is also shown that the initial pressure does not have a significant effect on N_D .

Figure 3.10 shows the variation of laser attenuation with time for initial conditions of 200 kPa and 303 K, at a range of ϕ_{ov} from 0.8 to 2.0. The onset of

nucleation, which varied between 0.7 and 1.6 s, is shown to be influenced by equivalence ratio, with richer mixtures causing earlier nucleation than lean ones. The greatest and fastest attenuation are also experienced by richer mixtures. Similar to Fig. 3.9, the droplet number density, N_D , is shown to be approximately constant, in the order of 10^{10} , quickly after the start of condensation, irrespective of the equivalence ratio. Additional graphs of variations of laser attenuation with time under initially quiescent conditions are shown in Appendix.

Shown in Fig. 3.11 is a comparison of the laser power attenuation results obtained in the present work with those presented by Marquez (2003), who worked on the same system, for stoichiometric iso-octane-air aerosols expanded from 150 and 250 kPa. The thick lines represent the results obtained in the present work, and the thin lines represent those from Marquez (2003). It is shown in Fig. 3.11 that the time for the onset of condensation agrees well between the present and previous results. However, the attenuation profile was different, with the present work displayed less and slower attenuation, typically by between 20% and 30%. Because a similar procedure was used by the present Author and by Marquez (2003), the reason for the discrepancy is unclear. However, nucleation in a vapour system is known to be a function of coexisting particles, which act as nucleation sites (e.g. Schwartz, 1996). Therefore, a suggested reason for the higher attenuation in the results by Marquez (2003) is due to the presence of a greater amount of impurities or particles in his mixture during expansion. This would result in a greater concentration of droplets. The greater number of impurities in the work of Marquez might be the results of an undocumented work, in which Marquez investigated the possibility of controlling the number density by generating nucleation sites through the burning of incense (Lawes, 2006). It was probable that residual traces of incense would have existed afterwards. Another possibility is particulates left over from

previous PIV (Section 2.4.4) experiments. The present Author took considerable care to remove such sources of contamination but the amount of care by Marquez is undocumented.

Figure 3.12 shows the variation of spatial laser power attenuation with time during the expansion of initially quiescent stoichiometric iso-octane aerosols expanded from an initial temperature and pressure of 303 K and of 200 kPa. It was obtained with the technique described in Section 3.4.2. Also shown in Fig. 3.12, is the orientation of the measurement locations as viewed from the power meter side. The onset of nucleation presented by the four measurements occurred simultaneously at about 1.7 s after the start of expansion. The laser power attenuation distribution throughout the next 0.7 s varied little among the four measurements, as shown by the shaded area in Fig. 3.12. This indicated that there were only small spatial variations in droplet properties.

3.4.2 Turbulent Conditions

Figure 3.13 shows typical variations of laser power attenuation with time during the expansion of turbulent stoichiometric iso-octane aerosols from an initial temperature and pressure of 303K and of 200 kPa, at u' of 1.0 and 4.0 m/s. Two expansions were carried out for each condition; the repeatability of the results was good. The onset of nucleation is shown in Fig. 3.13 to be almost independent of u' ; this agrees with the trend of temporal droplet distribution in Fig. 3.8. However, droplet evaporation is much quicker at high turbulence due to higher heat transfer rate.

3.5 Summary

Figure 3.14 shows a summary of cold calibration data obtained in this chapter. It shows a typical variation of pressure, temperature, fuel mass (m_{fg2} and m_{fl2}), droplet size, and number density of droplets with time from the start of expansion for an initially quiescent stoichiometric iso-octane-air mixture expanded at 250 kPa and 303K. The measured temporal variation of temperature, T_m , initially exhibited a polytropic relationship, as shown by the dashed curve in Fig. 3.14, in which the calculated polytropic index, γ , is 1.35. At the start of droplet nucleation, approximately one second after the start of expansion, the measured temperature departed from that of the polytropic expansion, in part due to the latent heat of condensation. Simultaneously, the liquid fuel mass, m_{fl2} , increased while the gaseous fuel mass, m_{fg2} , dropped abruptly. The short dashed line in Fig. 3.14 indicates the expected gaseous mass of fuel that would exist if condensation had not taken place, m_{fg2}' ; the difference between m_{fg2} and m_{fg2}' is equal to the liquid mass, m_{fl2} .

The onset of condensation, displayed by rapid changes in m_{fg2} and T in Fig. 3.14, was also evident by the increase in N_D and D_{10} . The droplet number density, N_D , is shown to be nearly constant almost immediately after the start of condensation. Also shown in Fig. 3.14 are the standard deviations of the droplet mean diameter, σ_D . The low values of σ_D indicate the near mono-dispersed distribution of droplet size that results in the present apparatus. This is also supported by the typical histograms in Fig. 3.14 which show a narrow droplet distribution at 1.5, 1.7 and 2.3 seconds after the start of expansion. The histograms, in addition, show that droplet distribution widened at later stage of expansion; this was probably caused by droplet evaporation or interaction between droplets.

The calibration data, shown in Sections 3.2 to 3.4, are used in the analysis of the combustion experiment results in Chapter 4. The results of measurements for aerosol characterisation are very consistent. Thus, there would be no need for simultaneous aerosol characterisation and combustion measurement.

Table 3.1 Initial (pre-expansion) conditions for aerosol characterisation in the present work.

Regime	T (K)	P (kPa)	ϕ_{ov}	orifice (mm)	u' (m/s)
Initially quiescent	303	150	0.8,1.0,1.1, 1.2, 1.4, 1.6	6	-
		200	0.8, 0.9, 1.0,1.1, 1.2 1.4, 1.6, 1.8, 2.0		
		250	0.8,1.0,1.1, 1.2, 1.4		
		300	0.8,1.0,1.1, 1.2		
Turbulent	303	200	1.0	25	1.0, 1.5, 2.5, 3.0, 4.0

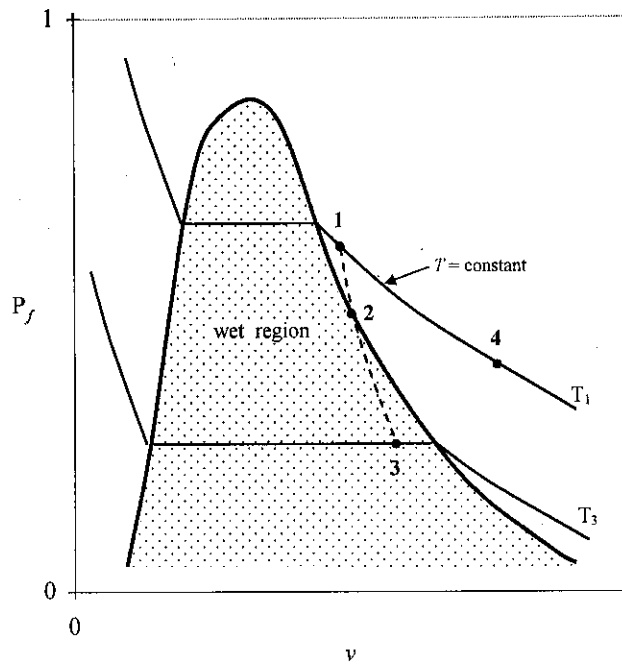
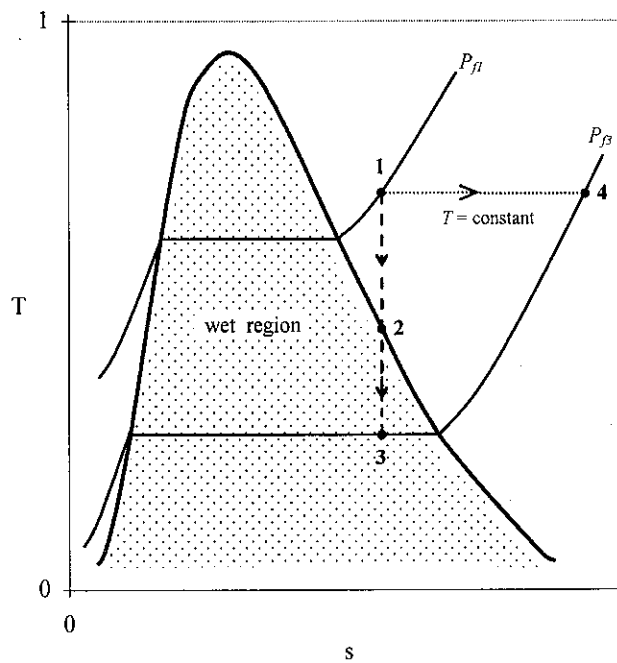
(a) P_f - v diagram(b) T - s diagram

Figure 3.1 Expansion paths for iso-octane in the present work on (a) P_f - v diagram, and (b) T - s diagram.

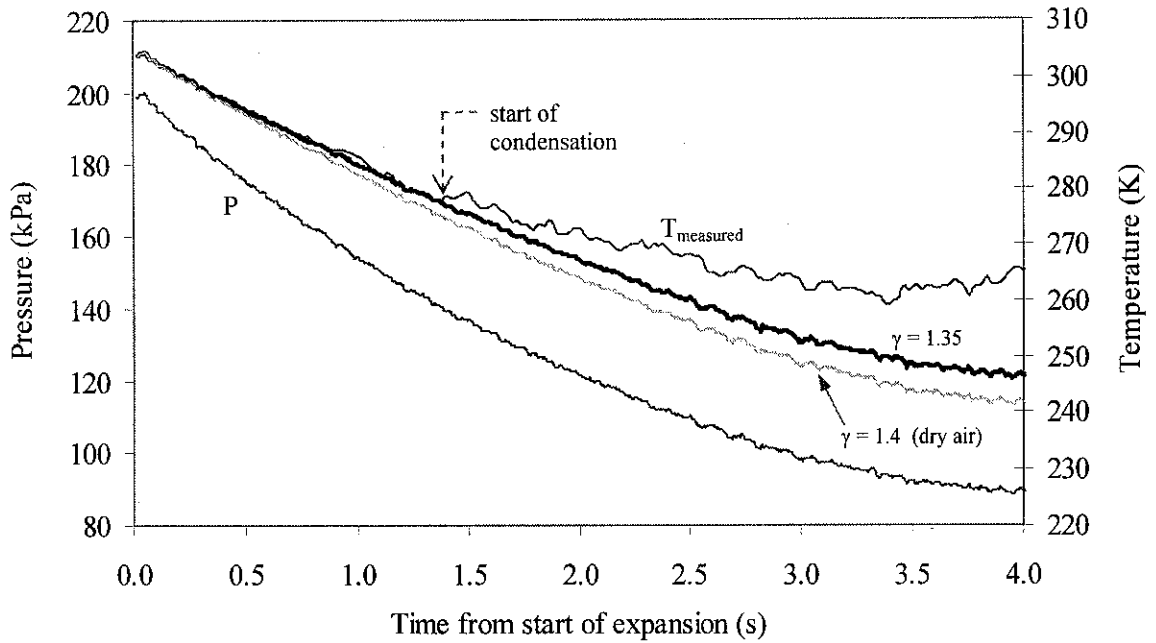


Figure 3.2 Variation in pressure and temperature in the explosion vessel with time during the expansion of initially quiescent stoichiometric iso-octane-aerosol from 200 kPa and 303 K.

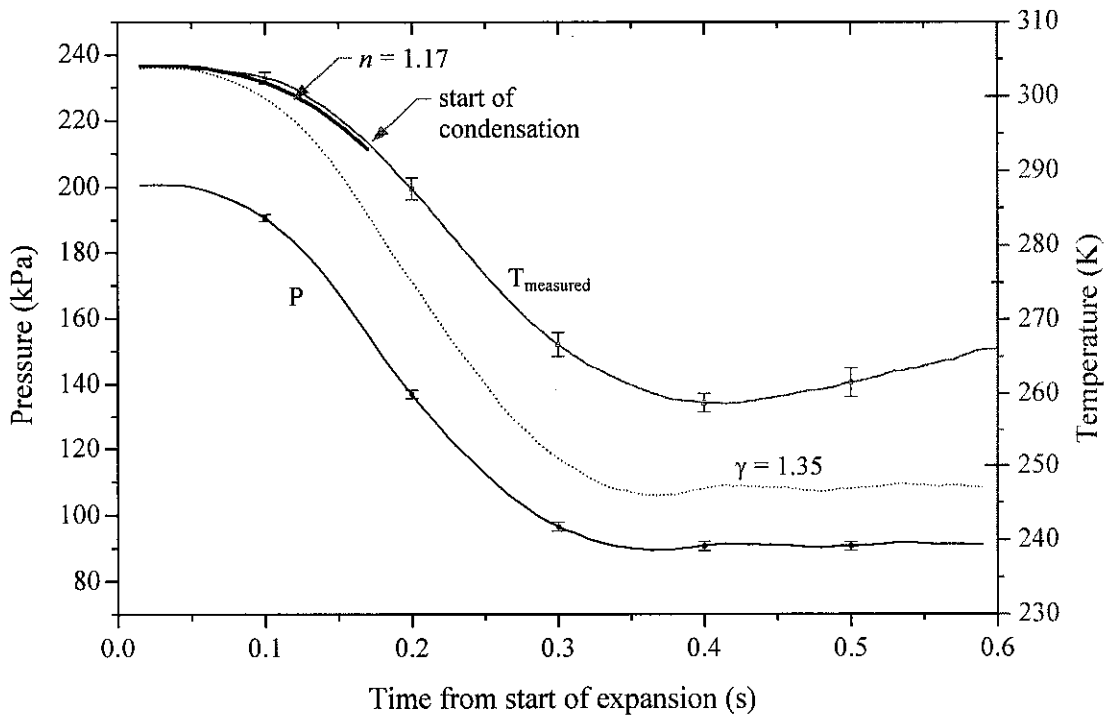


Figure 3.3 Typical average variation in pressure and temperature with time for stoichiometric turbulent iso-octane aerosols expanded from 200 kPa and 303 K at u' of 1.0 m/s.

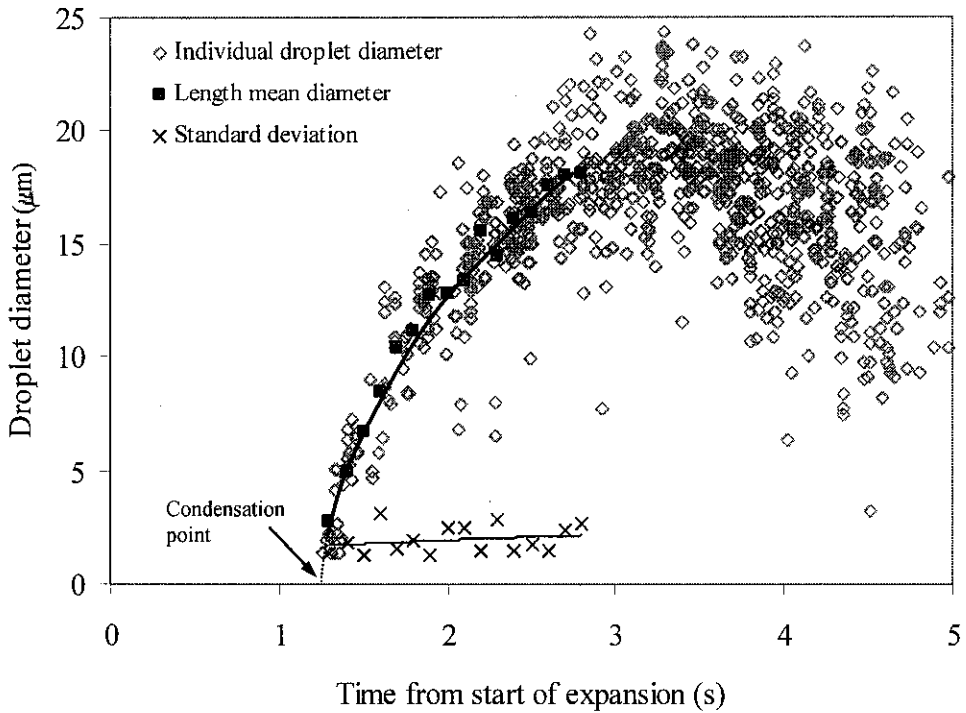


Figure 3.4 Variation of individual droplet diameter, D_{10} , and standard deviation, $\sigma_{D_{10}}$, with time for initially quiescent iso-octane-air aerosol ($\phi_{ov} = 0.8$) expanded from 250 kPa and 303 K.

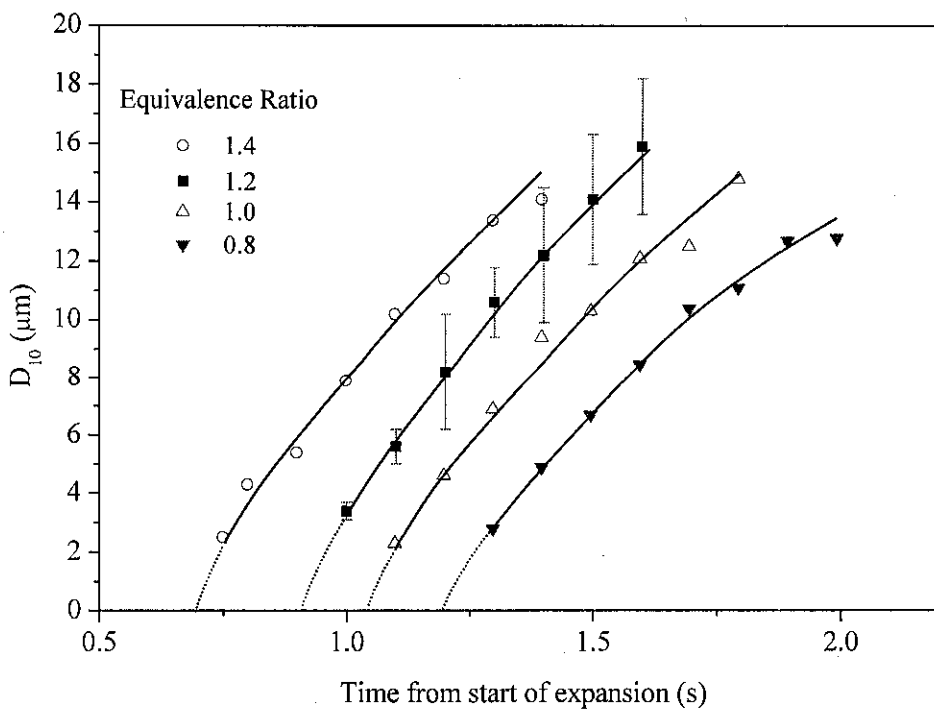


Figure 3.5 Variation of D_{10} with time for initially quiescent iso-octane-air aerosol expanded from 250 kPa and 303 K at various equivalence ratios.

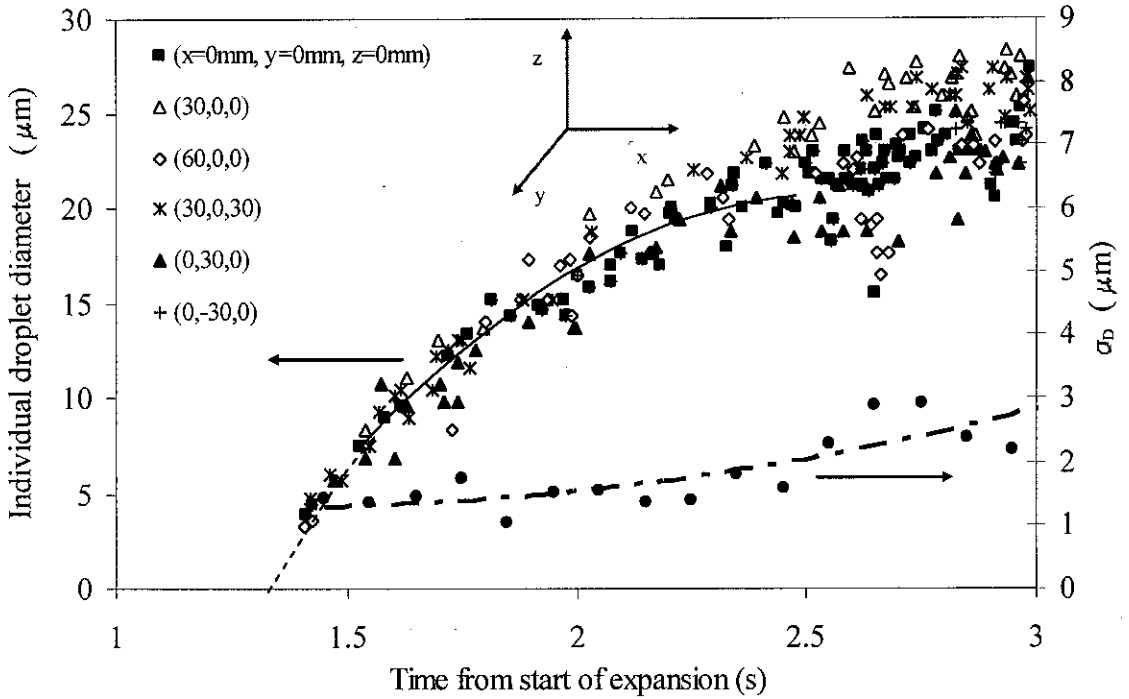


Figure 3.6 Spatial variation of individual droplet diameter and σ_D with time for iso-octane aerosols ($\phi_{ov} = 1.0$) expanded from 200 kPa and 303 K at six different positions in the explosion vessel. Reproduced from Marquez (2003).

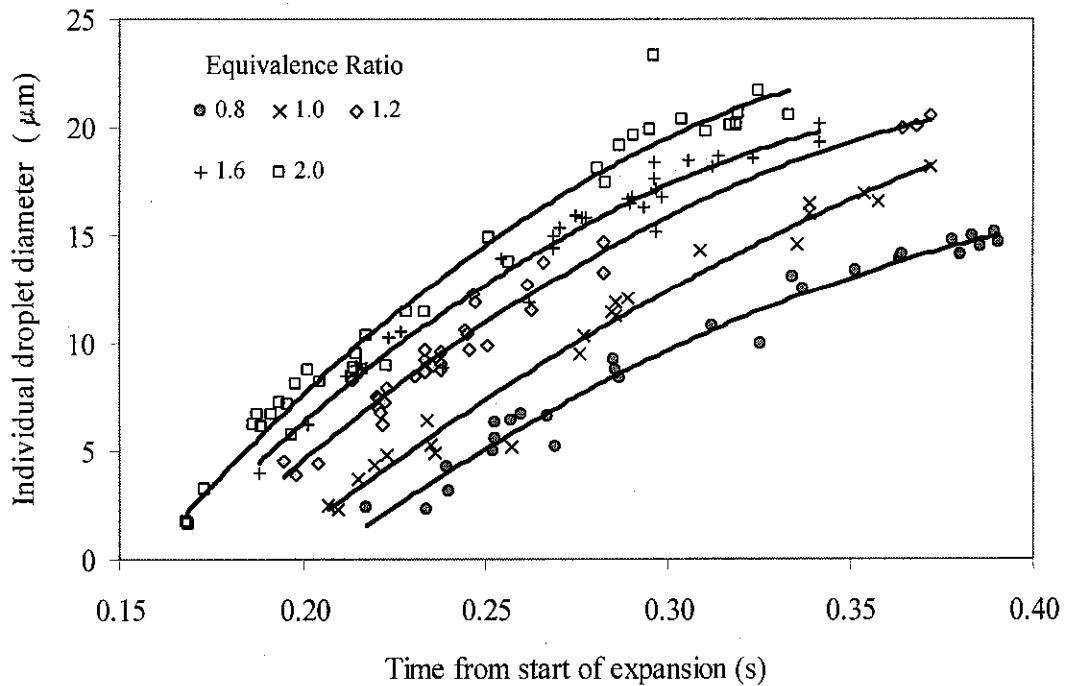


Figure 3.7 Variation of droplet diameter with time for turbulent iso-octane-air aerosol expanded from 200 kPa and 303 K; $u' = 1.0$ m/s, at various ϕ_{ov} .

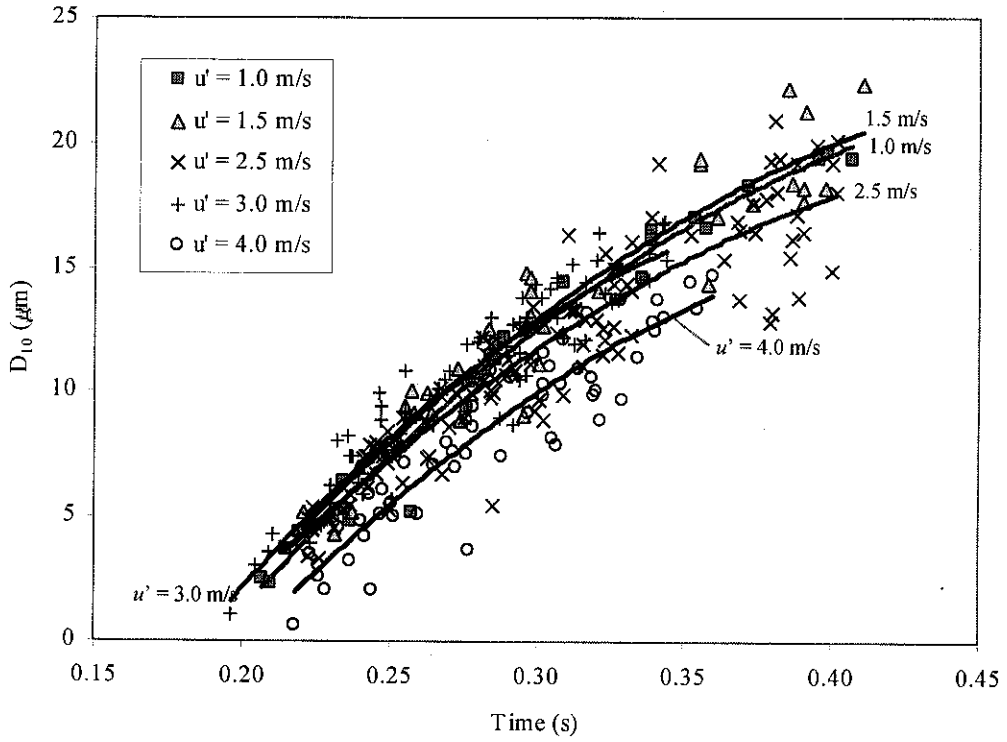


Figure 3.8 Variation of D_{10} with time for turbulent stoichiometric iso-octane-air aerosol expanded from 200 kPa, 303 K at various u' .

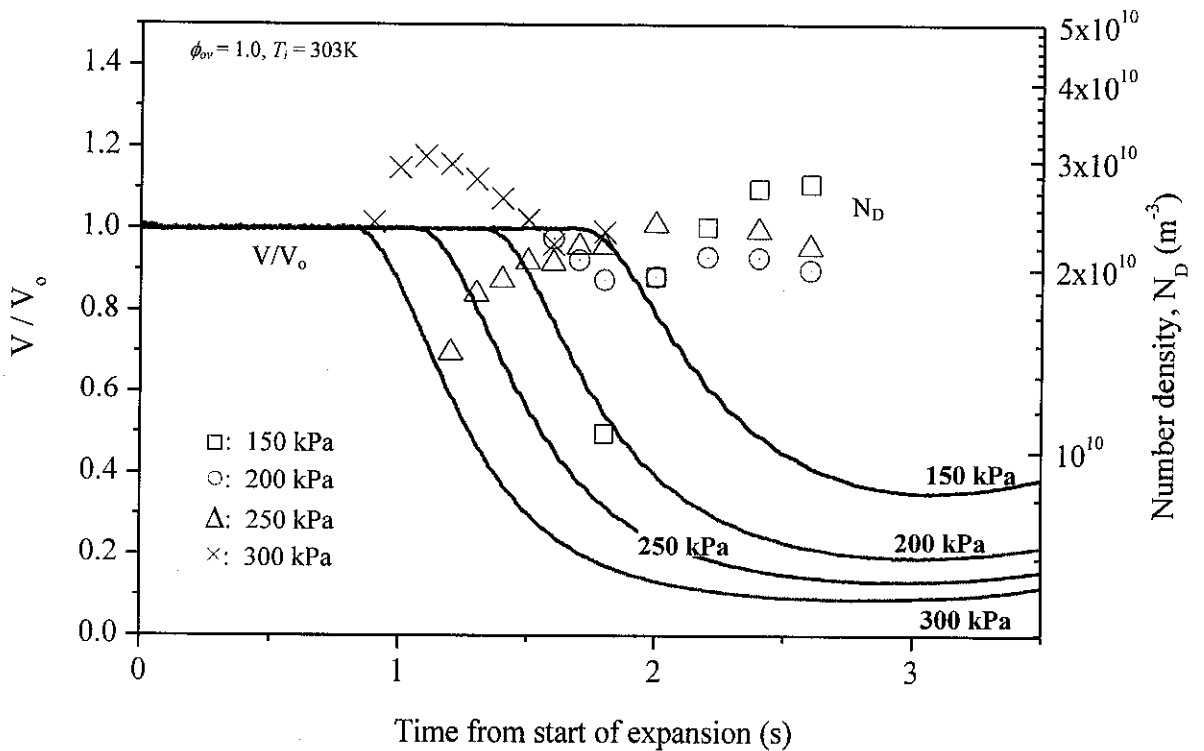


Figure 3.9 Variations of droplet number density and laser power attenuation with time from start of expansion for initially quiescent stoichiometric iso-octane aerosols expanded from various initial pressures.

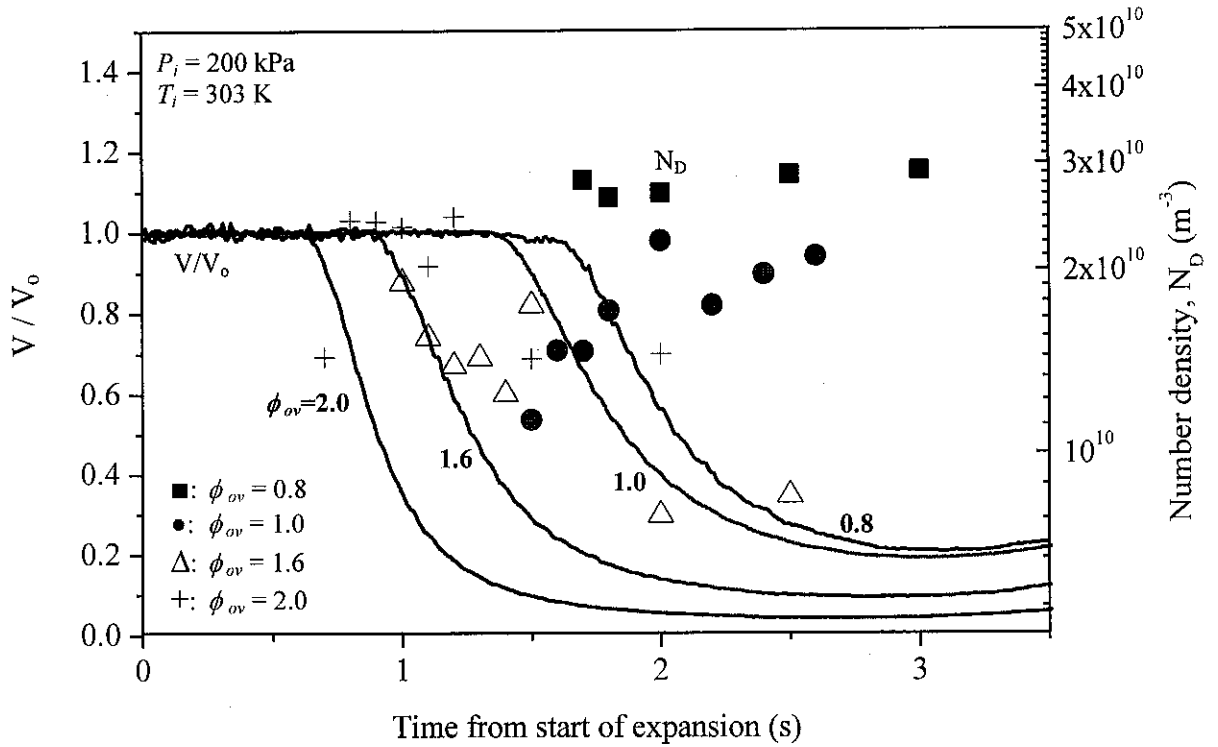


Figure 3.10 Variations of droplet number density and laser power attenuation with time from start of expansion for initially quiescent iso-octane aerosols expanded from 200 kPa and 303K, at various ϕ_{ov} .

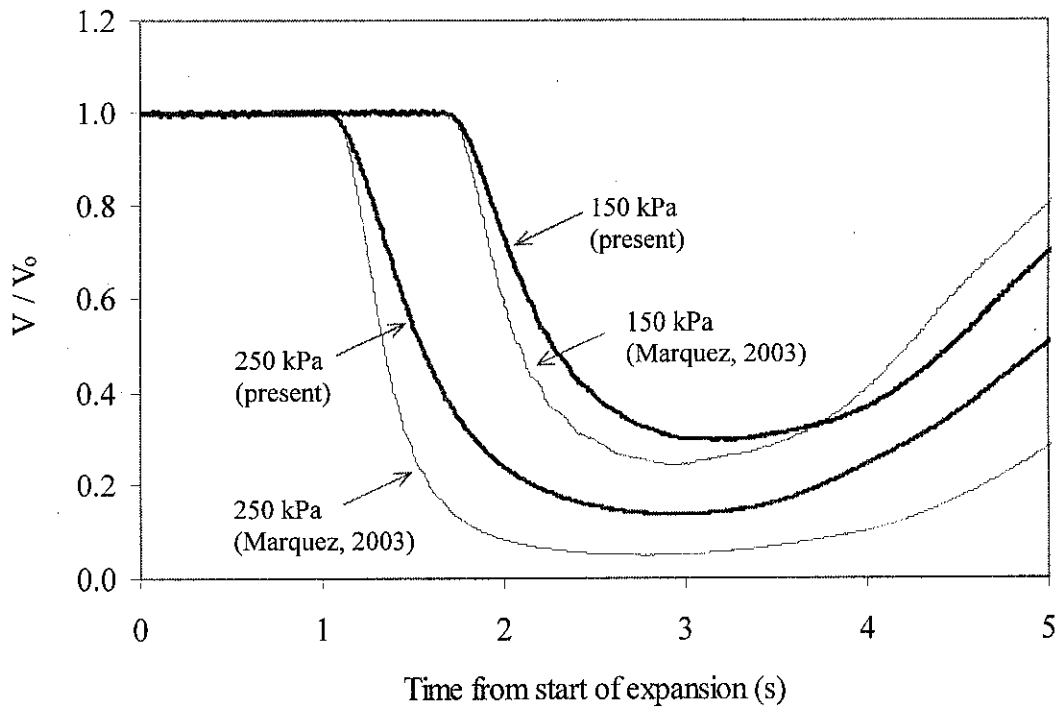


Figure 3.11 Comparison of laser power attenuation results with those of Marquez (2003), for initially quiescent iso-octane aerosols at $\phi_{ov} = 1.0$ expanded from 150 and 250 kPa.

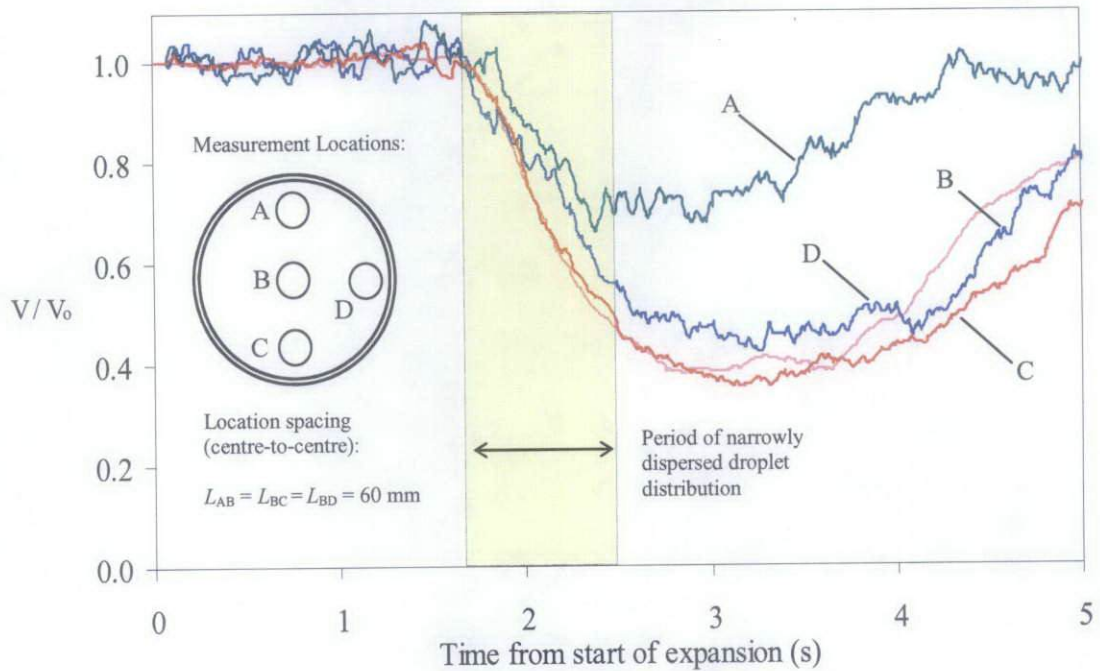


Figure 3.12 Typical multiple laser power attenuation produced by clouds of initially quiescent iso-octane aerosols at $\phi_{ov} = 1.0$ expanded from 200 kPa, 303K.

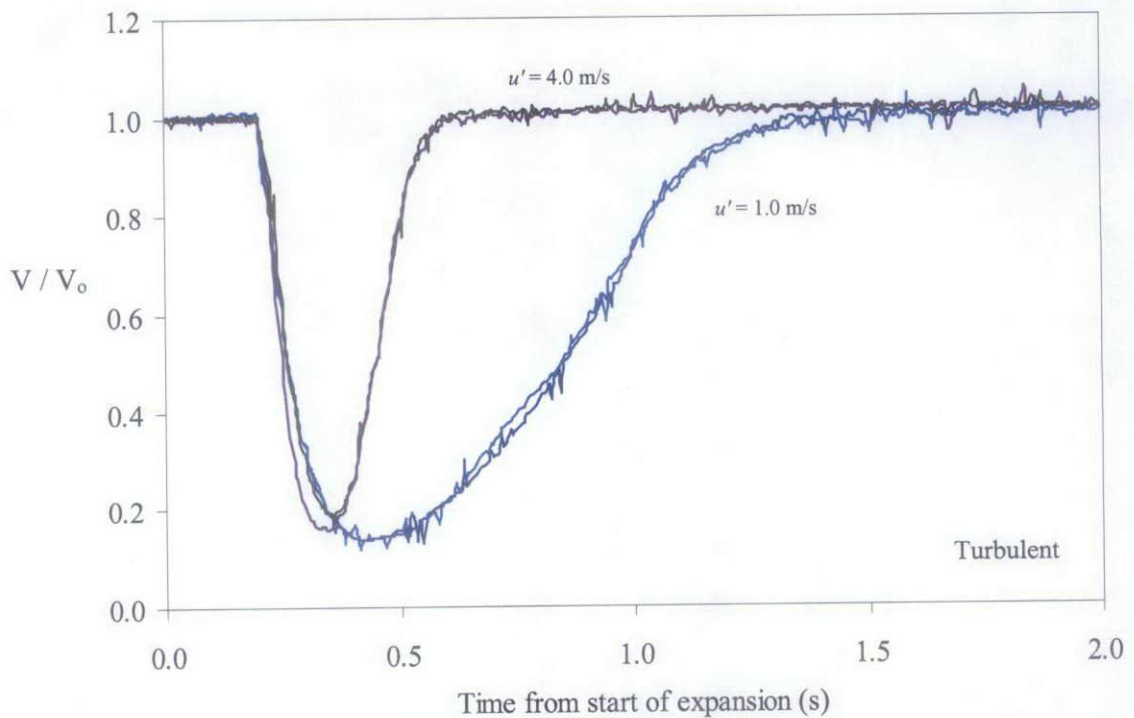


Figure 3.13 Laser power attenuation produced by clouds of turbulent stoichiometric iso-octane aerosols expanded from 200 kPa, 303K, at various u' .

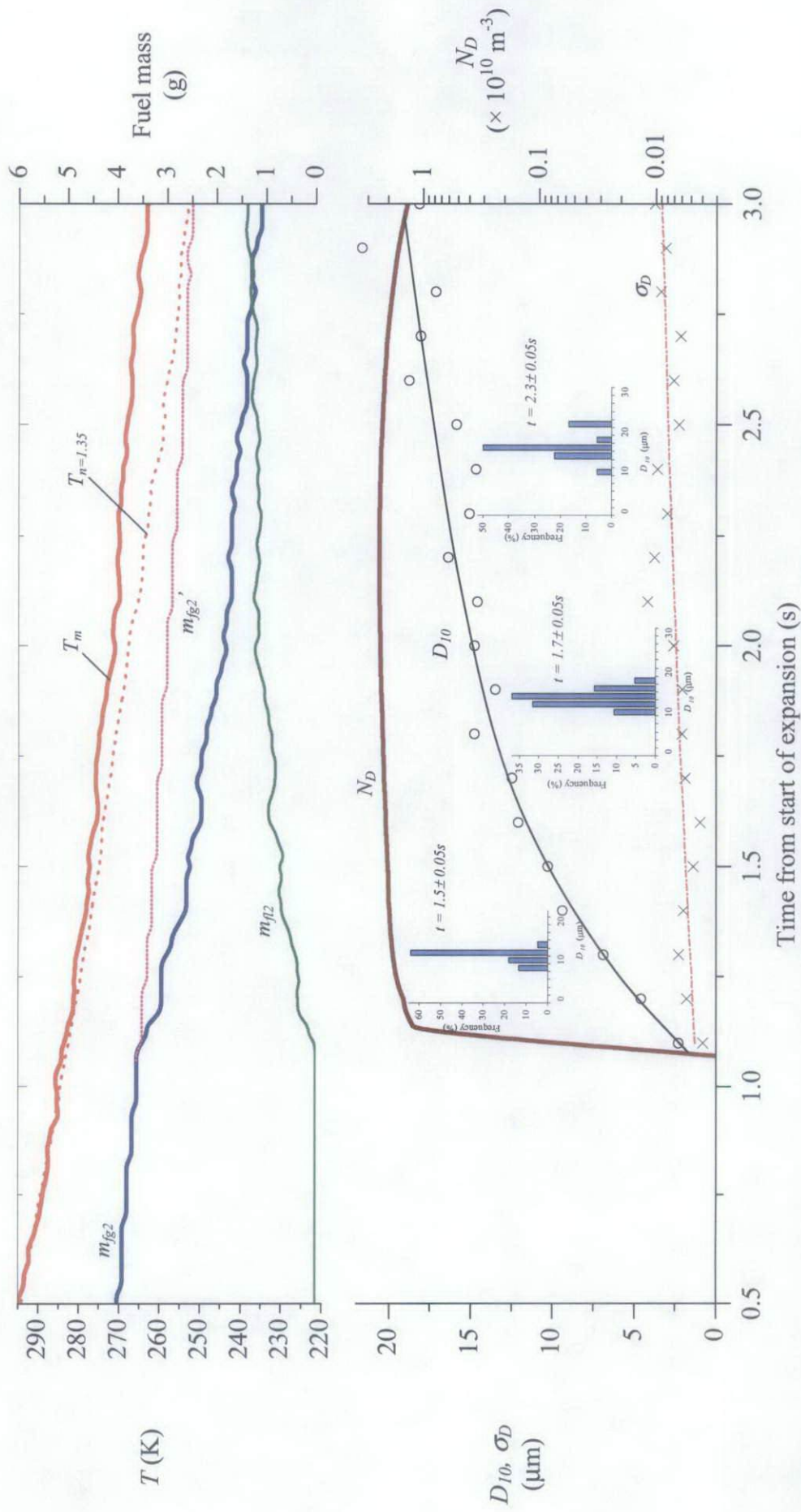


Figure 3.14 Typical variation of droplet size and number density of droplets, temperature and fuel mass against time for initially quiescent iso-octane aerosols expanded from 250 kPa, 303K, at $\phi_{ov} = 1.0$.

Chapter 4

Results

This chapter presents the experimental results. The laminar flame observations, which include photographs of aerosol flames at a range of initial conditions, are presented in Section 4.1. Inevitably, the production of a set of premixed combustion measurements at conditions of relevance to the aerosols was necessary in order to investigate the difference in burning rates between single and two-phase mixtures. The laminar burning rates of both gaseous and aerosol flames are presented in Section 4.2. The effect of buoyancy in both gaseous and aerosol flames of rich laminar mixtures is presented in Section 4.3. The phenomenon of oscillation in lean aerosol flames is presented in Section 4.4. Observations of turbulent aerosol flames are shown in Section 4.5, and this is followed in Section 4.6 by measurements of the turbulent burning rates of both gaseous and aerosol flames.

4.1 Laminar Flame Observations

In this section flame photographs of aerosol and gaseous flames at a range of initial conditions are presented. They were obtained mainly by the schlieren imaging technique described in Chapter 2. The photographs demonstrate a wide variety of flame structures.

4.1.1 Ignition

Shown in Fig. 4.1(a) are sequences of schlieren images of gaseous and aerosol flame kernels during the first 3 ms after ignition. Shown in Fig. 4.1(b) is the variation of the initial flame speed with radius (as explained in Section 2.4.3), for gaseous and droplets with D_{10} of 5 μm , 13 μm and 16 μm . Conditions for the aerosols were $\phi_{ov} = 2.0$, temperatures between 287 and 292 K, and pressures between 151 and 170 kPa. For the gaseous flame, conditions were $T = 303$ K and $P = 100$ kPa. All the flames were ignited using the same spark electrode, as described in Section 2.1.3.1, at identical ignition energy. The flame kernels in Fig. 4.1(a) are shown to drift upward. This was probably due to the effect of buoyancy, which is discussed in Section 4.3.

It is shown in Fig. 4.1 that the initial size (Fig. 4.1a) and rate of development (Fig. 4.1b) is an inverse function of droplet size, with the gaseous flame having the fastest initial rate of development and that for a droplet diameter of 16 μm being approximately 3 times smaller at 3 ms after ignition. These are probably due to the large energy required to evaporate droplets prior to ignition. The minimum ignition energy, E_{min} , defined by Ballal and Lefebvre (1978) as “the amount of energy required to heat a sphere of gas/droplet (whose diameter is equal to the quenching distance) to its adiabatic flame temperature,” increases with droplet size. This is discussed in Section 5.1. The trend of initial flame propagation rate was observed for a range of flame radii of up to 12 mm. This is known as the spark affected period, and is discussed in Section 4.2. It is also shown in Fig. 4.1 that at flame radii of between 7 and 12 mm, there is a ‘cross over,’ after which flame speed increases with droplet size. This is explained in Section 4.3.

4.1.2 Laminar Flame Propagation

Shown in Fig. 4.2 are sequences of flames within stoichiometric aerosols with droplet sizes of (a) 5 μm , (b) 10 μm and (c) 15 μm . The pre-ignition conditions were: (a) $P = 185 \text{ kPa}$, $T = 281 \text{ K}$, $\phi_g = 0.92$, (b) $P = 172 \text{ kPa}$, $T = 278 \text{ K}$, $\phi_g = 0.78$ and (c) $P = 155 \text{ kPa}$, $T = 272 \text{ K}$, $\phi_g = 0.63$. All flames are compared at similar radii as indicated in Fig. 4.2. Also shown in each photograph is the time from ignition. It must be noted that the small difference in P and T between the conditions in the three images has been shown, for gaseous flames, to have little effect on the flame structure (Bradley *et al.*, 1996). Hence, it is assumed that the difference in the structure is entirely due to the effects of droplets.

With the smallest droplets (Fig. 4.2(a)), the flame was initially smooth, without cells. The long cracks on the surface of the flame were originated by the perturbation from the spark electrode, and these changed very little throughout flame propagation. The first sign of a change in flame surface structure in Fig. 4.2(a) was observed at a radius of about 40 mm, as denoted by the shallow cells. At a radius of 60 mm the flame surface displayed scattered and an increasing number of cells. The flame became fully cellular after an extended period of time after the flame had developed beyond the radius of the vessel windows. The flame structure at larger droplet diameters was similar to those for 5 μm except that cells developed more rapidly. At a flame radius of 10 mm, all flames in Fig. 4.2 were smooth. However, for the 10 μm droplets, full cellularity was obtained by about 52 mm. For the 15 μm droplets, this was even earlier at about 34 mm.

Figure 4.3 shows a comparison between flame photographs, at $r \approx 55 \text{ mm}$, for gaseous and aerosol iso-octane-air at various equivalence ratios. The initial droplet size was, for all aerosol mixtures, 8 μm , and the initial pressures and temperatures

were between 122 and 170 kPa, and 271 and 292 K respectively. The initial conditions for the gaseous mixtures were $P = 100$ kPa and $T = 303$ K. Also shown with each photograph is the time from ignition. In Fig. 4.3(a) for a lean mixture ($\phi_{ov} = 0.8$), both the gaseous and aerosol flames were smooth, without wrinkles or cells. However, the aerosol flame is shown elongated upward, probably due to the effects of buoyancy and/or outward flow at the top of the vessel, as a result of the lower burning rate; this is discussed in Section 4.3. At stoichiometric conditions, as shown in Fig. 4.3(b), the aerosol flame displayed shallow cells, whereas the equivalent gaseous flame was smooth. At $\phi_{ov} = 1.2$, as shown in Fig. 4.3(c), the gaseous flame started to display large and shallow cells. However, at the same overall equivalence ratio, the aerosol flame was more cellular, as evident by the greater number of cells, which were also smaller in diameter and larger in amplitude. At $\phi_{ov} = 1.4$, as shown in Fig. 4.3(d), the degree of cellularity for both the gaseous and aerosol flames increased, but that of the former was less than the latter. For increasingly rich mixtures, the cell size and amplitude changed only slightly for aerosol, as shown in Figs. 4.3 (e) and (f), whereas the equivalent gaseous flames started to become less cellular. In Fig. 4.3(f), the gaseous flame ($\phi_{ov} = 1.8$), displayed cellularity at the bottom section of the flame while the top section was smooth. This was probably an effect of buoyancy, and is discussed in Section 4.3.

Figure 4.4 shows the regimes of aerosol combustion for iso-octane-air mixtures at various values of D_{10} and ϕ_{ov} , for a pressure range of between 90 and 150 kPa, and temperature of between 260 and 290 K. Also shown in the figure are the regimes for premixed flames ($D_{10} = 0 \mu\text{m}$) at $P = 100$ kPa, and $T = 303$ K. In Fig. 4.4, the square markers represent flames that remained smooth throughout observation, and the crosses represent cellular flames but that did not have increased

acceleration; these are addressed in Section 4.2.1. The triangles (within the shaded area) identify ‘accelerating’ flames; those that showed an increase in the burning rate after the onset of cellularity, in which Pe_{cl} (defined in Section 1.3), could be determined; this is discussed in Sections 4.2.2. Flames that accelerated right after the end of the spark affected period (discussed in Section 4.2), with no region of non-cellular flame growth, are identified by the full diamond markers; this generally applies to mixtures with ϕ_{ov} of greater than 1.4. The open diamond markers represent flames that were significantly influenced by buoyancy, which is discussed in Section 4.3. The circles identify oscillating flames which occurred in lean mixtures for a certain range of D_{10} . This is addressed in Section 4.4.

4.1.3 Comparison of Flame Images Obtained with Different Cameras

In the present work, for the first time at Leeds, a high-speed digital camera (Section 2.4.3) was used for studies of laminar and turbulent flames within aerosols. In previous studies by Atzler (1999), Mokhtar (2001) and Marquez (2003) for similar purposes, a drum camera was used. The differences between the images produced by the two cameras are compared in this Section. Shown in Fig. 4.5(a) are sequences of flame photographs obtained using the high-speed digital camera in the present work for aerosols at $\phi_{ov} = 1.2$, $P \approx 137$ kPa, $T \approx 278$ K, $D_{10} \approx 10$ μm . In Fig. 4.5(b) the flame images produced by the drum camera (Atzler, 1999) at similar conditions in the same explosion vessel are shown.

The images in Fig. 4.5(a), with the digital camera are considerably sharper and clearer than those obtained with the drum camera. In particular, the cells are much better defined, making studies of the onset of instabilities much more accurate than was previously possible. This is particularly well illustrated by the images at about 40 mm diameter. Here, any cellularity in the image from the drum camera is unclear,

yet the digital camera revealed that cellularity was well developed. For example, Atzler (1999) studied the photographs reproduced in Fig. 4.5(b) and reported that cellularity started at a flame radius of 50 mm. However, in Fig. 4.5(a) the same effect was shown to occur at a flame radius of approximately 18 mm. Clearly, previous measurements of the onset of cellularity are subject to considerable uncertainties.

4.1.4 Laser Sheet Images

Shown in Fig. 4.6 is a typical laser sheet image of an iso-octane-air aerosol ignited at $\phi_{ov} = 0.8$, $P = 110$ kPa, $T = 265$ K, and $D_{10} = 12$ μm . The laser sheet passed, from right to left in Fig. 4.6, through a 25 mm lateral window in the explosion vessel, as discussed in Section 2.4.4. The visible section of the spherical flame expanded from left to right. The flame front and the combustion products within are identified as the large black zone in Fig. 4.6. The white dots to the right of the flame front are the droplets in the cold reactants region. The image, shown in Fig. 4.6, displays an apparent heterogeneous droplet distribution, which contradicts the characterisation results in Chapter 3 and those by other workers (Hayashi *et al.*, 1976, Atzler, 1999, and Marquez, 2003) who also used the Wilson cloud chamber method (Wilson, 1897). This might be due to the relatively large laser sheet thickness of approximately 0.7 mm (as discussed in Section 2.4.4) in comparison to the droplet size of up to 20 μm , and the inter-drop spacing of between 165 μm and 330 μm as estimated by Atzler (1999). Hence, what appears to be large droplets in Fig. 4.6 could be the superposition of several droplets being visualised in front of others. In addition, the Gaussian laser beam intensity distribution could be another factor. This will result in droplets appearing to be smaller when located near the

edge of the laser sheet (out of plane) than when located near the central plane due to the variation in light scattering intensity.

The boundary at which droplets are fully evaporated near the flame front is clearly visible in Fig. 4.6. The sudden disappearance of droplets gives an indication that the rate of evaporation is rapid. The corresponding δ_l (defined in Section 1.2), was estimated to be approximately 0.07 mm, and was very much smaller than the resolution of the image (0.23 mm/pixel) in Fig. 4.6. Therefore, in order to determine whether droplets were fully evaporated near the flame front, simultaneous imaging by schlieren (Section 2.4.3) and laser sheet (Section 2.4.4) techniques, using a single digital camera was performed. To the knowledge of the Author, this is the first time that this experiment has been undertaken. This approach enabled visualisation of any droplets that might exist behind the flame front (as visualised by schlieren photography). Although Marquez (2003) had made a similar attempt, he used separate cameras for the two techniques and there was a strong tendency for non-synchronisation of electronic signals, which resulted in inaccuracies in his observations.

Figure 4.7 shows sequences of images from laminar flames of iso-octane-air aerosol using the simultaneous schlieren and laser sheet techniques. The aerosol mixture was ignited at $\phi_{ov} = 1.0$, $P = 162$ kPa, $T = 277$ K, and $D_{10} = 17$ μm . The laser sheet characteristics were similar to that described for Fig. 4.6, and likewise, the visible section of the spherical flame propagated from left to right. The time after ignition is indicated in each picture. The poor quality of the images, in comparison to Fig. 4.6 and to those by Marquez (2003), is due to the trade off in the optical settings, in order to obtain satisfactory simultaneous visualisation for both schlieren and laser sheet techniques. The greyscale images have been inverted to improve the clarity of the droplets; the liquid fuel droplets are shown in Fig. 4.7 as black dots on

the right of the flame front. The inset in each photograph shows the enhancement of droplets found in the zones indicated by the square within the dotted lines. The large circular 'black area' was a lighting effect resulting from over exposure (Ormsby, 2005), and was present throughout the experiments.

The photographs in Fig. 4.7 show a few black dots in the products side of the flame edge, suggesting that liquid fuel droplets survived the flame front. Clusters of such surviving droplets are shown to exist for a few milliseconds, before disappearing (evaporating). The top row of Fig. 4.7 shows an evaporating cluster between 17 and 19 ms after ignition, while the bottom row shows one between 26 and 28 ms after ignition. In addition, the images follow some drops as they traverse the flame. For example, at 17 ms, the inset shows 3 drops in the hot region (product side) and 2 drops in the cold region (reactant side). By 18 ms 2 of the 3 drops that were behind the flame have evaporated while the 2 drops that were in front of the flame have now entered it. By 19 ms only the 2 drops that were initially in the cold region now remain. Droplets that survive the flame front could have a significant effect on the cellular flame surface, such as that displayed in Fig. 4.3(c).

Inevitably, it is also arguable that the laser sheet might not be exactly co-planar with the centre-plane of the flame ball, thus making droplets (within the reactant region) appear to be visualised as if they were in the product region. Therefore, in order to verify the possibility of droplet survival shown in the photographs in Fig. 4.7, a simple mathematical analysis based on the d^2 evaporation law was performed. This is discussed in Chapter 5.

4.1.5 Effects of Flying Molten Metal from Spark Electrodes

During most of the present research, only laser sheet imaging and schlieren photography were used to observe flame propagation. However, towards the end of

the project some natural light movies were recorded and these revealed a potential problem that might have had serious implications in the interpretation of results. Flying points of lights, possibly caused by hot fragments from the spark electrodes were observed during combustion experiments. Clearly, these were a potential cause of some of the instabilities observed in Section 4.1.2. Therefore further investigation was required.

Shown in Fig. 4.8 are sequences of natural light images of a spark in air without fuel at $P = 100$ kPa and $T = 303$ K using the electric discharge spark ignition system described in Section 2.1.3.1. Also shown in each photograph is the time from the start of spark. The spark kernel, visualised as a round circular white object at the centre of the photograph, lasted for about 8 ms after the spark initiated. Interestingly, as shown in Fig. 4.8, after 6 ms splashes of small objects departed from the spark kernel body. These were probably fragments of flying molten metal from the electrodes as a result of high ignition temperature, which was above that of the melting point of the electrodes. The flying fragments are shown to disappear at about 20 ms after the start of the spark.

Shown in Fig. 4.9 are sequences of laminar flames recorded with natural lighting for aerosol at $\phi_{ov} = 1.2$, $P = 112$ kPa, $T = 271$ K, and $D_{10} = 24$ μm . By 23 ms, the hot fragments appear to exist only in the hot products and no trace of them is observed ahead of the flame front, probably because they are cooled down by the cold reactants. Figure 4.9 clearly shows that the fragments did not initiate any isolated flame pockets ahead of the main reaction zone. The large white area near the electrode in each of the images at 23 and 38 ms is not a spark kernel because, as shown in Fig. 4.8, the glow discharge from the spark lasted for only about 12 ms. The nature of the large white area is unclear and thus further investigation is required in the future.

To rule out the possibility that the presence of the hot fragments could have promoted cellularity in the flame, perhaps by creating traces of preheated gas ahead of the flame front, experiments using the laser ignition system described in Section 2.1.3.2 were carried out for comparison with the electric spark ignition. Figure 4.10 shows sequences of schlieren images of laminar flames in a quiescent aerosol at $\phi_{ov} = 1.0$, $P = 89$ kPa, $T = 268$ K, and $D_{10} = 9$ μm . In Figs. 4.10(a), the flame was ignited with a laser spark, while in Fig. 4.10(b) a spark electrode, as described in Section 2.1.3.1, was used. Also shown with each photograph is the time from ignition.

In Fig. 4.10(a), the laser beam passed, from left to right through a 25 mm lateral window in the explosion vessel, as discussed in Section 2.1.3.2. Shown in Fig. 4.10(a) are close up images of the initial kernel development for the laser ignited flame. The first image, taken 1 ms after the start of ignition, shows 2 ignition sites, distributed over about 15 mm. A classical laser ignition kernel was evident with toroidal growth normal to the axis and on-axis propagation towards the laser (Spiglanin *et al.*, 1995). The backward flame propagation (left kernel) with respect to the laser source direction corresponds to a range of reactant that was flammable but not readily ignitable by the laser pulse. The same overall flame shape remained for the next 8 ms. It is assumed that each ignition site corresponds to the laser induced breakdown of at least one droplet. Similar observations of multiple ignition sites were observed by Mokhtar (2001) using the same apparatus and laser ignition characteristics as in the present work. He recorded images at a higher framing rate (about 0.5 MHz) and reported observing shock waves propagating from the ignition sites at less than 20 μs after the start of ignition. By about 11 ms the ignition sites had clearly started to merge. Clearly after 16 ms the flame kernel had developed into a single ellipsoid-shape flame with a smooth surface, except for deep crack lines,

which were the result of perturbation caused by the merging of the two kernels. These cracks changed very little throughout the rest of flame propagation. A comparison between the laser and electric spark ignited flames in Figs. 4.10 (a) and (b) shows that they were very similar except for the effect of multiple droplet ignitions. They were initially smooth, but started to become wrinkled at about 40 ms after the start of ignition. In addition, Fig. 4.10 (b) shows an appearance of a bump at the bottom-left section of the flame. This might have been caused by flying hot fragments ahead of the flame front, which created a path of preheated droplet-gaseous mixture. However, the bump developed slowly with no cell division throughout flame propagation. It is clearly shown at 38 ms that there is a distinct difference between the single cell initiated, possibly, by the flying hot fragments and those developed later (as a result of the presence of fuel droplets). Thus it is evident that flying fragments, as observed in Figs. 4.8 and 4.9, did not cause cellularity, in which the range of unstable wave numbers increases, such as that described in Section 1.3. It is concluded that the flying hot fragments did not significantly affect the data presented in this thesis.

4.2 Burning Rates of Laminar Gaseous and Aerosol Flames

Burning rates of quiescent aerosol mixtures were measured at a range of initial conditions as summarized in Table 4.1. It comprises the mixture conditions at the time of ignition: ϕ_{ov} , ϕ_g , P , T , ρ_u , v and D_{10} ; the measured or calculated burning properties (as defined in Sections 1.2 and 1.3): ρ_b , S_s , u_l , L_b , δ_l , Ma_{sr} , r_{cl} , and Pe_{cl} , and a comment in relation to instabilities. The present experiments proved to be very repeatable. For stoichiometric mixtures, two experiments were undertaken at each condition, and, for example the difference between S_f at each condition was

typically less than 5 %. Hence, experiments at other conditions ($\phi_{ov} \neq 1.0$) were made once, unless the results were inconsistent with measurements at conditions by close proximity.

In the present work it was observed (Section 4.1) that some flames were smooth and stable throughout propagation while other flames became cellular and/or accelerated during the later stages of observation. The burning rates of the latter flames are discussed in Section 4.2.1. Yet other flames became cellular very early without any observable evidence of a smooth regime prior to transition to a cellular one. For these, the fundamental unstretched burning properties could not be determined and their burning rates are discussed in Section 4.2.2.

4.2.1 Initially Stable Flames

Shown in Figs. 4.11 (a) and (b) are the variations of flame speed with radius and with stretch rate (defined in Eq. (1.6)), respectively, for gaseous iso-octane-air at $\phi_{ov} = 0.8$, $P = 100$ kPa and $T = 303$ K. The point of ignition in Fig. 4.11 (b) is located to the right, at a high stretch rate, and flame propagation is from right to left. Figure 4.11 clearly exhibits four regimes of flame development, as discussed by Ali *et al.* (1993). Initially, between points (1) and (2), indicated in Figs. 4.11 (a) and (b), the flame speed was high due to the active radicals provided by the spark energy. However, high stretch rates caused the flame speed to decrease rapidly when the thermal energy of the spark was dissipated into the reactant and before normal flame chemistry developed. At point (2), a propagating flame probably was not yet established. Between points (2) and (3), spark plasma dynamics and flame stretch were operative in a regime of spark assisted flame propagation. Between points (3) and (4) flame speed increased as the rate of stretch reduced. All flames in the present work exhibited these trends. However, the spark affected period, between points (1)

and (3), was not important to the present work and hence was not measured in all cases. It is evident from Fig. 4.11 that flames are fully developed only at radii bigger than about 16 mm. Bradley *et al.* (1996), working at temperatures higher than 358 K, suggested that flames were not fully developed for the determination of burning rates at radii less than 10 mm. The late development of flames in the present research compared to previous gaseous flame studies at Leeds could be associated with the low temperature (≤ 303 K) at ignition used in the present work. The unstretched flame speed, S_s , is derived by a linear extrapolation to zero stretch, which is indicated by the continuous line in Fig. 4.11 (b). The laminar burning velocity is calculated from S_s using Eq. (1.8) in Section 1.2. The negative of the gradient of the extrapolation is the burnt gas Markstein length, L_b . A positive value of L_b , that is increasing flame speed with decreasing stretch rate, indicates a flame with little tendency to instabilities. Conversely, a mixture with negative L_b tends to develop instabilities much quicker (Bradley *et al.*, 1998).

Shown in Figs. 4.12 to 4.14 are the variations of flame speed with time, radius, and stretch rate, respectively, for the three aerosol flames presented in Figs. 4.3 (a) to (c), at $D_{10} = 8 \mu\text{m}$ and $\phi_{ov} = 0.8$ (triangles), $\phi_{ov} = 1.0$ (circles), and $\phi_{ov} = 1.2$ (diamonds). The flame contour tracings throughout propagation are also shown in Fig. 4.12, at intervals of 2 ms. In Fig. 4.13, corresponding schlieren photographs of the flames at the maximum viewable radius are shown. As in Fig. 4.11 (b), the solid lines in Fig. 4.14 are linear fits to the data points at which the flames were stable and were used to obtain S_s , and L_b . The spark affected region, described for Fig. 4.11 is also shown in Figs. 4.12 and 4.13.

The leanest mixture ($\phi_{ov} = 0.8$) in Figs. 4.12 and 4.13 was the slowest of those shown and was stable throughout the whole of the observed period. This is indicated by the smooth contours and flame surface in Figs. 4.12 and 4.13 respectively. This

flame was also significantly affected by buoyancy, as depicted by the larger spacing between the flame contours (Fig. 4.12) at the top portion of the flame than at the bottom, and by the vertically elongated flame shape (Fig. 4.13). This is discussed in Section 4.3. The flame for the stoichiometric mixture was initially smooth, but became wrinkled at later stages of propagation, as indicated by the photograph in Fig. 4.13. The transition from smooth to wrinkled is also shown in the flame contour tracings in Fig. 4.12. The flame of the richest mixture ($\phi_{ov} = 1.2$), shown in Figs. 4.12 and 4.13, was the fastest throughout the whole of the observed period and also had the highest degree of cellularity. All the flames in Figs. 4.12 and 4.13 displayed a gradual increase in S_n . However, at a critical radius, the flame for the rich mixture ($\phi_{ov} = 1.2$) became unstable, and later began to accelerate. This is shown clearly in Fig. 4.14, and is addressed in Section 4.2.2.

Shown in Fig. 4.15 is the variation of u_l , (defined in Section 1.2) with D_{l0} for laminar flames at ϕ_{ov} of 0.8, 1.0 and 1.2, at a range of pressures and temperatures. The data were obtained in the present work and from Atzler (1999) and Marquez (2003). The values were obtained by application of Eq. (1.8) to experimental results such as that in Fig. 4.14. Also shown in Fig. 4.15 are the data points for gaseous flames ($D_{l0} = 0$) at a pressure and temperature of 100 kPa and 293 K respectively. The slight difference in pressure and temperature for the different flames was unavoidable and was due to the method of thermodynamic aerosol generation, as described in Section 4.1. The gaseous (single phase) flames could not be studied within the range of pressures and temperatures of aerosols because at such conditions the mixture would be in the wet, or two-phase, regime. However, Bradley *et al.* (1998) have showed that, for gaseous flames, such small differences in pressure and temperature have little effect on u_l . For example, at a pressure of 100 kPa, an increase in temperature from 303 to 323 K, will increase u_l

by only 0.027 m/s, when using their empirical correlation for stoichiometric iso-octane-air, expressed by

$$u_l = 0.48 \left(\frac{T}{358} \right)^{1.01} \left(\frac{P}{100} \right)^{-0.282} \text{ m/s} \quad (4.1)$$

In the present work, generally, pressure and temperature decrease with D_{10} . This explains the slight decrease in u_l when D_{10} is increased. In Fig. 4.15, the average value of u_l , for each value of ϕ_{ov} , is shown to be only slightly lower than those for the gaseous flame. In addition, the corresponding standard deviations are small, between 3 and 6 %. Hence it is suggested that u_l is probably unchanged by the presence of droplets.

Shown in Fig. 4.16 is the variation of Ma_{sr} (defined in Section 1.2) with D_{10} for aerosols at equivalence ratios of 0.8 (crosses), 1.0 (circles), 1.1 (diamonds), and 1.2 (squares), and pressures between 82 and 241 kPa, and temperatures between 265 and 287 K. The full circle represent the gaseous data ($D_{10} = 0$) at $\phi_{ov} = 0.8$, $P = 138$ kPa, and $T = 277$ K. For richer mixtures ($\phi_{ov} > 1.2$), the values of Ma_{sr} could not be determined due to early onset of instabilities, and this is explained in Section 1.3. It is shown in Fig. 4.16 that Ma_{sr} decreases as D_{10} increases. As shown by Bradley *et al.* (1998), for gaseous flames, low values of Ma_{sr} are indicative of unstable flames. This, indeed, is also the case in the present work on aerosols. As shown in Fig. 4.16, low values of Ma_{sr} are favoured by aerosols of large droplets.

4.2.2 Flames with Early Onset of Instabilities

Figure 4.17 shows a graph of flame speed against stretch rate for two laminar flames of rich aerosols, one (circles) at $\phi_{ov} = 1.6$, $P = 146$ kPa, $T = 284$ K, and $D_{10} = 14 \mu\text{m}$, and another (diamonds) at $\phi_{ov} = 1.2$ (as in Figs. 4.12 to 4.14). After the

end of the spark affected period ($r < 12$ mm), the flame for aerosol at $\phi_{ov} = 1.2$, had a steady increase in flame speed, and the flame front remained smooth and free from instabilities, as a result of the high stretch rate ($0.22/\text{ms} < \alpha < 0.39/\text{ms}$). As the size of the flame increased and the stretch rate reduced ($\alpha < 0.22/\text{ms}$), the flame became unstable and exhibited cracks, which was followed by a cellular appearance. The point at which it became cellular is expressed as Pe_{cr} , as theoretically explained in Section 1.3. The cells continually developed and sub-divided, as described by Bradley *et al.* (1998), to yield an increase in cellularity until there was an increase in acceleration ($\alpha < 0.12/\text{ms}$) in the flame speed. The point at which the flame increased its acceleration is expressed as Pe_{cl} , as defined in Section 1.3. The influence of Pe_{cl} on instabilities is discussed in Section 5.2.1.

However, the flame for aerosol at $\phi_{ov} = 1.6$ in Fig. 4.17 was found to be cellular immediately after the end of the spark ignition period and as a result, the unstretched laminar burning properties such as L_b , S_s and u_l could not be determined. A similar problem was experienced in most flames of rich mixtures, generally at values of ϕ_{ov} greater than 1.2. Hence, it is difficult to systematically compare the burning properties of these flames. However, a solution to this shortcoming has been proposed by Lawes *et al.* (2005). They measured the turbulent burning velocity at radii of 10 and 30 mm, to compare burning rates at various ϕ_{ov} . In the present work, $S_{n,48}$, which corresponds to the flame speed at a radius of approximately 48 mm, was chosen because it was the maximum measurable flame radius within the field of view of the windows. This was less than the radius of the windows because buoyancy effects sometimes caused flames to rise towards the top of the field of view. It should be noted that $S_{n,48}$ is not a fundamental parameter, but is indicative of the burning rate. It does not distinguish any effect of instabilities.

Shown in Fig. 4.18 is the variation of $S_{n,48}$, with ϕ_{ov} and D_{10} (within $\pm 1 \mu\text{m}$) for aerosol and gaseous flames of iso-octane-air at similar initial pressures and temperatures. Also shown are the average values of unstretched flame speed at the conditions in which cellularity did not prevent its determination. The experimental results for the aerosol flames are represented by symbols for droplet sizes of $5 \mu\text{m}$ (squares), $8 \mu\text{m}$ (crosses), $10 \mu\text{m}$ (open circles), $15 \mu\text{m}$ (triangles) and $20 \mu\text{m}$ (diamonds). These were obtained at pressures between 110 and 170 kPa, and temperatures between 270 and 292 K. The solid lines were obtained by drawing a best fit curve through the experimental results. The full circle markers represent the results for gaseous flames at 100 kPa and 303 K. As explained in Sections 3.1, the gaseous flames could not be studied within the range of pressure and temperature of aerosols since at such conditions the mixture would be in the wet regime. Hence, for a more practical comparison with aerosol flames, values of $S_{n,48}$ for gaseous flames were estimated at conditions within the range of those for aerosols. To achieve this, an experiment with a gaseous flame at $\phi_{ov} = 0.8$, $P = 138 \text{ kPa}$ and $T = 277 \text{ K}$ was performed, by igniting an expanding mixture (as in aerosol generation) prior to onset of condensation. The value of $S_{n,48}$ for this experiment, represented by a full square symbol in Fig. 4.18, is lower than that at 100 kPa and 303 K by 0.38 m/s, but is in good agreement with an extrapolation of all of the aerosol results to $\phi_{ov} = 0.8$. For estimation of values of $S_{n,48}$ for gaseous flames at 138 kPa and 277 K, the results for gaseous flames were offset by 0.38 m/s, at all equivalence ratios. A best fit curve through the estimated values is shown by the dashed line in Fig. 4.18.

It is clearly shown in Fig. 4.18 that the values of $S_{n,48}$ for lean mixtures ($\phi_{ov} < 1.0$) are independent of D_{10} . However, at higher equivalence ratios, $S_{n,48}$ becomes a strong function of droplet diameter, in which $S_{n,48}$ increases with D_{10} . The variation

of $S_{n,48}$ with equivalence ratio has a similar parabolic profile for each droplet diameter. Nevertheless, although the peak of the curve for gaseous mixtures is at $\phi_{ov} = 1.1$, the ones for aerosols increase with D_{10} . These are discussed in Section 5.2.1.

4.3 Instabilities due to Buoyancy Effects

Shown in Fig. 4.19 are graphs displaying the temporal variations of flame radius (Section 2.4.3) and vertical and horizontal propagation distances for flames of iso-octane-air mixtures at $\phi_{ov} = 2.0$ and various D_{10} . The mixtures were ignited at pressures between 100 and 170 kPa, and temperatures between 290 and 303 K. The upward, downward, leftward and rightward propagation distances between the spark gap and the corresponding flame edge were measured at 1 ms intervals. Also shown in Fig. 4.19 are the corresponding pictures of the flames at the maximum viewable radius, and the flame contour plots at 2 ms intervals.

It is shown in the graph and schlieren image in Fig. 4.19(a) that for the gaseous flame, the upward distance of the flame propagation is always greater than the lower one. In addition, the upward distance of the flame propagation increases at a steady rate, whereas the downward one decelerates. This is also indicated by the significantly larger spacing between flame contours for the upper propagation as compared to the lower one. Conversely, the difference between the leftward and rightward propagations is shown to be small, the rightward propagation being very close to the flame radius. Obviously, the flame radius and horizontal propagation distances are shown to be at approximately midway between the upward and downward components.

The gap between the upper and lower curves for the gaseous flame in Fig. 4.19(a) is larger than that for any of the aerosols in Fig. 4.19 (b) to (d).

Furthermore, the deceleration in downward propagation is only experienced by the gaseous flame. The trend of results described for Fig. 4.19(a) is due to natural convection and is a consequence of the buoyancy force acting on the hot flame kernel. This is found to agree with the results by Andrews and Bradley (1973) on methane-air flames near the flammability limits. The bottom half of the gaseous flame in Fig. 4.19(a) is cellular, probably due to hydrodynamic instabilities, as a result of an upward flow of unburned gas which velocity exceeded the flame speed at the base of the flame. Conversely, the upper surface of the flame is smoother and has fewer, but larger, cells, than the bottom half of the flame. This is probably due to flame stabilization as a result of stretch rate, which occurs when the expanding flame front propagates through a velocity gradient in the unburned gas that is induced by the upward, buoyant acceleration of hot products (Andrew and Bradley, 1973).

With the presence of fine droplets ($D_{10} = 5 \mu\text{m}$), it is shown in Fig 4.19(b) that the flame is slightly more cellular than the gaseous one (Fig. 4.19(a)), and the downward distance of the flame propagation shows some acceleration as compared to the deceleration in the gaseous flame. Nevertheless the difference between the upper and lower curves in Fig. 4.19(b) is similar to that in Fig. 4.19(a), thus suggesting the presence of natural convection. Although the gap between the curves for the leftward and rightward propagation distances is small, it increases throughout flame propagation. This is probably explained by the tilting of the flame shape, which may be attributed to a perturbation in convection flow by (possibly) the electrode holder. However this effect was not observed in any other measurement.

With larger droplet sizes, flames burned faster, as indicated by the bigger gap between the flame contours in Figs. 4.19 (c) and (d), for D_{10} of 13 and 16 μm respectively, such that there was less time available for natural convection to be influential. This is also verified by the smaller difference between the measurements

of the upward and downward propagation distances, than that displayed in Figs. 4.19 (a) and (b). The absence of the effect of natural convection is due to the dominance of instabilities, as evident by the fine cells throughout, due to droplets. These promoted a faster burning rate, such that there was less time available for natural convection to be significant.

Figure 4.20 summarises the results for the vertical components of flame propagation in Fig. 4.19, but with the downward propagation distance indicated by a negative sign. The propagation rates for the fine aerosol ($D_{10} = 5 \mu\text{m}$) flames are shown in Fig. 4.20 to be similar to those for the gaseous flames, as indicated by their nearly identical propagation curves. Interestingly, it is shown that the curves for upward propagation for all values of D_{10} are coincident for approximately the first 25 mm of propagation; a similar trend is observed for downward propagation up to about 16 mm. This is probably because cellular flame instabilities are smaller (or zero) in the early stages than later during flame development.

4.4 Oscillating Flames

The phenomenon of oscillation of flame speed in spherically propagating aerosol flames, described by alternating fast and slow modes of flame propagation, was observed by Atzler (1999) and Marquez (2003). It is found only in flames of lean mixtures, with droplet size greater than $8 \mu\text{m}$, as shown in the map of flame regimes in Fig. 4.4. Shown in Fig. 4.21 is the variation of flame speed with radius for iso-octane-air aerosol at $\phi_{ov} = 0.8$, $D_{10} = 12 \mu\text{m}$, $P = 110 \text{ kPa}$, and $T = 265 \text{ K}$. Also shown in Fig. 4.21 are corresponding schlieren photographs of the flame at selected radii. Shown in the inset of Fig. 4.21 are corresponding flame contour plots. These illustrate the basic characteristics of an oscillating flame.

After the end of the spark affected period ($r \approx 12$ mm), the flame surface is smooth and the flame speed reduces to a minimum value, indicated as point *A* in Fig. 4.21. This is also shown by the narrow gap between the flame contours. The flame then accelerates, as also evident by the wider contour spacing, until it reaches a maximum value, at point *B*. At this stage, the flame displays a mild cellular surface structure. As the flame develops further, it slows down until it reaches another minimum value (point *C*), at which the flame surface becomes smooth and the gap between the flame contours becomes narrow again. The changes between fast and slow flame speed, and wrinkled and smooth flame structures continue throughout the observation.

Shown in Fig. 4.22 are typical variations of flame speed with time from ignition for iso-octane-air aerosols with $D_{10} = 12$ μm ($\phi_g = 0.56$, $P = 110$ kPa, $T = 264$ K) and $D_{10} = 15$ μm ($\phi_g = 0.52$, $P = 94$ kPa, $T = 261$ K). The symbols in Fig. 4.22 have been removed for clarity and are not intended to represent trends between measurements. It is indicated in Fig. 4.22 that the flame speeds for $D_{10} = 12$ μm and $D_{10} = 15$ μm are slightly different, but they are within the experimental errors. Moreover, the time intervals between the peaks of the oscillation for each of the flames are shown in Fig. 4.22 to be the same (31 ms). The difference between the flame speeds at $t < 20$ ms is probably due to the spark affected period explained in Section 4.2.

Shown in Fig. 4.23 are the variations of flame speed with radius for iso-octane-air at an overall equivalence ratio of 0.8, pressures between 94 and 138 kPa, and temperatures between 261 and 277 K. The droplet sizes were 0 μm (dash dot line), 1 μm (fine continuous line), 8 μm (fine and thick dash lines), 12 μm (thick continuous line), and 15 μm (medium continuous line). Similar to Fig. 4.22, the

symbols in Fig. 4.23 have been removed for clarity. The trends of flame speed oscillation and changes of surface structure of flame, displayed in Fig. 4.21, are also observed in Fig. 4.23. Clearly, the results at $D_{10} = 0 \mu\text{m}$ and $D_{10} = 1 \mu\text{m}$ are very similar, indicative of good repeatability of the experiment. However, at $D_{10} = 8 \mu\text{m}$, repeatability was poor, in which the flame speed for one experiment was oscillating, but was stable for the other, throughout propagation. This suggests that a D_{10} of $8 \mu\text{m}$ for this condition represents a transition point below which the flame is smooth and stable, and above which the flame starts to show oscillating behaviour (as indicated in Fig. 4.4).

One of the objectives of the present work was to identify the mechanisms responsible for oscillating flames. This was investigated by analyzing simultaneously the droplet velocity, flame speed and gas velocity ahead of the flame front throughout the propagation of an oscillating flame. The droplet velocity was obtained by PIV, described in Section 2.4.4.3, and the flame speed was determined from laser sheet images, described in Section 2.4.4.2. Figure 4.24 shows typical droplets velocity vectors, obtained by PIV analysis of laser sheet images from the same iso-octane aerosols as described for Fig. 4.6. This work was completed with help from a colleague, Mr. Gunnar Larsson. Likewise with Fig. 4.6, the left hand side area of Fig. 4.24 is the region of combustion products, where, in general, there were no droplets and hence no velocity vectors. It is generally shown in Fig. 4.24 that the droplet velocity is the largest within the vicinity of the flame front as a result of gaseous expansion; the droplets velocity reduces with distance from to the flame front. The droplet velocity at the flame front is identified as u_D and is compared with the corresponding flame speed and gaseous velocity in Section 5.2.3.3.

4.5 Turbulent Flame Observation

The effect of droplets on turbulence flames was examined at various values of r.m.s. turbulent velocity fluctuation, u' . Shown in Fig. 4.25 (a) to (e) are schlieren images of turbulent flames for stoichiometric iso-octane-air aerosol at $P = 128$ kPa, $T = 283$ K, $D_{10} = 4$ μm and u' of 1.0, 1.5, 2.5, 3.0 and 4.0 m/s. Figure 4.25(f) shows an image of a gaseous flame, at $u' = 4.0$ m/s, $P = 100$ kPa, and $T = 303$ K, being the closest practical gaseous condition to that of the aerosol in Fig. 4.25(e). In general, it is shown in Fig. 4.25 that turbulent flames wrinkle and deform considerably as compared to the nearly spherical laminar flames in Figs. 4.2 and 4.3. The degree of wrinkling is also shown to increase with u' .

In Figs. 4.25 (c) to (e), unknown 'black clouds' are observed at random locations close to the flame front. The 'black clouds' started to appear typically between 4 and 6 ms after ignition and increased in quantity throughout flame propagation. At low levels of u' , as in Figs. 4.25 (a) and (b), the 'black clouds' are not visible, but become increasingly prominent with an increase in u' . At $u' = 4.0$ m/s, in Fig. 4.25 (e), the flame surface is shown to be almost completely obscured by the 'black clouds', which consequently hindered measurement of flame radius. Although Marquez (2003), who performed a similar experiment, did not report such an observation of the 'black clouds,' the photographs of his turbulent aerosol flames revealed mild signs of it. He probably did not notice this because his experiments were at relatively lower levels of turbulence ($u' \leq 2.5$ m/s). The observation of 'black clouds' is remarkable because they seem to appear only in aerosol flames. Conversely, the turbulent gaseous flame, in Fig. 4.25(f), at $u' = 4.0$ m/s, did not show any sign of the presence of the 'black clouds.' Hence it

is probable that the appearance of the 'black clouds' in the aerosol turbulent flame is related to droplets in the reactants.

It was not clear if the 'black clouds' shown in Fig. 4.25 were real or just a schlieren optical effect. Therefore, selected turbulent aerosol experiments were repeated using the laser sheet imaging technique described in Section 2.4.4 to investigate the nature of the 'black clouds.' Figure 4.26 shows two laser sheet images of turbulent flames for aerosols at conditions similar to Figs. 4.25 (a) and (e) at $u' = 1.0$ m/s and $u' = 4.0$ m/s, respectively. For a laminar flame, the droplet particles were identified as discontinuities of white dots, similar to that shown in Fig. 4.5. However, in Fig. 4.26, 'clouds,' with no discontinuities indicative of droplets, were observed within the resolution of the laser sheet system. Hence it is more likely that the 'clouds' observed in the aerosol flames were clusters of many fine particles, which also suggests that it could be soot or smoke. It might be expected that soot will be generated in aerosols. However, the detailed formation mechanism is confused by the fact that it does not appear when laser ignition is used.

Figure 4.27 shows a schlieren image of a turbulent flame, ignited by the laser ignition system, described in Section 2.1.3.2, for an aerosol at conditions similar to that in Fig. 4.25(e). It is clearly shown in Fig. 4.27 that, unlike Fig. 4.25(e), there were no 'black clouds.' Hence, because hot metal fragments did not exist in the laser ignition experiments, it is suggested that it is these fragments that interact with droplets, possibly evaporating some of them to yield rich gaseous pockets to cause the 'black clouds.' The actual nature of the 'black clouds' is still unknown.

Qualitatively, the degree of wrinkling for the flames in Fig. 4.25(e) and 4.27 is quite similar. However, it is not known if the 'black clouds' have any effect on the burning rate. This is because, the burning rate from experiments with the spark

electrode (at $u' = 4.0$ m/s) could not be measured due to obscuration of the flame edge. In addition, multiple ignition sites, as described in Sections 4.1.5, were observed in the laser ignited flames, and hence valid measurements of flame speed could not be made. Thus comparison between the burning rates of flames ignited with laser ignition and those with spark electrode could not be made within the present study.

4.6 Burning Rates of Turbulent Gaseous and Aerosol Flames

Turbulent burning rates were studied by Marquez (2003) using similar apparatus and techniques to those in the present work. However, he did not undertake laser ignition studies. Although he made comparisons between turbulent flames of gaseous and aerosols, unfortunately the temperature difference between the two mixtures was too high at, 96 K, to provide realistic comparisons. Furthermore, the values of u' for the aerosols were 0.83, 1.67, and 2.50 m/s, as compared to 1.0 and 4.0 m/s for the gases. Therefore, in the present work, comparison between gaseous and aerosol flames have been made at, as near as possible, similar conditions.

4.6.1 Gaseous Studies

Shown in Fig. 4.28 is the variation of radius with time for stoichiometric iso-octane-air mixtures at $P = 100$ kPa, $T = 303$ K, and u' of 1.0 and 4.0 m/s; Fig. 4.29 shows a magnification of the early stage of flame propagation. In Figs. 4.30 and 4.31 are the variations of S_t with time and radius, respectively, for the mixtures in Fig. 4.28. Two ignition energies were used: one was a low ignition energy of about 25 mJ (as estimated by Ormsby (2006)) and the other was at a higher level of

approximately 400 mJ (as stated in Section 2.1.3.1), to compare their effects. In Fig. 4.28 the mixtures ignited by the 25 mJ spark are represented by triangles ($u' = 1.0$ m/s) and diamonds ($u' = 4.0$ m/s); those by the 400 mJ spark are represented by crosses ($u' = 1.0$ m/s) and circles ($u' = 4.0$ m/s). The lines in the graphs simply join the markers for reasons of clarity and are not intended to represent trends between measurements. In Figs. 4.29 to 4.31 the markers are not shown. For each condition, up to 5 explosions are plotted. The general trend in Figs. 4.28 to 4.31 is a sustained increase in S_t with time and radius with no evidence of flame speed stabilisation as was observed for the laminar cases in Section 4.2. The flame growth rates also increase with an increase in u' . However, as indicated in Figs. 4.30 and 4.31, turbulent flames also have a spark affected period like in the laminar flames described in Section 4.2.

In Figs. 4.28 to 4.30, it is shown that the flames ignited by the 25 mJ spark are generally slower and the results are more widely scattered, as compared to those ignited by the 400 mJ spark, for any level of u' . Furthermore, it is shown in Figs. 4.30 and 4.31, that during the initial kernel growth period, two of the 25 mJ flames had near zero values of S_t , which were sustained for about 4 ms. These very slow initial propagation rates were probably due to the phenomenon described by Maly (1984) as the random transport of the ignition kernel, due to flow field, towards the electrode, which consequently increased the heat loss from the flame kernel to the spark plug.

In Fig. 4.31, the plots of S_t against radius for $u' = 1.0$ m/s are shown to merge into a single narrow band of results, irrespective of the ignition energies. Interestingly, at the higher turbulence level ($u' = 4.0$ m/s), S_t for flames with the 400 mJ spark are slightly lower than those for the 25 mJ. At the higher turbulence there is more experimental scatter due to random variations of the effect of turbulence. Indeed, for the higher turbulent case, Fig. 4.31 suggests that in the early

stages the larger energy is beneficial, yet in the later stages the reverse is true. This might appear to be counter intuitive. However, this is clearly explained if one considers the mean values at each condition in Figs. 4.30 and 4.31. Figure 4.32 shows the variation in S_t with time and Fig. 4.33 shows the variation with radius. On each graph the symbols show values at specific times. The lower values of S_t with the higher ignition energy in the later stage are probably due to random experimental scatter. Moreover it is important to note that although Fig. 4.31 suggests little effect of ignition energy, Figs. 4.28 to 4.30 clearly show that the flame attains a given radius quicker with higher energy.

4.6.2 Aerosol Studies

Figures 4.34 and 4.35 are similar to Figs. 4.30 and 4.31 respectively, but for turbulent flames of stoichiometric iso-octane aerosols at $P = 128$ kPa, $T = 283$ K, $D_{10} = 4$ μm , u' of 1.0 m/s (diamond) and 2.5 m/s (square). The ignition energy was approximately 400 mJ. The results are limited to $u' \leq 2.5$ m/s due to obscuration of the flame edge by the 'black clouds' in flames at higher level of u' , as explained in Section 4.5. For each condition, 5 explosions are plotted. The trends for the turbulent aerosol flames in Figs. 4.34 and 4.35 are similar to those for the gaseous flames described in Section 4.6.1, in which S_t increases with time, radius and u' . Figures 4.34 and 4.35 also show that a larger scatter of results are found for turbulent aerosol flames at the higher turbulence as compared to the lower, a similar effect to that for the gaseous flames in Figs. 4.30 and 4.31.

Table 4.1 Laminar aerosol flames investigated in the present work.

No.	ϕ_{ov}	P (kPa)	T (K)	ϕ_p	D_{no} (μm)	ρ_a / ρ_b	ν (m^2/s)	L_b (mm)	S_s (m/s)	Ma_{sr}	δ (mm)	r_{ci} (mm)	Pe_{ci}	u_i (m/s)	D_{10}/δ	$S_{n,48}$ (m/s)	Remarks
1	0.8	202	274	0.54	11	7.80	6.47E-06	1.56	0.96	5.03	0.052	-	-	0.1233	0.21	0.90	stable
2	0.8	138	277	0.80	0	7.72	9.63E-06	3.63	1.43	10.26	0.052	-	-	0.185	0.00	1.23	stable
3	0.8	134	273	0.78	1	7.83	9.69E-06	2.97	1.37	8.06	0.055	-	-	0.176	0.02	1.21	stable
4	0.8	122	271	0.73	8	7.86	1.05E-05	2.42	1.40	6.44	0.059	-	-	0.178	0.14	1.28	stable
5	0.8	122	271	0.73	8	7.86	1.05E-05										oscillating
6	0.8	110	264	0.56	12	8.04	1.12E-05										oscillating
7	0.8	94	261	0.52	15	8.10	1.28E-05										oscillating
8	0.9	110	266	0.62	14	8.62	1.12E-05										oscillating
9	1.0	96	274	0.99	4	8.80	1.35E-05	2.66	2.49	7.52	0.048	-	-	0.283	0.08	2.22	stable
10	1.0	96	274	0.99	4	8.80	1.35E-05	2.65	2.53	7.59	0.047	-	-	0.287	0.09	2.21	stable
11	1.0	93	271	0.93	7	8.92	1.37E-05	2.16	2.43	6.00	0.050	-	-	0.272	0.14	2.22	stable
12	1.0	93	271	0.93	7	8.92	1.37E-05	2.12	2.44	5.92	0.050	-	-	0.273	0.14	2.24	stable
13	1.0	89	268	0.83	9	9.00	1.40E-05	1.72	2.48	4.96	0.051	-	-	0.275	0.18	2.28	stable
14	1.0	89	268	0.83	9	9.00	1.40E-05	1.74	2.5	5.03	0.050	-	-	0.277	0.18	2.29	stable
15	1.0	85	266	0.80	10	9.06	1.44E-05	1.13	2.43	3.53	0.054	-	-	0.269	0.19	2.29	stable
16	1.0	85	266	0.80	10	9.06	1.44E-05	1.18	2.45	3.62	0.053	-	-	0.270	0.19	2.29	stable
17	1.0	82	265	0.78	11	9.07	1.50E-05	-0.42	2.25	0.45	0.061	-	-	0.248	0.18	2.31	stable
18	1.0	82	265	0.78	11	9.07	1.50E-05	-0.40	2.31	0.45	0.059	-	-	0.255	0.19	2.39	stable
19	1.0	137	278	0.99	7	8.72	9.69E-06	1.55	2.24	5.22	0.038	-	-	0.252	0.18	2.08	stable
20	1.0	137	278	0.99	7	8.72	9.69E-06	1.42	2.15	5.30	0.039	-	-	0.246	0.18	2.02	stable
21	1.0	134	277	0.95	8	8.77	9.83E-06	1.38	2.16	5.12	0.040	-	-	0.246	0.20	2.04	stable
22	1.0	134	277	0.95	8	8.77	9.83E-06	1.38	2.18	5.13	0.040	-	-	0.248	0.20	2.05	stable
23	1.0	130	275	0.89	10	8.82	9.99E-06	1.21	2.20	4.59	0.040	-	-	0.249	0.25	2.09	stable
24	1.0	130	275	0.89	10	8.82	9.99E-06	1.23	2.24	4.72	0.039	-	-	0.254	0.25	2.13	stable

Table 4.1 Laminar aerosol flames investigated in the present work (continued).

No.	ϕ_{bu}	P (kPa)	T (K)	ϕ_b	D_{10} (μm)	ρ_b / ρ_b	ν (m^2/s)	L_b (mm)	S_s (m/s)	Ma_{sr}	δ (mm)	T_{el} (mm)	Pe_{el}	u_i (m/s)	D_{10}/δ_i	$S_{n,48}$ (m/s)	Remarks
25	1.0	128	273	0.85	12	8.86	1.01E-05	0.96	2.16	3.78	0.041	-	-	0.244	0.29	2.09	stable
26	1.0	128	273	0.85	12	8.86	1.01E-05	0.98	2.20	3.87	0.041	-	-	0.248	0.29	2.12	stable
27	1.0	122	272	0.78	14	8.90	1.05E-05	0.37	2.12	2.11	0.044	-	-	0.238	0.32	2.07	stable
28	1.0	122	272	0.78	14	8.90	1.05E-05	0.40	2.14	2.21	0.044	-	-	0.240	0.32	2.09	stable
29	1.0	117	270	0.74	15	8.86	1.08E-05									2.13	oscillating
30	1.0	117	270	0.74	15	8.97	1.08E-05									2.13	oscillating
31	1.0	112	269	0.71	16	8.98	1.12E-05										oscillating
32	1.0	112	269	0.71	16	8.98	1.12E-05										oscillating
33	1.0	108	266	0.64	17	9.09	1.13E-05										oscillating
34	1.0	108	266	0.64	17	9.09	1.13E-05										oscillating
35	1.0	185	281	0.92	5	8.65	7.33E-06	0.95	2.05	4.71	0.031	-	-	0.237	0.16	1.98	stable
36	1.0	185	281	0.92	5	8.65	7.33E-06	0.95	2.07	4.73	0.032	-	-	0.239	0.16	1.98	stable
37	1.0	180	280	0.86	7	8.68	7.46E-06	0.95	2.03	4.59	0.032	-	-	0.233	0.22	1.95	stable
38	1.0	180	280	0.86	7	8.68	7.46E-06	0.88	2.01	4.29	0.032	-	-	0.231	0.22	1.93	stable
39	1.0	176	278	0.82	9	8.74	7.57E-06	0.86	2.04	4.20	0.032	-	-	0.233	0.28	1.96	stable
40	1.0	176	278	0.82	9	8.74	7.57E-06	0.90	2.07	4.37	0.032	-	-	0.237	0.28	1.99	stable
41	1.0	172	277	0.78	10	8.76	7.72E-06	0.72	2.16	3.78	0.031	-	-	0.247	0.32	2.09	stable
42	1.0	172	277	0.78	10	8.76	7.72E-06	0.81	2.12	4.06	0.032	-	-	0.242	0.31	2.12	stable
43	1.0	169	276	0.75	12	8.80	7.74E-06	0.73	2.10	3.73	0.033	56.09	1726	0.238	0.37	2.03	accelerating
44	1.0	169	276	0.75	12	8.80	7.74E-06	0.77	2.07	3.84	0.033	-	-	0.236	0.37	2.01	stable
45	1.0	162	275	0.69	14	8.84	8.03E-06	0.74	2.13	3.67	0.033	49.47	1481	0.240	0.42	2.08	accelerating
46	1.0	162	275	0.69	14	8.84	8.03E-06	0.45	2.08	2.67	0.034	49.03	1439	0.236	0.41	2.04	accelerating
47	1.0	155	272	0.63	15	8.93	8.23E-06	-0.43	2.01	-0.13	0.037	38.04	1040	0.225	0.41	2.12	accelerating
48	1.0	155	272	0.63	15	8.93	8.23E-06	-0.07	2.05	0.95	0.036	46.57	1299	0.230	0.42	2.06	accelerating

Table 4.1 Laminar aerosol flames investigated in the present work (continued).

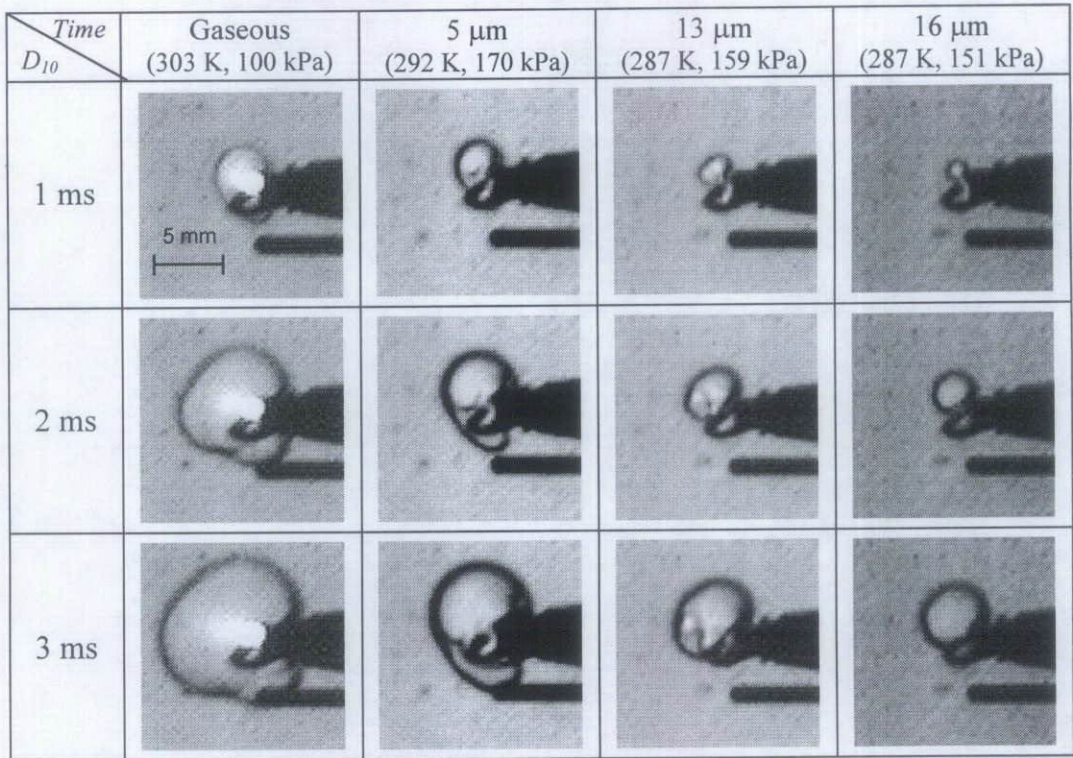
No.	ϕ_{ox}	P (kPa)	T (K)	ϕ_p	D_{10} (μm)	ρ_b / ρ_b	ν (m^2/s)	L_b (mm)	S_s (m/s)	Ma_{sr}	δ (mm)	r_{cl} (mm)	Pe_{cl}	u_i (m/s)	D_{10}/δ_i	$S_{10,46}$ (m/s)	Remarks
49	1.0	141	269	0.57	17	9.00	8.91E-06	-0.35	2.08	0.16	0.039	34.20	881	0.231	0.44	2.21	accelerating
50	1.0	141	269	0.57	17	9.00	8.91E-06	-0.85	1.98	-1.15	0.041	35.58	876	0.220	0.42	2.25	accelerating
51	1.0	134	267	0.54	18	9.06	9.19E-06	-1.41	1.95	-2.47	0.043	44.09	1030	0.215	0.42	2.22	accelerating
52	1.0	134	267	0.54	18	9.06	9.19E-06	-1.80	1.92	-4.49	0.044	40.39	929	0.211	0.41	2.07	accelerating
53	1.0	206	278	0.66	14	8.77	6.41E-06	0.96	1.61	4.32	0.035	45.1	1293	0.183	0.40	1.55	accelerating
54	1.0	206	278	0.66	14	8.77	6.41E-06	0.50	1.75	2.95	0.032	45.2	1407	0.199	0.44	1.74	accelerating
55	1.0	163	269	0.50	27	9.01	7.68E-06	-2.16	1.63	-4.50	0.042	40.6	963	0.181	0.64	2.33	accelerating
56	1.1	138	278	0.99	9	8.88	9.53E-06	1.32	2.54	5.62	0.033	-	-	0.286	0.27	2.40	stable
57	1.1	124	273	0.85	16	9.01	1.04E-05	1.15	2.69	4.83	0.035	39.7	1139	0.298	0.46	2.59	accelerating
58	1.1	121	272	0.82	17	9.03	1.05E-05	0.18	2.38	1.66	0.040	39.8	996	0.263	0.43	2.39	accelerating
59	1.1	118	271	0.80	18	9.07	1.07E-05	-0.17	2.47	0.70	0.039	36.6	932	0.272	0.46	2.54	accelerating
60	1.1	118	271	0.80	18	9.07	1.07E-05	-0.13	2.44	0.82	0.040	38.9	978	0.269	0.45	2.49	accelerating
61	1.1	116	271	0.77	19	9.09	1.09E-05	-0.55	2.41	-0.29	0.041	37.8	919	0.265	0.46	2.49	accelerating
62	1.1	111	269	0.72	21	9.14	1.12E-05									2.67	accelerating
63	1.1	102	264	0.59	23	9.30	1.18E-05									2.47	accelerating
64	1.1	95	263	0.60	26	9.30	1.26E-05									2.35	accelerating
65	1.1	169	278	0.80	13	8.89	7.79E-06	0.64	2.24	3.50	0.031	27.2	881	0.252	0.42	2.24	accelerating
66	1.1	169	278	0.80	13	8.89	7.79E-06	0.24	2.15	2.00	0.032	20.5	638	0.239	0.41	2.20	accelerating
67	1.1	165	277	0.77	14	8.92	7.94E-06	-0.22	2.07	0.43	0.034	18.9	553	0.232	0.41	2.24	accelerating
68	1.1	165	277	0.77	14	8.92	7.94E-06	-0.09	2.10	0.87	0.034	19.5	578	0.235	0.41	2.22	accelerating
69	1.1	241	287	0.95	4	8.55	5.81E-06	1.08	2.07	6.41	0.024	31.3	1304	0.242	0.17	2.03	accelerating
70	1.1	235	286	0.90	6	8.67	5.90E-06	0.94	2.00	5.41	0.026	27.1	1059	0.230	0.23	1.98	accelerating
71	1.1	230	284	0.86	8	8.72	5.98E-06	0.97	1.96	5.36	0.027	29.6	1113	0.225	0.30	1.93	accelerating
72	1.1	224	283	0.81	10	8.75	6.08E-06	0.82	2.00	4.67	0.027	28.2	1061	0.229	0.38	1.97	accelerating

Table 4.1 Laminar aerosol flames investigated in the present work (continued).

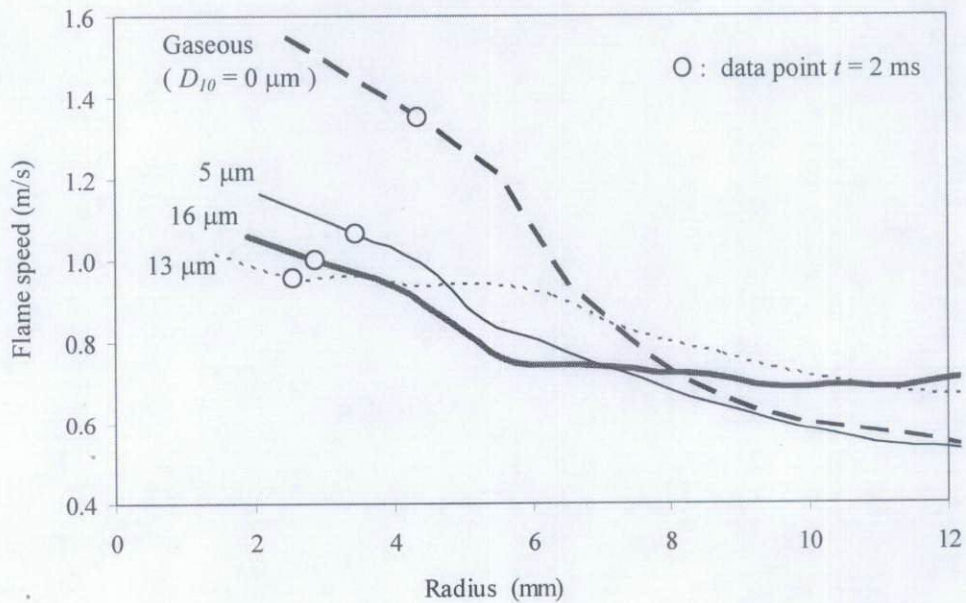
No.	ϕ_{sv}	P (kPa)	T (K)	ϕ_B	D_{10} (μm)	ρ_u / ρ_b	ν (m^2/s)	L_b (mm)	S_s (m/s)	Ma_{S_s}	δ_i (mm)	r_{cl} (mm)	Pe_{cl}	U_i (m/s)	D_{10}/δ_i	$S_{0.46}$ (m/s)	Remarks
73	1.1	209	279	0.70	16	8.87	6.37E-06	0.09	2.04	1.53	0.028	23.4	842	0.230	0.57	2.26	accelerating
74	1.1	209	279	0.70	16	8.87	6.37E-06	0.38	2.11	2.78	0.027	24.2	903	0.238	0.60	2.13	accelerating
75	1.1	209	279	0.70	16	8.87	6.37E-06	-0.21	1.97	0.36	0.029	18.7	650	0.222	0.56	2.27	accelerating
76	1.1	204	278	0.67	18	8.90	6.46E-06	-0.46	1.73	-0.38	0.033	17.9	537	0.194	0.55	1.94	accelerating
77	1.2	145	282	1.13	4	8.69	9.30E-06	1.33	2.64	6.15	0.031	-	-	0.303	0.13	2.50	stable
78	1.2	146	282	1.13	4	8.69	9.30E-06	1.10	2.62	5.28	0.030	41.9	1383	0.301	0.13	2.56	accelerating
79	1.2	143	281	1.09	8	8.75	9.42E-06	0.82	2.55	4.06	0.032	27.8	860	0.291	0.25	2.62	accelerating
80	1.2	139	279	1.04	10	8.77	9.57E-06	1.10	2.62	5.08	0.032	20.6	644	0.299	0.31	2.73	accelerating
81	1.2	135	278	1.00	12	8.81	9.71E-06	1.31	2.70	5.88	0.032	18.3	578	0.307	0.38	2.73	accelerating
82	1.2	132	276	0.96	15	8.86	9.83E-06	-	-	-	-	-	-	-	-	2.84	accelerating
83	1.2	124	275	0.88	19	8.90	1.04E-05	-	-	-	-	-	-	-	-	2.82	accelerating
84	1.2	119	272	0.82	21	9.00	1.06E-05	-	-	-	-	-	-	-	-	2.76	accelerating
85	1.2	112	271	0.77	24	9.01	1.12E-05	-	-	-	-	-	-	-	-	2.68	accelerating
86	1.2	102	265	0.60	25	9.20	1.19E-05	-	-	-	-	-	-	-	-	2.42	accelerating
87	1.2	95	264	0.61	26	9.23	1.26E-05	-	-	-	-	-	-	-	-	2.37	accelerating
88	1.2	191	283	0.96	6	8.68	7.12E-06	0.40	2.27	2.85	0.027	-	-	0.261	0.22	2.22	stable
89	1.2	186	282	0.95	8	8.70	7.25E-06	1.19	2.43	6.45	0.026	-	-	0.279	0.31	2.32	stable
90	1.2	186	282	0.95	8	8.70	7.25E-06	1.20	2.41	6.45	0.026	-	-	0.277	0.30	2.30	stable
91	1.2	186	282	0.95	8	8.70	7.25E-06	1.25	2.42	6.67	0.026	-	-	0.278	0.31	2.31	stable
92	1.2	174	280	0.92	14	8.75	7.67E-06	1.22	2.51	6.40	0.027	38.4	1440	0.287	0.52	2.45	accelerating
93	1.2	170	279	0.87	16	8.77	7.81E-06	-0.12	2.21	0.73	0.031	17.7	571	0.252	0.52	2.40	accelerating
94	1.2	235	286	0.89	8	8.69	5.87E-06	0.68	2.19	3.50	0.023	19.5	839	0.252	0.34	2.22	accelerating
95	1.2	224	282	0.79	14	8.78	6.04E-06	-	-	-	-	-	-	-	-	2.33	accelerating

Table 4.1 Laminar aerosol flames investigated in the present work (continued).

No.	ϕ_{ov}	P (kPa)	T (K)	ϕ_g	D_{10} (μm)	ρ_u / ρ_b	ν (m^2/s)	L_b (mm)	S_s (m/s)	Ma_{Sr}	δ (mm)	r_d (mm)	Pe_d	u_j (m/s)	D_{10}/δ	$S_{H,48}$ (m/s)	Remarks
96	1.4	146	282	1.22	8	8.43	9.26E-06									2.64	accelerating
97	1.4	139	280	1.13	13	8.47	9.58E-06									2.77	accelerating
98	1.4	133	278	1.06	17	8.54	9.90E-06									2.83	accelerating
99	1.4	125	275	0.94	22	8.59	1.04E-05									2.61	accelerating
100	1.4	112	272	0.86	25	8.62	1.15E-05									2.32	accelerating
101	1.4	103	267	0.70	26	8.80	1.20E-05									2.02	accelerating
102	1.4	95	265	0.68	26	8.93	1.26E-05									2.01	accelerating
103	1.4	197	286	1.14	8	8.34	6.99E-06									2.59	accelerating
104	1.6	153	286	1.43	9	8.29	8.46E-06									2.09	accelerating
105	1.6	146	284	1.32	14	8.09	9.33E-06									2.38	accelerating
106	1.6	139	282	1.20	20	8.16	9.59E-06									2.54	accelerating
107	1.6	125	277	1.07	25	8.30	1.03E-05									2.37	accelerating
108	1.6	112	273	0.93	31	8.41	1.12E-05									1.97	accelerating
109	1.8	156	287	1.45	10	7.77	8.65E-06									1.40	slow flame
110	1.8	139	283	1.30	22	7.87	9.56E-06									1.94	slow flame
111	1.8	125	279	1.16	27	7.95	1.03E-05									1.77	slow flame
112	1.8	112	274	0.99	28	8.07	1.12E-05									1.58	slow flame
113	1.8	101	270	0.86	29	8.19	1.19E-05									1.40	slow flame
114	2.0	170	282	1.73	5	7.34	8.25E-06									0.62	slow flame
115	2.0	159	288	1.52	13	7.41	8.68E-06									1.06	slow flame
116	2.0	151	287	1.50	16	7.47	8.97E-06									1.26	slow flame
117	2.0	142	284	1.38	24	7.52	9.45E-06									1.42	slow flame
118	2.0	127	280	1.26	26	7.63	1.02E-05									1.45	slow flame



(a)



(b)

Figure 4.1 Effect of droplets on ignition and initial kernel growth. A gaseous flame and several aerosol flames with different droplet diameters are shown for iso-octane-air at $\phi_{ov} = 2.0$, (a) schlieren images for up to 3 ms after ignition, (b) variation of flame speed with radius. The circles indicate the flame radius at 2 ms after ignition.

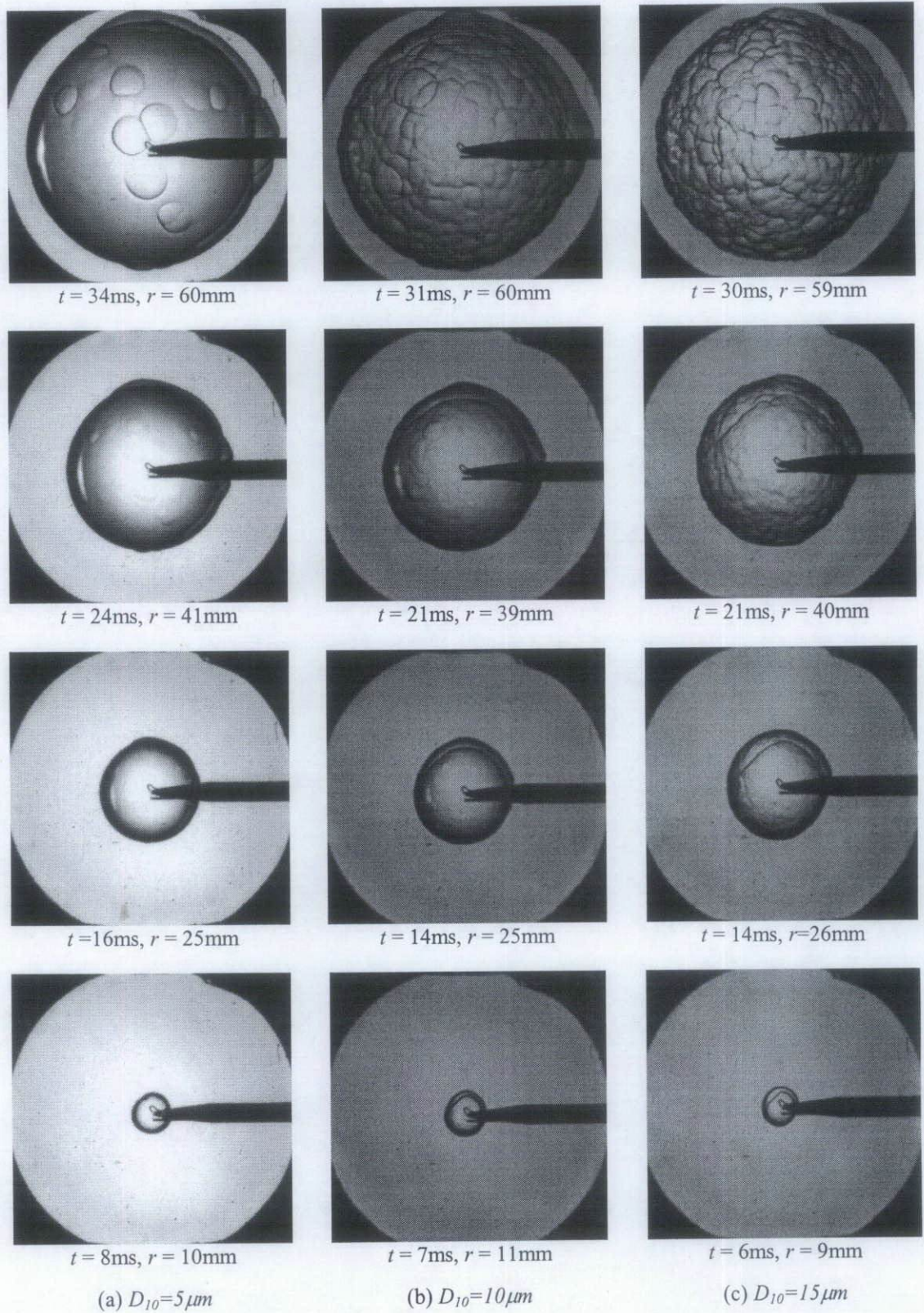


Figure 4.2 Sequences of schlieren images of flames within aerosols at $\phi_{ov} = 1.0$, and (a) $P = 185$ kPa, $T = 281$ K, and $\phi_g = 0.92$, (b) $P = 172$ kPa, $T = 278$ K, and $\phi_g = 0.78$, and (c) $P = 155$ kPa, $T = 272$ K, and $\phi_g = 0.63$.

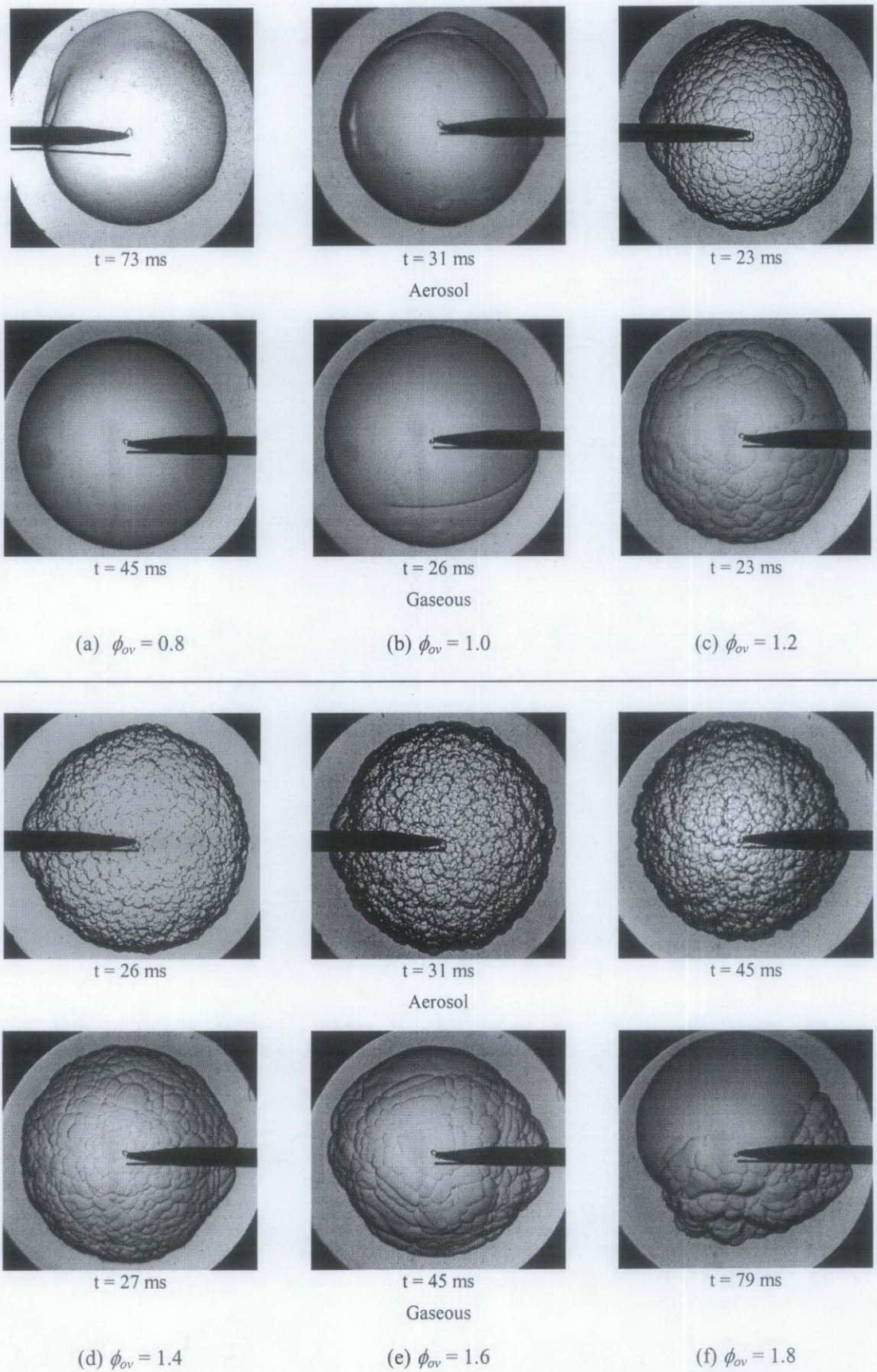


Figure 4.3 Comparison, at various ϕ_{ov} , between schlieren images of flames for iso-octane-air aerosols at $D_{10} = 8 \mu\text{m}$ and pressures and temperatures between 122 and 170 kPa, and 271 and 292 K respectively, and for the equivalent gaseous flames at $P = 100 \text{ kPa}$, $T = 303 \text{ K}$; $r \approx 50 \text{ mm}$.

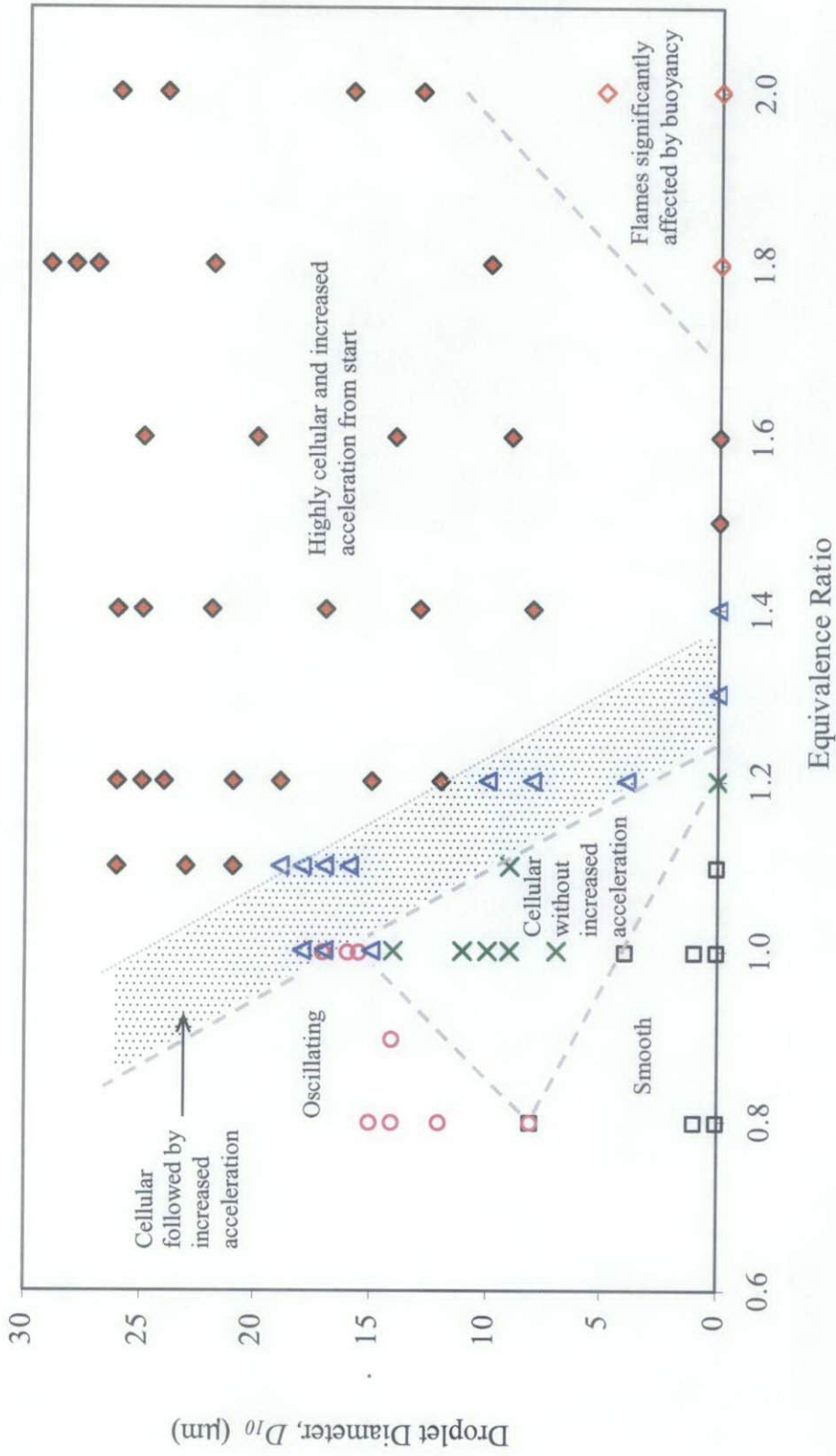


Figure 4.4 Map of flame regimes for iso-octane-air mixtures at various ϕ_{ov} , D_{10} , pressures between 90 and 150 kPa, and temperatures between 260 and 303 K.

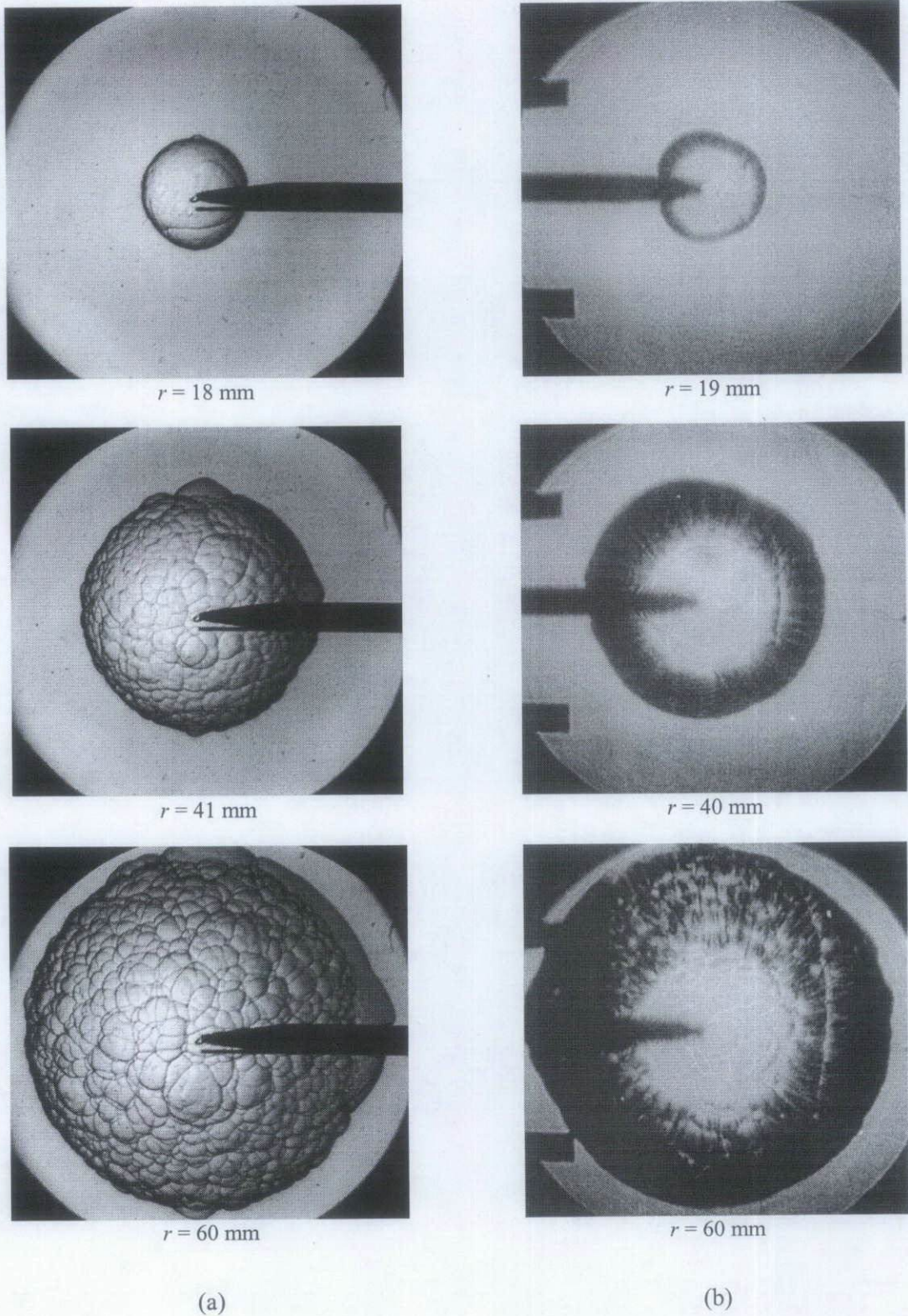


Figure 4.5 Comparison of observed flame structures of iso-octane-air aerosol at $\phi_{ov} = 1.2$ obtained by different imaging recording systems; (a) with digital camera, at $P = 139$ kPa, $T = 279$ K, $D_{10} = 10$ μm , and (b) with drum camera (Atzler, 1999) $P = 137$ kPa, $T = 278$ K, $D_{32} = 10$ μm .

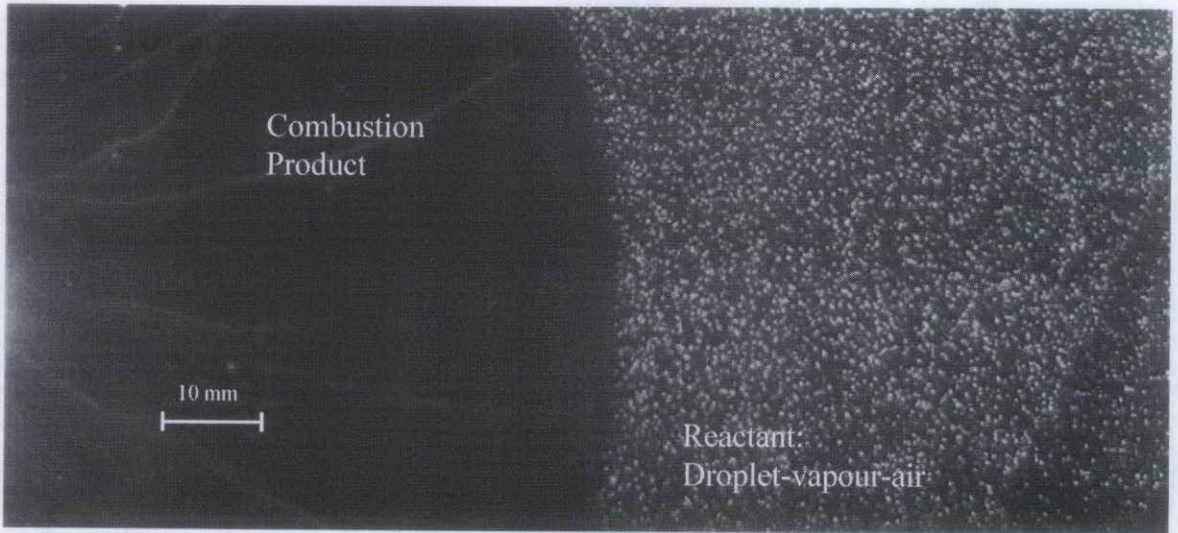


Figure 4.6 Typical laser sheet image of iso-octane aerosol droplet flame at $\phi_{ov} = 0.8$, $D_{10} = 12 \mu\text{m}$, $P = 110 \text{ kPa}$, $T = 265 \text{ K}$, $r \approx 69 \text{ mm}$.

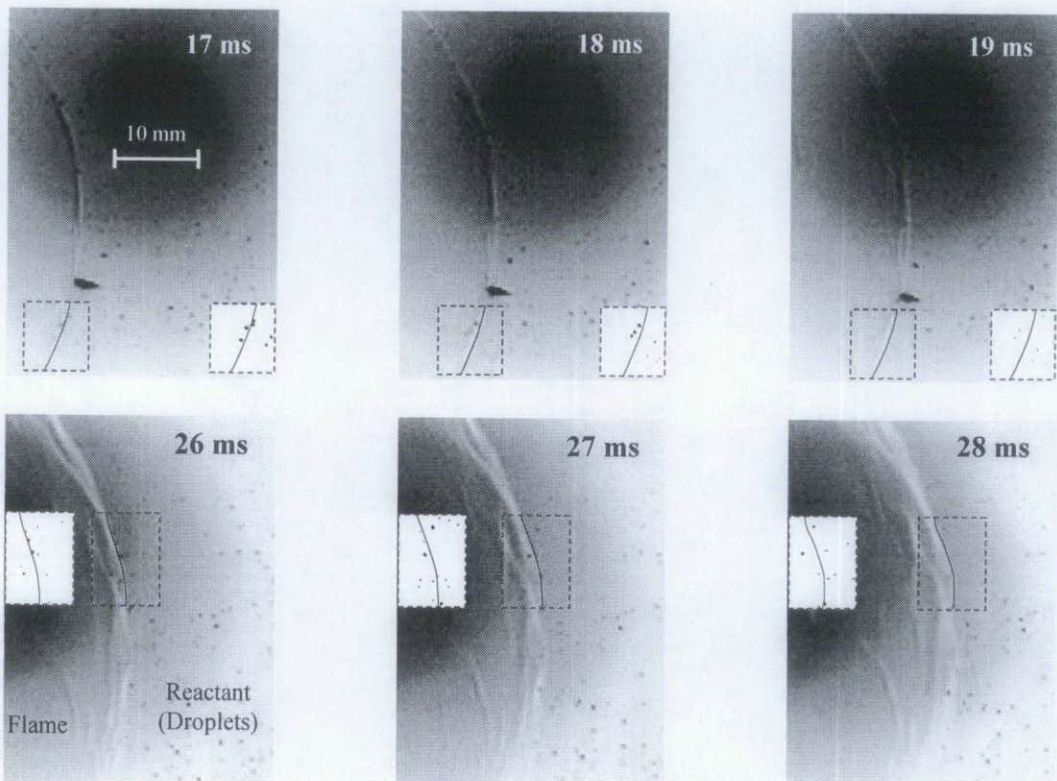


Figure 4.7 Sequences of simultaneous laser sheet and schlieren images for iso-octane-air aerosol at $\phi_{ov} = 1.0$, $P = 162 \text{ kPa}$, $T = 277 \text{ K}$, $D_{10} = 17 \mu\text{m}$.

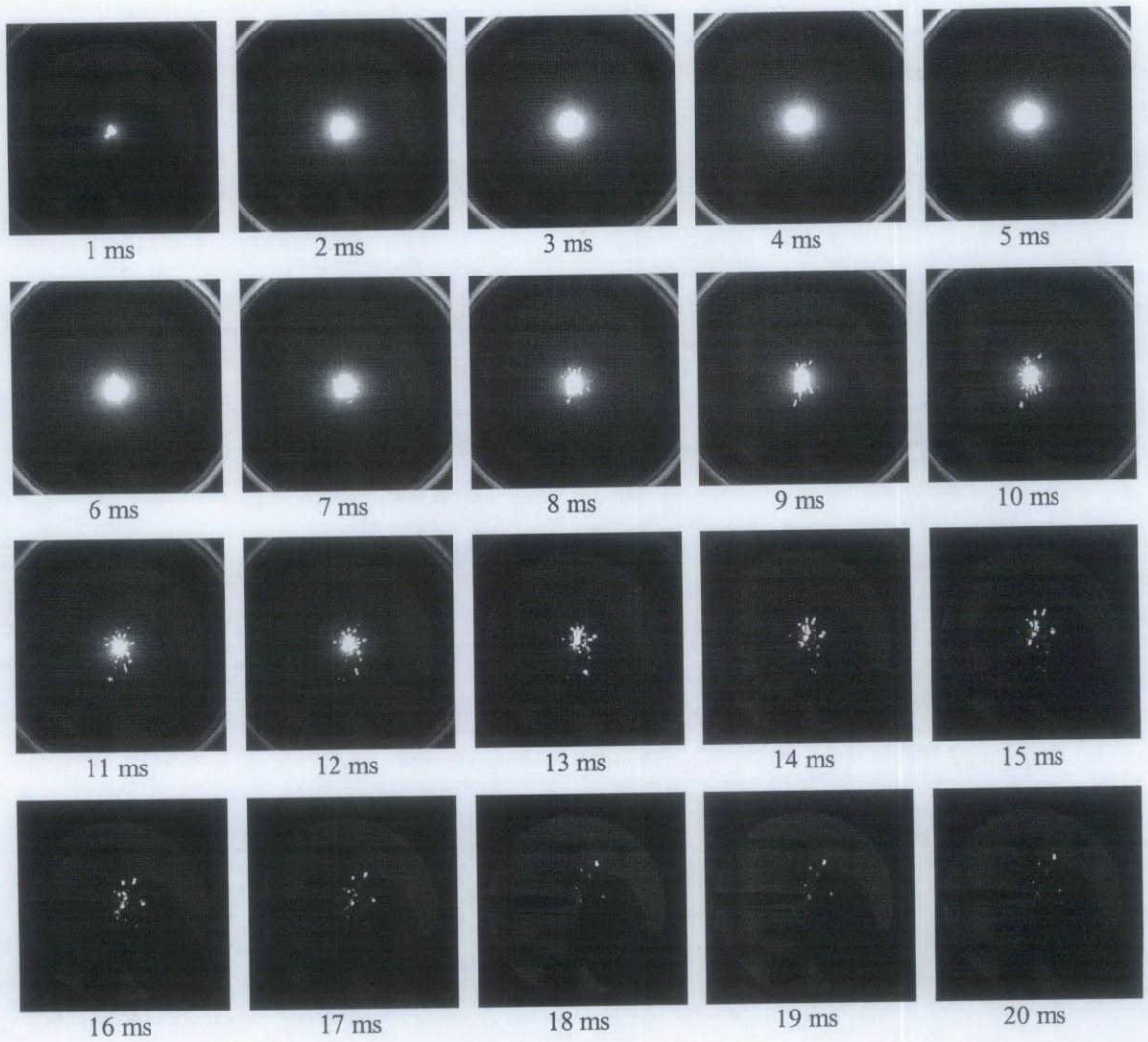


Figure 4.8 Natural light imaging of electric spark (Section 2.1.3.1) in air at $P = 100$ kPa and $T = 303$ K.

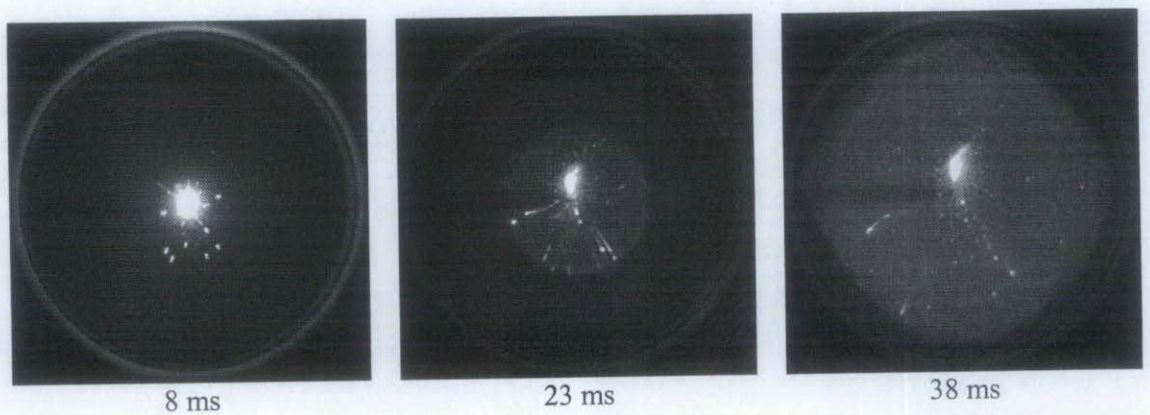
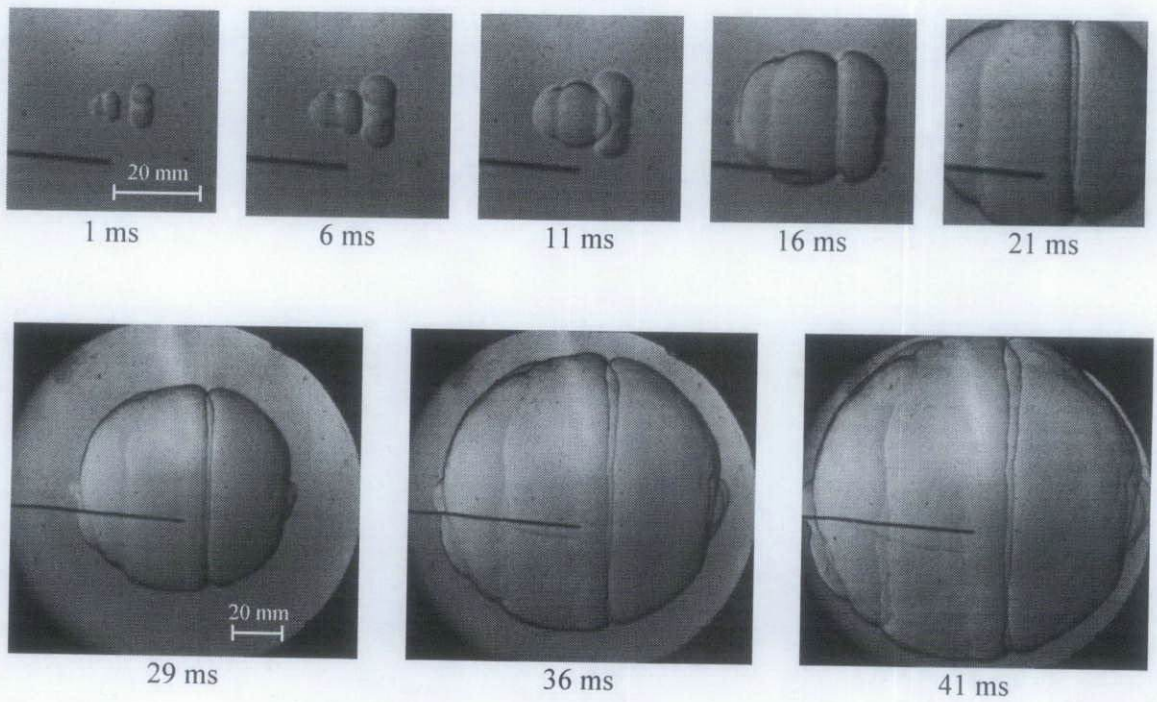
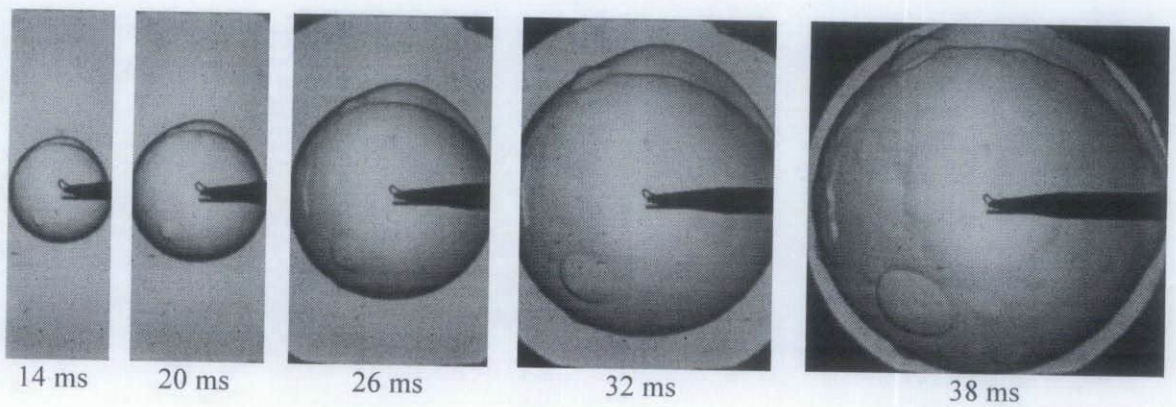


Figure 4.9 Natural imaging of laminar flames for aerosol at $\phi_{ov} = 1.2$, $P = 112$ kPa, $T = 271$ K and $D_{10} = 24$ μm .



(a) kernel development following laser ignition.



(b) kernel development following electric discharge spark ignition.

Figure 4.10 Schlieren images of laminar flames for aerosol at $\phi_{ov} = 1.0$, $P = 89$ kPa and $T = 268$ K; (a) with laser ignition, and (b) with electric discharge spark ignition.

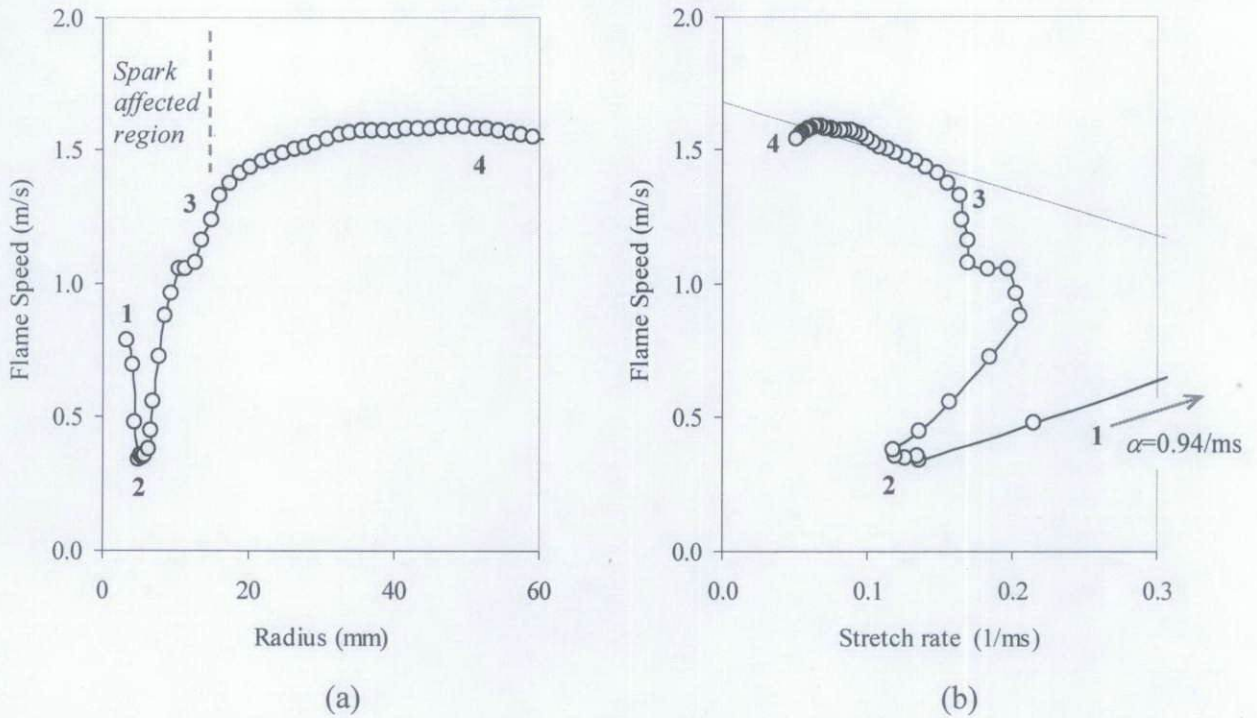


Figure 4.11 Variation of flame speed with (a) radius and (b) stretch rate, for gaseous iso-octane-air at $\phi_{ov} = 0.8$, $P = 100$ kPa, and $T = 303$ K.

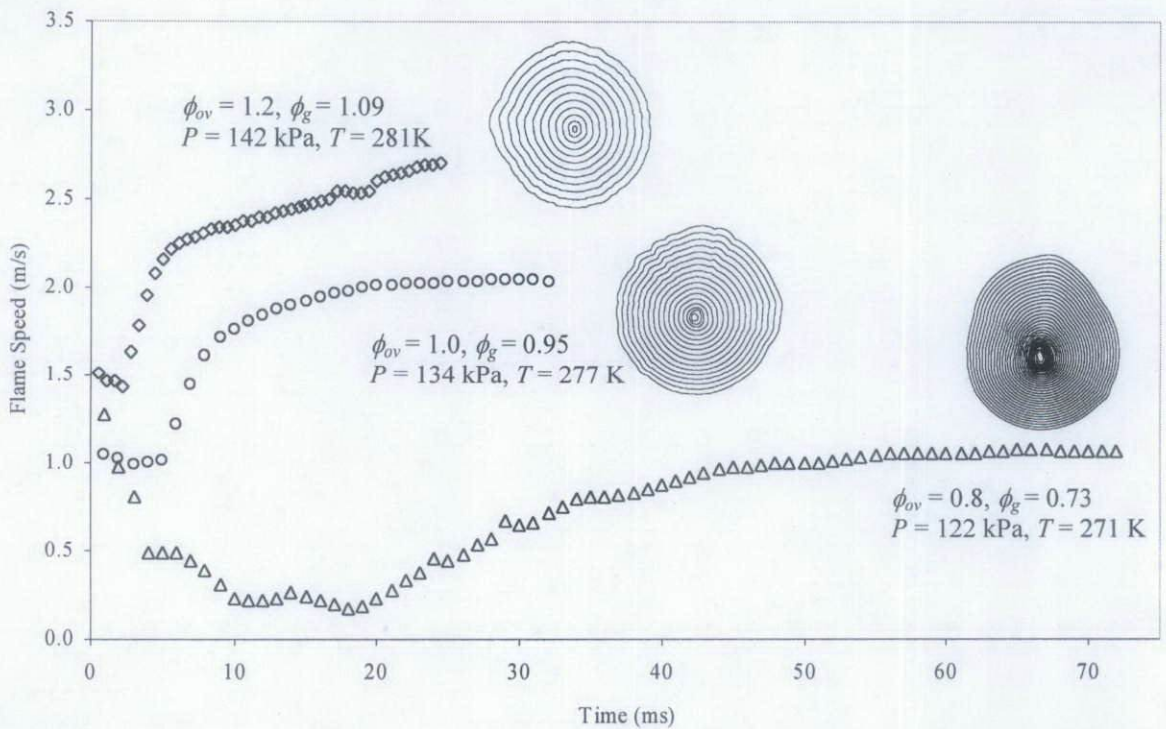


Figure 4.12 Variation of flame speed with time after ignition for aerosols at $D_{10} = 8$ μm , and $\phi_{ov} = 0.8$ (triangles), $\phi_{ov} = 1.0$ (circles), and $\phi_{ov} = 1.2$ (diamonds). Also shown for each case are flame contour tracings throughout propagation at intervals of 2 ms.

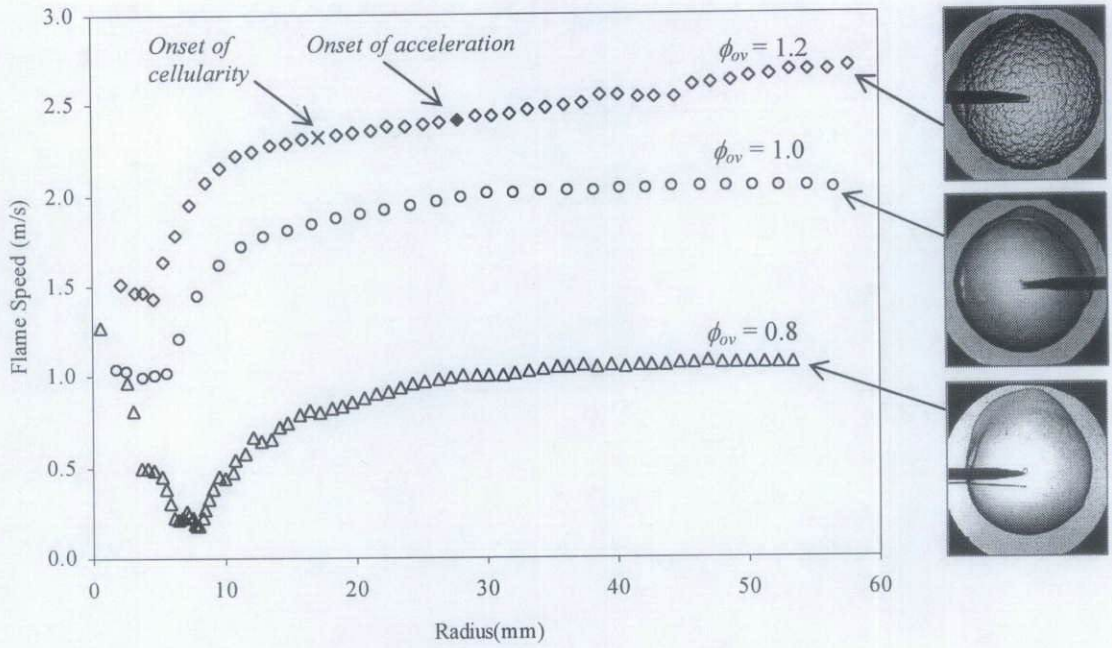


Figure 4.13 Variation of flame speed with radius for the aerosol flames in Fig. 4.12. Also shown for each case are the last flame images within the field of view of the access windows.

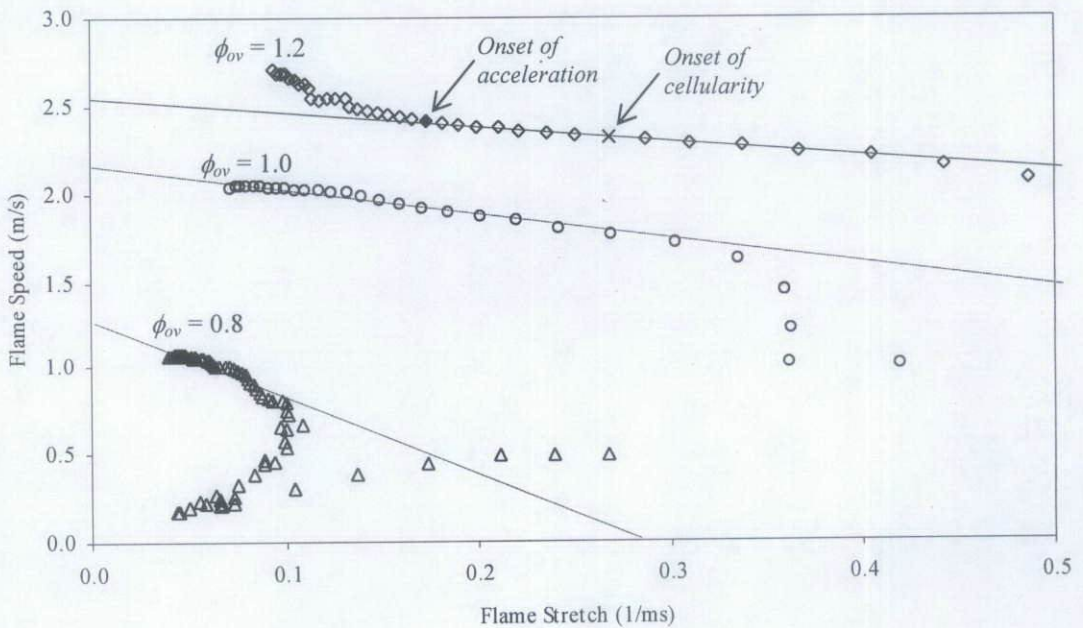


Figure 4.14 Variation of flame speed with stretch for the aerosol flames in Fig. 4.12.

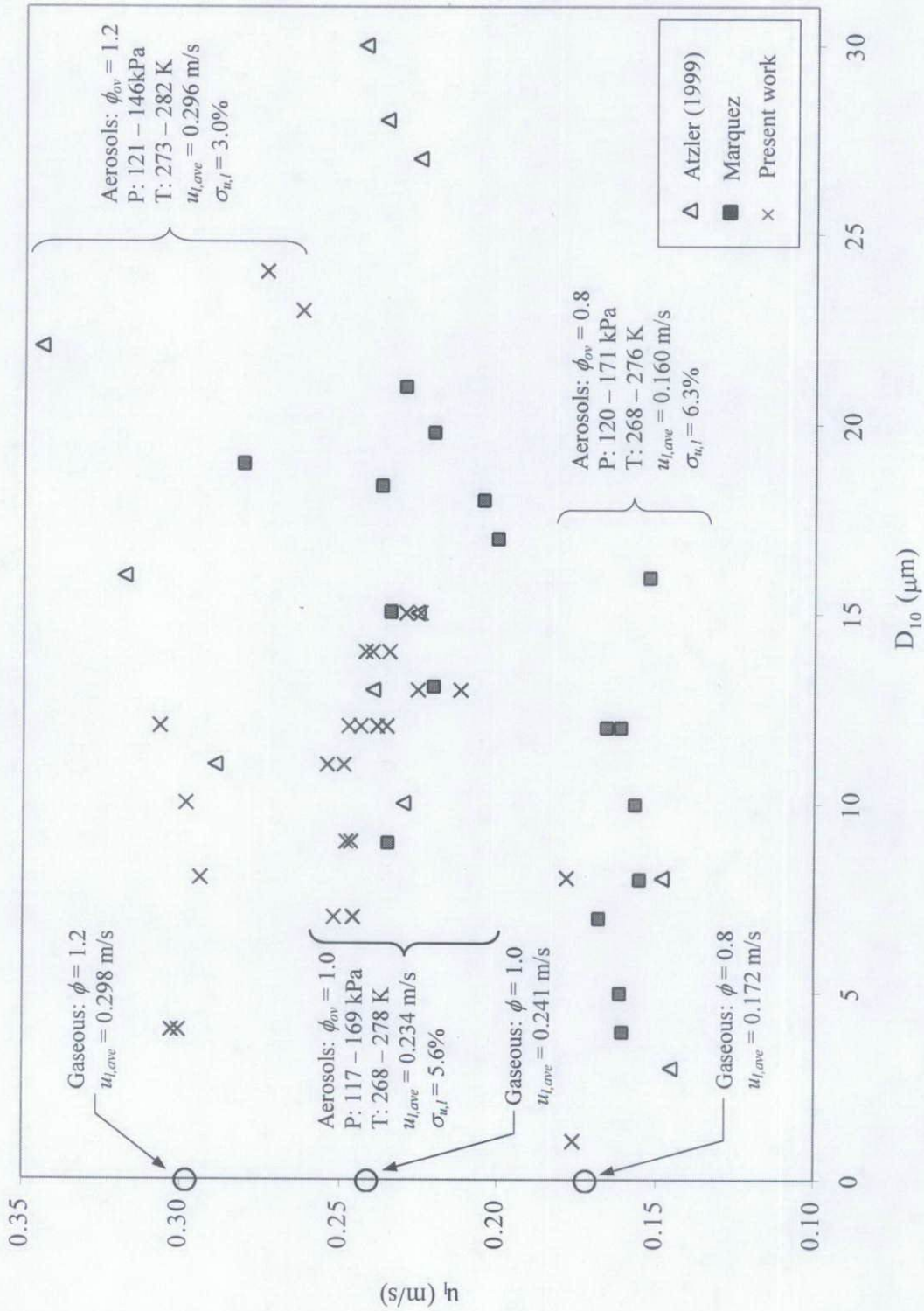


Figure 4.15 Variation of u_l with D_{10} for iso-octane-air aerosol flames at various ϕ_{ov} .

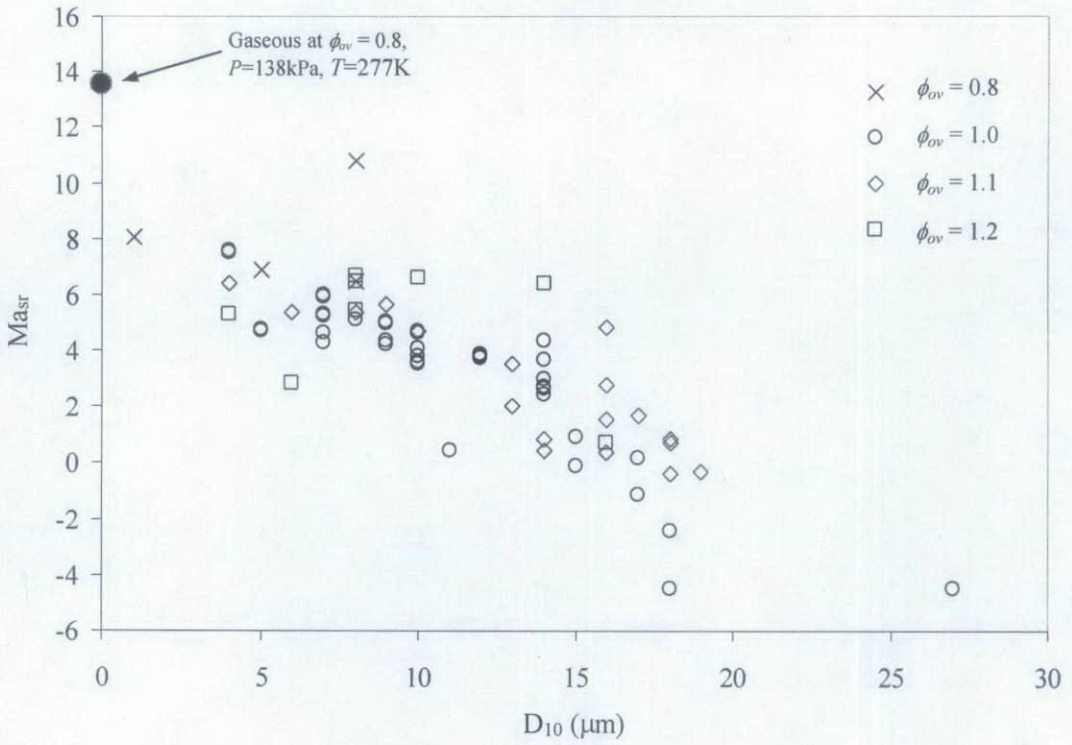


Figure 4.16 Variation of Ma_{sr} with D_{10} for iso-octane-air aerosol flames at pressures of between 82 and 241 kPa, temperatures of between 265 and 287 K, and various equivalence ratios.

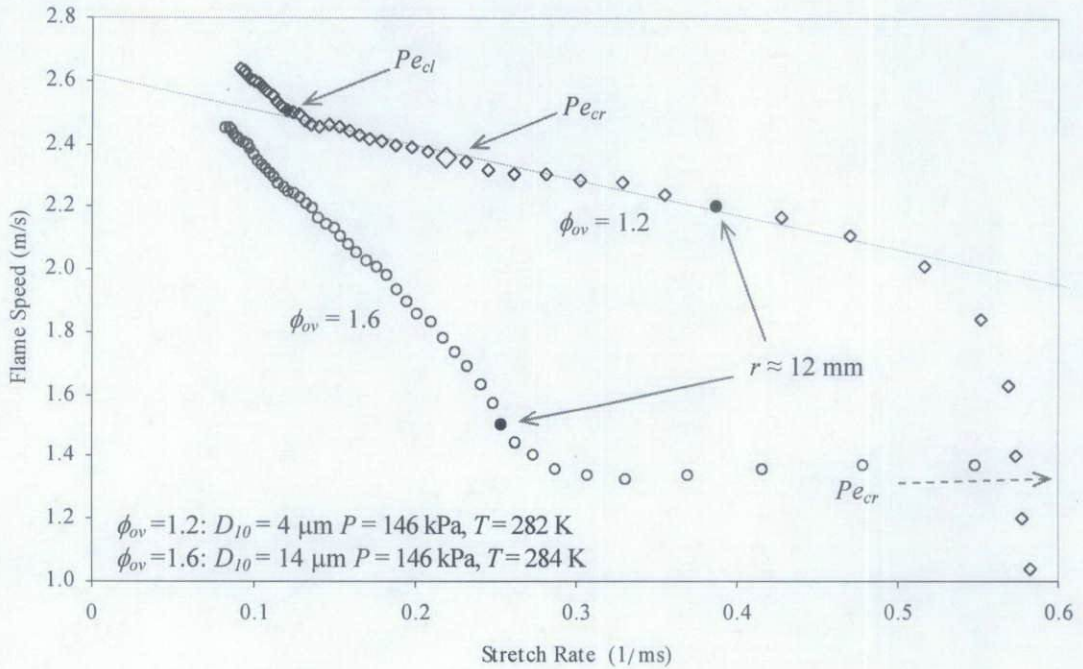


Figure 4.17 Typical variation of flame speed with stretch rate for rich iso-octane-air aerosols; crosses are for $\phi_{ov} = 1.2$ and $D_{10} = 4 \mu m$, and circles are for $\phi_{ov} = 1.6$ and $D_{10} = 14 \mu m$.

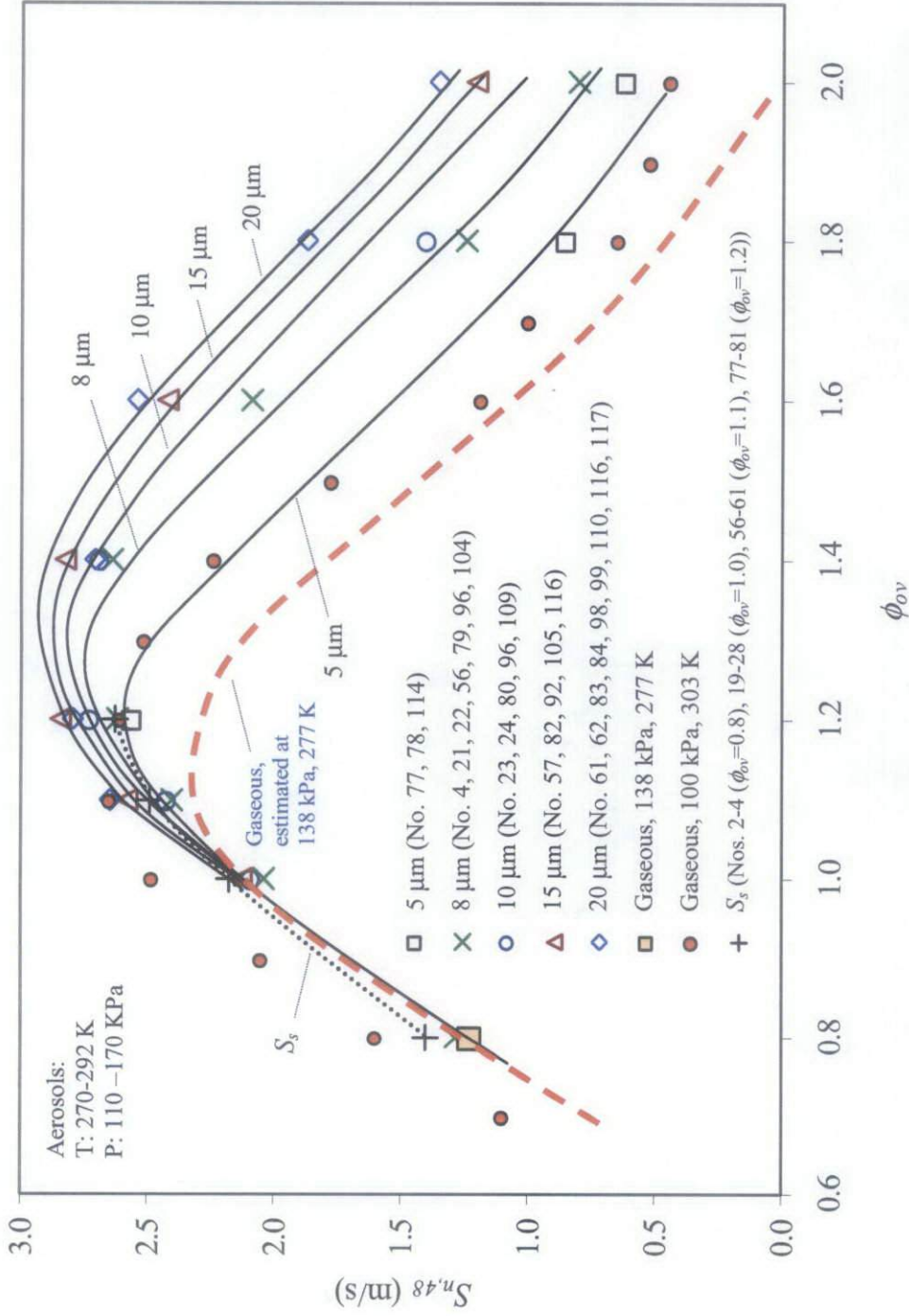


Figure 4.18 Variation of $S_{n,48}$ with ϕ_{ov} and D_{10} for iso-octane-air mixtures. Also shown are values of S_s when measurements are permissible. The numbers in the parenthesis represent the data from which the average of shown values are obtained. Full details of operating conditions for each data point are given in Table 4.1.

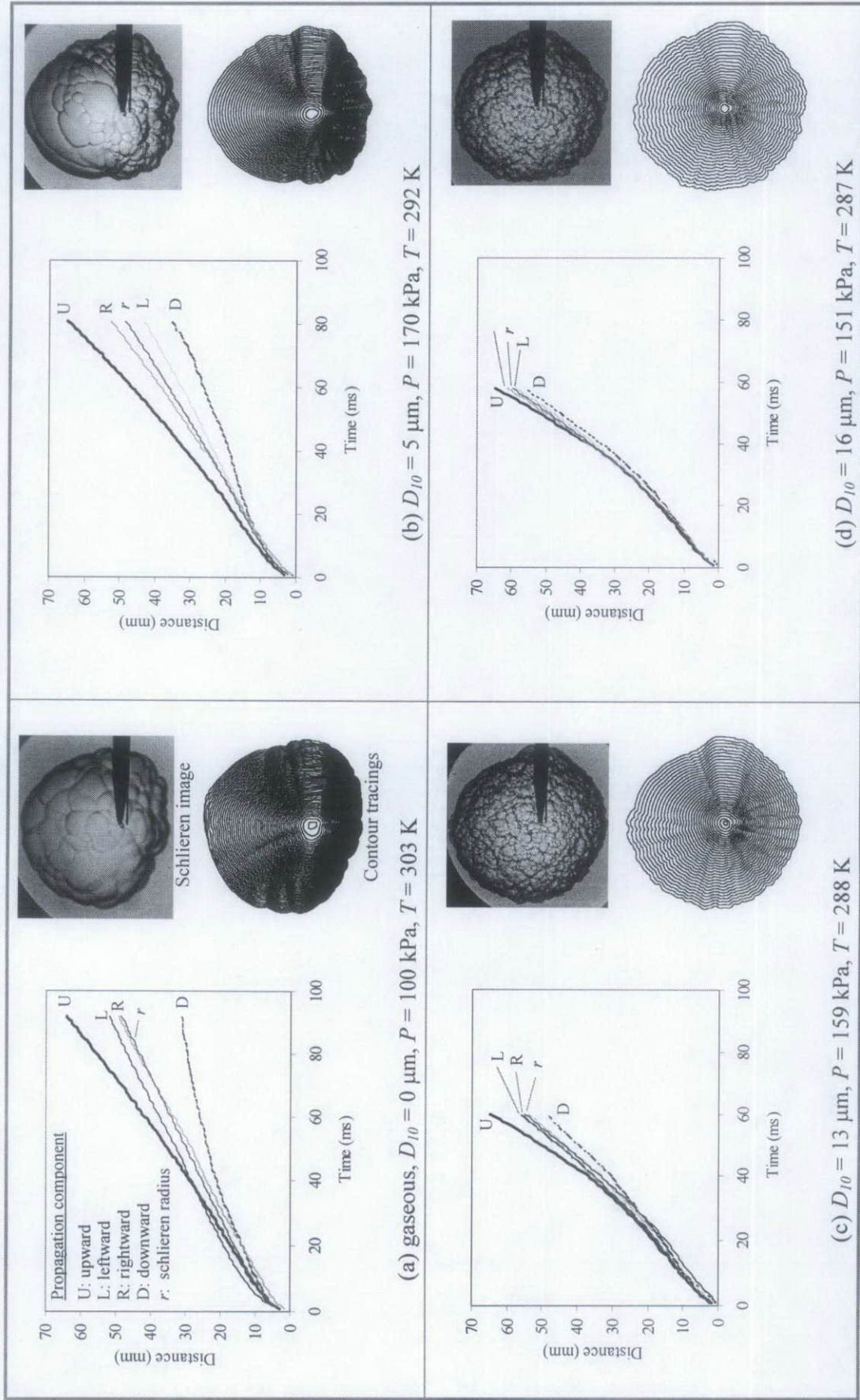


Figure 4.19 Flame propagation distance from spark electrode as a function of time from start of ignition for iso-octane-air mixtures at $\phi_{ov} = 2.0$; (a) gaseous and (b to d) aerosol.

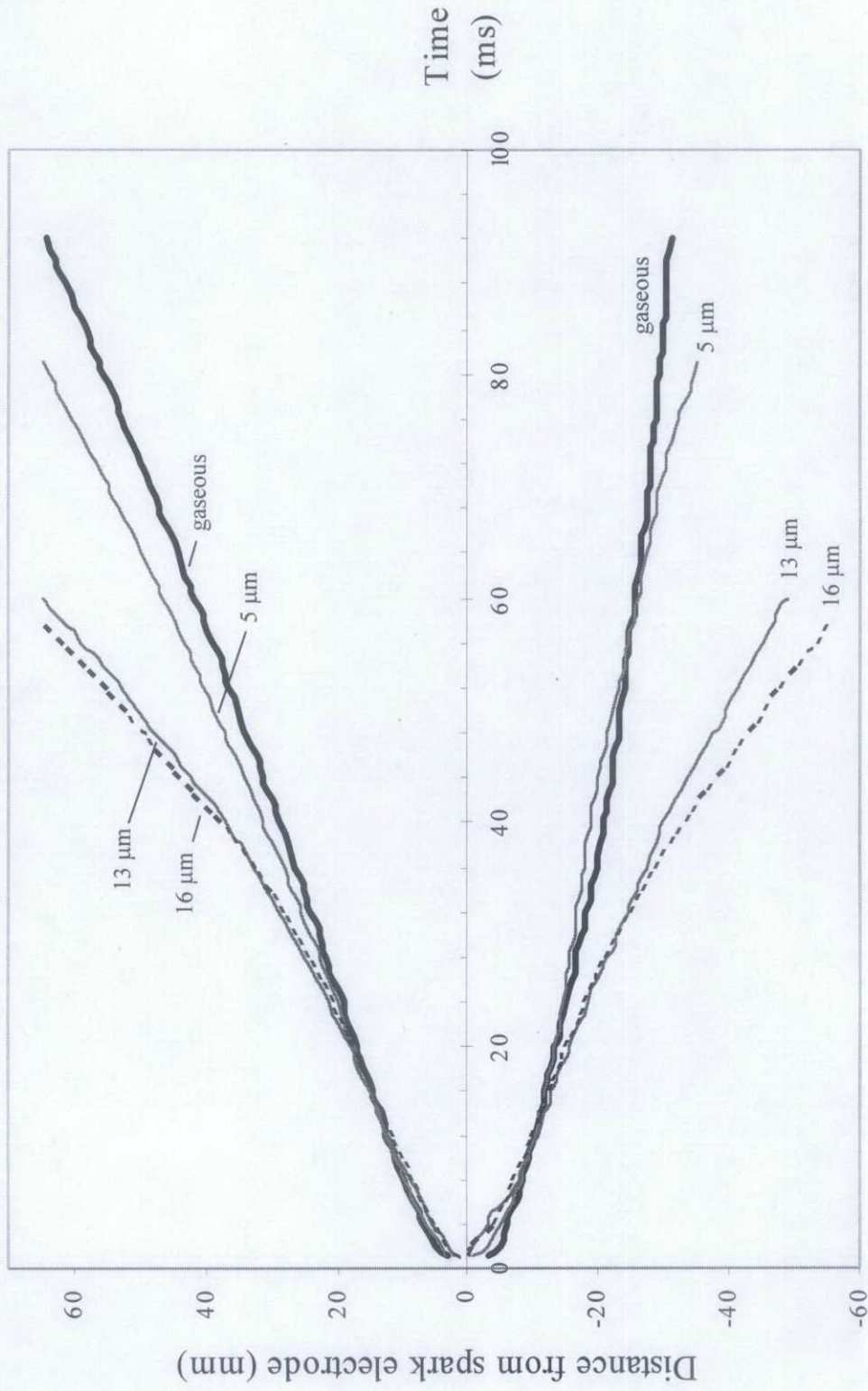


Figure 4.20 Comparison of vertical flame propagation distance from spark electrode as a function of time for iso-octane-air gaseous and aerosol at $\phi_{ov} = 2.0$. Negative distances indicate downward flame propagation.

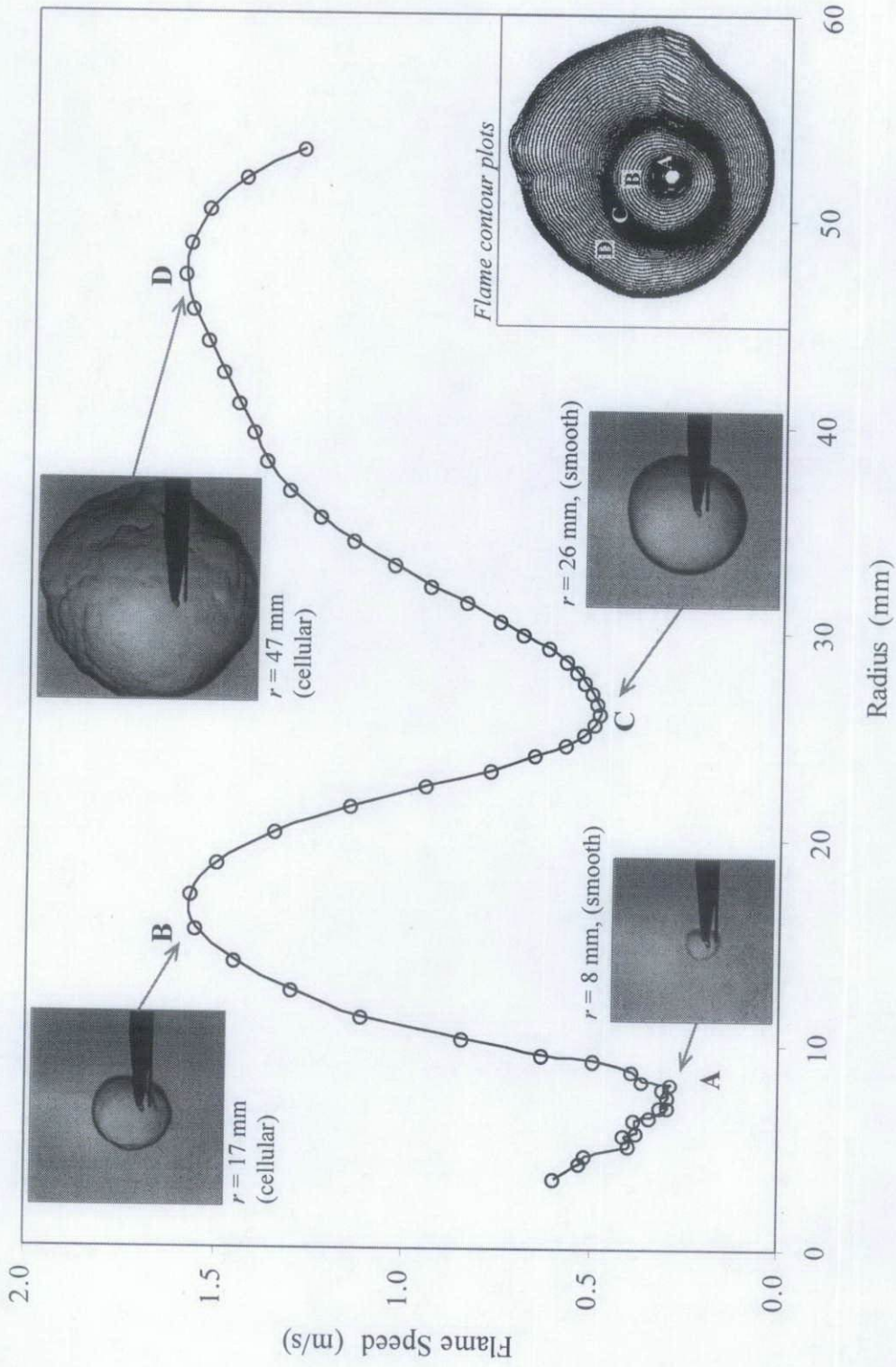


Figure 4.21 Typical variation of flame speed with radius for an oscillating flame of iso-octane-air aerosol at $\phi_{ov} = 0.8$, $D_{10} = 12 \mu\text{m}$, $P = 110 \text{ kPa}$, $T = 265 \text{ K}$. Also shown are the corresponding schlieren images and superimposition of flame edges throughout propagation.

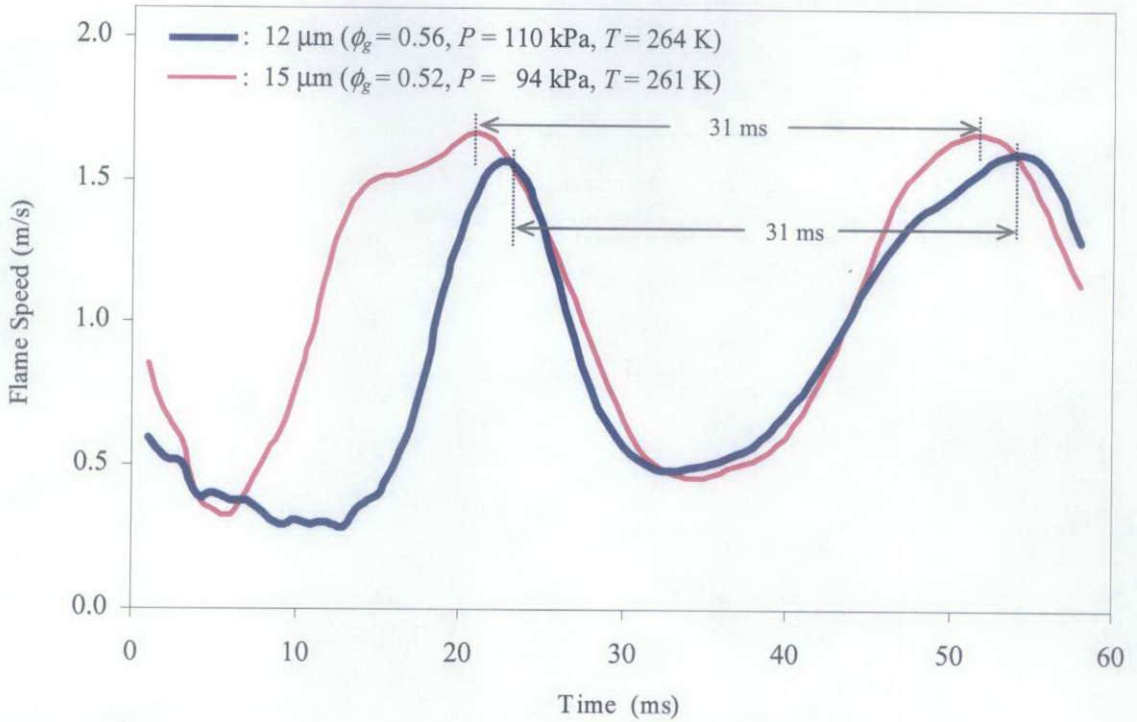


Figure 4.22 Variation of flame speed with radius for iso-octane-air aerosol at $\phi_{ov} = 0.8$ and D_{10} of 12 and 15 μm .

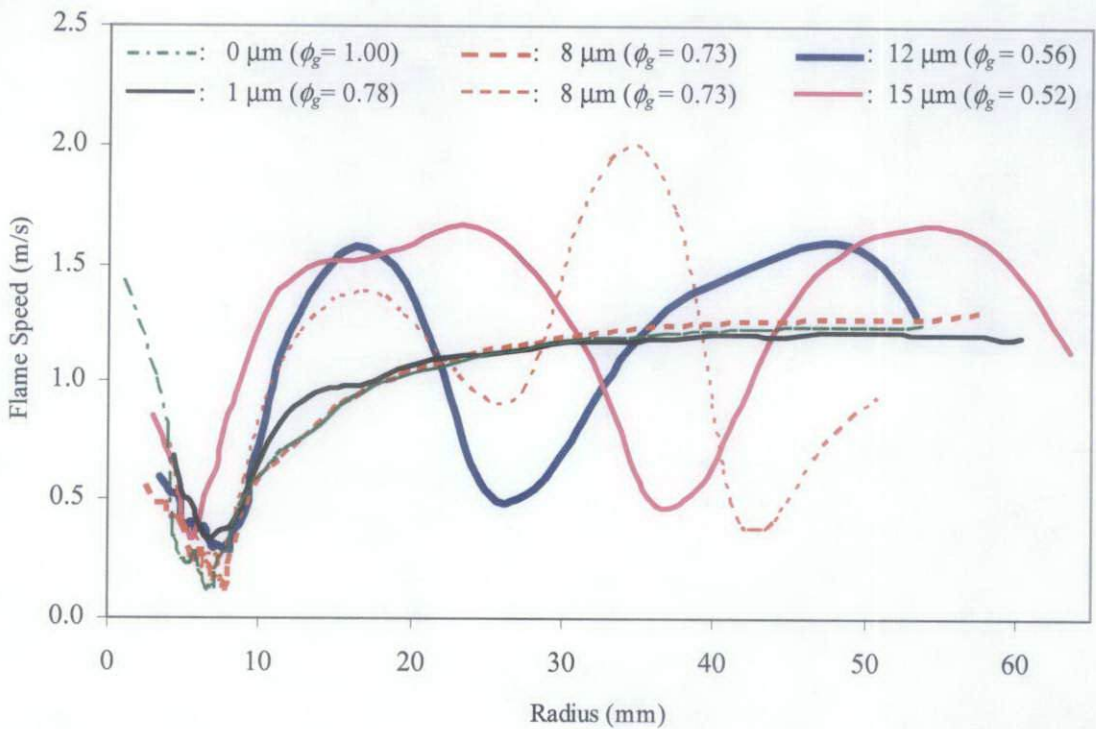


Figure 4.23 Variation of flame speed with radius for iso-octane-air aerosol at $\phi_{ov} = 0.8$ at D_{10} between 0 and 15 μm , pressures between 94 and 138 kPa, and temperatures between 261 and 277 K.

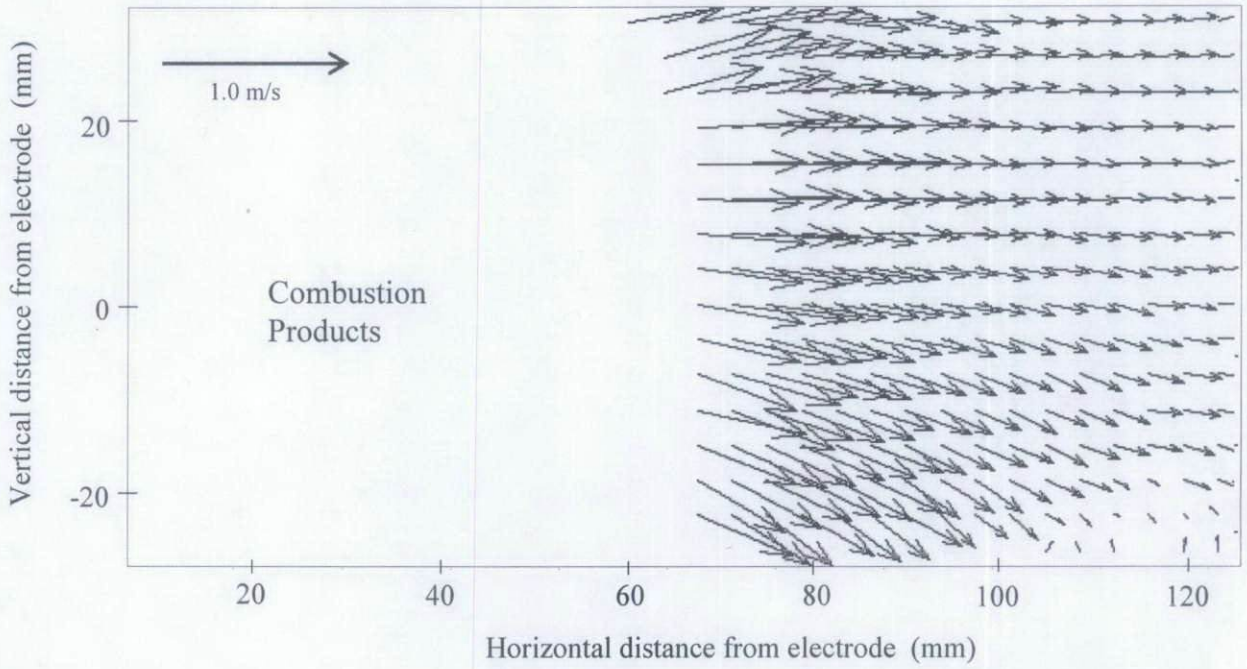


Figure 4.24 Typical velocity vectors obtained from PIV analysis of laser sheet images of droplets between 44 ms and 45 ms after ignition, for an oscillating flame of iso-octane-air aerosol at $D_{10} = 12 \mu\text{m}$, $P = 110 \text{ kPa}$ and $T = 264 \text{ K}$.

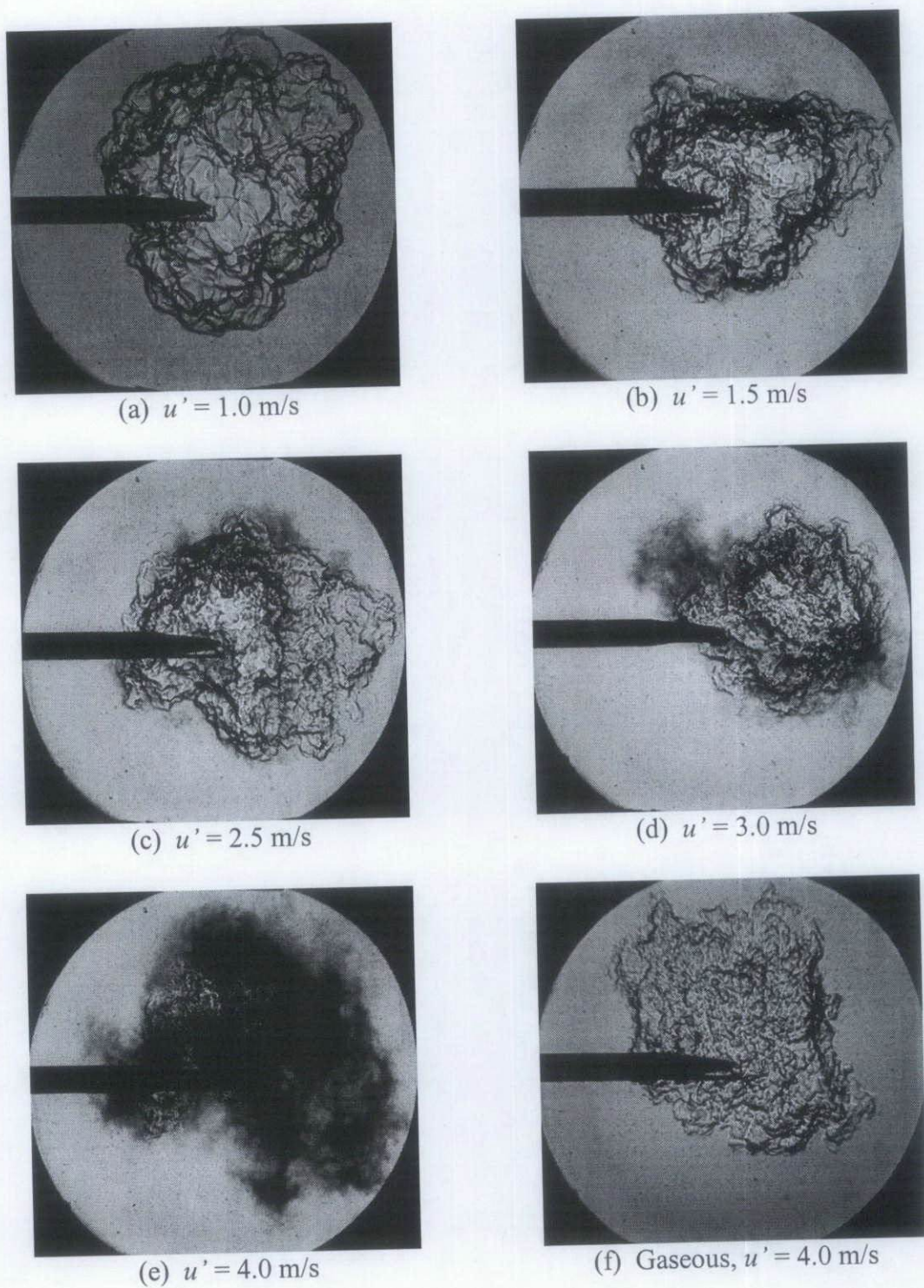


Figure 4.25 Schlieren images of turbulent flames in stoichiometric iso-octane-air using the same spark electrode and energy for, (a) to (e) aerosols at $P = 128$ kPa, $T = 283$ K, $D_{10} = 4$ μm , $\phi_g = 0.85$ and u' as shown, and (f) gas at $u' = 4.0$ m/s, $P = 100$ kPa, $T = 303$ K.

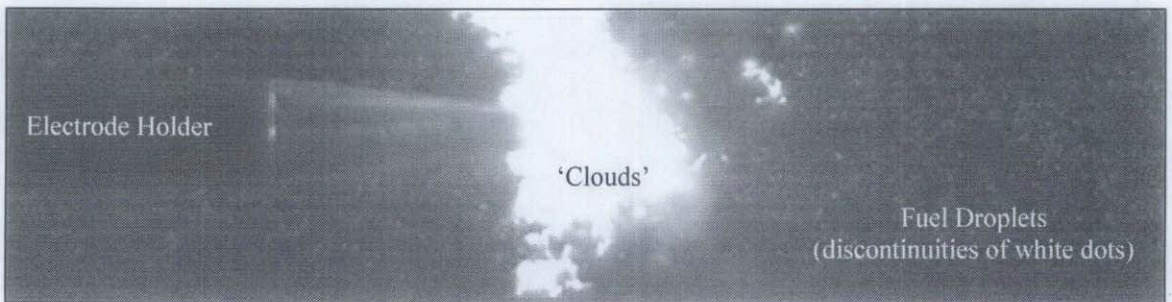
(a) $u' = 1.0$ m/s, $t = 16$ ms(b) $u' = 4.0$ m/s, $t = 5$ ms

Figure 4.26 Laser sheet images of flames of turbulent stoichiometric iso-octane-air mixtures at $P = 128$ kPa, $T = 283$ K, and (a) $u' = 1.0$ m/s and (b) $u' = 4.0$ m/s.

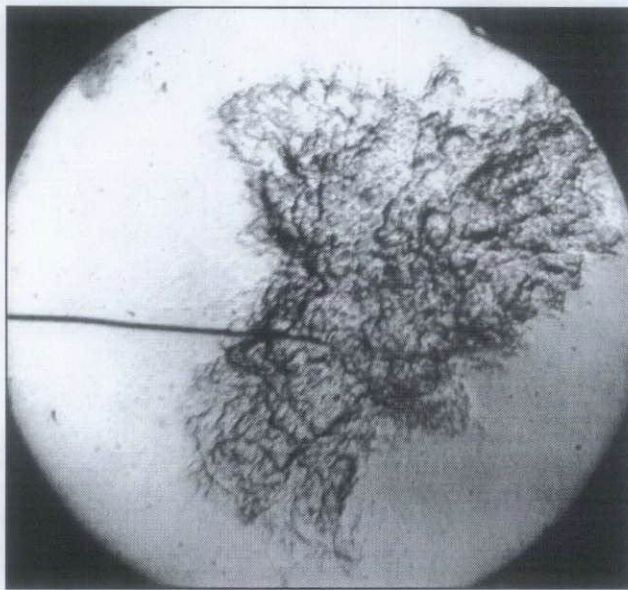


Figure 4.27 Schlieren image of turbulent flames with laser ignition for stoichiometric iso-octane-air aerosol at same conditions with that in Fig. 4.25(e).

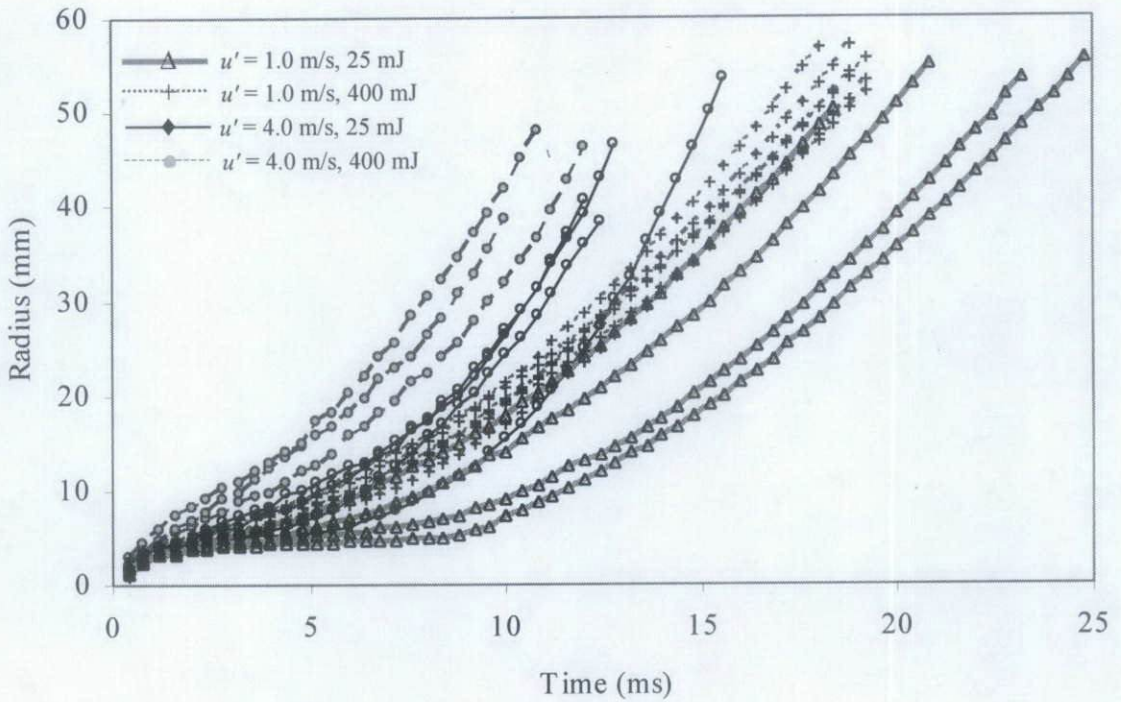


Figure 4.28 Flame radius against time for turbulent gaseous mixtures of stoichiometric iso-octane-air ignited using different ignition energies at $P = 100$ kPa, $T = 303$ K and u' of 1.0 and 4.0 m/s.

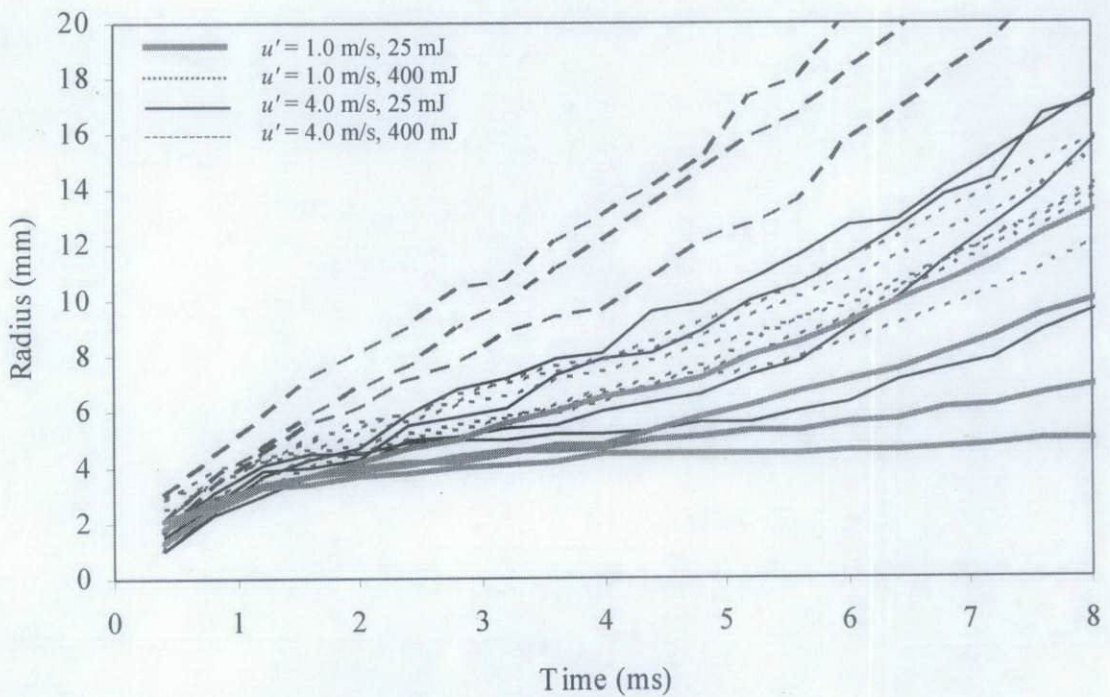


Figure 4.29 Magnification of the initial stage of the graph in Fig. 4.28. For clarity, the symbols have been removed.

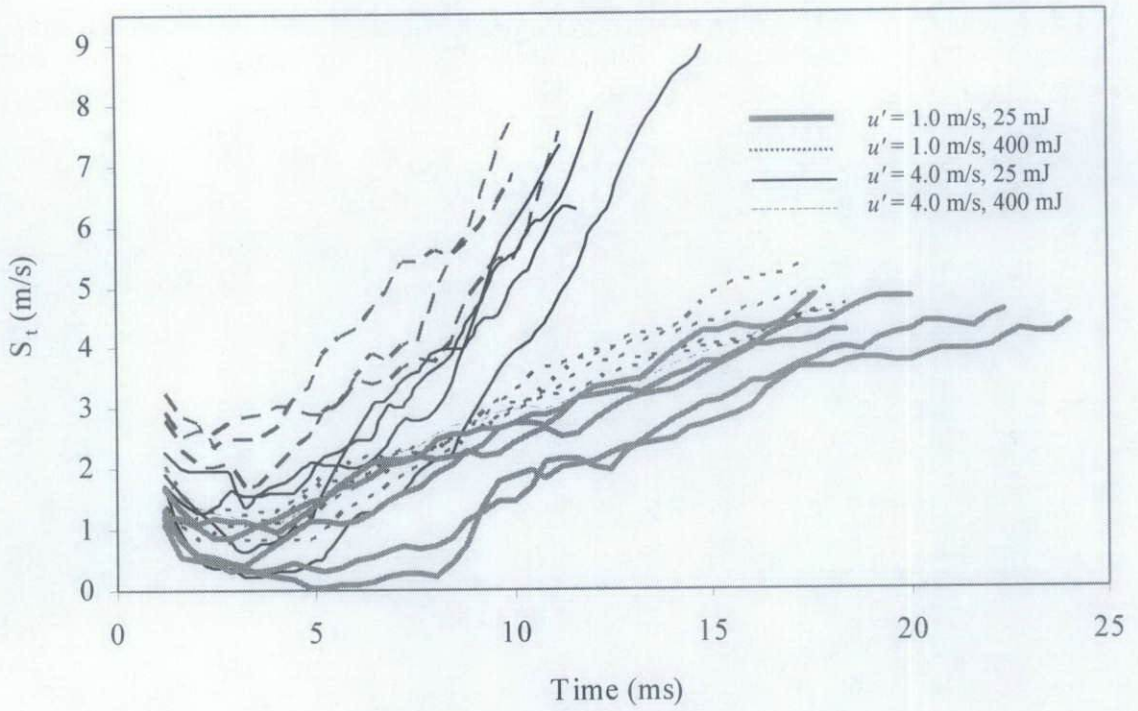


Figure 4.30 Variation of S_t with time for the turbulent gaseous flames in Fig. 4.28.

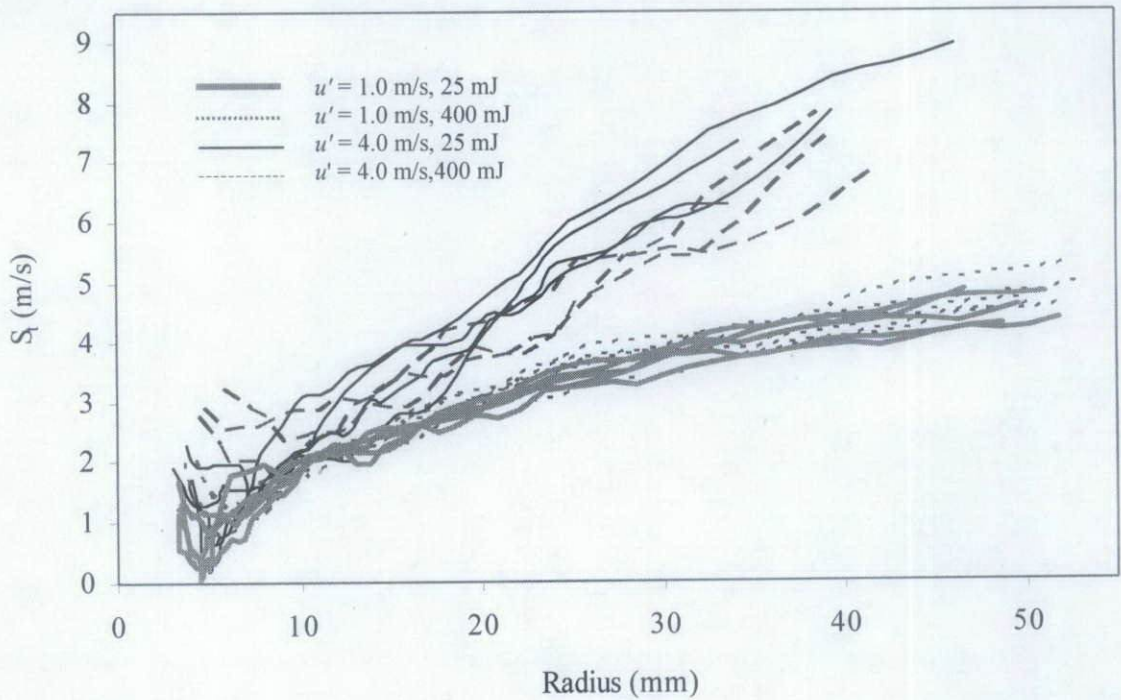


Figure 4.31 Variation of S_t with radius for the turbulent gaseous flames in Fig. 4.28.

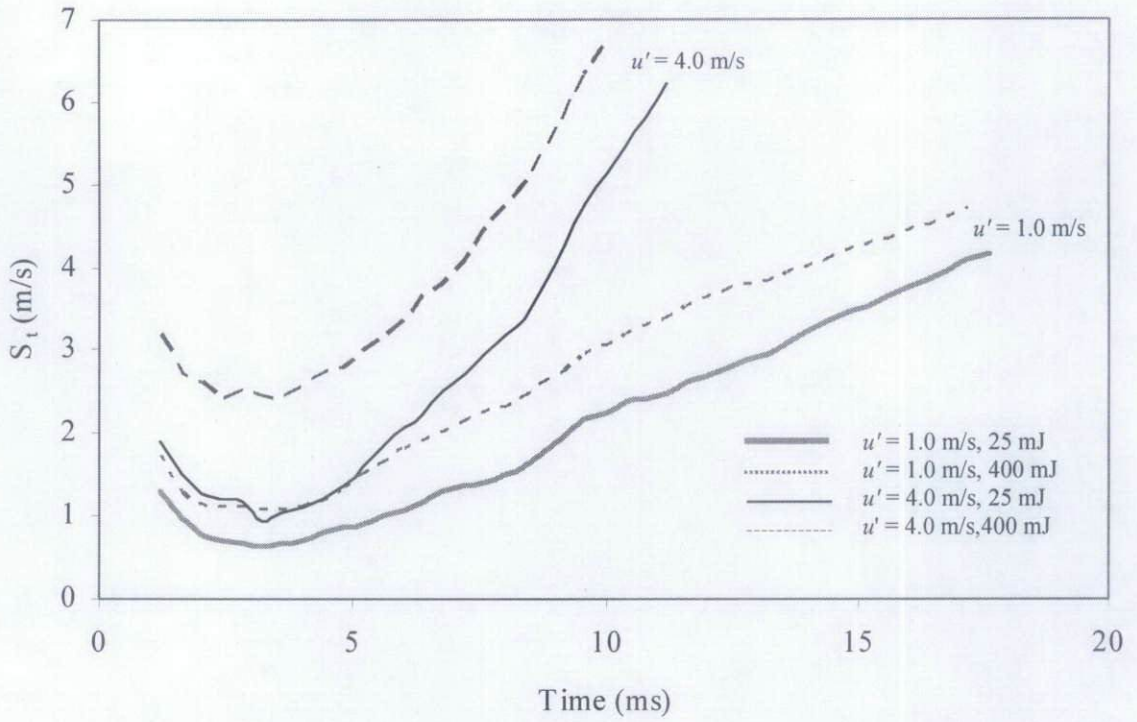


Figure 4.32 Variation of average S_t with time for the turbulent gaseous flames in Fig. 4.30.

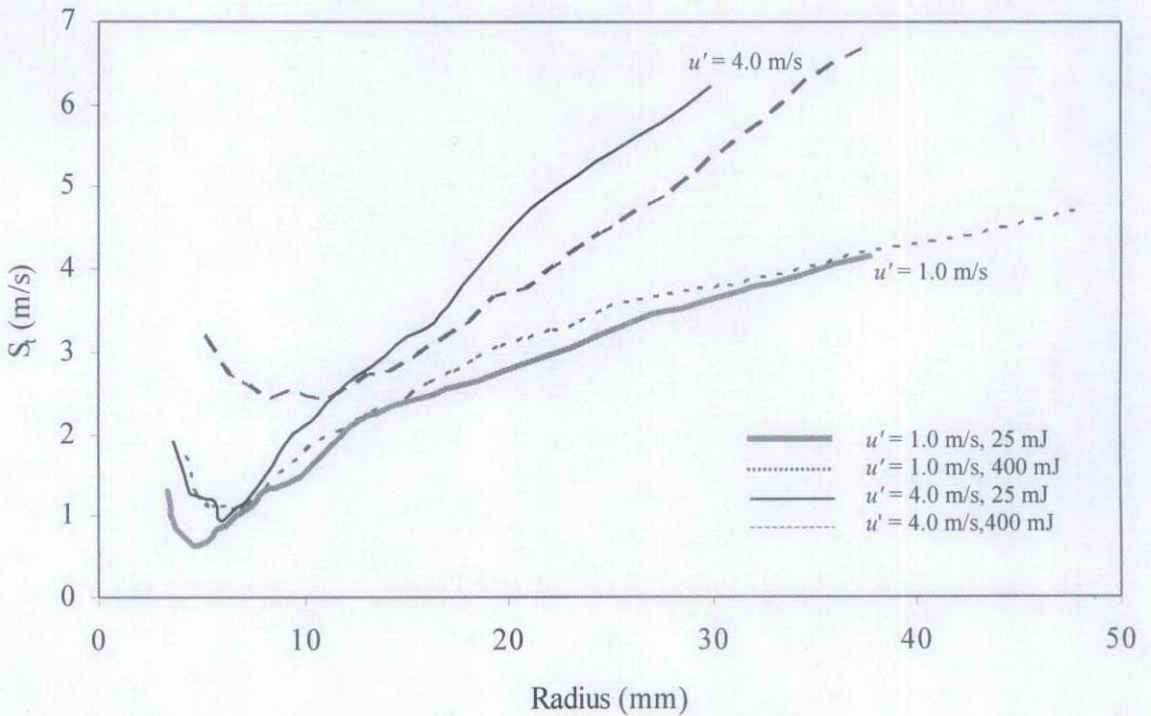


Figure 4.33 Variation of average S_t with radius for the turbulent gaseous flames in Fig. 4.31.

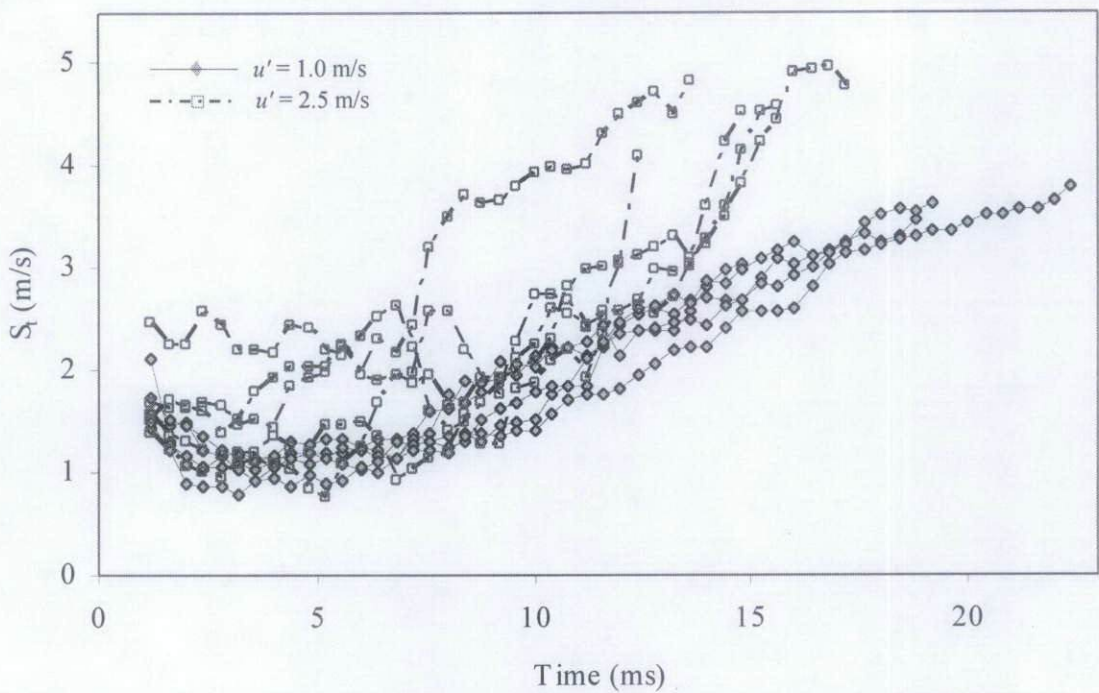


Figure 4.34 Variation of S_t with time for turbulent flames of stoichiometric iso-octane aerosol ignited at $P = 128$ kPa, $T = 283$ K, $D_{10} = 4$ μm , and u' of 1.0 and 2.5 m/s.

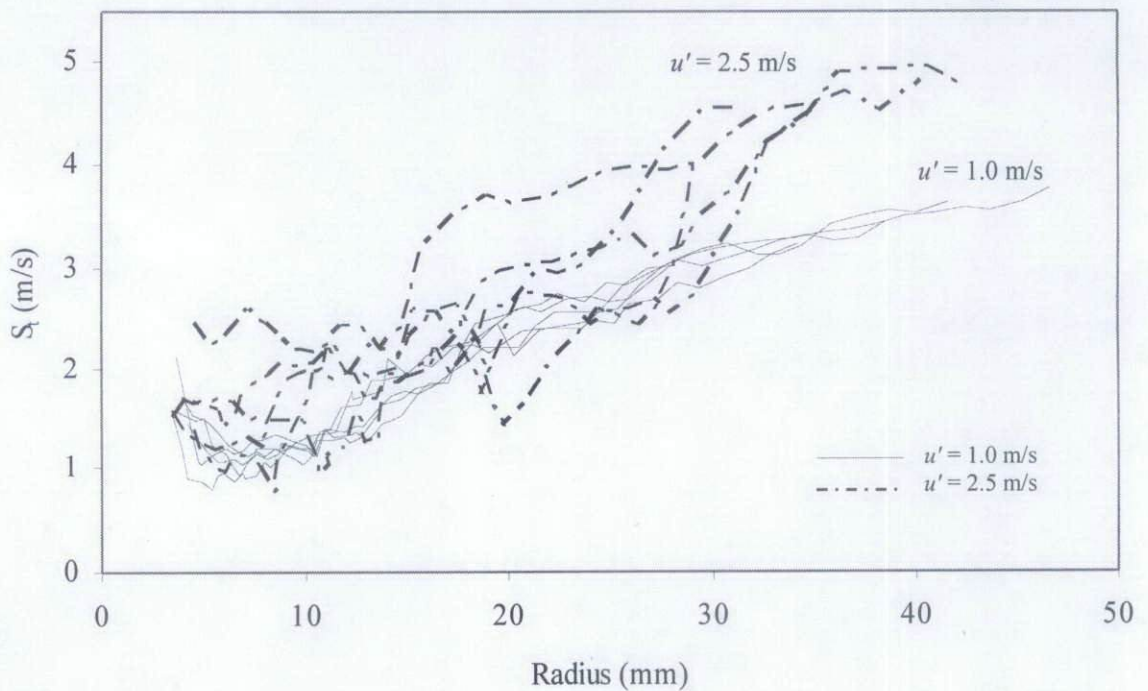


Figure 4.35 Variation of S_t with radius for turbulent flames of stoichiometric iso-octane aerosol ignited at $P = 128$ kPa, $T = 283$ K, $D_{10} = 4$ μm , and u' of 1.0 and 2.5 m/s.

Chapter 5

Discussion

Previous observations by various workers on the influence of droplets in flames are addressed in Chapter 1. This has become the motivation for the present research, in which the techniques and results are presented in Chapters 2, 3 and 4. In this Chapter, the outcomes of the present research are discussed in relation to the results in Chapter 4 and to related previous theoretical and experimental work.

In Section 5.1, the effects of the droplets on the ignitability of quiescent aerosols are discussed. When fully developed, some of the aerosol flames displayed enhanced burning rates relative to equivalent gaseous flames. This enhancement and its relationship to instabilities are discussed in Section 5.2. Several proposed mechanisms for enhanced burning rates are also discussed in Section 5.2. As opposed to laminar flames, the effect of droplets in turbulent flames is suggested to be minimal, the burning rate being similar to an equivalent gaseous flame, and this is discussed in Section 5.3.

5.1 Ignitibility of Quiescent Aerosol

It is demonstrated in Section 4.1.1 that aerosol mixtures are difficult to ignite, as compared to gaseous mixtures, and therefore require a larger spark energy. This is because the ignition of an aerosol is more complex than for gaseous flames (Mokhtar, 2001) due to factors such as the interaction of individual droplets with air and with other droplets. A detailed study of aerosol ignition is beyond the scope of

the present work. However, certain basic aspects related to aerosol ignition and the stage prior to full development of aerosol flames are discussed below.

5.1.1 Effect of Droplet Size

It is shown in Fig. 4.1 that, within the spark affected period, droplets influence the initial growth rate of the flame kernel, with quicker propagation for gaseous mixtures than for aerosols. A similar relationship has been demonstrated theoretically and experimentally by Ballal and Lefebvre (1978), who showed that the minimum ignition energy, E_{min} (defined in Section 4.1.1) increases with droplet size. However, the droplet sizes of the iso-octane mixtures in their studies were between 30 and 180 μm , which were larger than in the present work. Figure 5.1 shows the variation of E_{min} with droplet size, suggested by the theory of Ballal and Lefebvre (1978), for the iso-octane aerosols in the present work at $\phi_{ov} = 1.0$, $P = 100$ kPa, and $T = 270$ K. It shows that E_{min} is proportional to the square of D_{10} . However, the theoretical values of E_{min} shown in Fig. 5.1 are much lower than those required in the present work by an order of 10^4 . Indeed, the energy required for consistently successful ignition using the electric spark in the present work was estimated to be about 400 mJ, as stated in Section 2.1.3; and that reported for laser ignition by Mokhtar (2001), using the same apparatus and laser ignition characteristics as in the present work, was 32 mJ. This discrepancy between the work of Ballal and Lefebvre (1978) and the experiments at Leeds might be explained by Fig. 5.2, reported by Rao and Lefebvre (1976), which shows the variation of ignition energy with spark duration for kerosene sprays ($\phi_{ov} = 0.75$) injected into a flowing air stream in a duct at various air velocities and mean droplet sizes. It is shown in Fig. 5.2 that the ignition energy increases dramatically if the spark duration is reduced or increased. Hence, the high energy required during laser

ignition (Mokhtar, 2001) was probably because the spark duration was very short (12 ns), and conversely the lower energies in the work by Ballal and Lefebvre (1978) was due to longer spark durations of between 60 and 100 μs . The duration of the present electric spark was not measured by Atzler (1999), who first used the present unit, due to 'practical reasons.' However, an indirect measurement by the present Author, as explained in Section 4.1.5, from natural light imaging of the spark glow, showed that the duration of the present electric spark (about 8 ms) was significantly longer than that in the laser ignition (Mokhtar, 2001).

5.1.2 Effect of Ignition Energy

In Section 5.1.1 the minimum ignition energy required to establish a flame is discussed. In this Section the effect of ignition energy on the subsequent rate of flame propagation is addressed.

The effect of different ignition energies on laminar gaseous combustion was studied by Bradley *et al.* (1996a). They varied the ignition energy between 4.1 and 10.4 mJ for stoichiometric methane-air mixtures to ascertain its effects upon the subsequent flame development. They plotted the associated flame speeds against flame radius for different energies, as shown in Fig. 5.3. It is demonstrated in Fig. 5.3 that higher ignition energy will result in a higher initial flame speed. However, at radii greater than 6 mm, after the spark affected period discussed in Section 4.2.1, the flame speed becomes independent of ignition energy.

A similar trend to that in Fig. 5.3 was also observed in aerosol flames as shown in Fig. 5.4 by the graph of flame speed against radius. This was obtained with different ignition types and energies, for laminar flames of stoichiometric aerosols at $T = 270\text{ K}$, $P = 120\text{ kPa}$ and $D_{10} = 14\text{ }\mu\text{m}$. The triangles represent the results from the present work, which used an electric spark with ignition energy of 400 mJ (as

explained in Section 2.1.3.1); the squares represent those with laser ignition (Mokhtar, 2001) at 32 mJ. The significantly higher energy required for the electric spark in the present work than that for the laser ignition by Mokhtar (2001) was most probably due to the heat loss from the spark to the electrodes and their holder due to the long glow discharge. It is shown in Fig. 5.4 that within the first 5 mm radius of flame propagation, the flame speed that resulted from the electric spark was higher than that for the 32 mJ laser ignition. This probably was due to the difference in ignition energy as demonstrated in Fig. 5.3. However, after a flame radius of about 10 mm, the two flame speeds are similar throughout the subsequent flame propagation. These differences have been reported by Bradley *et al.* (1996a) for laser and spark ignition of gaseous flames.

5.2 Laminar Flame Propagation

The difficulty in igniting aerosol mixtures and the need for a large spark are discussed in Section 5.1. In this Section, some of the important aspects of laminar flames in quiescent aerosols, after the spark affected period, are discussed. The enhancement in the burning rate of these flames relative to equivalent gaseous flames, demonstrated in Section 4.2.2, is discussed in Section 5.2.1. It is proposed that this enhancement is due to flame instabilities, and this is discussed in Section 5.2.2. Possible mechanisms for the oscillating flames presented in Section 4.4, are discussed in Section 5.2.3.

5.2.1 Enhancement in Burning Rates

In Section 4.2.2, it is shown, through Fig. 4.18, that droplets increase the flame propagation rate relative to that for gaseous mixtures at $\phi_{ov} > 0.9$. This is associated

with earlier onset of instabilities in aerosol flames than in gaseous flames. In this Section, the previous work on instabilities and burning rates for gaseous flames, reviewed in Chapter 1, is compared with the results for the aerosols presented in Chapter 4.

As explained in Section 4.2.1, flames are more prone to develop instabilities at small values of Ma_{sr} and particularly when it is negative, and as shown in Fig. 4.16 this is favoured by a large drop diameter. In order to compare the susceptibility of a flame to cellularity, critical Peclet numbers, Pe_{cr} and Pe_{cl} were defined by Bradley *et al.* (1998) to represent the flame radius, normalised by the flame thickness, at which cellular instabilities are first observed (Pe_{cr}) and at which flame acceleration increased above that for the smooth or non-cellular laminar flame (Pe_{cl}). This subject is reviewed in Section 1.3. (During the preparation of this thesis, Bradley *et al.* (submitted for publication) suggested that a better parameter for instabilities would be the critical Karlovitz stretch factor, K (defined in Section 1.4.4.1), instead of Pe_{cl}).

Shown in Fig. 5.5 is the variation in Pe_{cr} and Pe_{cl} with D_{10} for flames in stoichiometric iso-octane-air aerosols at pressures and temperatures between 134 and 185 kPa, and 267 and 281 K respectively. The circles identify experimental results for Pe_{cr} and the squares those for Pe_{cl} . The dashed line is a linear curve fit to the experimental data for Pe_{cr} and the continuous line is a linear fit to the experimental data for Pe_{cl} . For small droplets ($D_{10} < 12 \mu\text{m}$), there was no evidence of any enhanced flame acceleration within the period of flame observation (although it is probable that acceleration will occur at larger radii). Hence, values of Pe_{cl} could not be determined. However, because flames become cellular before flame acceleration commences, measurements of Pe_{cr} were possible. Conversely, for larger values of D_{10} , flames become cellular very early, within the ignition affected region,

and hence values of Pe_{cr} could not be accurately obtained. Clearly, it is shown in Fig. 5.5 that the general trend is to a reduction in the critical Peclet numbers with D_{10} , indicating that aerosol flames become unstable more quickly as D_{10} is increased. The large diamond represents the predicted value of Pe_{cl} for gaseous iso-octane-air flames ($D_{10} = 0$) at $Ma_{sr} = 5.7$ ($P = 100$ kPa and $T = 303$ K). Prior to the present work, it was not possible to determine the values of Pe_{cl} at such a gaseous condition because the flame was smooth throughout propagation within the radius of the vessel's window, r_{window} , and thus Pe_{cl} could be attained only at a much greater flame radius ($r > r_{window}$). However, with a known value of Ma_{sr} for the gaseous flame, the predicted value of Pe_{cl} was obtained from a previous gaseous data correlation (Gu *et al.*, 2000), which is presented below. Extrapolation of the continuous line (Pe_{cl}) to zero diameter shows good agreement with the gaseous data.

Bradley *et al.* (1998) and Gu *et al.* (2000) showed that Pe_{cl} can be correlated with Ma_{sr} . Shown in Fig. 5.6 is the variation of Pe_{cl} with Ma_{sr} , reproduced from Gu *et al.* (2000), for various gaseous mixtures of methane-air, iso-octane-air and 90% iso-octane / 10% n-heptane-air at various equivalence ratios, pressures and temperatures. The scatter in Fig. 5.6 is significant. However, the best fit curve through all the gaseous data demonstrates some generality in the onset of cellular instabilities in gaseous flames. It shows that Pe_{cl} increases with Ma_{sr} , or more importantly, that at low values of Ma_{sr} flames accelerate at smaller flame radii (smaller Peclet numbers).

Shown in Fig. 5.7 is the variation of Pe_{cl} with Ma_{sr} for the present aerosols at $\phi_{ov} = 1.0$ (diamonds) and $\phi_{ov} = 1.1$ (circles). These were obtained from experiments with droplet diameters between 3 and 24 μm , pressures between 118 and 183 kPa, and temperatures between 269 and 282 K. The thick continuous line is the best fit curve through the diamond markers for droplets between 15 and 24 μm , within

which the ratio D_{10}/δ_l is calculated to be about 0.42. In the present work, this ratio is used because any disturbance of the reaction zone by droplets is likely to be a function of it. Large droplets, relative to the flame thickness are more likely to penetrate the reaction zone. The long dashed line represents the best fit curve through the circle markers for droplets between 13 and 19 μm ($D_{10}/\delta_l \approx 0.46$). Also shown in Fig. 5.7 is the best fit curve through the gaseous data ($D_{10}/\delta_l = 0$) from Fig. 5.6, which is represented by the thin continuous line. Clearly, it is shown in Fig. 5.7 that the dimensionless groups Pe_{cl} , Ma_{sr} and D_{10}/δ_l are valid for the aerosol (present work) and gaseous mixtures. Hence, it is proposed that Fig. 5.7 presents a generalisation, and thus can be applied for any mixture conditions.

The thick continuous line and the long dashed line clearly show that the trends in the effect of Ma_{sr} on Pe_{cl} are similar to that for gaseous flames, but that the magnitudes are lower. The crosses in Fig. 5.7 show measurements at smaller values of D_{10} (between 3 and 12 μm), obtained from the curve fit for Pe_{cl} in Fig. 5.5. They indicate how the effect of Ma_{sr} on Pe_{cl} varies as a function of D_{10}/δ_l between the upper and lower curves, to yield the trends tentatively shown by the short dashed lines.

A possible mechanism for flame acceleration due to instabilities was presented, for gaseous flames, in terms of a spherical explosion flame instability theory of Bechtold and Matalon (1987). They identified the wave numbers of flame wrinkling that were unstable and led to flame instability. Bradley (1999) empirically modified the theory based on experiments with spherically propagating laminar flames of gases in an explosion bomb (Bradley and Harper, 1994) to allow for the lag between the onset of cellularity and the associated flame acceleration. The theory of Bechtold and Matalon (1987), and the modifications by Bradley (1999), are

reviewed in Section 1.3. It is summarised graphically in Fig. 1.2 by a peninsula within which the wave numbers are associated with flame instability and cellularity, which increase the burning rate.

From the peninsula, as in Fig. 1.2, and by applying Eq. (1.14), from the fractal approach by Al-Shahrany *et al.* (2005) and Lawes *et al.* (2005), the burning velocity enhanced by instabilities, u_n , was predicted. Shown in Fig. 5.8 are the variations of cellular burning velocity enhancement, $u_n/u_{n,Pe-cl}$, defined in Section 1.3, plotted against Pe for aerosol flames in the present work. The conditions for Fig. 5.8(a) were at $\phi_{ov} = 1.0$, $D_{10} = 12 \mu\text{m}$, $Ma_{sr} = 3.73$, $P = 169 \text{ kPa}$ and $T = 276 \text{ K}$, and those for Fig. 5.8(b) were at $\phi_{ov} = 1.0$, $D_{10} = 14 \mu\text{m}$, $Ma_{sr} = 3.67$, $P = 162 \text{ kPa}$ and $T = 275 \text{ K}$. The symbols in Fig. 5.8 represent experimental data. The dashed lines are linear curve fits through the region prior to cellular acceleration and the solid curves were obtained from application of Eq. (1.14). Figure 5.8(a) shows good agreement between the theoretical prediction and experiment. However in Fig. 5.8(b) there is an overestimation of the theoretical prediction of cellular burning velocity enhancement.

Shown in Fig. 5.9 are graphs, similar to those in Fig. 5.8, which were derived from the results of previous workers. The reproduction of a graph from Lawes *et al.* (2005), in Fig. 5.9(a), comprises experimental data for an aerosol flame (crosses) at $\phi_{ov} = 1.2$, $D_{10} = 17 \mu\text{m}$, $Ma_{sr} = 6.3$, $P = 172 \text{ kPa}$ and $T = 279 \text{ K}$, and for a gaseous flame (diamonds) at $\phi = 1.0$, $Ma_{sr} = 6.4$, $P = 1000 \text{ kPa}$ and $T = 358 \text{ K}$. The graph in Fig 5.9(b) is calculated by the present author from the experimental data of Haq (1998) for a methane-air flame at $\phi = 1.2$, $P = 1016 \text{ kPa}$ and $T = 300 \text{ K}$. Good agreement between the theoretical prediction and experiment is shown in Fig. 5.9(a).

However overestimation of the theoretical prediction of cellular burning velocity enhancement is shown in Fig. 5.9(b).

Collectively, it is evident from Figs. 5.8 and 5.9 that there is a mix of good and poor agreement between the theoretical prediction of cellular burning velocity enhancement and experiments for the gaseous flames. This demonstrates that the correlation in Eq. (1.14), which was derived by the fractal approach proposed by Al-Shahrany *et al.* (2005), is probably not robust. A possible reason for the inconsistency is because it is difficult to accurately determine the transition from Pe_{cr} to Pe_{cl} . Indeed, as shown in Section 4.1.3, earlier experiments did not have sufficient optical quality to accurately define Pe_{cr} . In addition, some flames probably display rapid transition, whereas for others, the transition is more gradual. Further research is required in order to correct the theoretical prediction.

5.2.2 Mechanisms for Instabilities in Aerosol Flames

It is shown in Section 5.2.1 that the presence of droplets in the reaction zone of aerosol flames is a contributory factor to instabilities, which lead to burning rate enhancement. Several mechanisms for such instabilities have been proposed and they are discussed here.

In one of earliest works on aerosol combustion, Mizutani and Nakajima (1973b) proposed that the burning rate enhancement was the result of turbulence generated by the flame itself, either from a laminar or turbulent initial condition, due to the complex thermal expansion of gas which intensifies transport processes. However, this is arguable, as they did not report measurements of turbulence during the combustion event. Furthermore, in relation to the present work, none of the laminar aerosol flames, presented in Section 4.1, resembled the turbulent aerosol flames in Section 4.5.

Another possible mechanism for instabilities was proposed by Hayashi *et al.* (1976) and Nomura *et al.* (1998) to be due to the physical presence of droplets passing through the reaction zone which produced distortion on it and consequently flame acceleration. However this was negated by Atzler (1999), who found that the introduction of non evaporating hollow glass spheres in a laminar gaseous propane-air mixture did not alter the flame surface, which was smooth and similar to that without glass spheres.

Hence, the mechanism of flame instabilities is probably related to the heat loss from the flame and local rapid expansion through droplet evaporation. Nevertheless droplet evaporation can also cause high gradients in mixture strength (variations in local equivalence ratio), which might have an effect on the flame. To overcome such doubts, Atzler (1999) investigated the effect of a water aerosol in a gaseous propane-air mixture ($\phi_{ov} = 1.3$) using the same expansion technique as for the experiments in the present work. He reported a well developed cellular surface structure that manifests instabilities, as compared to the smooth flame in a similar experiment without water aerosol, although the introduction of water had clearly diluted the mixture rather than enriched it. This shows that the heat loss from the flame due to evaporation of water droplet has a significant role in the development of instabilities. Furthermore, the effect of heat loss due to droplet evaporation was mathematically shown, by Greenberg *et al.* (1999) using linear stability analysis, to play a dominant role in the manifestation of instabilities in aerosols.

The influence of heat loss from the flame due to droplet evaporation can be explained in terms of heat and mass diffusion effects embodied in the Lewis number, Le , which is defined by the ratio of thermal to mass diffusivities of the reactant. Clavin (1985) and Harper (1989) demonstrated that Markstein number increases linearly with Le for a wide range of mixtures. Droplets near the flame front

will absorb heat as they evaporate; this reduces the heat diffusion from the reaction zone, but is unlikely to change the mass diffusion. Hence droplets reduces Le and, hence, Ma_{sr} , and as discussed in (Harper, 1989), a reduction in Ma_{sr} results in a greater propensity to cellularity. For a larger droplet, the reduction in Ma_{sr} is expected to be greater, as is demonstrated in Fig. 4.16.

The above mechanism is probably compounded by disturbances of the reaction zone as droplets evaporate. It is demonstrated in the present work that at certain conditions, droplets can survive the flame front. Figure 5.10 shows the variation of droplet lifetime, τ_D , estimated from Eq. (1.33), with droplet diameter near the flame front for a stoichiometric iso-octane-air aerosol at $P = 100$ kPa, $T = 273$ K and $T_\infty = 2275$ K. The dashed line represents t_l , defined as the estimated time taken for the flame front, at a propagation speed, S_n , to reach a droplet located within a distance of δ_l , and this is simply given by

$$t_l = \frac{\delta_l}{S_n} \quad (5.1)$$

If τ_D is larger than t_l , the droplet may not be fully evaporated and may survive, for a short time, behind the flame front. Hence, part of the curve in Fig. 5.10 that lies above the dashed line indicates droplet sizes for which complete evaporation may not take place within the preheat zone. This supports the observations of droplet survival shown in Fig. 4.7, and also contradicts the complete evaporation assumptions made by modellers such as Greenberg *et al.* (1999) and Nicoli *et al.* (2005). If droplets evaporate in the preheat zone, this will result in a gaseous mixture in the reaction zone. However, droplet evaporation in the reaction zone, as evident in Fig. 5.10, will clearly disrupt it locally and trigger instabilities.

5.2.3 Mechanisms for Oscillating Flames

Flame speed oscillations have been observed in some spherical flames of premixed gases (Haq, 1998; Bradley, 2001), but with significantly smaller amplitudes than those for the aerosol flames mentioned in Section 4.4. In oscillating flames there are also changes in flame structure. The possible mechanisms responsible for oscillations in the aerosol flames considered in the present work are discussed below.

5.2.3.1 Effect of Acoustic Waves

There has been no known analysis of the interaction between acoustic waves and spherical aerosol flames. However, it has been demonstrated theoretically (Clavin and Sun, 1991) that an acoustic oscillation of a planar flame, propagating in a tube, can be amplified significantly when an aerosol is present. Nevertheless, the frequencies of flame oscillation, as implied in Fig. 4.22, are of about 32 Hz ($1/0.031 \text{ s}^{-1}$), while those of acoustic waves are significantly higher; in the order of between 1500 and 4000 Hz (Bradley *et al.*, 2001; Farrell *et al.*, 2004). Hence, it is tentatively suggested that the oscillations in flame speed in the present work probably are not associated with acoustic oscillations. Further work is required in order to study any possible influence of acoustic waves on oscillating aerosol flames.

5.2.3.2 Effect of Radiation from Burning Particles

Radiation from burning particles may have played a role in the occurrence of flame oscillations. This was observed by Hanai *et al.* (1998) in clouds of Polymethylmethacrylate (PMMA) fuel particles at similar conditions to those of the present research, near the lean limit of flammability. They suggested that particles, which are not burnt completely in the reaction zone, pass through the flame front, absorbing heat and thus causing a reduction in flame speed. Behind the flame front

these particles burn in a second luminous flame front, which emits heat to the particles and gas in the unburnt mixture. As a result, the flame burns rapidly into this preheated zone and consumes it. Conversely, when the flame reaches the zone of cold, not preheated mixture, the flame speed slows down and a new cycle begins.

The mechanism of flame propagation in dust flames is different from that in aerosols, in that the temperature of the droplets is limited by the boiling temperature, whereas dust particles can be heated to a much higher temperature (Strehlow, 1984). Furthermore, the thickness of the particle flames observed by Hanai *et al.* (1998) was of the order of tens of millimetres. This is much larger than that estimated (in Table 4.1) for aerosols in the present work (between 25 and 65 μm). Therefore, it is concluded that radiation might play an important role in dust flames, but probably not in aerosols.

5.2.3.3 Effect of Droplet Inertia

The effect of droplet inertia leading to a time dependent variation of equivalence ratio at the flame front was shown theoretically by Clavin and Sung (1991). This was investigated, in the present vessel by Atzler *et al.* (2001) and Marquez (2003). They compared the experimental data with modelled predictions of oscillations in flame speed caused by the aerodynamic interaction of the gas motion ahead of the flame front with the droplets. The main assumptions of the model are presented below.

The case of an initially quiescent and homogeneous two phase mixture is considered in which the fuel droplets are vaporised only in the preheat zone of the flame, that vaporisation is complete, and that gaseous mixing is instantaneous. Due to the expanding flame, the velocity of the gas that surrounds the droplets is not constant and a varying drag force exists. Droplet inertia results in a lag between the droplet and gas velocities. The flame speed depends on the equivalence ratio in the

reaction zone and this depends on the number density of droplets that enter it. During a time interval, dt , the flame propagates through a volume of gas, $V_g = A u_n dt$. During this time, the number of droplets entrained into the flame, N , is given by

$$N = N_{DL} A (S_n - u_D) dt \quad (5.2)$$

where N_{DL} is the droplet number density at the leading edge of the flame, and u_D is the droplet velocity at the same point. Thus the number density of droplets that enter the flame, N_{DF} , is

$$N_{DF} = N_{DL} \left(\frac{S_n - u_D}{u_n} \right) \quad (5.3)$$

The equivalence ratio within the reaction zone is given by

$$\phi = \phi_g + \frac{N_{DL}}{N_{Dr}} (\phi_{ov} - \phi_g) \left(\frac{S_n - u_D}{u_n} \right) \quad (5.4)$$

where N_{Dr} is the number density in the reactants remote from the flame. Three limiting cases are revealed from Eq. (5.4):

1. Obviously, ϕ cannot be less than ϕ_g . If $u_D > S_n$, then the droplets move away from the flame, N_{DL} reduces to zero and the initial gaseous phase equivalence ratio results.
2. If $u_D = u_g = S_n - u_n$, then the term in the second set of brackets becomes unity, $N_{DL} = N_{DF}$ and, hence, $\phi = \phi_{ov}$. This corresponds to the case in which the droplets have negligible inertia.
3. If $u_D = 0$, the equivalence ratio attains a maximum and this results in

$$\phi_{\max} = \phi_g + \frac{\rho_u}{\rho_b} (\phi_{ov} - \phi_g). \text{ This corresponds to the case in which the}$$

droplets have infinite inertia. Since $\rho_u / \rho_b > 1$, $\phi_{\max} > \phi_{ov}$.

Figure 5.11 shows a graphical representation of Eq. (5.4) for a mixture with $\phi_{ov} = 1.0$ and $\phi_g = 0.75$ (Atzler *et al.*, 2001). It shows the effect of a variation in droplet velocity on the resulting local (at the reaction zone) equivalence ratio (thick line). For example, when the droplet velocity is 0.5 m/s, the droplets are entrained into the flame at a faster rate than in the surrounding vapour, resulting in a local equivalence ratio of 1.45. Conversely, if the droplet velocity is higher than that of the flame speed, no droplets will be entrained into the reaction zone and the local equivalence ratio will be equal to ϕ_g (0.75). This is the case for $u_D > 2.2$ m/s. Clearly, when the droplet velocity is equal to the local gas velocity, ϕ_{ov} will exist at the flame front. Figure 5.11 shows that there are three possible solutions for droplet velocities between about 1.25 and 1.8 m/s. A variation in local equivalence ratio will affect the local flame speed, burning velocity and gas velocity. These are shown as a function of local ϕ in Fig. 5.11. For the highest value of ϕ , if ϕ increases, the burning velocity reduces. Hence, less droplets are entrained and ϕ reduces again to yield a stable solution. Similarly, the lowest value of ϕ yields a stable solution. However, the middle value corresponds to a range of ϕ in which the burning velocity increases with ϕ . In this range, if ϕ increases, the burning velocity increases, more droplets are entrained into the flame and ϕ increases further. Similarly, if ϕ decreases, the burning velocity decreases, fewer droplets are entrained and ϕ decreases further. Hence, this solution is unstable.

Figure 5.11 shows a possible mechanism to explain the pulsating expanding spherical flame. Initially, following ignition, the droplet velocity near the flame front is equal to zero. Therefore, the equivalence ratio in the reaction zone is ϕ_{max} . The flame causes the gas droplet velocity to begin to accelerate. Hence, fewer droplets are entrained by the flame and the equivalence ratio decreases as in regime 1. As the

stoichiometric equivalence ratio is approached, the droplets continue to accelerate towards that of the gas velocity, while the burning velocity and gas velocities reduce as their peak values are passed as in regime 2. The point at which S_n and u_g reach their maximum values is defined as the critical equivalence ratio, $\phi_{critical}$. The droplet and gas velocities become equal at ϕ_{ov} ($= 1.0$). After this, inertia results in droplet velocities that are higher than the gas velocity as the latter continues to reduce. Therefore, the equivalence ratio within the reaction zone tends towards $\phi = \phi_g$ (regime 3), and would attain this value when $u_D = S_n$. Eventually, the droplets approach equilibrium with the surrounding gas and more droplets are entrained as ϕ begins to increase through ϕ_{ov} and $\phi_{critical}$ (regime 4) as the droplets once again lag behind the gas velocity. The cycle then is repeated.

This mechanism necessitates that ϕ_{ov} , at which the droplet velocities are equal to the gas velocity, must be less than $\phi_{critical}$. If ϕ_{ov} were greater than $\phi_{critical}$, then as the droplet and gas velocities became equal at ϕ_{ov} , the burning velocity and gas velocity still would be accelerating as $\phi_{critical}$ was approached. Hence, it would be unlikely that the droplet velocity would exceed the gas velocity and steady state would be attained at ϕ_{ov} . This critical value occurs at approximately $\phi = 1.1$ for gaseous iso-octane-air flames (Bradley *et al.* 1998). Hence, it might be expected that flame oscillations, by the proposed mechanism, occur when $\phi_{ov} < 1.1$.

Shown in Fig. 5.12 is a comparison of experimental and numerical results, made by Atzler *et al.* (2001), which shows the variation in flame speed with time; experimental results are represented by symbols and the solid line represents numerical results. The comparison shows that there is a very good qualitative agreement in the general trend, amplitude and frequency of oscillation between the simulation and measured data. However, there are differences in the maximum

values of flame speed. The difference could be attributed to the limitations of the model. The important effects of cellularity discussed in Section 5.2.2, which increase the flame speed, were not included in the model. For simplification, spherical symmetry was considered, hence, the mathematical model only considered propagation in the radial direction, but as discussed in Section 4.1 the flame kernel was usually distorted and this might affect the burning rate.

The numerical data exhibits several abrupt changes in S_n cyclically, an example is shown between points 1 and 2 in Fig. 5.12 and this corresponds to the regime 2 in Fig. 5.11. An assumption in the numerical data is that immediately to the left of $\phi_{critical}$ in Fig. 5.11; S_n and u_g start to decrease, while droplets are still accelerating. At ϕ_{ov} , $u_D = u_g$ and the model assumes that instantaneously at this point ϕ at the reaction front reduces to ϕ_g . Due to the sudden reduction in ϕ at the reaction front the model produces a sudden reduction in S_n to point 2. In reality, there is a gradual variation in ϕ and S_n . It is assumed in the model that due to droplet inertia, there is a delay in the reduction of u_D towards the new value of u_g . The model also assumed that after the point at which $u_D = S_n$, the droplets start to 'feed' the reaction zone again, which produces a small variation in S_n represented between points 2 and 3 in Fig. 5.12 and corresponding to regime 3 in Fig. 5.11. After some time, the model assumed that ϕ at the reaction front becomes rich again, which produces another sudden variation in S_n represented in Fig. 5.12 between points 3 and 4, that corresponds to regime 4 in Fig. 5.11. The increase in S_n and u_g produces droplet acceleration and the cycle starts again.

Experimental support from the present work for the above mechanism is shown in Fig. 5.13, in which S_n (thick line), u_g (fine line) and u_D (triangles) are compared as a function of time from ignition for the aerosol flames presented in

Figs. 4.6 and 4.24. As explained in Section 4.4, these results were obtained from simultaneous laser sheet imaging and PIV analysis. Due to the complexity of image processing caused by the shape of the flame in Fig. 4.6, as described in Section 2.4.5.2, only the radial component of each S_n and u_D was measured, as a function of the distance from spark plug (which corresponds to flame radius), at discrete times from ignition. The values for u_g were obtained from Eq. (1.2). Indicated by the dashed lines in Fig. 5.13 are values of S_n estimated by Marquez (2003) for gaseous combustion, using correlations by Bradley *et al.* (1998), at representative equivalence ratios equal to those of ϕ_{ov} , ϕ_g and $\phi_{critical}$.

The relationship between the gas phase and droplet velocities is remarkable. At $t = 25$ ms (the first measured value of u_D), the droplet velocity is considerably lower than that of the gas (resulting in an increase in local ϕ). This is proposed to be due to droplet inertia such that the droplets do not faithfully follow the flow when the flame is accelerating rapidly. At $t = 28$ ms, the droplet and gas phase velocities converge. As the gas velocity continues to increase rapidly at $t = 31$ ms, the droplet velocity again lags behind. The flame speed drops at $t = 35$ ms because the reaction front becomes richer ($\phi > 1.1$). At $t = 37$ ms, the droplet and gas phase velocities converge again; thereafter the difference between u_D and u_g is small, but still significant. The cycle continues with convergence and divergence of velocities occurring when u_g is near the minimum and maximum values. It is evident from Fig. 5.13 that the aerosol flame speed varied within the limits represented by the gaseous phase mixtures at ϕ_g and $\phi_{critical}$. This supports the modelling assumptions, above, that the effective ϕ for aerosol combustion might vary between these limits. Thus the results support the hypothesis that the effect of droplet inertia on flame oscillations might be important, possibly dominant.

5.3 Turbulent Studies

Burning rate enhancement of two-phase as compared to single-phase combustion in laminar studies and its mechanisms have been discussed in Section 5.2. However, unlike a laminar flame, which has a characteristic burning velocity that depends uniquely on the properties of the mixture and the initial conditions, a turbulent flame has a propagation velocity that depends also on the flow field parameters (Turns, 2000). The effects of turbulence in aerosol flames on the burning rate are discussed below.

5.3.1 Flame and Droplet Induced Turbulence

It was concluded by Mizutani and Nakajima (1973a) that even under turbulent conditions, additional turbulence was generated due to the interaction between the flame and droplets. However, as discussed in Section 5.2.2 for the laminar studies of Mizutani and Nakajima (1973b), they did not provide any evidence of measurements of turbulence during the combustion event. Furthermore, it was also pointed out by Nakabe *et al.* (1988) that the method used by Mizutani and Nakajima (1973a) to measure turbulent burning velocity in burners was susceptible to large errors for flames with brush type appearance.

Mizutani and Nakajima (1973a) also found the effect of droplet addition to be greater for lower flow velocities ($V = 1.2$ m/s) or weaker intensities of turbulence ($u' = 0.13$ m/s). This suggests that the enhancing effects of instabilities triggered by an aerosol may be present, as for the laminar cases, at low turbulence, but that they are diminished by the additional contribution from externally generated turbulence.

From the experimental results for laminar flames in Section 4.1.4 and also from the calculation evidence discussed in Section 5.2.2, it is suggested that at certain conditions, droplets penetrate the reaction zone, and this triggers instabilities

and causes burning rate enhancement relative to gaseous flames. The same comment, on the influence of droplets in the reaction zone of laminar flames, could probably apply for turbulent aerosol flames. This is mainly because u_t in turbulent flames is significantly greater than u_n in laminar flames, thus droplets in turbulent flames have a greater tendency to penetrate the flame front. Despite this possibility, it is shown in Section 4.6 that turbulent burning velocity for aerosols is quite similar to that for gaseous combustion, when evaluated at the same conditions. This is further discussed in Section 5.3.2.

5.3.2 Effects of Stretch Rate and Turbulence

In Section 4.6, the burning rates of turbulent gaseous and aerosol flames are presented; however, to make accurate comparison between them would not be realistic because the initial conditions for the gaseous and aerosol flames were not the same. For example, Figs. 5.14 and 5.15 show variations of S_t with time and radius for turbulent flames of stoichiometric iso-octane-air gaseous (Section 4.6.1) and aerosols (Section 4.6.2) at $u' = 1.0$ m/s. However, the gaseous mixtures were obtained at $P = 100$ kPa, $T = 303$ K and the aerosols were obtained at $P = 128$ kPa, $T = 283$ K. Therefore, although Figs. 5.14 and 5.15 suggest that aerosol flames are slower this is more likely to be due to the lower initial temperature than to any real effect of the aerosol. In order to make a real comparison of the two, the data in Figs. 5.14 and 5.15 need to be expressed in terms of the fundamental dimensionless groups that influence the burning rate.

Shown in Fig. 5.16 are the present gaseous and aerosol data expressed in terms of the dimensionless groups suggested by Bradley (1992) and similar to that shown in Fig. 1.5. The experimental values of u_t/u_l are plotted as a function of the wrinkling factor, u'/u_l , and the flame stretch factor KLe , using data from Figs. 5.14 and 5.15.

The data points for gaseous mixtures are represented by the open triangle markers, and those for the aerosols are represented by the solid circle markers. The lines represent the correlation of Fig. 1.5 and each are labelled with the corresponding values of KLe . Similarly, Fig. 5.17 shows the present gaseous and aerosol data expressed in terms of dimensionless groups suggested by Bradley *et al.* (2005), in which U , defined by the ratio u_t/u'_k , is plotted against KMa_{sr} , which expresses the reduction in burning velocity due to stretch. The experimental data were obtained from measurements at $r = 30$ mm. Ormsby (2005) and Liu (2006) suggested that at this radius, flames were essentially fully developed. The same symbols as in Fig. 5.16 are used in Fig. 5.17 to represent the experimental data from the present work. Also shown in Fig. 5.17 are the experimental data for gaseous iso-octane at equivalence ratios of 0.8, 1.0 and 1.1, and $u' = 2.0$ m/s ($P = 500$ kPa, $T = 360$ K) from Ormsby (2005), represented by solid triangle markers. The correlation by Bradley *et al.* (2005) is represented by the continuous curve.

In Fig. 5.16, it is clear that in terms of groupings there is no obvious distinction between turbulent aerosol and gaseous flames (an increase in the parameter u_k'/u_l or KLe has a similar quantitative effect on u_t/u_l). Similarly, there is no significant difference in turbulent burning rates for the aerosol and gaseous flames in Fig. 5.17, where an increase in KMa_{sr} gives similar effect on U , irrespective of whether gaseous or aerosol.

It is interesting to compare the experimental data with the correlations (Bradley, 1992, Bradley *et al.*, 2005). Clearly in Figs. 5.16 and 5.17 the values for experiments are lower than that for the correlation. A possible reason for this is due to the effect of ignition. In the experiments of the present work and those by Ormsby (2005), the flame was ignited by a central spark, in which the flame development, as discussed in Section 4.6.1, was a function of ignition energy.

However, the data from which the correlation of Bradley (1992) is based, were obtained mainly from experiments in burners and the flame on them was readily developed (Lawes, 1987), and thus ignition did not have any significant role as compared to the experiments in the present work. Similarly, the data for the correlation of Bradley *et al.* (2005) were obtained from twin kernel implosion experiments in the Leeds bomb (Al-Shahrany, 2004), in which measurements were obtained in the later stage of flame development, and thus were not influenced by the effect of ignition. This clearly demonstrates that the correlation for turbulent burning velocity must include a parameter to take into account the effect of ignition as well as the effect of their development. Further work is recommended.

In conclusion, it is shown in this Section that although laminar flames are faster for aerosols as compared to gaseous mixtures, the presence of droplets does not cause any increase in the flame propagation rate under turbulent conditions. The discrepancies between the experiments and turbulent correlations are also highlighted in this Section.

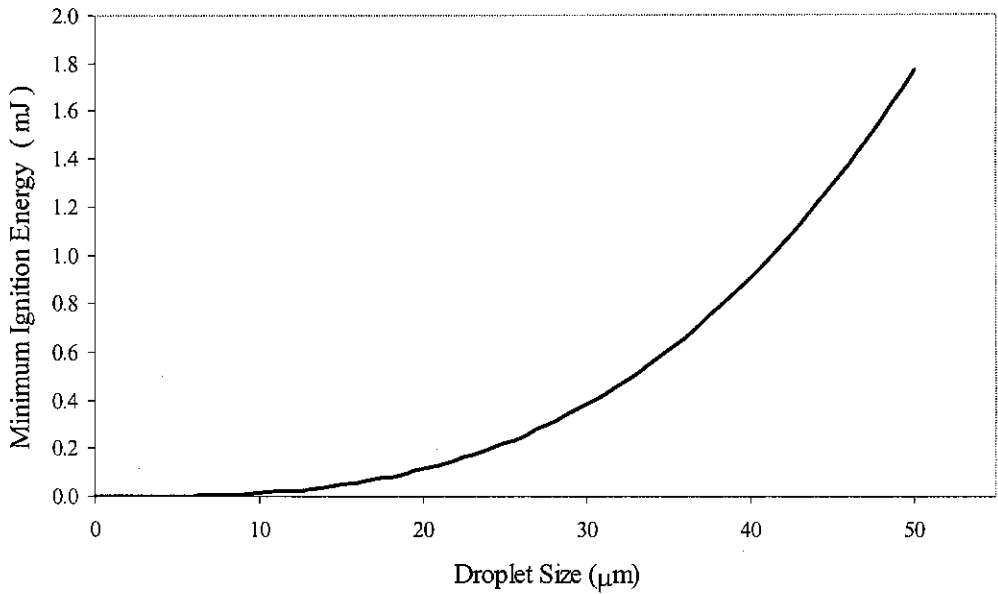


Figure 5.1 Effect of droplet size on the predicted minimum ignition energy calculated using the correlations of Ballal and Lefebvre (1978). Data are for stoichiometric iso-octane-air aerosol at $P = 100$ kPa, $T = 270$ K.

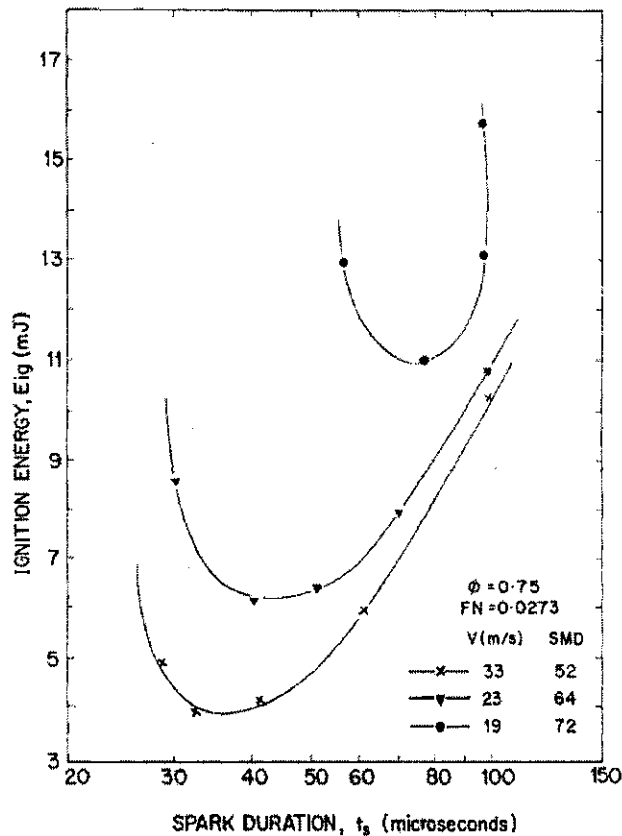


Figure 5.2 Variation of ignition energy with spark duration for kerosene sprays ($\phi_{ov} = 0.75$) in flowing air at various air velocities and mean droplet sizes. Reproduced from Rao and Lefebvre (1976).

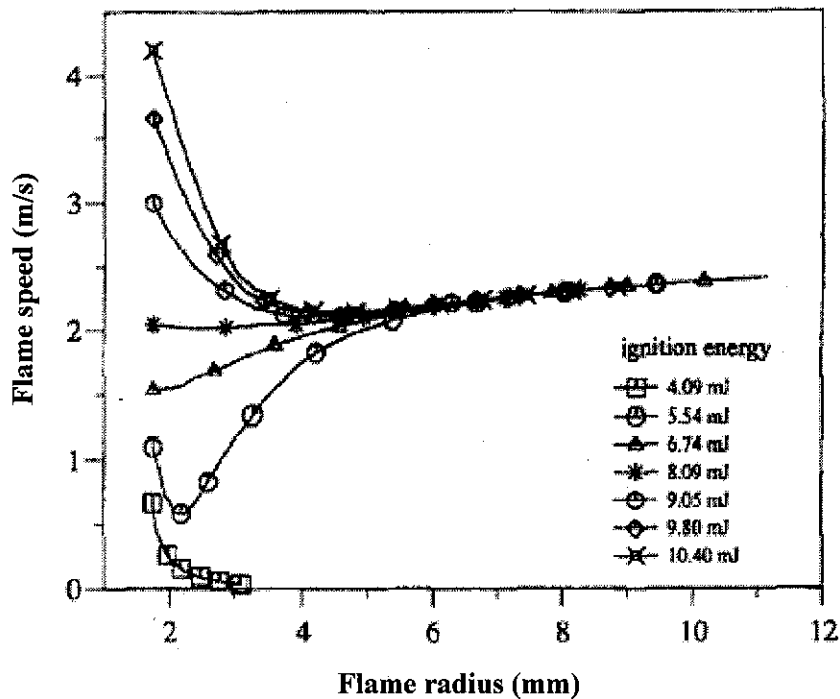


Figure 5.3 Variation of flame speed with radius for stoichiometric methane-air mixtures at different ignition energies. Reproduced from Bradley *et al.* (1996a).

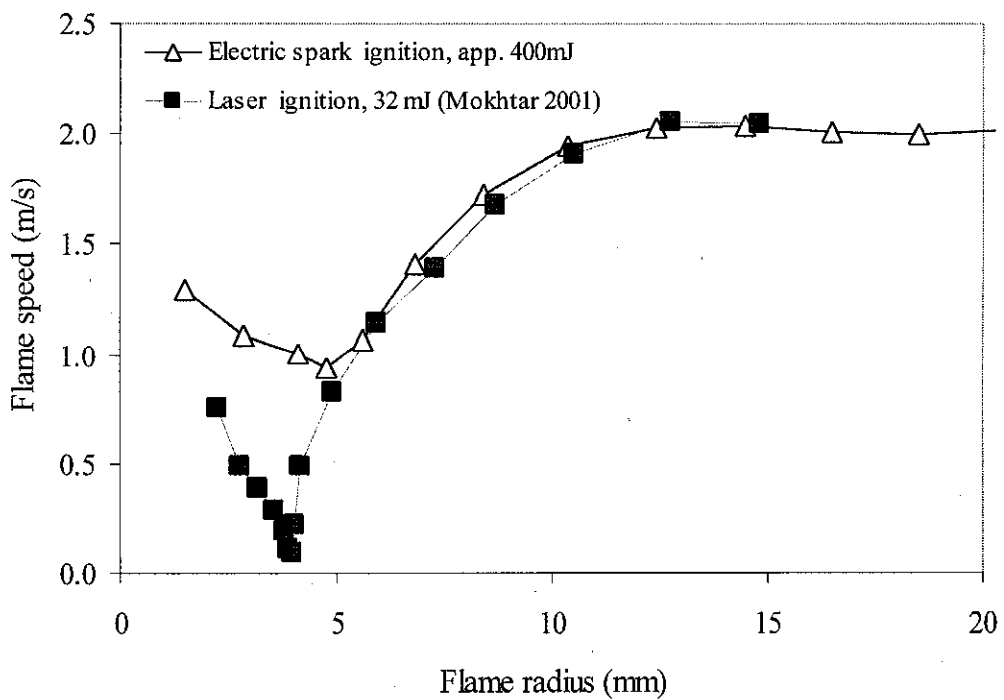


Figure 5.4 Variation of flame speed with radius for different ignition types and energies. Laminar flames within aerosols at $\phi_{ov} = 1.0$, $T = 270$ K, $P = 120$ kPa and $D_{10} = 14$ μm .

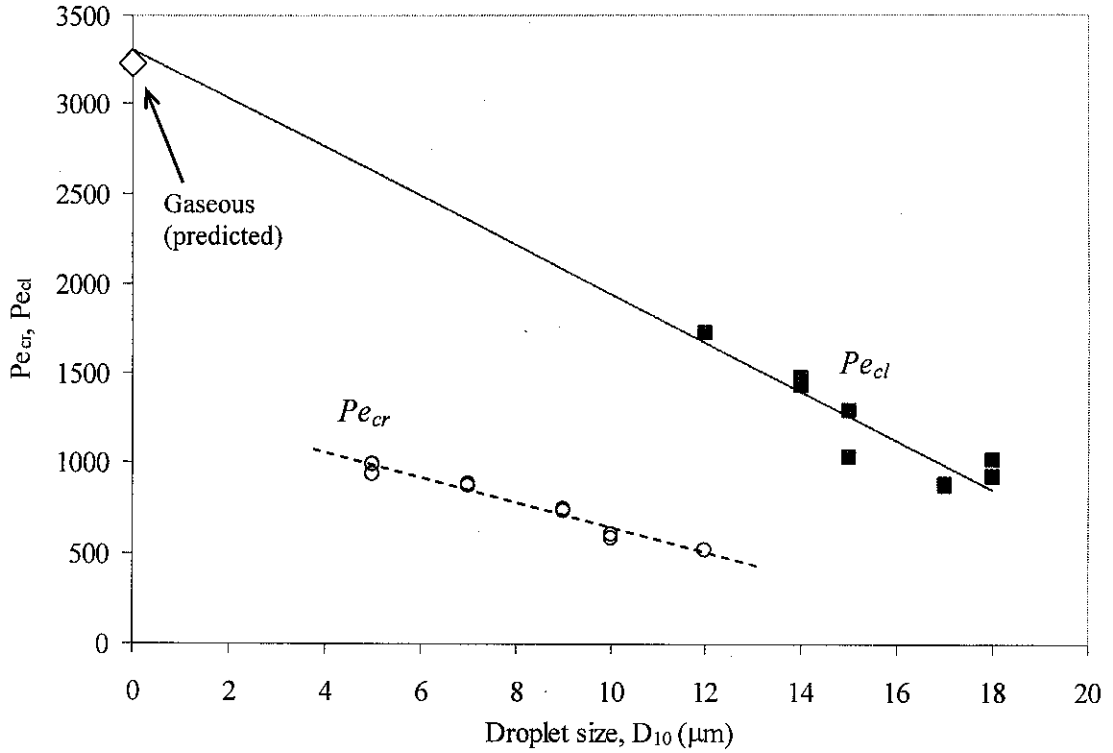


Figure 5.5 Pe_{cl} and Pe_{cr} for stoichiometric iso-octane-air aerosol flames as a function of D_{10} , at pressures of between 134 and 185 kPa, and temperatures of between 267 and 281 K.

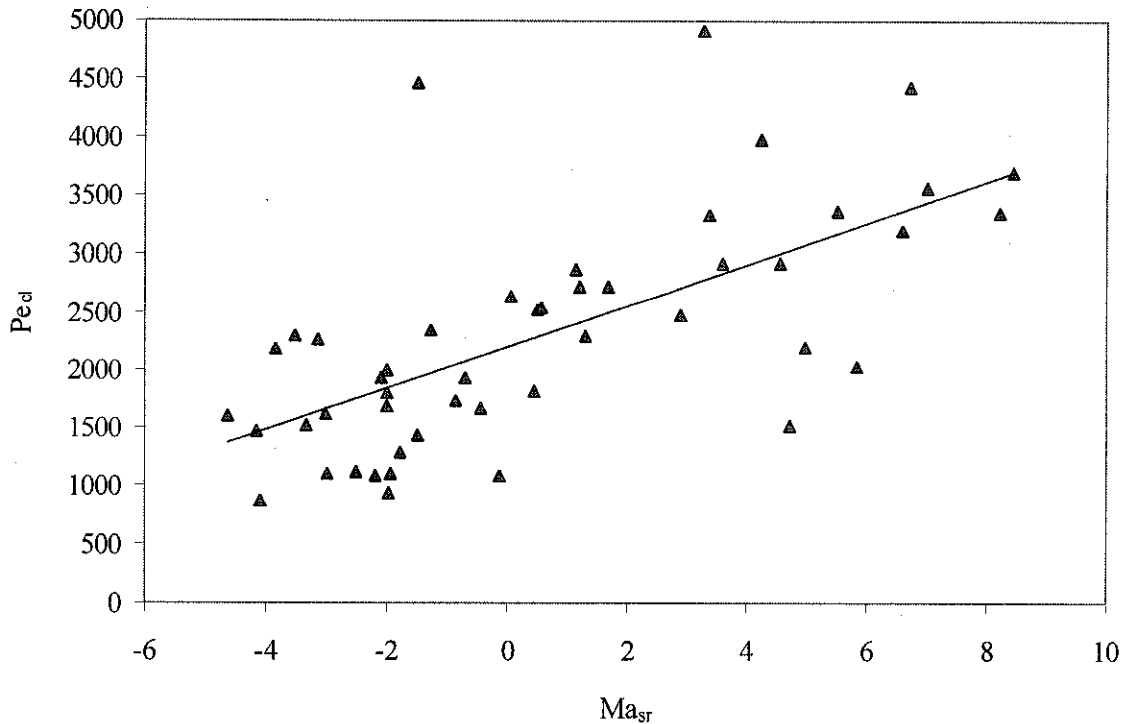


Figure 5.6 Variations of Pe_{cl} with Ma_{sr} for various gaseous flames. Reproduced from Gu *et al.* (2000).

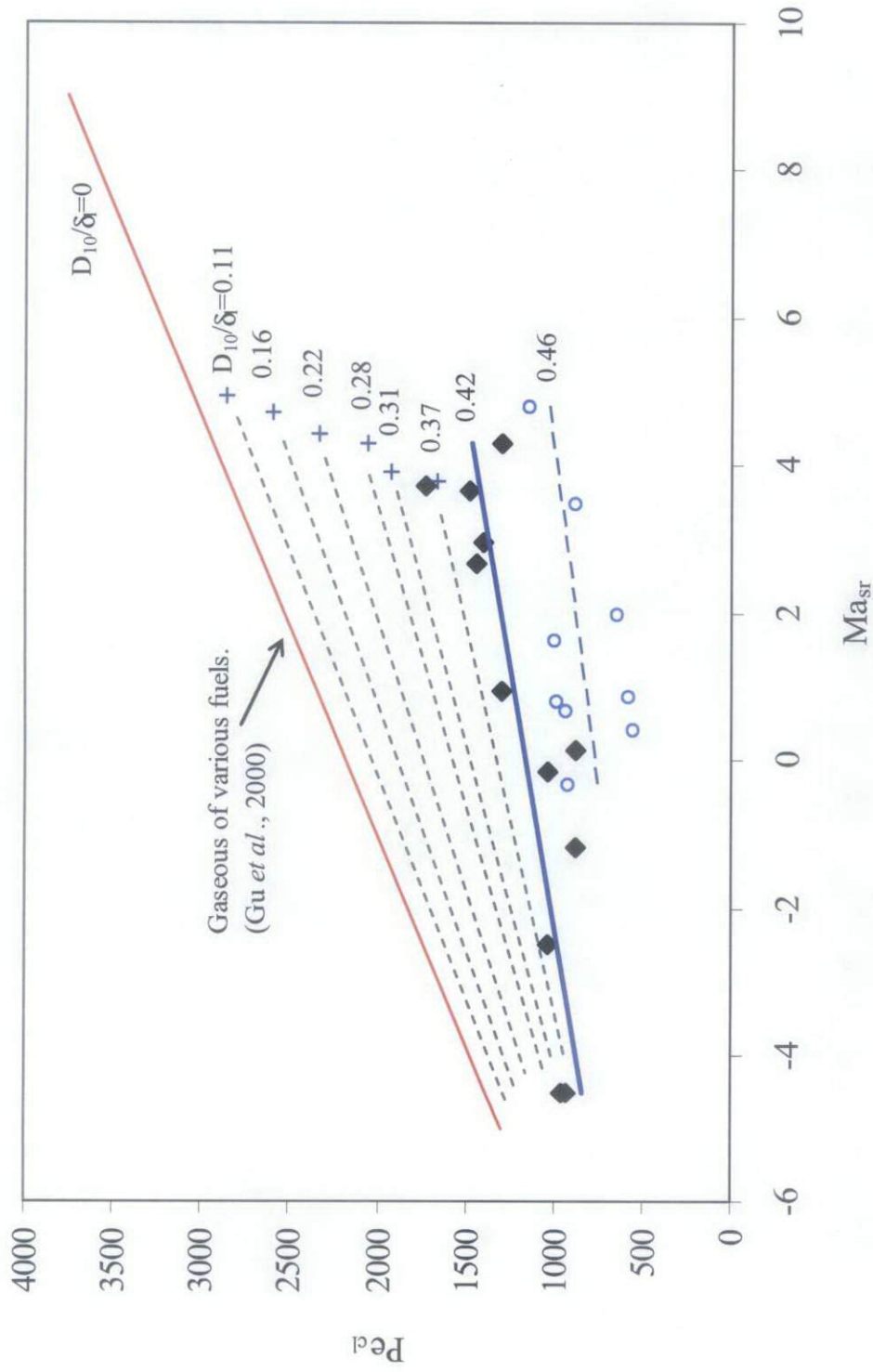


Figure 5.7 Variations of Pe_{cl} with Ma_{sr} for aerosol flames at $\phi_{ov} = 1.0$ (diamonds and crosses) and at $\phi_{ov} = 1.1$ (circles). Also shown is the linear curve fit for the gaseous flames (Gu *et al.*, 2000) in Fig. 5.6.

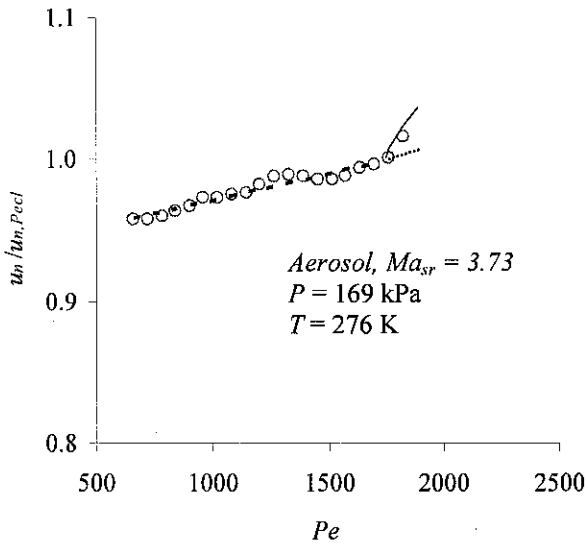
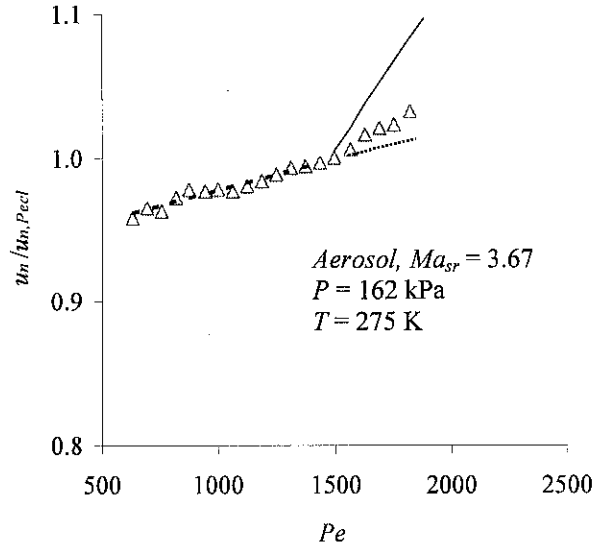
(a) $\phi_{ov} = 1.0$ and $D_{10} = 12 \mu\text{m}$.(b) $\phi_{ov} = 1.0$ and $D_{10} = 14 \mu\text{m}$.

Figure 5.8 Dimensionless burning velocity, u_n / u_{n-Pecl} , as a function of Pe for aerosol iso-octane-air flames.

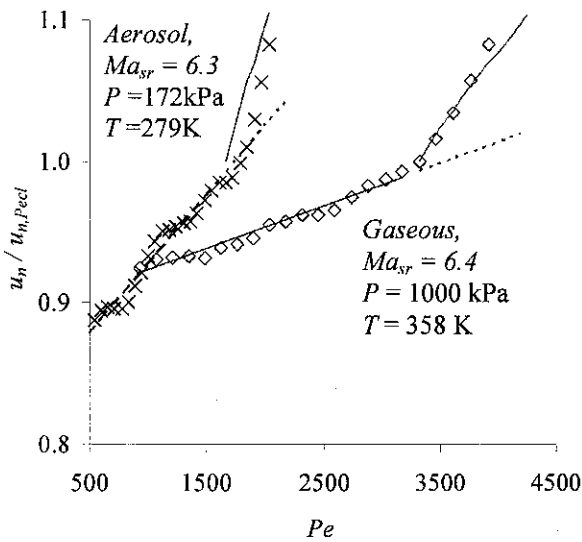
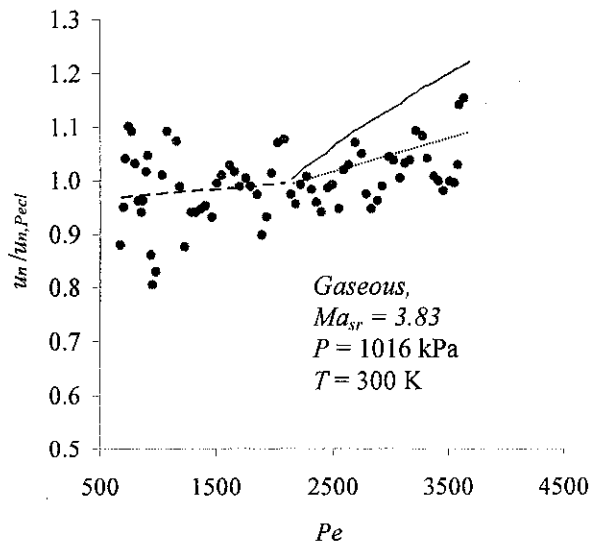
(a) iso-octane flames: aerosol at $\phi_{ov} = 1.2$, $D_{10} = 17 \mu\text{m}$ and gaseous at $\phi_{ov} = 1.0$; reproduced from Lawes *et al.* (2005).(b) gaseous methane-air at $\phi = 1.2$, calculated using data from (Haq, 1998).

Figure 5.9 Dimensionless burning velocity, u_n / u_{n-Pecl} , as a function of Pe for aerosol and gaseous flames, obtained from data of previous works.

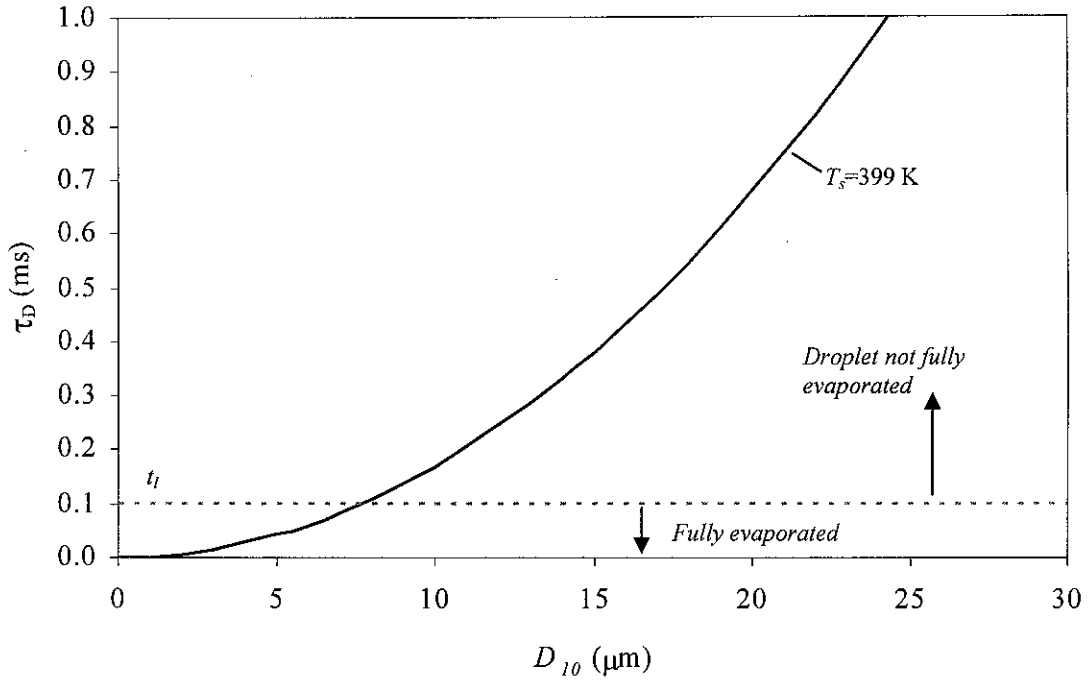


Figure 5.10 Estimation of droplet lifetime using the d^2 -law for stoichiometric iso-octane-air aerosol at $P = 100$ kPa, $T = 273$ K, assuming $T_\infty = 2275$ K.

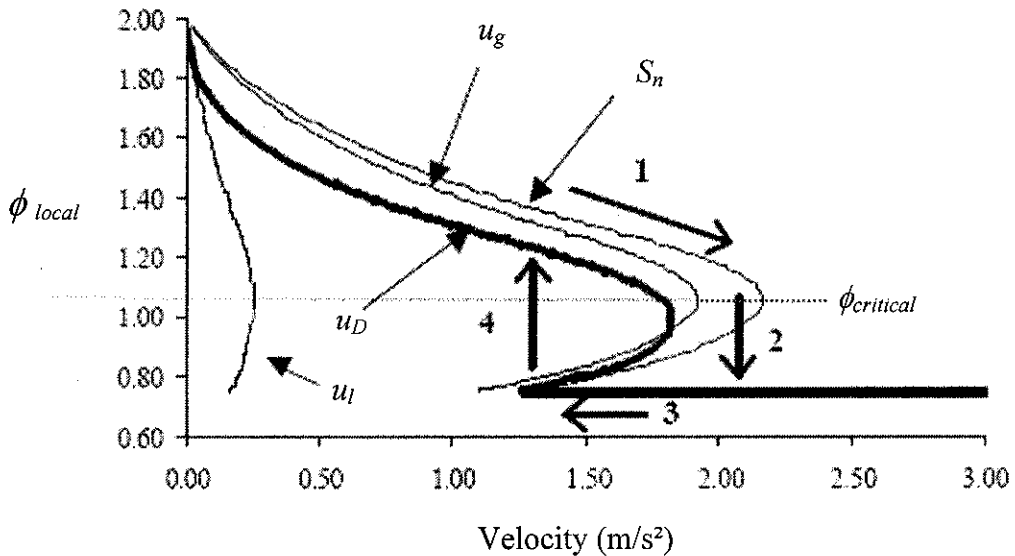


Figure 5.11 Graphical representation of Eq. (5.4) showing the effect of a variation of u_D on the local ϕ (at the reaction zone) and resulting values of S_n , u_g and u_l for an iso-octane aerosol at $\phi_{ov} = 1.0$ and $\phi_g = 0.75$. Reproduced from Atzler *et al.* (2001).

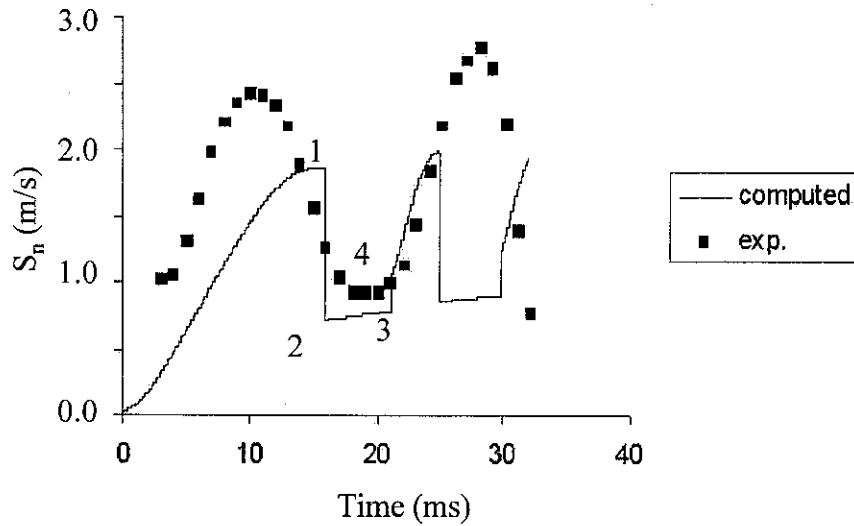


Figure 5.12 Variation of S_n with time for an oscillating aerosol flame of iso-octane; comparison of experimental ($\phi_{ov} = 1.0$, $\phi_g = 0.75$) and numerical results ($\phi_{ov} = 0.95$). Reproduced from Atzler *et al.* (2001).

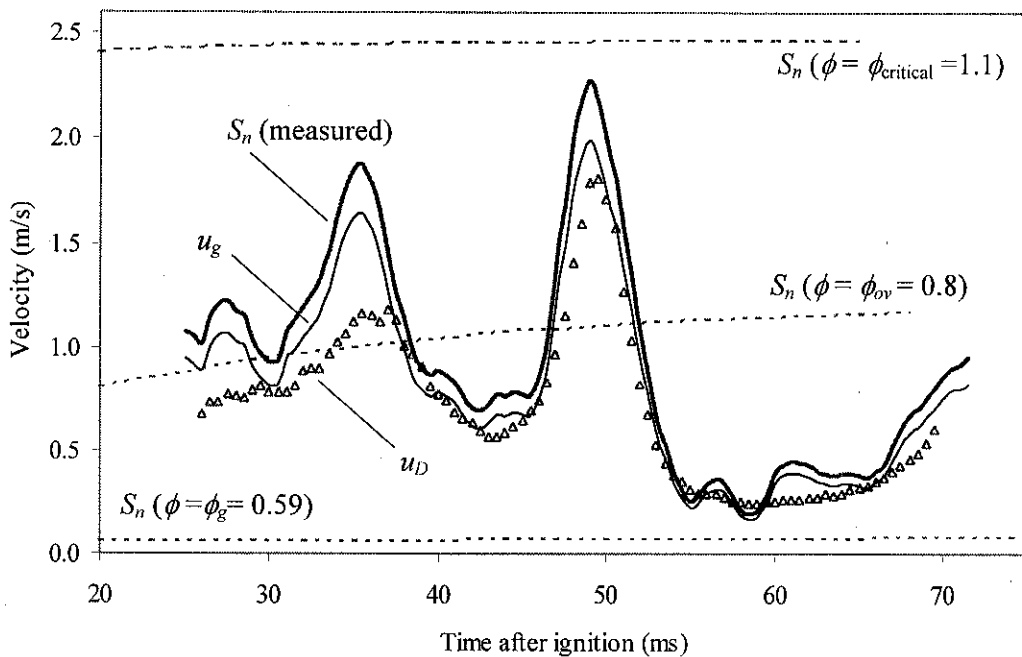


Figure 5.13 Variation of S_n , u_g , and u_D with time after ignition for an aerosol flame at $\phi_{ov} = 0.8$, $P = 110$ kPa, $T = 265$ K, $D_{10} = 12$ μm . Also shown are values of S_n , estimated by Marquez (2003), for gaseous flames at $\phi = 0.59$, $\phi = 0.8$ and $\phi = 1.1$.

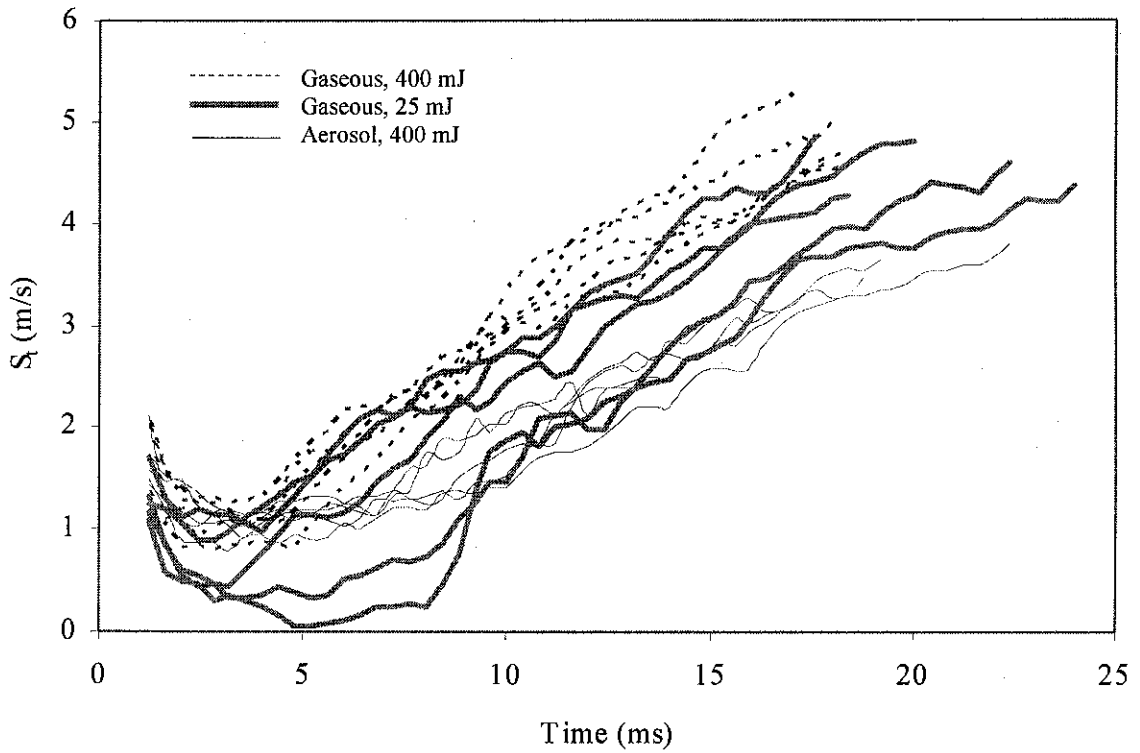


Figure 5.14 Variation of S_t with time for the turbulent flames in Figs. 4.31 and 4.34 at $u' = 1.0$ m/s.

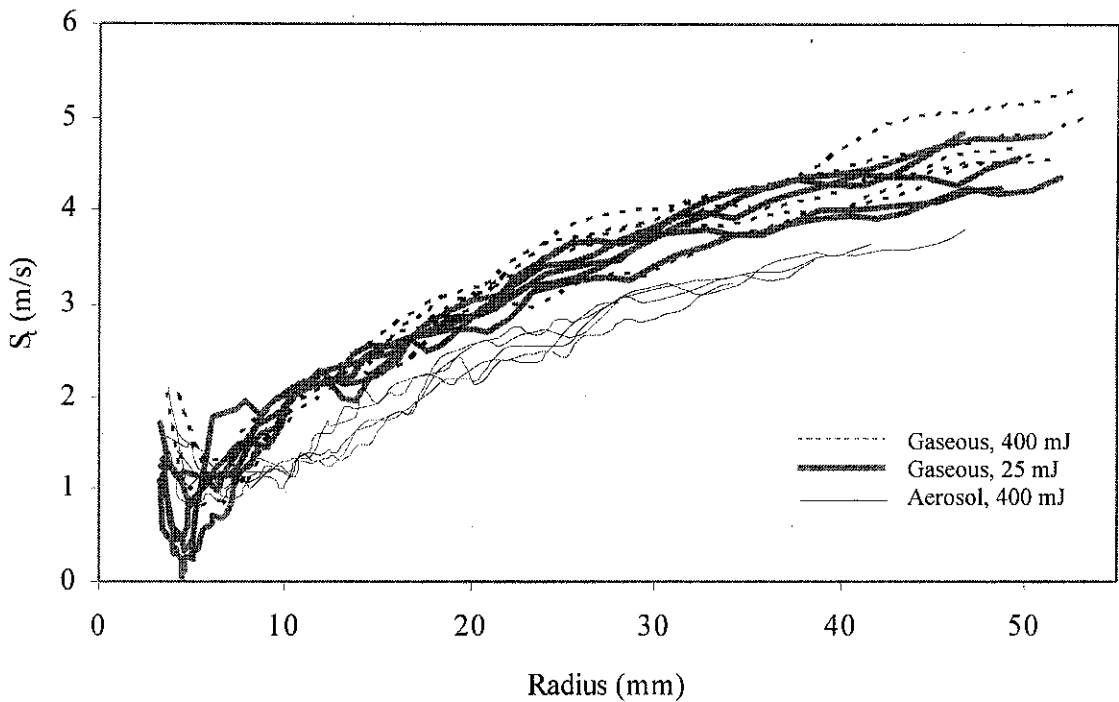


Figure 5.15 Variation of S_t with radius for the turbulent flames in Fig. 4.30 and 4.35 at $u' = 1.0$ m/s.

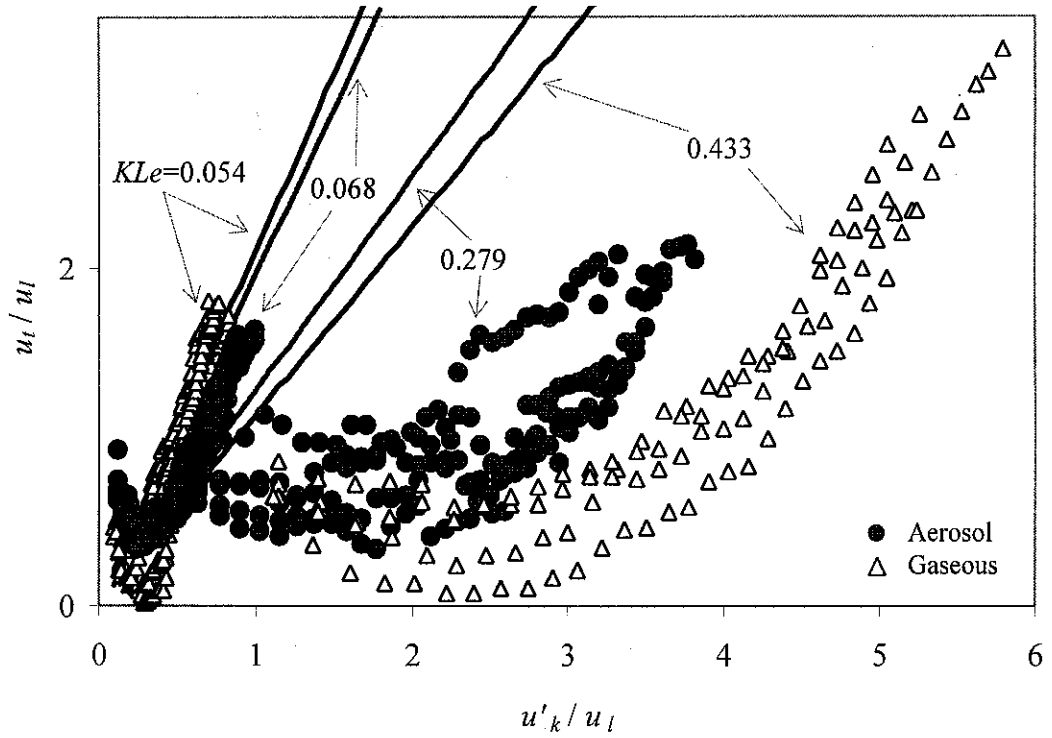


Figure 5.16 Comparison of the variation of turbulent burning velocity in terms of dimensionless groups for iso-octane-air flames at $\phi_{ov} = 1.0$.

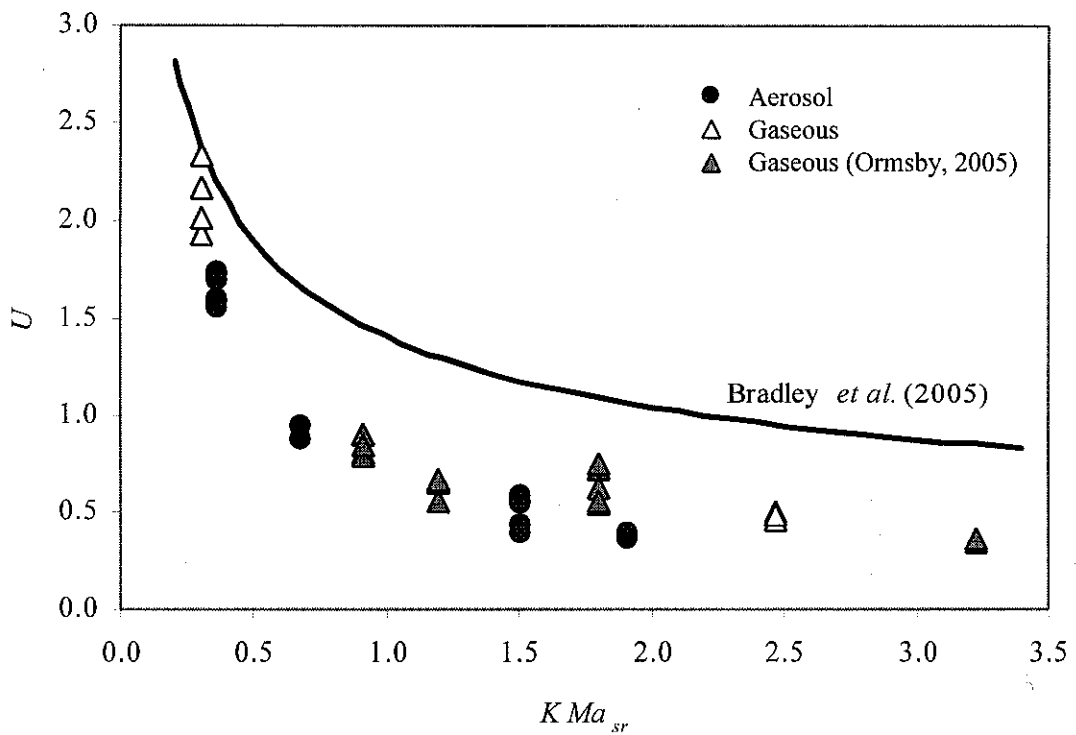


Figure 5.17 Variations of $U (u_l / u'_k)$ with $K Ma_{sr}$ for iso-octane-air in the present work and Ormsby (2005), and for the theoretical expression by Bradley *et al.* (2005).

Chapter 6

Conclusions and Suggestions for Further Research

The present thesis comprises a fundamental study of spherical premixed and aerosol flames of iso-octane-air mixtures. It utilised a combustion apparatus based on the Wilson cloud chamber principle for the observation of flame propagation under laminar and turbulent conditions using schlieren photography and planar laser sheet imaging. The effects of equivalence ratio, arithmetic mean droplet diameter, mixture temperature and pressure on flame speed, burning velocity and cellularity have been investigated. The results for gaseous combustion were compared with those for aerosols. Important aspects of aerosol flame structure and burning rates have been revealed by the present work. For some experimental conditions, strong flame oscillations were observed, as addressed in Section 4.4, and possible causes for this phenomenon were examined.

The main conclusions that are drawn from the present work are itemised in Section 6.1. This is followed by some suggestions for further research in Section 6.2.

6.1 Conclusions

1. Aerosols were generated in a well controlled environment in a novel combustion apparatus based on the Wilson cloud chamber principle, as described in Section 2.3. This method uses the cooling of a fuel-air mixture by expansion to cause the condensation of a part of the initially evaporated fuel

into a fog of droplets. The expansion method offered some flexibility to cover a wide variety of conditions through the use of different pre-expansion pressures, temperatures and equivalence ratios. The droplets generated in the present work were homogeneously distributed in space, and were of nearly equal size. These are important pre-requisites for a well defined fundamental study of aerosol combustion. The aerosols in the present work comprised droplets, vapour and air. This resembles a condition in, for example, a Direct Injection Spark Ignition (DISI) engine, in which a mixture of liquid and vapour can exist within the reaction zone, as highlighted in Section 1.6.1.

2. Data on burning properties for quiescent iso-octane-air aerosol at equivalence ratios of between 0.8 and 2.0 were collected, as presented in Table 4.1, to investigate their effects on instabilities. The arithmetic mean diameters of the aerosols were up to 30 μm , and these were within the range relevant to the current trend of engine research. The aerosols were characterised experimentally and theoretically, as described in Chapter 3, for a range of mixture pressures, temperatures and overall equivalence ratios. It would have been informative to be able to vary, for example, the liquid fraction, drop size and number density independently. Nevertheless these parameters are often not independent in practical applications and the present results have revealed valuable new information.
3. The present studies were based on investigations of spherically expanding explosions, its theoretical descriptions being well established for gaseous combustion (as addressed in Section 1.2). A wide range of experimental results for gaseous iso-octane-air flames were available, for example in

Ormsby (2005), but these were obtained at higher temperature, typically at 358 K, as compared to between 260 and 290 K for aerosols. Therefore, additional data for gaseous iso-octane-air flames at temperatures, closer to those of the aerosols, were produced for comparison. A slight difference in temperature and pressure between gases and aerosol flames was inevitable because of the method of thermodynamic aerosol generation, as described in Section 4.1. However, Bradley *et al.* (1998) have shown that, for gaseous flames, such small difference in pressures and temperatures have little effect on laminar burning velocity. Therefore, in the opinion of the present Author, the comparisons between the aerosol and gaseous mixtures are valid despite the slightly different test conditions.

4. The scatter in the fundamental unstretched laminar burning velocities within the aerosol flames was small, with a maximum standard deviation of 6.3 %, when compared at the same equivalence ratio and similar range of initial mixture conditions, as discussed in Section 4.2.1 and shown in Fig. 4.15. In addition, the difference between the average unstretched laminar burning velocity for the aerosol flames and that for the gaseous flames at similar condition is small, between 0.7 and 6.9 %. This contradicts the results of Atzler (1999) who suggested that there was an enhancement in the unstretched laminar burning velocity of aerosol flames with respect to gaseous flames at similar conditions. In the opinion of the present Author, it is probable that Atzler had mistakenly measured the unstretched laminar burning velocity using flames that were already cellular and accelerating immediately after the end of the spark affected period, whereas it is discussed in Section 4.2.2 that with such an early flame acceleration the unstretched laminar burning properties such as L_b , S_s and u_l

could not be determined. This is supported by the fact, discussed in Section 4.1.3, that the images of Atzler's flame were less clear than those recorded in the present work, such that early presence of cells might not have been observed.

5. Enhancement in flame speed and stretched laminar burning velocity in aerosol flames relative to that of similar equivalent gaseous flames is reported in Section 4.2.2 and is illustrated in Fig. 4.18. For lean mixtures ($\phi_{ov} < 1.0$), the flame speed and stretched burning velocities are similar for aerosols and gaseous mixtures, with no effect of drop size. However, for rich mixtures, enhancement is shown to increase with droplet size. The enhancement was probably caused by the more rapid development of a cellular structure (instabilities) in aerosols than in gases, which in turn, increased the flame surface area and burning rate. In Section 5.2.1 it was proposed that the early development of cellular structure in aerosols was caused by a physical mechanism represented by the Markstein number, Ma_{sr} , which decreases with equivalence ratio and droplet diameter. Thus, it is concluded that the effect of stretch on aerosol flames is weaker than in gaseous flames. In addition to the Markstein number, the critical Peclet numbers, Pe_{cr} and Pe_{cl} , used by Bradley *et al.* (1998) to compare the susceptibility of laminar gaseous flames to cellularity, are also important in the study of aerosol instabilities. These have been measured for laminar aerosol flames in the present work, and are reported in Section 5.2.1.

6. Prior to the present work, it was not possible to determine the values of Pe_{cl} for gaseous flames that were smooth throughout their propagation within the radius of the vessel's window. However, with known values of Ma_{sr} for the gaseous

flames, predicted values of Pe_{cl} could be obtained, as discussed in Section 5.2.1, from a gaseous data correlation in Gu *et al.* (2000), which is presented in Fig. 5.6. The prediction method was validated by extrapolation of the Pe_{cl} to zero diameter, as demonstrated in Fig. 5.5.

7. In addition to the use of Ma_{sr} and Pe_{cl} to quantify the susceptibility of laminar gaseous and aerosol flames to instabilities, a new dimensionless parameter, the ratio of droplet diameter to flame thickness, D_{10}/δ_f , has been introduced in the present work. This is discussed in Section 5.2.1, and is introduced because any disturbance of the reaction zone by droplets is likely to be a function of it. The validity of this parameter is evident in Fig. 5.7, which implies its generalisation, along side Ma_{sr} and Pe_{cl} .
8. In Section 4.2.2, it is explained that quantification of flame instabilities, for example in terms of L_b , Ma_{sr} and Pe_{cl} , is limited to aerosols at $\phi_{ov} \leq 1.2$ due to early onset of cellularity (immediately after the end of the spark ignition period) among the richer flames. This limitation was also experienced in researches related to gaseous combustion, for example in Ormsby (2005). However, in the present work, an alternative parameter, $S_{n,48}$, has been proposed as a partial solution to this predicament. This parameter, as implied in Fig. 4.18, is proven to provide an effective approach in demonstrating the burning rate enhancement as a function of drop size and equivalence ratio.
9. In very rich mixtures ($\phi_{ov} \geq 1.8$), gaseous flames were observed to be influenced by buoyancy or natural convection, characterised by significantly faster upward flame propagation than that of downward propagation. This is discussed in

Section 4.3, and was also reported by Andrews and Bradley (1973). However, with the presence of droplets, the flames became unstable quickly and burned faster such that there was less time for natural convection to be influential.

10. The correlation in Fig. 5.7 between Pe_{cl} and Ma_{sr} for aerosol flames shows that Pe_{cl} increases with Ma_{sr} , and the same trend was found in gaseous flames by Bradley *et al.* (1998) and Gu *et al.* (2000). They showed it to be independent of the type of fuel, equivalence ratio, pressure and temperature. More importantly, the correlation shows that aerosol mixtures experience earlier instabilities (lower values of Pe_{cl}) than do gaseous flames. In addition, the ratio of D_{10}/δ_l , as discussed in Section 5.2.1, is proven to be useful to demonstrate the influence of droplet size on instabilities within aerosol flames. It represents the likelihood that droplets will survive into the reaction zone.
11. Simultaneous schlieren and laser sheet techniques were used to demonstrate that droplets can survive the flame front, as discussed in Section 4.1.4. This experimental evidence is supported in Section 5.2.2 by calculations of droplet lifetime, which values are generally larger than the time taken by droplets to traverse the reaction zone. This contradicts the complete evaporation assumption made in experiments (Marquez, 2003) and in theoretical works (Greenberg *et al.*, 1999 and Nicoli *et al.* 2005). Droplet evaporation in the reaction zone will clearly disrupt it and locally trigger instabilities.
12. The peninsula of instabilities (Section 1.3) and the fractal approach given in Eq. (1.14) was applied to the experimental data (of the present work, Haq, 1998 and Lawes *et al.*, 2005) to predict the burning velocity enhancement by

instabilities. However, it is revealed in Section 5.2.1 that there is a mix of good and poor agreement between the theoretical prediction and experimental values of the cellular burning velocities. Hence, this suggests that the fractal approach is probably not robust. One possible reason for the inconsistency is due to the difficulty of accurately determining the transition from Pe_{cr} to Pe_{cl} . Some flames probably display rapid transition, whereas for others, the transition is more gradual. Furthermore, it is evident in Section 4.1.3 that earlier experiments did not have sufficient optical quality to accurately define Pe_{cr} . Further research is required to correct the theoretical prediction.

13. Oscillating flames, characterised by alternating fast and slow modes of flame propagation, were observed for aerosols with overall equivalence ratios of between 0.8 and 1.0 at droplet diameters larger than 8 μm . This is presented in Section 4.4. The phenomenon of flame oscillation was investigated using a simple aerodynamic model (Atzler *et al.*, 2001). It suggested that due to droplet inertia, the real equivalence ratio within the reaction zone varied and, at times, was larger than the overall equivalence ratio. Consequently this influenced the instantaneous flame speed and led to oscillations. The modelled predictions were verified in Section 5.2.3.3 by an experiment with simultaneous measurements of flame speed and droplet velocity using a single camera. The experiment showed a phase lag between variations in flame speed and droplet velocity. Although the experiment was difficult and subject to inaccuracy the present Author believes them to be sufficiently accurate to confirm the modelled predictions.

14. The present work has enabled identification of the regimes (Fig. 4.4) of laminar aerosol combustion for iso-octane-air mixtures, at various values of D_{10} and ϕ_{ov} within the limits of flammability ($0.8 \leq \phi_{ov} \leq 2.0$), in terms of surface structure (smooth or cellular) and flame speed (stable, accelerating, oscillating) as well as buoyancy affected flames (Section 4.3).

15. In turbulent aerosol flames, 'black clouds' were observed especially at higher turbulence, as addressed in Section 4.5. These obscured the flame edge and consequently hindered measurement of flame radius. Although no account of the 'black clouds' was given in Marquez (2003), who performed a similar experiment, the images of his turbulent aerosol flames, when studied by the present Author, revealed mild signs of them. It was probable that Marquez did not notice them because his experiments were at relatively lower levels of turbulence ($u' \leq 2.5$ m/s). Further experiments by the present Author on turbulent aerosol flames using laser ignition showed no 'black clouds,' thus suggesting that some effect of electric spark ignition, probably flying hot fragments from the spark electrode, which interacted with droplets causing them to vaporise, might be the cause. Because spark electrodes are also used for ignition in DISI engines, it is also possible that the 'black clouds' might be present in such engines. The actual nature of the 'black clouds' is still unknown and further work is recommended.

16. The effect of ignition energy in turbulent flames is demonstrated in Section 4.6.1, in which flames ignited by low energy spark are generally slower than those ignited with higher energy spark, possibly as a result of heat loss from the flame kernel to the spark plug. However, once the flames start to

accelerate (out of the spark affected period) their trend is similar to that shown by the correlation of Abdel-Gayed *et al.* (1987) and Bradley *et al.* (2005).

17. Although laminar flames are faster within aerosols than within gaseous mixtures, as demonstrated in Section 5.2.1, the presence of droplets does not cause any increase in the flame propagation rate under turbulent conditions. This is discussed in Section 5.3.2. It is shown that the enhancing effects of instabilities triggered by the presence of an aerosol are not applicable to turbulent flames due to the strong effect of stretch, which damps down instabilities. Therefore, any reliable correlation of turbulent burning velocities for gaseous flames is probably applicable for aerosols.

18. Turbulent burning velocities from the correlations (Bradley, 1992, Bradley *et al.*, 2005) are clearly shown in Section 5.3.2 to be over predicted when compared with the experimental data of the present work and those in Ormsby (2005). This is probably due to the effect of ignition. The flame in the present work and in Ormsby (2005) was ignited by a central spark, in which the flame development, as discussed in Section 4.6.1, was a function of ignition energy. Conversely, the data from which the correlation of Bradley (1992) is based, were obtained from experiments in burners and the flame on them was already developed (Lawes, 1987), and thus ignition did not have any significant role as compared to the present work. Similarly, the data for the correlation of Bradley *et al.* (2005) were obtained from twin kernel implosion experiments in the later stage of flame growth, and thus were not influenced by the effect of ignition. Hence, it is clearly demonstrated that the correlation for turbulent

burning velocity must include a parameter to take into account the effect of ignition and the effect of their development.

6.2 Suggestions for Further Research

1. In the experiment with simultaneous laser sheet and schlieren techniques, described in Section 4.1.4, it has been demonstrated that droplets can survive the flame front, although the camera recorded at a rate of only one frame per millisecond. Since it is shown in Section 5.2.2 that the calculated droplet lifetime for the range of droplet sizes in the present work ($D_{10} < 30 \mu\text{m}$) is in the order of a tenth of a millisecond, the use of a faster camera would enable more accurate tracking of the existence or disappearance of droplets at the flame front.
2. From the experience of the present Author, the wall temperature of the present explosion vessel can increase to a value higher than the operating temperature by between 1 and 5 K, after each combustion experiment as a result of heat transfer from the flame, particularly during the summer. Therefore, the explosion vessel requires cooling down, which normally takes between 30 and 120 minutes, prior to the next experiment. Thus the productivity of the study is reduced. To overcome this problem a mechanical cooling system is recommended to quickly reduce the temperature of the explosion vessel to the required operating temperature.
3. Measurement of burning properties of gaseous flames at initial pressure and temperature closer to those of aerosols could provide a more accurate

comparison between gases and aerosol flames. This may be achieved by igniting the mixture during expansion but before the onset of condensation.

4. Experiments at higher pressures are required in order to assess the effect of pressure on aerosol combustion. In a recent work, Nomura *et al.* (2006) studied the effect of pressure on ethanol-droplet-vapour-air mixtures at pressures between 200 and 1000 kPa using a technique similar to that in the present work. However their work was limited to droplet diameters of 8 μm and measurements of flame speed at a flame radius of 30 mm. The maximum safe operating pressure of the current explosion vessel is only 300 kPa at ignition (Atzler, 1999). Therefore, the use of the Leeds Mk-2 bomb (Bradley *et al.*, 1996b) is recommended in aerosol studies as this would allow initial pressures of up to 1000 kPa to be studied. In addition, the use of such a high pressure bomb would enable experiments with larger droplets ($> 30 \mu\text{m}$) than in the present work, which may therefore provide additional evidence to assess the interaction between droplets and the flame front. This is important because a larger range of droplet sizes exist in gas turbines.
5. The effects of equivalence ratio and droplet size on turbulent aerosol flames were not studied in the present research. Therefore combustion characteristics at a wide range of conditions, for example, the variation of flame speed with equivalence ratio as in Fig. 4.18 for laminar flames, remain unexplored. This probably offers an interesting extension to the present work.
6. It is argued in Point (12) of Section 6.1 that the fractal approach proposed by Al-Shahrany *et al.* (2005) is possibly not robust. Extended research is required

in order to understand and rectify the disagreement between the predicted and experimental values of cellular burning velocity. A suggested approach would be to consider the most recent proposal by Bradley *et al.*, (2007), that is to re-express the data bank of experimental and theoretical values of Pe_{cl} , in terms of a dimensionless critical Karlovitz stretch factor, K_{cl} , given by $\alpha (\delta/u_l)$.

7. The wavelength and amplitude of flame cells, which can be used to determine flame surface area, has never been quantified. Bradley (1999) assumed constant proportionality between the diameter and amplitude of cells throughout flame propagation, and therefore did not include amplitude as a parameter in the expression for wave number in Eq. (1.12). However, such an assumption has never been proven by experiment. A suitable method for this study must be researched, for example with the use of Planar Laser-Induced Fluorescence (PLIF) from the OH radical (Bradley *et al.*, 2000).
8. The ‘black clouds,’ addressed in Section 4.5, were probably soot, which is an element of exhaust emissions from spray combustion. With the increasing demand for stricter emission regulations, as addressed in Section 1.1, understanding of the detailed mechanisms of soot formation around droplets would be imperative. This might be achieved through the use of Laser Induced Incandescent (LII), for example in Tait and Greenhalgh (1993) and Lui *et al.* (2006).
9. Further to the availability of data from the present study of combustion on homogeneous droplet clouds, it would be useful to link the results with real engines. Therefore research on combustion with sprays, perhaps in an explosion

vessel, should be undertaken to investigate the interaction between turbulence and sprays. This would be interesting because in an explosion vessel complications that are experienced in real engines, such as moving piston and varying ambient pressure and temperature, can be eliminated.

References

Abdel-Gayed, R. G., Al-Khishali, K. and Bradley, D., Turbulent Burning Velocities and Flame Straining in Explosions, Proc. Roy. Soc. London, A391, pp. 393-414, 1984.

Abdel-Gayed, R. G., Bradley, D., Lawes, M., and Lung, F., Premixed Turbulent Burning During Explosion, 21st Symposium (International) on Combustion, The Combustion Institute, pp. 497-504, 1986.

Abdel-Gayed R. G., Bradley D. & Lawes M., Turbulent Burning Velocities: A General Correlation in Terms of Straining Rates, Proc. Roy. Soc. London, A414, pp. 389-413, 1987.

Akamatsu, F., Nakabe, K., Mizutani, Y., Katsuki, M., and Tabata, T., Structure of Spark-Ignited Spherical Flames Propagating in a Droplet Cloud, in Developments in Laser Techniques and Applications to Fluid Mechanics (ed. R.J. Adrian, *et al.*), Springer-Verlag, Berlin, pp. 212-223, 1996.

Al-Shahrany, A. S., Experimental and Theoretical Studies of Combustion Rates at High Pressure, PhD Thesis, School of Mechanical Engineering, University of Leeds, 2004.

Al-Shahrany, A. S., Bradley, D., Lawes, M., and Woolley, R., Measurement of Unstable Burning Velocities of Iso-octane-air Mixtures at High Pressure and Derivation of Laminar Burning Velocities, 30th Symposium (International) on Combustion, Proc. Combustion Institute, Vol. 30, pp. 225-232, 2005.

Andrews G. E. and Bradley D., Determination of Burning Velocities, A Critical Review, Combustion and Flame, Vol. 18, pp. 133-153, 1972.

Andrews, G. E. and Bradley, D., Limits of Flammability and Natural Convection for Methane-Air Mixtures, 14th Symposium (International) on Combustion, The Combustion Institute, pp. 1119-1128, 1973.

Annamalai K. and Ryan W., Interactive Processes in Gasification and Combustion, Part I: Liquid Drop Arrays and Clouds, Progress in Energy and Combustion Science, Vol. 18, pp. 221-295, 1992.

Ashurst W. T., Darrieus-Landau Instability, Growing Cycloids and Expanding Flame Acceleration, Combustion Theory Modelling, pp. 405-428, 1997.

Atashkari, K., Experimental Study of Flow and Turbulence in a V-Flame Burner and a S.I. Engine, PhD Thesis, School of Mechanical Engineering, University of Leeds, 1997.

Atzler, F., Fundamental Studies of Aerosol Combustion, PhD Thesis, School of Mechanical Engineering, University of Leeds, 1999.

Atzler, F., Demoulin, F. X., Lawes, M. and Lee, Y., Oscillations in the Flame Speed of Globally Homogeneous Two Phase Mixtures, Proc. of the 18th International Colloquium on the Dynamics of Explosions and Reactive Systems, Paper No. 83, 2001.

Aung, K. T., Tseng, L. K., Ismail, M. A. and Faeth, G. M., Response to Comment by S. C. Taylor and D. B. Smith on 'Laminar Burning Velocities and Markstein Numbers of Hydrocarbon/Air Flames', Combustion & Flame, Vol. 109, pp. 526-530, 1995.

Bachalo, W. D., Rosa, A. B., Sankar, S. V., Diagnostic for Fuel Spray Characterization, in: Combustion Measurements (N Chigier, Ed.), Hemisphere, New York, pp. 229-278, 1991.

Ballal, D. R. and Lefebvre, A. H., Ignition and Flame Quenching of Quiescent Fuel Mists, Proc. R. Soc. London, A364, pp. 277-294, 1978.

Ballal, D. R. and Lefebvre, A. H., Flame Propagation in Heterogeneous Mixtures of Fuel Droplets, Fuel Vapor and Air, 18th Symposium (International) on Combustion, The Combustion Institute, pp. 321-328, 1981.

Bechtold, J. K., and Matalon, M., Hydrodynamic and Diffusion Effects on the Stability of Spherically Expanding Flames, *Combustion and Flame*, Vol. 67, pp. 77-90, 1987.

Boilson, D., Hemsworth, H. P. L. de Esch, R., Krylov, A., Massmann, P., Rada, M., and Svensson, L., Effect of Argon Seeding on the Negative Ion Yield of the Kamaboko III Ion Source, *Fusion Engineering and Design*, Vol. 66-68, pp. 609-614, 2003

Borghini, R., in: *Recent Advances in the Aerospace Sciences* (C. Bruno and C. Casci, Eds.), Plenum Press, New York, 1985.

Bradley, D., Instabilities and Flame Speeds in Large-Scale Premixed Gaseous Explosions, *Phil. Trans. R. Soc. London*, A357, pp. 3567- 3581, 1999.

Bradley, D., Gaskell, P. H., and Gu, X. J., Burning Velocities, Markstein Lengths and Flame Quenching for Spherical Methane-Air Flames: A Computational Study, *Combustion and Flame*, Vol. 104, pp. 176-198, 1996a.

Bradley, D., Gaskell, P. H., Gu, X. J. and Sedaghat, A., Premixed Flamelet Modelling: Factors Influencing the Turbulent Heat Release Rate Source Term and the Turbulent Burning Velocity, *Combustion and Flame*, Vol. 143, pp. 227-245, 2005.

Bradley, D., Haq, M. Z., Hicks, R. A., Kitagawa, T., Lawes, M., Sheppard, C. G. W., and Woolley, R., Turbulent Burning Velocity, Burned Gas Distribution, and Associated Flame Surface Definition, *Combustion and Flame*, Vol. 133, pp. 415-430, 2003.

Bradley, D., and Harper, C. M., The Development of Instabilities in Laminar Explosion Flames, *Combustion and Flame*, Vol. 99, pp. 562-572, 1994.

Bradley, D., Hicks, R. A., Lawes, M., and Sheppard, C. G. W., Study of Turbulence and Combustion Interaction: Measurement and Prediction of the Rate of Turbulent Burning. Technical Report, Department of Mechanical Engineering, The University of Leeds, UK, 1996b.

Bradley, D., Hicks, R. A., Lawes, M., Sheppard, C. G. W., and Woolley, R., The Measurement of Laminar Burning Velocities and Markstein Numbers of Iso-Octane-Air and Iso-Octane-n-Heptane-Air Mixtures at Elevated Temperatures and Pressures in an Explosion Bomb, *Combustion and Flame*, Vol. 115, pp.126-144, 1998.

Bradley, D., Lau, A.K.C. and Lawes, M., Flame Stretch Rate as a Determinant of Turbulent Burning Velocity, *Phil. Trans. R. Soc. London*, A338, pp. 359-387, 1992.

Bradley, D., Lawes, M. and Liu, K., Limiting Flame Stretch Rates for Flame Instabilities and Flame Quenching, Submitted for publication at 5th International Seminar on Fire and Explosion Hazards, Edinburgh, 2007.

Bradley, D., Sheppard, C.G.W., Woolley, R., Unstable Explosion Flames and Acoustic Oscillations, 18th International Colloquium on the Dynamics of Explosions and Reactive Systems, Seattle USA , 2001.

Bradley, D., Sheppard, C. G. W., Woolley, R., Greenhalgh ,D. A., and Lockett, R. D., The Development and Structure of Flame Instabilities and Cellularity at Low Markstein Numbers in Explosions, Vol. 122, pp. 195-209, 2000.

Brundish, K. D., Foster T. J., Gray C. R., Seoud R. E. & Wilson C. W., The Use of Axially Fuel Staged Combustion in Gas Turbine Combustors, *Proc. 4th Int. Conf. on Technologies & Combustion for a Clean Environment*, Lisbon, Portugal, 1997.

Burgoyne, J. H. and Cohen, L., The Effect of Drop Size on Flame Propagation in Liquid Aerosols, *Proc. Roy. Soc. London*, A225, pp. 375-392, 1954.

Chiu, H. H., Modern Developments in the Mechanics and Combustion of Many Droplet Systems, in: *Mechanics and Combustion of Droplets and Spray* (H. H. Chiu, N. Chigier, Eds), pp. 163-186, Begell House, New York, 1995.

Chiu, H. H. and Croke, E. J., *Group Combustion of Liquid Fuel Sprays*, University of Illinois at Chicago, Energy Technology Laboratory Report 81-2, 1982.

Chiu, H. H. and Liu, T. M., *Group Combustion of Liquid Droplets*, *Combustion Science and Technology*, Vol. 17, pp. 127-142, 1977.

Clavin, P., *Dynamic Behaviour of Premixed Flame Fronts in Laminar and Turbulent Flows*, *Progress in Energy and Combustion Science*, Vol. 11, pp. 1-59, 1985.

Clavin, P. and Sung, J., *Theory of Acoustic Instabilities of Planar Flames Propagating in Sprays or Particle-Laden Gases*, *Combustion Science and Technology*, Vol. 78, pp. 265-288, 1991.

Darrieus G., *Propagation d'un Front de Flamme*, Unpublished Work Presented at La Technique Moderne, Paris, France, 1938.

Dixon-Lewis, G., *Structure of Laminar Flames*, 23rd Symposium (International) on Combustion, The Combustion Institute, pp. 305-324, 1990.

Dowdy D. R., Smith D. B., Taylor S. C. & Williams A., *The Use of Expanding Spherical Flames to Determine Burning Velocities and Stretch Effects in Hydrogen Air Mixtures*, 23rd Symposium (International) on Combustion, The Combustion Institute, pp. 325-332, 1991.

Durao, D. F. G. and Heitor, M. V., *Modern Diagnostic Techniques for Combusting Flows: An Overview*, in *Combusting Flow Diagnostics*, (D.F.G. Durao *et al.* Eds.), Kluwer Academic Publishers, pp. 1-45, 1992.

Eckstein, J., Freitag, E., Hirsch, C., Sattelmayer, T., Bank, R., Schilling, T., Forced Low-Frequency Spray Characteristics of a Generic Airblast Swirl Diffusion Burner, *Journal of Engineering for Gas Turbines and Power*, Vol. 127, pp. 301-306, 2005.

Eder, A. and Jordan, M., The Schlieren Technique, in: *Optical Measurements: Techniques and Applications* (F. Mayinger, F. and O. Feldmann, Eds), Springer, Berlin, pp. 5-16, 2001.

El-Banhawy, Y., and Whitelaw, J. H., Experimental Study of the Interaction Between a Fuel Spray and Surrounding Combustion Air, (1981), *Combustion and Flame*, Vol. 42, pp. 253-275, 1981.

Faeth, G. M., Evaporation and Combustion in Sprays, *Progress in Energy and Combustion Science*, Vol. 9, pp. 1-76, 1983.

Farrell, J. T., Johnston, R. J., and Androulakis, I. P., Molecular Structure Effects on Laminar Burning Velocities at Elevated Temperature and Pressure, SAE Paper No. 2004-01-2936, 2004.

Fujimoto, M., Nishida, K., Hiroyasu, H. and Tabata, M., Influence of Mixture Stratification Pattern on Combustion Characteristics in a Constant-volume Combustion Chamber, SAE Paper No. 952412, 1995.

Gillespie, L., Lawes, M., Sheppard, C. G. W., and Woolley, R., Aspects of Laminar and Turbulent Burning Velocity Relevant to S.I. Engines, SAE Paper No. 2000-01-0192, 2000.

Godsave, G. A. E., Studies of the Combustion of Drops in a Fuel Spray - The Burning of Single Drops of Fuel, Fourth Symposium (International) on Combustion, The Combustion Institute, pp. 818-830, 1952.

Gökalp, I., Chauveau, C., Simon, O., Chesneau, X., Mass Transfer from Liquid Fuel Droplets in Turbulent Flow, *Combustion and Flame*, Vol. 89, pp. 286-298, 1992.

Gökalp, I., Chauveau, C., Durox, D., Lacas, F., Legrand, B., Shafirovich, E., Preliminary Analysis of a High Pressure Spray and Cloud Combustion Module for the ISS, Fifth International Microgravity Workshop, Cleveland, Ohio, 1999.

Greenberg, J. B., McIntosh, A. C., Brindley, J., Instability of a Flame Front Propagating Through a Fuel-Rich Droplet-Vapour-Air Cloud, *Combustion Theory Modelling*, Vol. 3, pp. 567-584, 1999.

Greenberg, J. B., Stability Boundaries of Laminar Premixed Polydisperse Spray Flames, *Atomization and Sprays*, Vol. 12, pp. 123-143, 2002.

Greenhalgh, D. A., Jermy, M. C., Doherty, W. G., Hussain, M., The Response of Fuel Injector Sprays to Acoustic Forcing, *Proceedings of ESDA 2004: 7th Biennial ASME Conference Engineering Systems Design and Analysis*, ASME paper ESDA 2004-58617, Manchester, 2004.

Groff, G. E., The Cellular Nature of Confined Spherical Propane-Air Flames, *Combustion and Flame*, Vol. 48, pp. 51-62, 1982

Groves, J. S., Personal Communications, 2006.

Gu, X. J., Haq, M. Z., Lawes, M., and Woolley, R., Laminar Burning Velocity and Markstein Lengths of Methane-Air Mixtures, *Combustion and Flame*, Vol. 121, pp. 41-58, 2000.

Hanai, H., Maruta, K., Kobayashi, H. and Niioka, T., Pulsating Flame Propagation of PMMA-Particle-Cloud in Microgravity, 27th Symposium (International) on Combustion, The Combustion Institute, pp. 2675-2681, 1998.

Haq, M. Z., Fundamental Studies of Premixed Combustion, PhD Thesis, School of Mechanical Engineering, University of Leeds, 1998.

Harper, C. M., Turbulence and Combustion Instabilities in Engines, PhD Thesis, School of Mechanical Engineering, University of Leeds, 1989.

Hayashi, S. and Kumagai, S., Flame Propagation in Fuel Droplet-Vapor-Air Mixtures, Proc. Combustion Institute, Vol. 15, pp. 445-452, 1974.

Hayashi, S. and Kumagai, S., Sakai, T, Propagation Velocity and Structure of Flames in Droplet-Vapor-Air Mixtures, Combustion Science and Technology, Vol. 15, pp. 169-177, 1976.

Heywood, J. B., Internal Combustion Engine Fundamentals, McGraw Hill, 1983.

Ishima, T., Sukena, R., Liu, C., Obokata, T., Kawachi, K., Kobayashi, K., Relationship between Fuel Injection Rate and Spray Characteristics of the Swirl Nozzle for Gasoline Engine, Proceedings of the Fifth International Symposium on Diagnostics and Modeling of Combustion in Internal Combustion Engines (COMODIA 2001), Paper 3-12, pp. 493-498, 2001.

Kalitan, D. M., Hall, J. M., and Petersen, E. L., Ignition and Oxidation of Ethylene-Oxygen-Diluent Mixtures with and Without Silane, Journal of Propulsion and Power, Vol. 21, pp. 1045-1056, 2005.

Kwon, S., Tseng, L. -K., and Faeth, G. M., Laminar Burning Velocities and Transition to Unstable Flames in $H_2/O_2/N_2$ and $C_3H_8/O_2/N_2$ Mixtures, Combustion and Flame, Vol. 90, pp. 230-246, 1992.

Landau, L. D., On the Theory of Slow Combustion, Acta Phys.-chim, URSS, 19, 77, 1944, in Collected Papers of Landau, (D.Ter Haar, Ed.), Pergamon Press, 1965.

Larsson, G., Turbulence Related Cyclic Variation in Combustion, PhD Thesis, School of Mechanical. Engineering, University of Leeds, in preparation.

Law, C. K., Dynamics of Stretched Flames, 22nd Symposium (International) on Combustion, The Combustion Institute, pp. 1381-1402, 1988.

Lawes, M., Personal Communications, 2006.

Lawes, M., *Effects of Turbulence on Combustion in Engines*, PhD Thesis, School of Mechanical Engineering, University of Leeds, 1987.

Lawes, M., *Lecture Note on Diffusion Flames, Droplet Evaporation and Droplet Combustion*, University of Leeds, 2004.

Lawes, M., Marquez, N, and Sulaiman, S. A., *On Instabilities and Flame Structures of Laminar Aerosol Flames*, Proc. of the European Combustion Meeting 2005, Paper No. 81, Louvain-la-Neuve, Belgium, 2005.

Lawes, M., Ormsby, M. P., Sheppard, C. G. W., and Woolley, R., *Variation of Turbulent Burning Rate of Methane, Methanol, and Iso-octane Air Mixtures with Equivalence Ratio at Elevated Pressure*, *Combustion Science and Technology*, Vol. 177, pp. 1273-1289, 2005.

Lefebvre, A. H., *Atomization and Sprays*, Hemisphere Publishing, New York, 1989.

Liu, K., *Personal Communications*, 2006.

Lui, F., Daun, K. J., Beyer, V., Smallwood, G. J., and Greenhalgh, D. A., *Some Theoretical Considerations in Modelling Laser-Induced Incandescence at Low Pressures*, Submitted to *Applied Physics B*, 2006.

Maly, R., *Spark Ignition: Its Physics and Effect on the Internal Combustion Engine*, in *Fuel economy in Road Vehicles Powered by Spark Ignition Engines*, (J. C. Hilliard and G. S. Springer, Eds.), Plenum Press, New York, 1984.

Marquez, N., *Fundamental Studies of Aerosol Flames*, PhD Thesis, School of Mechanical Engineering, University of Leeds, 2003.

Mathieu, J.P., *Optics*, (translated by J.W. Blaker) Oxford: Pergamon, 1975.

Metghalchi, M. and Keck, J., Burning Velocities of Mixtures of Air with Methanol, Iso-octane and Indolene at High Pressure and Temperature, *Combustion and Flame*, Vol. 48, pp. 191-210, 1982.

Mizutani, Y., and Nakajima, A., Combustion of Fuel Vapour-Drop-Air Systems: Part I, Open Burner Flames, *Combustion and Flame*, Vol. 20, pp. 343-350, 1973a.

Mizutani, Y., and Nakajima, A., Combustion of Fuel Vapour-Drop-Air Systems: Part II, Spherical Flames in a Vessel, *Combustion and Flame*, Vol. 21, pp. 351-357, 1973b.

Mokhtar, A. S., Fundamental Study of Ignition and Combustion of Two Phase Flows at Gas Turbine Conditions, PhD Thesis, School of Mechanical Engineering, University of Leeds, 2001.

Myers, G. D. and Lefebvre, A. H., Flame Propagation in Heterogeneous Mixtures of Fuel Drops and Air, *Combustion and Flame*, Vol. 66, pp. 193-210, 1986.

Nakabe, K., Mizutani, Y., Hirao, T. and Tanimura, S., Burning Characteristics of Premixed Sprays and Gas-Liquid Coburning Mixtures, *Combustion and Flame*, Vol. 74, pp. 39-51, 1988.

Nakamura, M., Akamatsu, F., Kurose, R., and Katsuki, M., Combustion Mechanism of Liquid Fuel Spray in a Gaseous Flame, *Physics of Fluids*, Vol. 17, pp. 123301-123314, 2005.

Nicoli, C., Haldenwang, P., and Suard, S., Analysis of Pulsating Spray Flames Propagating in Lean Two-Phase Mixtures with Unity Lewis Number, *Combustion and Flame*, Vol. 143, pp. 299-312, 2005.

Nomura, H., Izawa, K., Ujiie, Y., Sato, J., Marutani, Y., Kono, M. and Kawasaki, H., An Experimental Study on Flame Propagation in Lean Fuel Droplet-Vapor-Air Mixtures Using Microgravity Conditions, 27th Symposium (International) on Combustion, The Combustion Institute, pp. 2667-2674, 1998.

Nomura, H., Kawasumi, I., Ujiie, Y., Sato, J., Effects of Pressure on Flame Propagation in a Premixture Containing Fine Fuel Droplets, 31st Symposium (International) on Combustion, Proc. Combustion Institute, Vol. 31, Article in Press, 2006.

Ormsby, M. P., Turbulent Flame Development in a High-Pressure Combustion Vessel, PhD Thesis, School of Mechanical Engineering, University of Leeds, 2005.

Ormsby, M. P., Personal Communications, 2006.

Peters, N., Laminar Flamelet Concepts in Turbulent Combustion, Twenty-first Symposium (International) on Combustion, The Combustion Institute, Pittsburgh, pp. 1231-1250, 1988.

Polymeropoulos C. E., Flame propagation in Liquid Fuel, Fuel Vapor and Air Mixtures, Chemical and Physical Processes in Combustion (Combustion Institute), pp. 1-4, 1983.

Polymeropoulos, C. E., Flame Propagation in Aerosols of Fuel Droplets, Fuel Vapour and Air, Combustion Science and Technology, Vol. 40, pp. 217-232, 1984.

Rao, K. V. L. and Lefebvre, A. H., Minimum Ignition Energies in Flowing Kerosine-Air Mixtures, Combustion and Flame, Vol. 27, pp. 1-20, 1976.

Richards, G. A. and Lefebvre, A. H., Turbulent Flame Speeds of Hydrocarbon Fuel Droplets in Air, Combustion and Flame, Vol. 78, pp. 299-307, 1989.

Scott, M. J., Distribution of Strain Rate and Temperature in Turbulent Combustion, PhD Thesis, School of Mechanical Engineering, University of Leeds, 1992.

Schick, R. J., An Engineer's Practical Guide to Drop Size, Spraying Systems Co., Bulletin No. 459, 1997.

Searby, G. and Quinard, J., Direct and Indirect Measurements of Markstein Numbers of Premixed Flames, *Combustion and Flame*, Vol. 82, pp. 298-311, 1990.

Sivashinsky, G. I., Diffusional-Thermal Theory of Cellular Flames, *Combustion Science and Technology*, Vol. 15, pp. 137-146, 1977.

Schwartz, S. E., Cloud Droplet Nucleation and Its Connection to Aerosol Properties, *Proc. 14th Int. Conf. Nucleation and Atmospheric Aerosols*, Elsevier Science, Oxford, pp. 770-779, 1996.

Spalding, D. B., The Combustion of Liquid Fuels, 4th Symposium (International) on Combustion, The Combustion Institute, pp. 847-864, 1952.

Spiglanin, T. A., McIlroy, A., Fournier, E. W., Cohen, R. B., Syage, J. A., Time-Resolved Imaging of Flame Kernels: Laser Spark Ignition of H₂/O₂/Ar Mixtures, *Combustion and Flame*, Vol. 102, pp. 310 - 328, 1995.

Stårner, S. H., Gounder, J., and Masri, A. R., Effects of Turbulence and Carrier Fluid on Simple, Turbulent Spray Jet Flames, *Combustion and Flame*, Vol. 143, pp. 420-432, 2005.

Strehlow, R. A., *Combustion Fundamentals*, McGraw-Hill, New York, 1984.

Su, T. F., Chang, C. T., Reitz, R. D., Farrell, P. V., Pierpont, A. D. and Tow, T. C., Effects of Injection Pressure and Nozzle Geometry on Spray SMD and D.I. Emissions, SAE Paper No. 952360, 1995.

Tait, N. P., and Greenhalgh, D. A., PLIF Imaging of Fuel Fraction in Practical Devices and LII Imaging of Soot, *Deutsche Bunsen-Gesellschaft für Physikalische Chemie*, Vol. 97, pp. 1619-1625, 1993.

Tsushima, S., Saitoh, H., Akamatsu, F. and Katsuki, M., Observation of Combustion Characteristics of Droplet Clusters in a Premixed-Spray Flame by Simultaneous Monitoring of Planar Spray Images and Local Chemiluminescence, 27th Symposium (International) on Combustion, The Combustion Institute, pp. 1967-1974, 1998.

Turns, S. R., An Introduction to Combustion: Concepts and Applications, McGraw-Hill, New York, 2000.

Wilson, C. T. R., Condensation of Water Vapour in the Presence of Dust-free Air and Other Gases, Proc. R. Soc. London, Vol. 189, pp. 265-307, 1897.

Wilson, C. T. R., On a Method of Making Visible the Paths of Ionising Particles through a Gas, Proc. R. Soc., London, A85, pp. 285-288, 1911.

Yaws, C. L., Handbook of Vapor Pressures, Vol. 3, Gulf Publications Co., Houston, 1994.

Zhu, M., Dowling, A. P., and Bray, K. N. C., Combustion Oscillations in Burners With Fuel Spray Atomizers, ASME Paper 99-GT-302, 1999.

Zhu, M., Dowling, A. P., and Bray, K. N. C., Self-Excited Oscillations in Combustors With Spray Atomizers, ASME Paper 2000-GT-0108, 2000.

Zhu, M., Dowling, A. P., and Bray, K. N. C., Integration of CFD and Low-order Models for Combustion Oscillations in Aeroengines, Fifteenth International Symposium on Airbreathing Engines, ISABE-2001-1088, 2001.

Appendix

Additional Characterisation Measurements

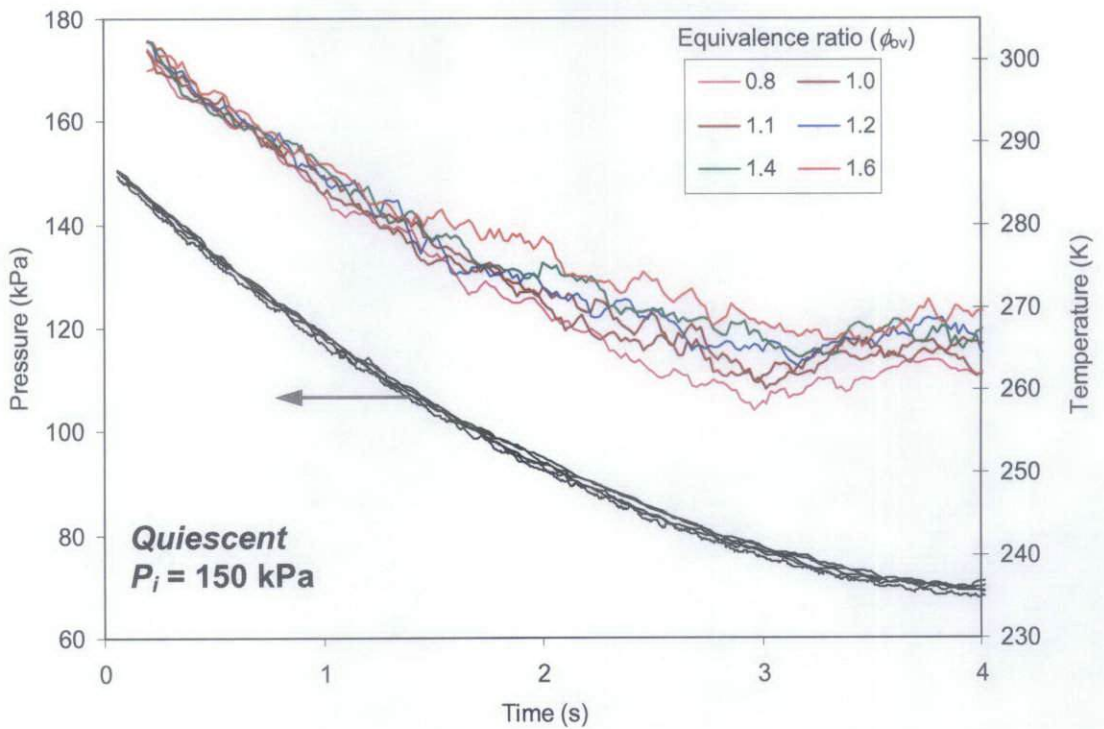


Figure A1 Variation in chamber pressure and temperature with time during the expansion of quiescent iso-octane mixtures at various ϕ_{ov} from 150 kPa and 303 K.

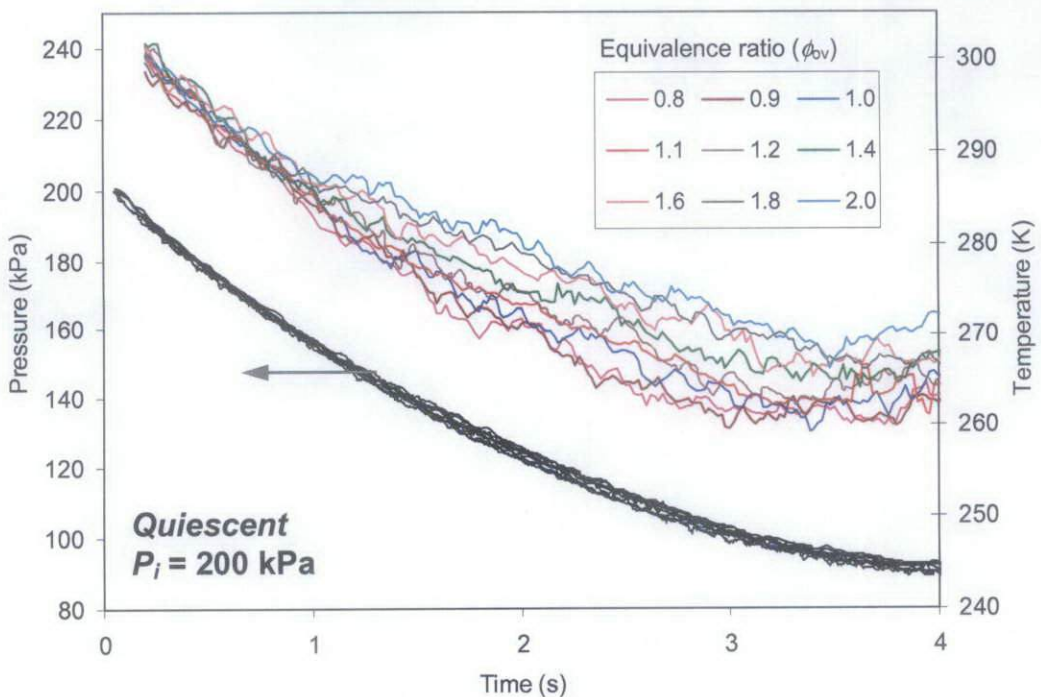


Figure A2 Variation in chamber pressure and temperature with time during the expansion of quiescent iso-octane mixtures at various ϕ_{ov} from 200 kPa and 303 K.

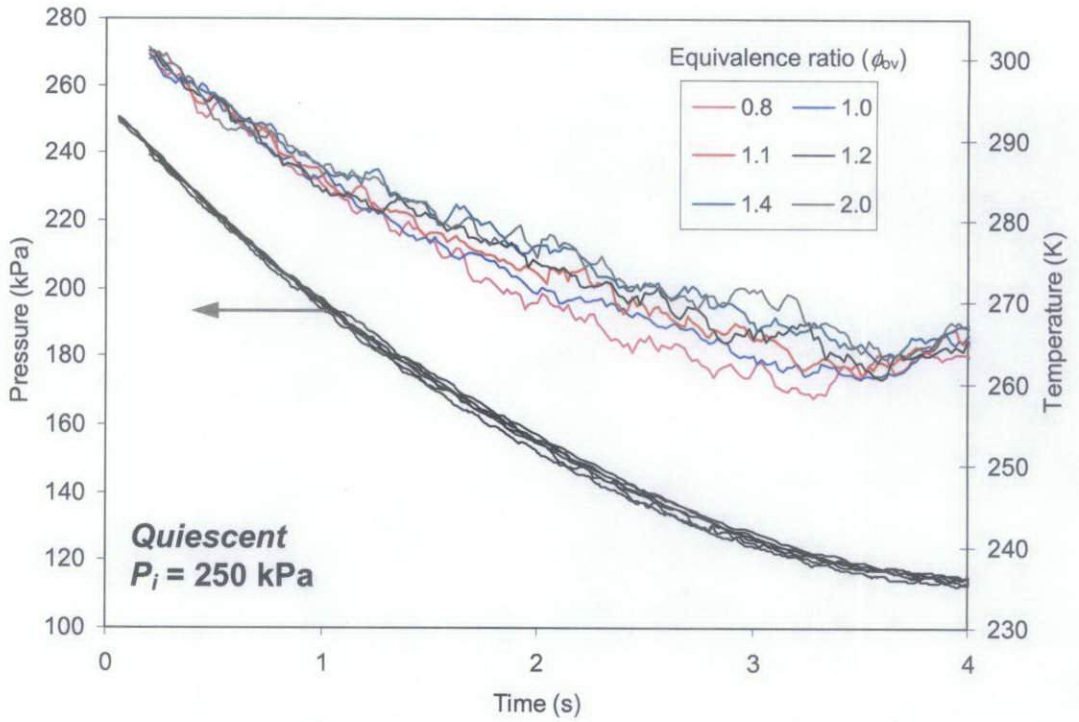


Figure A3 Variation in chamber pressure and temperature with time during the expansion of quiescent iso-octane mixtures at various ϕ_{ov} from 250 kPa and 303 K.

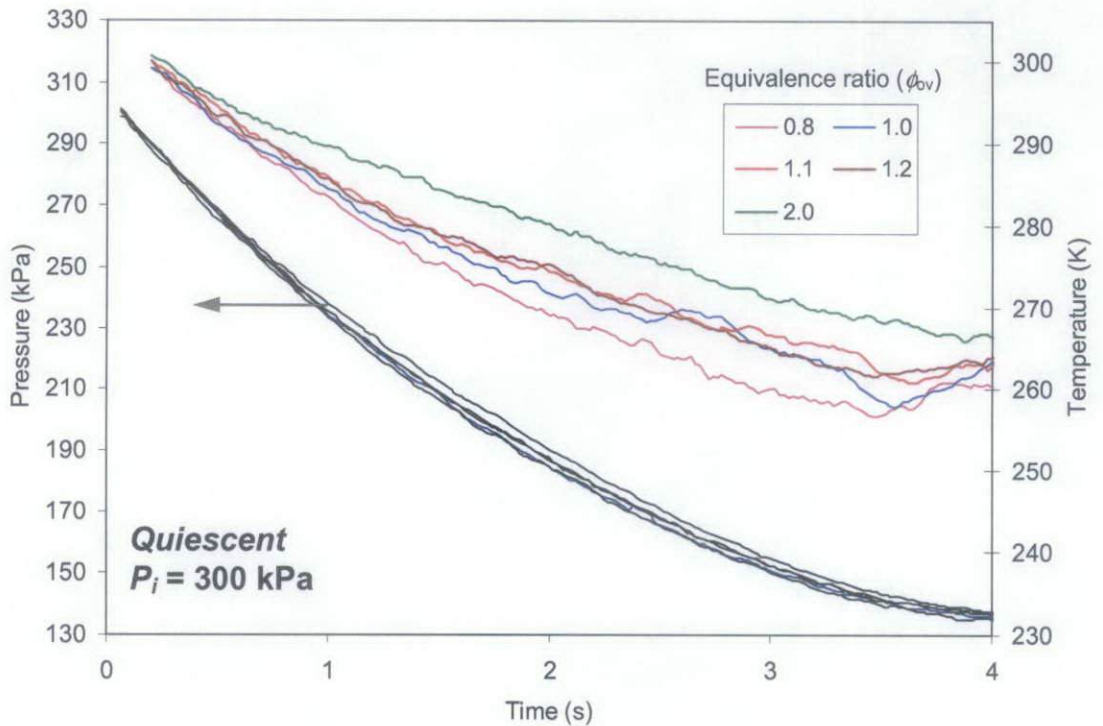


Figure A4 Variation in chamber pressure and temperature with time during the expansion of quiescent iso-octane mixtures at various ϕ_{ov} from 300 kPa and 303 K.

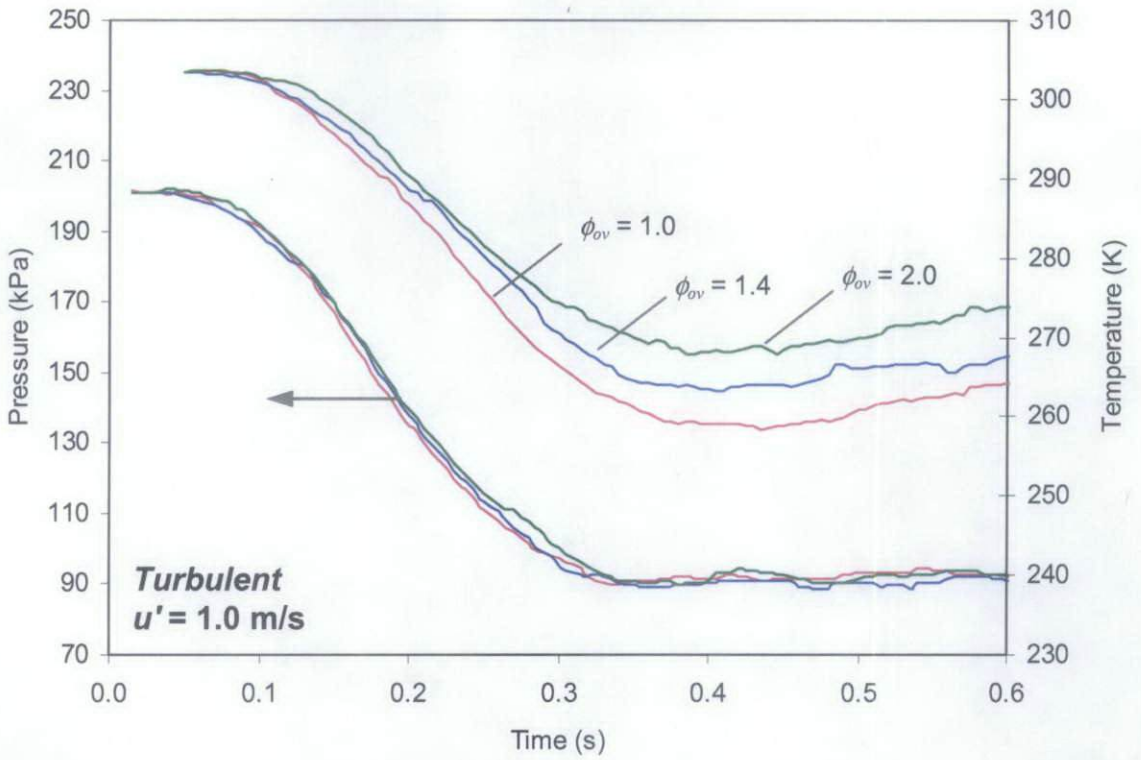


Figure A5 Variation in pressure and temperature with time for turbulent iso-octane aerosols expanded from 200 kPa and 303 K at u' of 1.0 m/s.

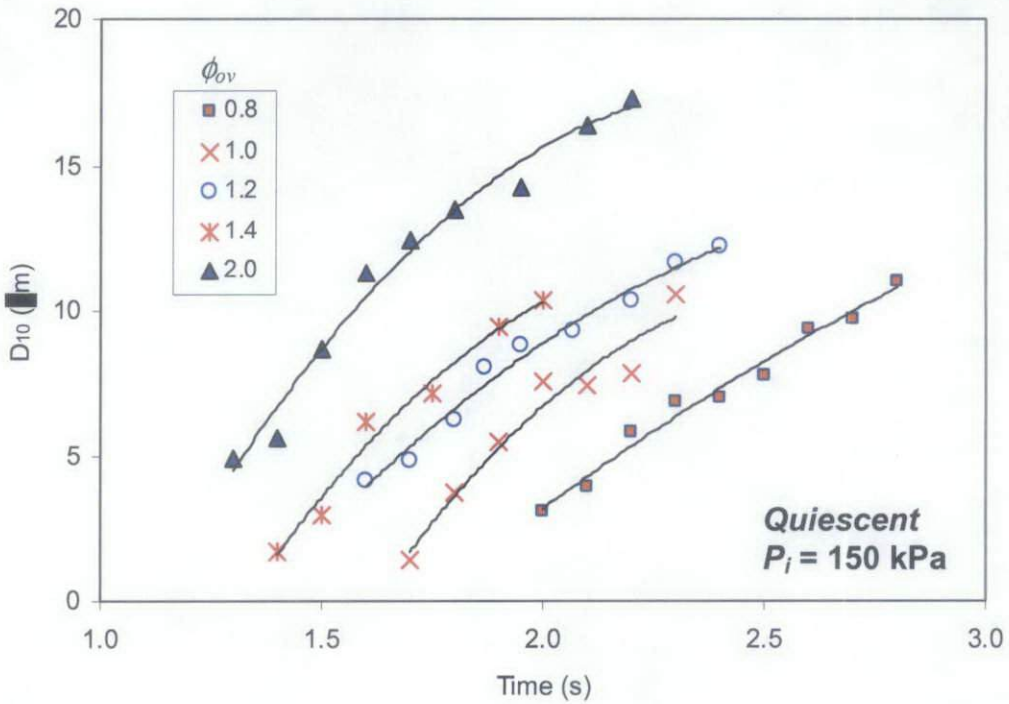


Figure A6 Variation in D_{10} with time for quiescent iso-octane mixtures expanded from 150 kPa and 303 K at various equivalence ratios.

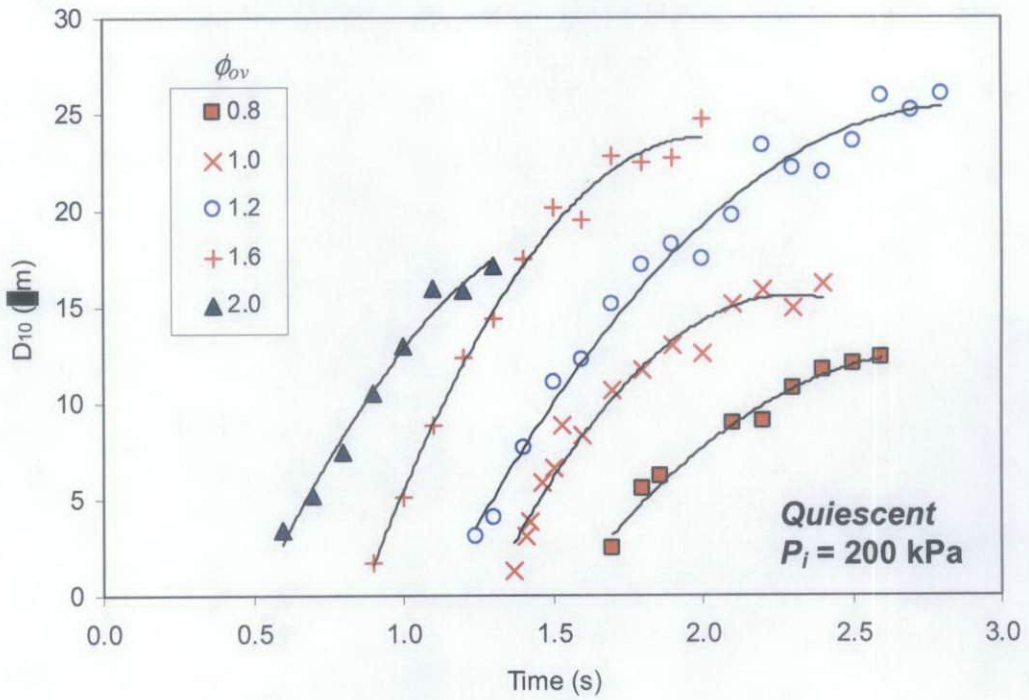


Figure A7 Variation in D_{10} with time for quiescent iso-octane mixtures expanded from 200 kPa and 303 K at various equivalence ratios.

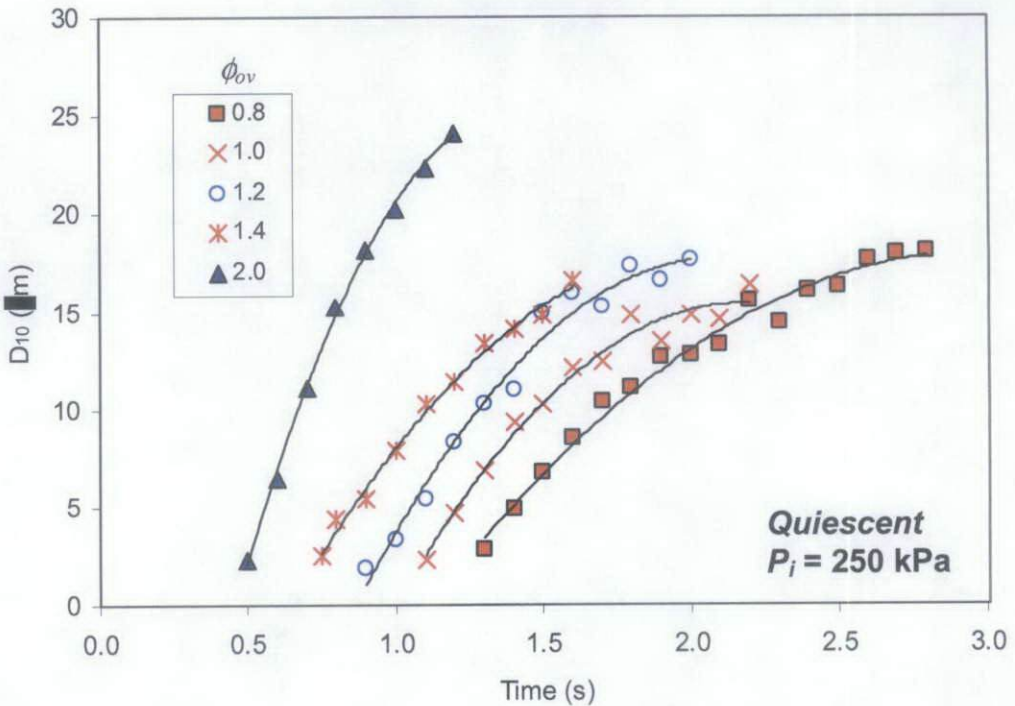


Figure A8 Variation in D_{10} with time for quiescent iso-octane mixtures expanded from 250 kPa and 303 K at various equivalence ratios.

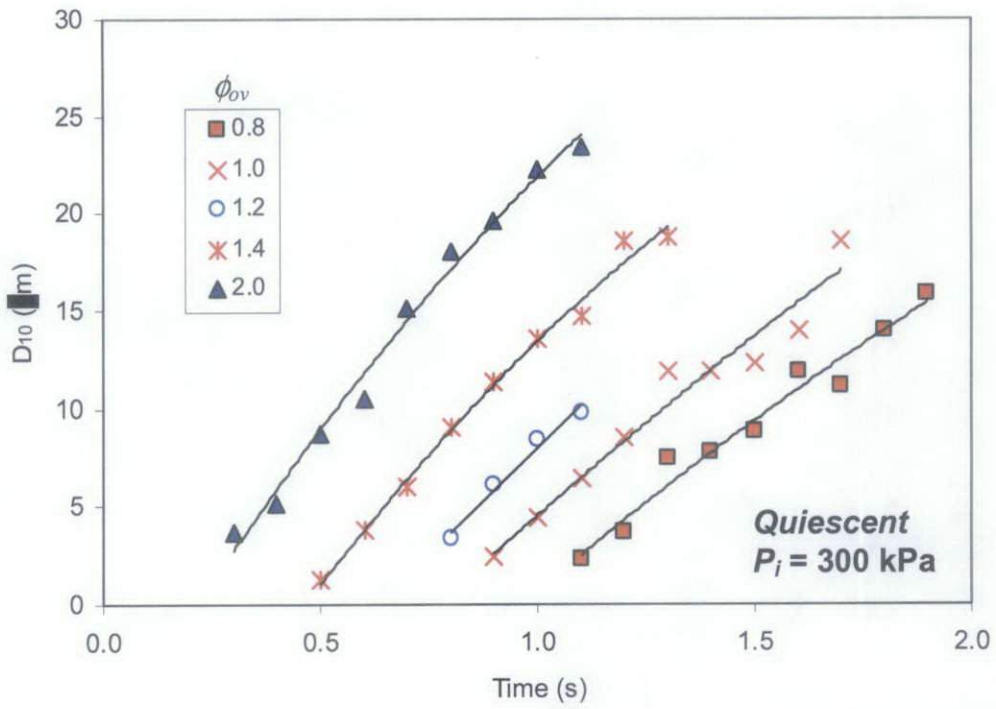


Figure A9 Variation in D_{10} with time for quiescent iso-octane mixtures expanded from 300 kPa and 303 K at various equivalence ratios.

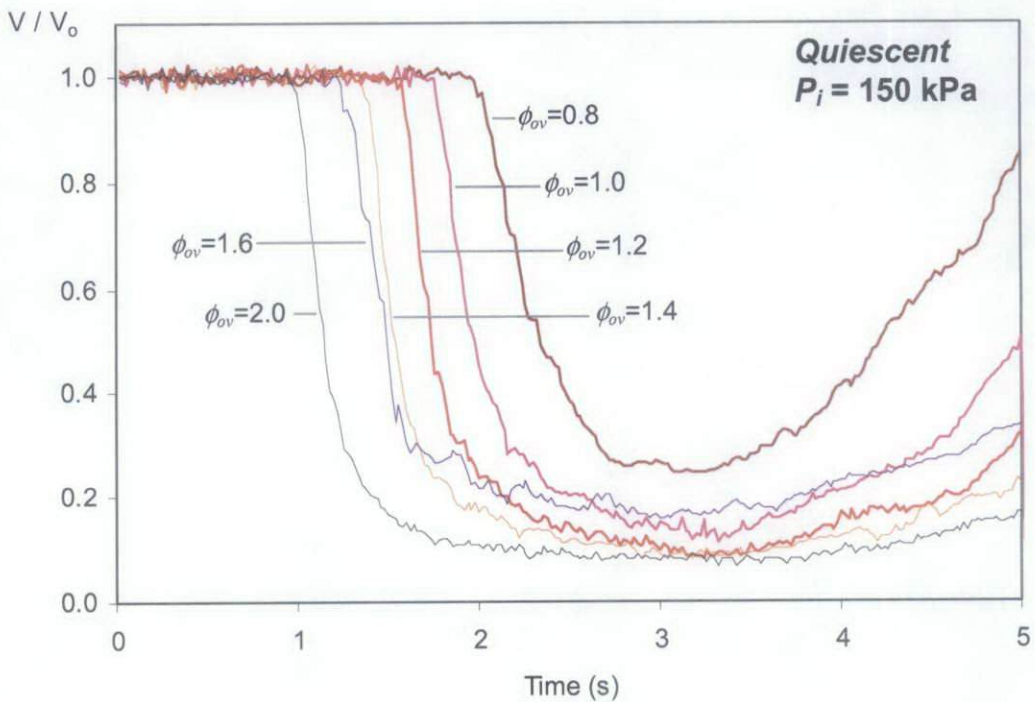


Figure A10 Laser power attenuation produced by clouds of quiescent iso-octane aerosols expanded from 150 kPa, 303 K, at various equivalence ratios.

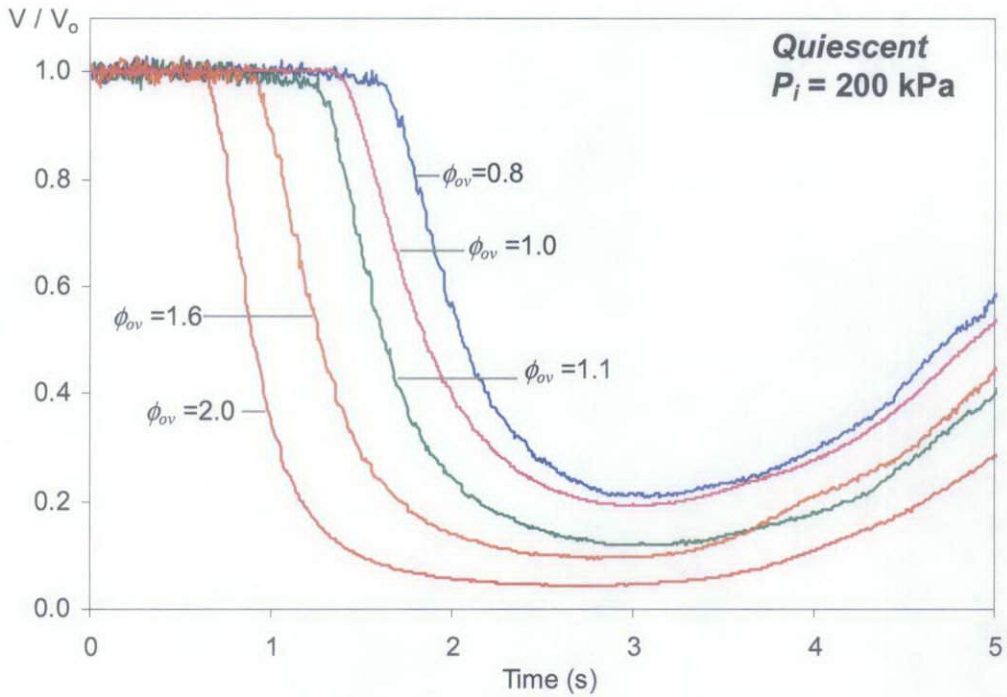


Figure A12 Laser power attenuation produced by clouds of quiescent iso-octane aerosols expanded from 200 kPa, 303K, at various equivalence ratios.

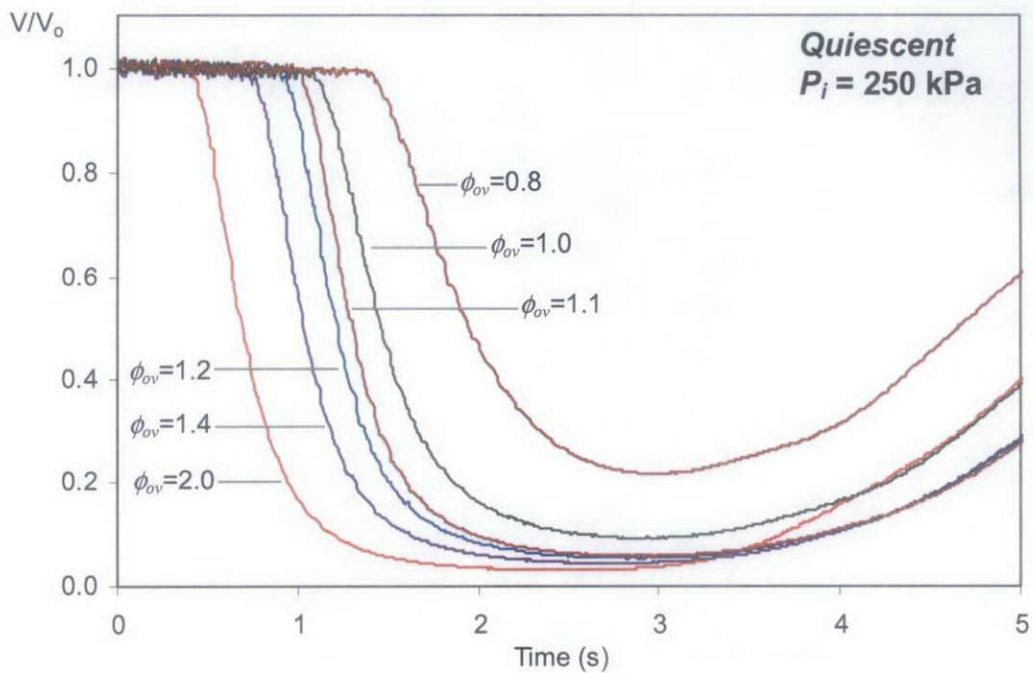


Figure A13 Laser power attenuation produced by clouds of quiescent iso-octane aerosols expanded from 250 kPa, 303K, at various equivalence ratios.

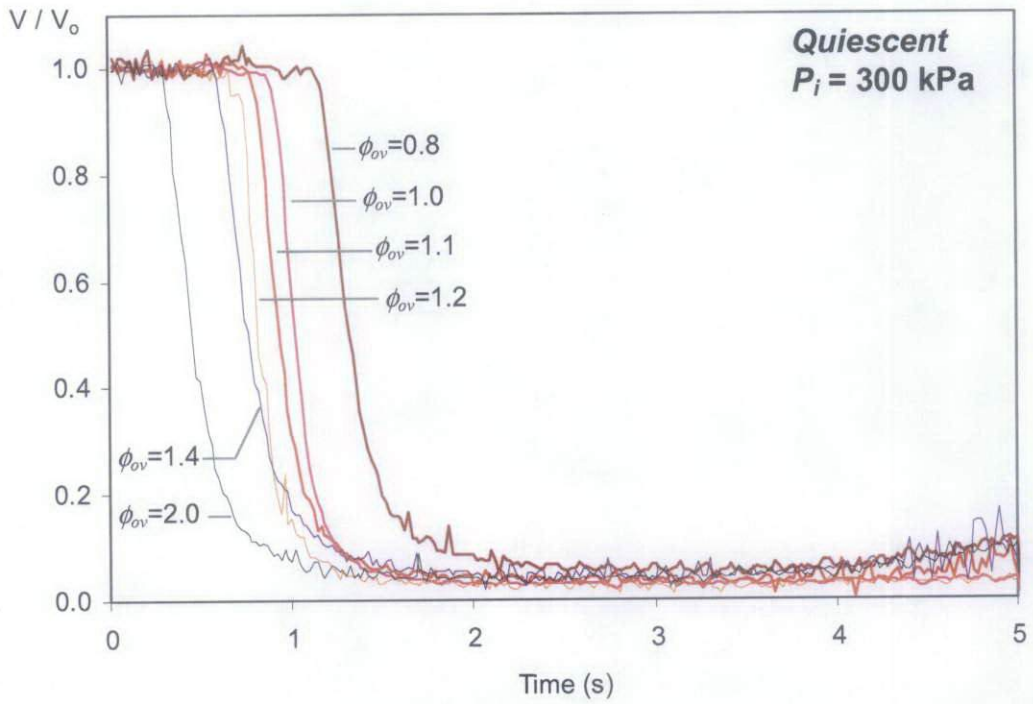


Figure A14 Laser power attenuation produced by clouds of quiescent iso-octane aerosols expanded from 300 kPa, 303K, at various equivalence ratios.